Experimental observations of the correspondence of Alfvénic and compressional waves in the Solar Wind high-speed streams with the geomagnetic activity at high latitudes in the Ultra Low-Frequency range

by

Giuseppina Carnevale

University of L'Aquila - INGV

Department of Physical and Chemical Sciences
PhD thesis - Space Physics

Supervisors

Prof. Patrizia Francia Dott. Mauro Regi Dott. Stefania Lepidi

Contents

Introduction

This work aims to investigate the effects of Alfvénic and compressional fluctuations, typically present in corotating high-speed streams, on the geomagnetic activity at high latitudes in the Pc5 frequency range, which is a range of frequency comparable to that of Alfvén waves in the Solar Wind (SW) at 1 AU. The study of Pc5 pulsations is important in the framework of space weather since they are responsible for the energization, transport and precipitation of electrons in the radiation belts

The structure of the thesis is the following: the first chapter is about the SW and the interplanetary magnetic field (IMF), with a peculiar focus on the corotating solar wind structures and on the types of waves that are observed in plasma in MHD approximation, especially compressive and transversal Alfvén waves. Since the SW is a plasma characterized by a high Reynolds number (turbulent behavior), the first chapter also briefly discusses MHD turbulence, particularly the Alfvénic one, describing the tools necessary for its analysis. The second chapter regards the geomagnetic field in its more general treatment, with particular attention to the variations to which the field is subject, especially related to its interaction with the SW, with a specific interest in the Pc5 frequency range. Chapter 3 describes the data utilized, both for SW and ground analysis. Chapter 4 contains the description of a rotation procedure from the HEE to the MEMFA reference frame, utilized to identify the main magnetic field direction and the presence of Alfvén waves. This Chapter also shows a reliability test of the method, via Monte Carlo tests, in identifying Alfvén waves in the presence of white and red noise. Chapter 5 regards the individuation of a composite quiet background for the geomagnetic power to re-scale the geomagnetic data for the next analysis. Chapter 6 regards the joint analysis between Solar Wind with its IMF and the geomagnetic power at the ground in the Pc5 range at different latitudes: in particular, the investigation of the effects of four selected co-rotating high-speed streams on geomagnetic fluctuations, taking into account the Alfvénic or non-Alfvénic nature of solar wind fluctuations, the geoeffective component of the interplanetary electric field, the coherence analysis between the solar wind powers and the ground power at high latitudes.

Chapter 1

The Solar Wind

1.1 The Solar Wind and the Interplanetary Magnetic Field

The Solar Wind (SW) is a continuous flow of ionized plasma, primarily electrons, protons, and minor ions, that pervades the interplanetary space, flowing outward from the Sun. The discovery of the existence of the SW goes back to the early 1950s, when the German physicist Ludwig Biermann, observing the comets and their characteristic of having their tails always turned in an anti-solar direction, developed a model for the interaction of the particles constituting the comets with those coming from the Sun [1, 2]. He hypothesized that the emission by the Sun of a constant flow of particles was capable of pushing away some frozen particles of the comets, forming their tail, regardless of the heliographic latitude. Some years later, in 1957, Hannes Alfvén hypothesized that the Solar Wind was magnetized and that its flow would shape the magnetic field around the comet, creating an elongated magnetic tail extending in the antisolar direction [3]. At the same time, Chapman hypothesized that the solar wind particles had very high thermal velocities even far from the Sun so that they could escape its gravitational attraction [4]. Indeed, the solar corona, the outermost layer of the Sun's atmosphere, is a region where temperatures reach high values (greater than 10^6K). Here the plasma is fully ionized, and it is composed of electrons and protons, with a small percentage of ionized helium and partially ionized heavy ions.
In 1958 Eugene Parker proposed a hydrodynamic theoretical description for the solar Corona [5], in which he showed that the SW expansion is a direct consequence of the high coronal temperature. The SW velocity rapidly increases, as soon as it moves away from the solar surface, till a critical point close to the Sun, from where the SW becomes supersonic. According to Parker model, the SW flows with an approximately constant velocity until it is balanced by the pressure of the interstellar medium. This boundary is called heliopause, whos its crossing was experimentally observed by Voyager 2 on 5 November 2018 at

119 AU [6].

On the other hand, the Sun has a magnetic field that extends throughout the surrounding space, for this reason, it is called Interplanetary Magnetic Field (IMF). The Sun's magnetic field has a complex and dynamic structure influenced by the Sun's differential rotation. The Sun is not a solid body and it rotates at different rates depending on the latitude: the solar equator rotates faster than the higher latitudes. If the Sun did not rotate, the field lines would be radial, and the plasma would move them away in the same direction; but, in the presence of the Sun's rotation, the heliospheric magnetic field transported by the solar wind (according to the Alfvén theorem, see section 1.3) gets wrapped into a spiral (Figure 1.1 a).
The angular solar speed, the distance, and the radial velocity determine the spiral curvature. On the ecliptic plane the spirals form an angle Ψ with the radial direction given by

$$\tan \Psi = \frac{r\Omega}{v_{sw}} \tag{1.1}$$

where Ω is the angular velocity of the Sun ($2.7 \times 10^{-6} rad \cdot s^{-1}$), r is the distance from the Sun and v_{sw} is the SW radial velocity. At the Earth's orbit the the angle between the IMF and the Earth-Sun direction is on average $\sim 45°$. Clearly, according to equation 1.1, a faster wind corresponds to a lower curvature, and a slower wind corresponds to a higher curvature.

Definitive confirmation of the IMF polarity came from the exploration in interplanetary space made by the Ulysses space probe, which performed the first exploration at high heliospheric latitude in 1998. It was confirmed that, at that time and at all latitudes, the magnetic field had a magnetic polarity directed outward the northern hemisphere of the Sun and inward in the southern hemisphere [7]. The magnetic lines that originate from the opposite hemispheres meet in the equatorial zone with opposite polarity (entering or leaving the Sun) and are separated by a current that circulates in the equatorial plane of the dipole and that constitutes the heliospheric current sheet (Figure 1.1 b). On a large scale, the IMF can be schematized as a dipolar structure (Figure 1.1 b), but the Sun's overall magnetic field becomes distorted and twisted over time, mainly due to its differential rotation, with different effects at various scales. The interaction of the solar plasma with these twisted magnetic field lines results in the generation of sunspots, solar flares, and other solar phenomena. The number of sunspots and the dipole polarity reversion varies with an 11-year cycle, called the solar activity cycle (a complete magnetic cycle, called the Hale cycle, comprises two solar cycles). During the solar cycle, the Sun's magnetic activity increases and decreases. At the maximum of the solar cycle, the solar activity is elevated: sunspots are more numerous, solar flares (sudden and intense releases of energy on the Sun's surface) are more frequent and, there is a higher occurrence of Coronal Mass Ejections (CMEs; large expulsions

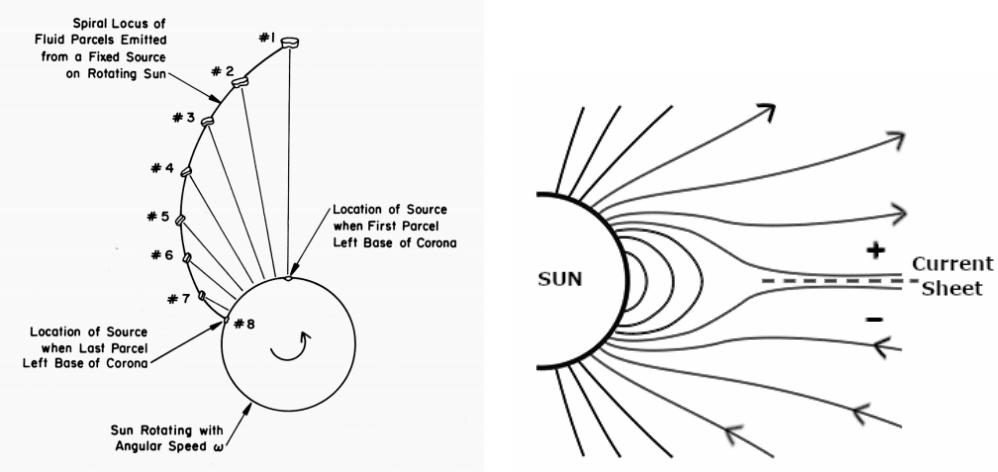

(a) *Locations of a succession of fluid parcels emitted at a constant speed from a source fixed on the rotating Sun. As the wind expands into the interplanetary space, due to its high electrical conductivity, it carries the solar magnetic field lines with it, forming the IMF Parker spiral.*

(b) *Simplified model of the solar magnetic field, with closed field lines near the dipole equator (dipole configuration) and magnetic field lines "drawn outward" at high latitudes by the expanding plasma; these lines become "open" field lines (that eventually return to the Sun but first they extend to very large heliocentric distances).*

Figure 1.1

of plasma and magnetic field from the Sun's corona, released into space). At the minimum, solar activity is subdued: sunspots become less frequent, and the Sun's surface appears relatively calm, solar flares and CMEs are less frequent and less intense. It's important to note that while these features are observed on average, solar activity can be widely variable, and significant events can occur at any point in the solar cycle.

Since the Sun's magnetic field is a distorted dipole, the plane separating the magnetic field lines of opposite polarity is wavy. It resembles a dancer's skirt, as schematized in figure 1.2, as it rotates (hence the *"ballerina"* model proposed by Alfvén in 1977 [9]) and it is more deformed during higher solar activity.

It is meaningful to note that the solar cycle and its related events are of particular importance when they interact with the terrestrial magnetosphere (see chapter 2) because they influence space weather, satellite operations, and communication systems on Earth.

SW and IMF are closely related: since the SW is a highly ionized collisionless plasma, it carries with it the IMF, in accordance with the Alfvén theorem, which states that electrically conducting fluids and embedded magnetic fields are constrained to move together in the limit of large magnetic Reynolds numbers (R_m). This number is a dimensionless quantity that estimates the relative effects of advection (or induction) of a magnetic field by the motion of a conducting medium to the magnetic diffusion. For more details, see the section

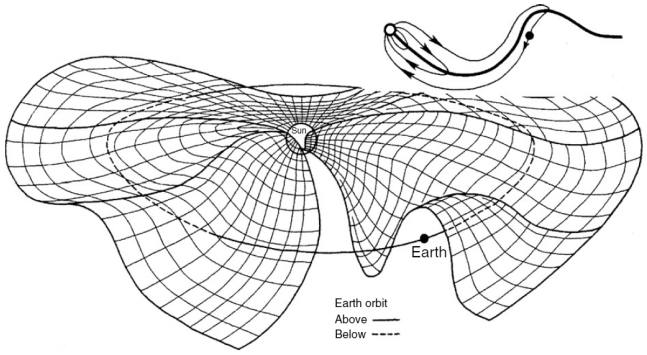

Figure 1.2: *Three-dimensional sketch of the wavy structure of the interplanetary current sheet and associated magnetic field lines. When the Sun rotates, an observer near the ecliptic will alternately lie above and below the current and will see a changing sector pattern. The inset shows a meridional cross-section with the Earth below the current sheet. [8]*

1.3.

1.2 Structure of the Solar Wind

Since the beginning of the space age, remote sensing outside the Earth's magnetosphere has provided detailed measurements of the interplanetary medium, which on average are in accordance with Parker's model. Analysis of SW in-situ measurements allows us to classify the SW mainly into three different types based on its characteristics: slow wind, fast wind, and wind attributed to transient phenomena. The classification is often related to the speed, temperature, density, and other properties of the solar wind. The existence of these diverse wind types implies a non-uniform solar corona and suggests that the SW emanates from different coronal structures. [10].

The *slow solar wind* originates from regions of the Sun's corona associated with streamers, which are elongated structures over the solar equator structured by closed magnetic fields; the *slow solar wind* is characterized by a relatively lower speed, typically around 400 km/s and it is denser than the fast wind. It is associated with the *helmet streamers* (figure 1.3a), which are bright, active areas characterized by closed magnetic field loops emerging from the photosphere and containing dense plasma. They have an elongated shape because they are dragged by the solar wind moving away from the Sun, in a range of latitudes within $\pm 40°$ from the Sun's equator (called the *band of streamers*). Their distribution and quantity follow the solar cycle activity; they are often absent during the solar minimum.

The *fast wind* originates from the coronal holes (CHs), as those shown in

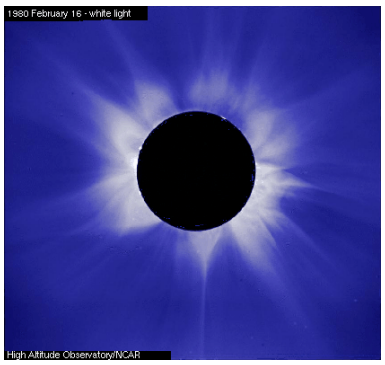

(a) *Helmet streamers observed by the coronagraph aboard Skylab, on 16 February 1980 (maximum of SC 21).*

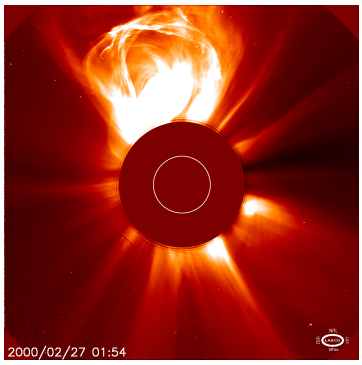

(b) *Coronal mass ejection observed by the coronagraph LASCO aboard SOHO spacecraft, on 27 February 2000 (maximum of SC 23).*

Figure 1.3

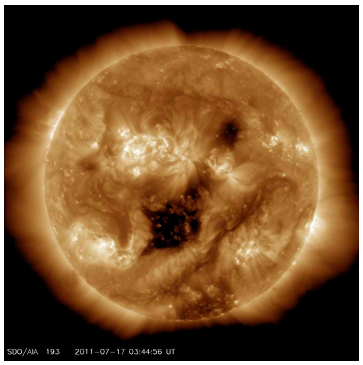

(a) *Equatorial coronal hole, observed on 17 July 2011 (in the ascending phase of solar cycle) by SDO/AIA at X rays (193 Å).*

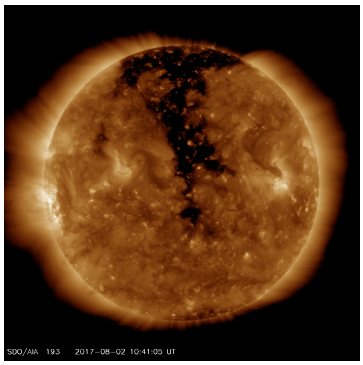

(b) *Polar coronal hole, observed on 2 August 2017 (in the descending phase of solar cycle) by SDO/AIA at X rays (193 Å).*

Figure 1.4

Figure 1.4 taken from Solar Dynamics Observatory/Atmospheric Imaging Assembly (SDO/AIA) in the band-pass at 193 Å. Coronal holes are regions of lower density and open unipolar magnetic field lines in the Sun's corona, characterized by cold plasma [11]. For this reason, they appear darker than the surrounding regions. Satellite observations, and in particular the contribution of the Ulysses mission in the 1990s, have provided direct evidence that CHs are the sources of the fast solar wind, characterized by magnetic field lines open to interplanetary space. CHs often form in regions where the Sun's magnetic field is weaker and open, allowing the solar wind to stream more freely. The

distribution and characteristics of CHs vary with the solar cycle. During solar minimum, coronal holes tend to be concentrated near the solar poles. As the Sun approaches solar maximum, CHs become more evenly distributed at various latitudes. The differential rotation of the Sun causes the migration of CHs across the solar disk over time. CHs near the solar equator have a faster rotation period than those near the poles. The largest and most stable ones extend in the declining phase from the polar regions to lower latitudes towards the equatorial zone (figure 1.4b). During the solar minimum, the CHs are located at the north and south polar regions of the Sun, determining, in this phase, a configuration of the global magnetic field closer to that of a magnetic dipole. The CHs that appear during the declining phase of the solar cycle persist for many solar rotations. For this reason, the solar wind streams coming from the coronal holes recur to the Earth's orbit every 27 days, corresponding to the solar synodic period, namely the time needed for a structure of the photosphere, e.g. a sunspot or a CH, to complete an entire solar rotation and return to the same position for a terrestrial observer. This time is equal to the effective rotation period of the Sun (sidereal period) plus an additional time consequent to the orbital motion of the Earth.

Transient solar wind phenomena refer to temporary and non-recurring dynamic events in the SW that deviate from the typical almost stationary flow. These events are often associated with disturbances on the Sun's surface and in its corona, leading to variations in the solar wind's speed, density, and magnetic field.

A transient phenomenon of significant importance is the Coronal Mass Ejection (CME) (Figure 1.3b), which is an ejection of large quantities of coronal plasma from the Sun's corona (due to the sudden breakdown of the closed magnetic lines of the active regions) ejected from the Sun's corona that propagates in the interplanetary space over a few hours, becoming an Interplanetary Coronal Mass Ejection (ICME) and, due to its strong magnetic field, it can disturb the Earth's magnetosphere. CMEs are characterized by an intense magnetic field and a very high velocity, therefore they are preceded by an interplanetary shock, and they are remotely observed with satellite coronographs. CMEs are sometimes associated with solar flares (large releases of energy with time scales of a few minutes); while they represent distinct phenomena, they can occur together due to their common origin in regions of intense magnetic fields on the Sun.

Satellites in orbit near the Earth have been instrumental in acquiring key insights into the primary characteristics of the solar wind at 1 Astronomical Unit (AU $\sim$ 150 million km). Despite the high variability of the solar wind, it is possible to determine typical averaged values for its most common parameters distinguishing between slow and fast wind, (excluding transient phenomena of higher variability) as shown in table 1.1.

The SW at 1 AU results as a super-Alfvénic collisionless plasma, which

Typical values of several SW parameter at 1 AU		
Parameter	Slow wind	Fast wind
Number density	$\sim 15\ cm^{-3}$	$\sim 4\ cm^{-3}$
Bulk velocity	~ 350 km/s	~ 600 km/s
Proton temperature	$\sim 5 \times 10^4$ K	$\sim 2 \times 10^5$ K
Magnetic field	~ 6 nT	~ 6 nT
Alfvén speed	~ 30 km/s	~ 60 km/s
Proton cyclotron frequency	~ 0.1 Hz	~ 0.1 Hz
Debye length	~ 4 m	~ 15 m
Distance between 2 proton collisions	~ 1.2 AU	~ 40 AU

Table 1.1

can be treated in MHD approximation (see section 1.3); furthermore, the fast wind is less dense, faster, and with a higher proton temperature with respect to the slow wind. The different characteristics of the solar wind indicate the significant difference in the nature of the fast wind coming from the *coronal holes* and the slow wind originating from the *helmet streamers*. Another difference lies in the fact that the slow wind initially co-rotates with the Sun and is then released to dozens of solar radii (R_s). Furthermore, while the slow wind begins to accelerate at about $3R_s$, reaching a velocity of about $250km/s$ at the distance of $10R_s$, the fast wind begins to accelerate in the low corona, reaching $300km/s$ at $3R_s$ and $\sim 600\ km/s$ at $10\ R_s$, after that, it keeping this velocity practically constant [12, 13].
A similar characteristic between the two types of solar wind is in the flow density nmv^2 (where n is the proton number density, m is the proton mass and v the flow speed), which by itself would not allow distinguishing different flow tubes; this means that the dynamic pressure is similar for the two types of solar wind.

In the next paragraph, there is a description of the corotating streams, which will be studied in the analysis work.

1.2.1 Corotating Interaction Regions

The interplay between the coronal magnetic field and the expansion of the SW produces both a highly structured solar corona and a spatially variable solar wind.

As the Sun rotates, streams of different speeds become radially aligned within the low-latitude heliospheric regions. The faster SW encounters the slower wind ahead while simultaneously leaving the slower wind trailing behind. Because these radially aligned plasma parcels originate from different positions on the Sun at different times, they are connected by different magnetic field lines, preventing them from merging [16]. Consequently, compression forms in front of the rising-speed portion of a high-speed stream, and a rarefaction forms

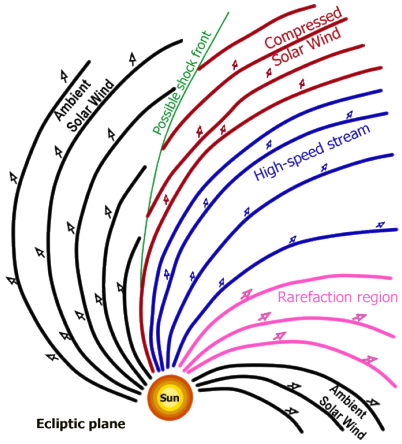

(a) *Sketch of a stream structure in the ecliptic plane [14] (adapted from [15]). The spiral structure is a consequence of solar rotation. The spiral curvature changes as the solar wind velocity changes. When the high-speed stream (in blue) compresses the slower ambient solar wind (in black), a compression region downstream (in red) and a rarefaction region upstream (in pink) are formed.*

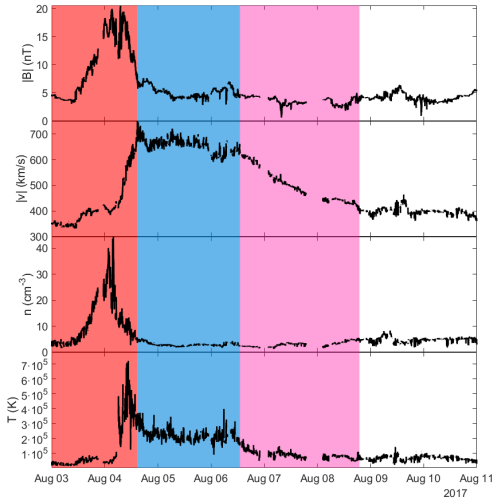

(b) *The IMF intensity, the SW flow speed, density, and temperature are shown in a typical corotating stream at 1 AU. The red colored part corresponds to Stream Interface (SI) or Corotating Interaction Region (CIR), the blue one corresponds to Fast Wind (FW) or High-Speed Stream (HSS), the pink one corresponds to Rarefaction Region (RR) and the white one corresponds to the Ambient Solar Wind (ASW).*

Figure 1.5

on the trailing edge [16], [15]. The density, pressure, and temperature increase near the stream interface, characterized by an increase in the magnetic field (red colored part in figure 1.5a); this region prevents mixing between slow and fast wind. These particular structures are called *Stream Interaction Regions* (SIRs). The declining phase of the solar cycle is the most appropriate phase to observe these structures because they are not overwhelmed by intense phenomena that occur at the maximum solar activity. Since the coronal holes tend to be long-lived, often persisting for months, the interaction regions and high-speed streams tend to sweep past an observer at regular intervals of approximately a solar rotation period. In this way, the SIRs persist for at least one complete corotation of the Sun and they are therefore called *Corotating Interaction Regions* (CIRs); figure 1.5a shows a schematic example of this structure. A Corotating Interaction Region (CIR) is therefore the result of the interaction of fast SW with slower SW ahead. CIRs have a very large three-dimensional extent and are the dominant large-scale structure in the heliosphere on the declining and minimum phase of the solar activity cycle.

The magnetic field lines in the slow wind are more "curved" due to lower

velocities and those on the fast wind are more "radial" due to their higher velocities. At $1AU$ the interface between the flows can be a tangential discontinuity, at greater distances, the compression region evolves into a pair of shock waves formed by a wave traveling forward in the slow solar wind and another that comes back in the fast wind. The density and magnetic field enhancements associated with the positive speed gradient are prominent features. In figure 1.5b are shown variations in plasma parameters observed as the stream structures corotate past a spacecraft at $\sim 1AU$; note that the highest densities tend to occur ahead of the strongest magnetic fields within the speed gradient. Four regions can be identified: the ambient, undisturbed, slow solar wind (ASW - in white in figure 1.5b); the solar wind, which has been compressed and accelerated by the interaction with the fast solar wind (SI or CIR - in red in figure 1.5b); fast stream plasma, which has been compressed and decelerated by the interaction with the slow solar wind (FW or HSS - in blue in figure 1.5b), and the rarefaction region (RR - in pink in figure 1.5b), followed again by the ambient solar wind. At 1AU these structures persist for days and interact with the geomagnetic field.

1.3 MHD approximation

When the gas temperature is sufficiently high, it spontaneously tends to ionize itself and become a plasma, which is an ionized gas characterized by a *local* separation of electrons and ions but *globally* neutral. Therefore, plasma consists of electrically charged particles that respond collectively to electromagnetic forces. Nearly all the matter in the universe exists in the plasma state. Figure 1.6 shows the typical range of temperatures and densities of the most well-known plasmas in the universe; the temperature in the horizontal axis is expressed in eV and 1 eV corresponds to 11606 K (average energy and temperature are related by Boltzmann's relation: $E = k_B T$).

The terms "*local*" and "*global*" must be quantified concerning a fundamental quantity for plasmas: the Debye length. The Debye length for a species i $\lambda_D = \sqrt{\epsilon_0 k_B T_i / n_i {q_i}^2}$ is an important length scale associated with electrostatic effects. Within a sphere of radius λ_D (Debye sphere), single particle processes can take place. Outside the Debye sphere, the behavior of electrons and ions is determined by the ambipolar electric field; therefore electrons and ions move together relative to each other, in a so-called collective motion. Collective plasma processes become important if the number of particles within a sphere of radius λ_D is large ($n_i {\lambda_D}^3 >> 1$) and if λ_D is much smaller than the typical scale lengths ($\lambda_D << L$). In the SW at 1 AU the Debye lengths for ions and electrons are approximately the same through much of the heliosphere. If interest lies in phenomena occurring on spatial scales larger than the Debye sphere ($L > \lambda_D$) and frequency scales lower than both the ion cyclotron frequency and the plasma frequency ($\omega \ll \omega_c \ll \omega_{pe}$), the plasma can be treated as a single fluid: electrons

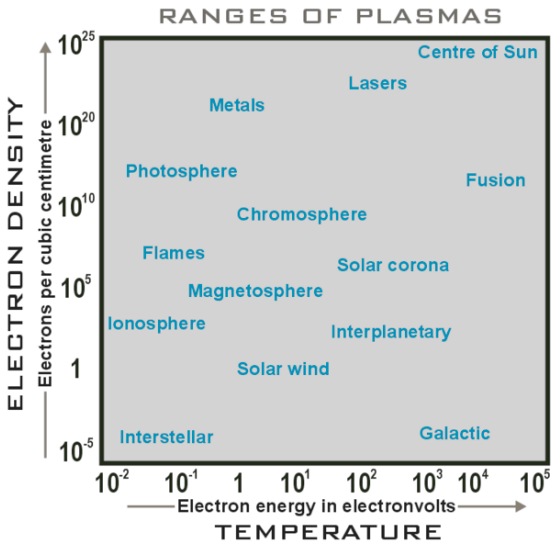

Figure 1.6: Chart of the typical range of temperatures and densities of plasmas, adapted from [17]

and their motions are not recognizable as a separate plasma component, they are treated as electric currents in a moving electro-conducting fluid satisfying Maxwell's equations and fluid Navier-Stokes equations of motion. Thus, MHD couples Maxwell's equations with hydrodynamics (Navier-Stokes equations) to describe the macroscopic behavior of plasmas.

Such a single fluid treatment of a plasma in a magnetic field is described by the following system of equations:

$$\frac{\partial \rho}{\partial t} + \nabla \cdot (\rho \mathbf{v}) = 0 \tag{1.2}$$

$$\frac{\partial (\rho \mathbf{v})}{\partial t} + (\mathbf{v} \cdot \nabla)\, \mathbf{v} = -\nabla \cdot \mathbf{P} + \mathbf{j} \times \mathbf{B} + \mathbf{F} \tag{1.3}$$

$$\nabla \times \mathbf{B} \simeq \mu_0 \mathbf{j} \tag{1.4}$$

$$\nabla \times \mathbf{E} = -\frac{\partial \mathbf{B}}{\partial t} \tag{1.5}$$

$$\nabla \cdot \mathbf{B} = 0 \tag{1.6}$$

$$\nabla \cdot \mathbf{E} = \frac{\rho_q}{\epsilon_0} \tag{1.7}$$

where $\mathbf{P}$ is the pressure tensor and $\mathbf{F}$ are external forces (expressed per unit volume). In the equation (1.4) the time derivative of the electric field has been neglected because the MHD approximation concerns slow frequency domain ($\omega \ll \omega_c \ll \omega_{pe}$), that is $\partial E/\partial t \simeq 0$. In most plasmas, Debye's length is small enough (in the SW $\lambda_D \sim 10$ m) and the plasma frequency large enough (in the SW $\omega_{pe} \sim 10$ kHz) to satisfy the MHD conditions. Macroscopic properties

such as density, bulk velocity, and temperature often give a more convenient way of describing plasma dynamics.
Expressing J by the generalized ohm law

$$J = \sigma \left(\mathbf{E} + \mathbf{v} \times \mathbf{B} \right) \tag{1.8}$$

and replacing it in the equation (1.4), we get

$$\nabla \times \mathbf{B} = \mu_0 \sigma \left(\mathbf{E} + \mathbf{v} \times \mathbf{B} \right) \tag{1.9}$$

Taking the curl of equation (1.9) and using the equations (1.6) and (1.5) we finally get the induction equation:

$$\frac{\partial \mathbf{B}}{\partial t} = \nabla \times (\mathbf{v} \times \mathbf{B}) + \eta \nabla^2 B \tag{1.10}$$

where $\eta = \frac{1}{\mu_0 \sigma}$ is the magnetic diffusivity.

The ratio between the first (induction) term and the second (diffusion) term on the right side in equation 1.10 defines the *Magnetic Reynold number* R_m (adimensional):

$$R_m = \frac{\nabla \times (\mathbf{v} \times \mathbf{B})}{\eta \nabla^2 B} \simeq \frac{\mathcal{U}\mathcal{L}}{\eta} \tag{1.11}$$

where $\mathcal{U}$ is a typical velocity scale of the flow and $\mathcal{L}$ is a typical length scale of the flow.
If $R_m \ll 1$, $\nabla \times (\mathbf{v} \times \mathbf{B})$ can be neglected and the induction equation (1.10) becomes a diffusion equation for the magnetic field.

$$\frac{\partial \mathbf{B}}{\partial t} \simeq \eta \nabla^2 B \tag{1.12}$$

hence the magnetic field will tend to relax towards a purely diffusive state.
If $R_m \gg 1$, the diffusion term can be neglected, and the induction equation becomes:

$$\frac{\partial \mathbf{B}}{\partial t} \simeq \nabla \times (\mathbf{v} \times \mathbf{B}) \tag{1.13}$$

This equation is the well-known Alfvén theorem. It states that in a perfectly conductive fluid ($\sigma \to \infty$) the flow of the magnetic field, through a surface defined by a closed line in motion with the fluid itself is constant, as schematically represented in Figure 1.7. In other words, in a fluid with infinite electric conductivity, the magnetic field is "frozen" into the fluid and moves along with it by conserving the magnetic flux. Explicitly $R_m \gg 1$ means $\eta \to 0 \implies \sigma \to \infty$, hence a turbulent fluid with infinite electrical conductivity corresponds to a large magnetic Reynolds number; in this case, the flux lines of the magnetic field are advected with the fluid flow.

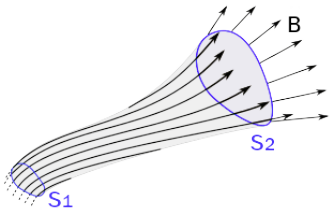

Figure 1.7: The magnetic flux through the cross-section S1 is equal to the magnetic flux through the cross-section S2.

A fully ionized - highly conductive plasma, as can be considered the SW, is largely within the $R_m >> 1$ limit, according to R_m for the SW at 1 AU that is $R_m \sim 10^4$ [18], so equation 1.13 holds. The field lines can be seen as flow lines and, since there is an almost total absence of collisions, the particles remain constrained to their original line. In other words, the fluid motion carries the "frozen-in" magnetic field. This implies that, due to high electrical conductivity, the SW drags the magnetic field present at the base of the corona into interplanetary space.

1.4 Waves in plasmas and Alfvén waves

The high electrical conductivity in plasma has the effect of coupling particles and electromagnetic fields. Consequently, plasmas support a wide variety of wave phenomena. One way to schematize the electromagnetic fields in plasma is to consider them as the sum of two contributions: one static or equilibrium part and one oscillating or perturbation part. In the ideal MHD treatment, the plasma corresponds to a conductive fluid, which can be the seat of time-dependent processes, such as various types of oscillations. The ideal treatment includes the following assumptions:

- the fluid is homogeneous and of infinite extension
- conductivity is very high ($\sigma \to \infty \quad \Rightarrow \; \boldsymbol{E} + \boldsymbol{v} \times \boldsymbol{B} = 0$)
- the fluid is immersed in a uniform static magnetic field $\boldsymbol{B_0}$
- waves are small in amplitude

Notice that the electric field in a perfect conductor vanishes (the electric current would become arbitrarily large if it did not), as can be also seen from equation (1.8). Nonetheless, the fluid we are considering is generally in motion. Because of the presence of the magnetic field, the electric field vanishes only in a reference frame moving with the flow itself, where $\boldsymbol{E} + \boldsymbol{v} \times \boldsymbol{B} = 0$
The hypothesis of small amplitude waves allows us to "*linearize*" the MHD

equations which by their nature are nonlinear. In this situation and in the absence of perturbations, the fluid is at rest ($v_0 = 0$). To simplify the formalism, the magnetic field B_0 can be considered uniform and directed along the z-axis of the reference system $\boldsymbol{B_0} = (0, 0, B_0)$. In an unperturbed state, the value of density ρ_0, pressure p_0 and field B_0 are constant, known and finite quantities in space and time (zero-order quantities). When a perturbation with a small amplitude occurs, the parameters of the fluid can be written as:

$$\begin{aligned} \rho &= \rho_0 + \rho^{'} & \rho^{'} &<< \rho_0 \\ p &= p_0 + p^{'} & p^{'} &<< p_0 \\ B &= B_0 + b^{'} & b^{'} &<< B_0 \\ v &= v_0 + v^{'} & v_0 = 0 &\Rightarrow v = v^{'} \end{aligned}$$

Knowledge of the system requires the evaluation of the previous quantities that characterize the perturbed state; the *linearization* consists in their approximation, together with their derivatives, as infinitesimal of the first order, so equations within only first-order terms remain. In this way, being $\mathbf{J}^{'} = \sigma\left(\mathbf{E} + \mathbf{v} \times \mathbf{B}\right)$, and starting from:

$$\begin{cases} \frac{\partial \rho^{'}}{\partial t} + \rho_0 \nabla \cdot \mathbf{v}^{'} = 0 \\ \rho_0 \frac{\partial \mathbf{v}^{'}}{\partial t} = -{v_s}^2 \nabla \rho^{'} + \mathbf{J}^{'} \times \mathbf{B_0} \\ \frac{\partial \mathbf{b}^{'}}{\partial t} = \nabla \times \left(\mathbf{v}^{'} \times \mathbf{B_0}\right) \end{cases} \tag{1.14}$$

the mathematical expression for $\mathbf{v}^{'}$ is obtained:

$$\frac{\partial^2 \mathbf{v}^{'}}{\partial^2 t} - {v_s}^2 \nabla \left(\nabla \cdot \mathbf{v}^{'}\right) + \mathbf{v}_a \times \left\{\nabla \times \left[\nabla \times \left(\mathbf{v}^{'} \times \mathbf{v}_a\right)\right]\right\} = 0$$

where $\mathbf{v}_a = \frac{\mathbf{B}_0}{\sqrt{\mu_0 \rho_0}}$ is the *Alfvén velocity*, $v_s = \sqrt{\gamma p / \rho}$ is the sound speed, while the mathematical expression for $\mathbf{b}^{'}$ is:

$$\omega \mathbf{b}^{'} + k \times \left(\mathbf{v}^{'} \times \mathbf{B}_0\right) = 0 \tag{1.15}$$

Assuming that perturbed quantities behave like a plane wave, each perturbed quantity has its amplitude multiplied by an exponential of the type $e^{\{i(\mathbf{k}\cdot\mathbf{r} - \omega t)\}}$ where $\mathbf{k} = \frac{2\pi}{\lambda}\hat{\mathbf{k}}$ defines the direction of propagation of the wave. By deriving twice with respect to time, it will appear a term $-\omega^2$, and by deriving with respect to space, it will appear a term ik, obtaining the dispersion relations that link the frequency ω to the wave vector $\mathbf{k}$:

$$\begin{aligned} -\omega^2 \mathbf{v}^{'} + \left({v_s}^2 + {v_a}^2\right)\left(\mathbf{k} \cdot \mathbf{v}^{'}\right)\mathbf{k} + \\ + \left(\mathbf{k} \cdot \mathbf{v_a}\right)\left[\left(\mathbf{v_a} \cdot \mathbf{k}\right)\mathbf{v}^{'} - \left(\mathbf{v_a} \cdot \mathbf{v}^{'}\right)\mathbf{k} + \left(\mathbf{k} \cdot \mathbf{v}^{'}\right)\mathbf{v_a}\right] = 0 \end{aligned} \tag{1.16}$$

This expression is very general because the only hypothesis made is on the uniformity of the magnetic field $\boldsymbol{B_0} = (0, 0, B_0)$ and the perturbations as monochromatic waves. As it can be seen, many scalar products in equation 1.16 depend on the orientation of the wave vector $\mathbf{k}$ in relation to velocity. Various cases can occur.

▶ In the case of $\boxed{\mathbf{k} \parallel \mathbf{B_0} \parallel \mathbf{v_a}}$ the expression 1.16 becomes:

$$\left(k^2 {v_a}^2 - \omega^2\right) \mathbf{v}' + \left(\frac{v_s}{v_a}\right)^2 k^2 \left(\mathbf{v}' \cdot \mathbf{v_a}\right) \mathbf{v_a} = 0 \tag{1.17}$$

⊵ **Subcase a)** $\mathbf{v}' \parallel \mathbf{k} \rightarrow \mathbf{v}' \parallel \mathbf{v_a}$

The oscillation of the fluid occurs along the direction of propagation. By developing the 1.17 and the 1.15 we get:

$$\frac{\omega^2}{k^2} = {v_s}^2$$

$$\mathbf{b}' = 0$$

So the phase velocity of the wave is $\pm v_s$. It is by definition a longitudinal wave $\left(\mathbf{k} \parallel \mathbf{v}'\right)$ and compressive wave $\left(\rho' \neq 0\right)$. It follows that a magnetohydrodynamic fluid behaves like any other fluid, and supports ***compression and rarefaction sonic waves***.

⊵ **Subcase b)** $\mathbf{v}' \perp \mathbf{k} \rightarrow \mathbf{v}' \perp \mathbf{v_a}$

The oscillation of the fluid occurs perpendicular to the direction of propagation. In this case, by developing the 1.17 and the 1.15 we get:

$$\frac{\omega^2}{k^2} = {v_a}^2 \tag{1.18}$$

$$\mathbf{b}' = -\frac{k}{\omega} B_0 \mathbf{v}' \tag{1.19}$$

So, in this case, the wave propagates transversely $\left(\mathbf{v}' \perp \mathbf{k}\right)$ with Alfvén velocity and $\mathbf{b}'$ it is directed as $-\mathbf{v}'$. These are called transverse Alfvén wave or simply ***Alfvén wave***.

▶ In the case of $\boxed{\mathbf{k} \perp \mathbf{B_0} \rightarrow \mathbf{k} \perp \mathbf{v_a}}$ from 1.16 phase velocity results:

$$\frac{\omega}{k} = \pm\sqrt{{v_s}^2 + {v_a}^2}$$

and from 1.15:

$$\mathbf{b}^{'} = \frac{k}{\omega} v^{'} \mathbf{B_0}$$

So, in this case, it is a single wave that has a sonic component (${v_s}^2$) and an Alfvénic component (${v_a}^2$), while $\mathbf{b}^{'}$ is parallel to $\mathbf{B_0}$. This is called a *Magnetosonic wave* or *compressive Alfvén wave* or *fast wave.*

▶ The last case is that in which the wave propagates in any generic direction with respect to the magnetic field, $\mathbf{k}$ and $\mathbf{B}$ form a generic angle θ. In this case, we break down the three components from the 1.16:

$$\begin{cases} {v_x}^{'} \left(-\omega^2 + k^2 {v_a}^2 + k^2 {v_s}^2 \sin^2\theta\right) + {v_z}^{'} \left(k^2 {v_s}^2 \sin\theta\cos\theta\right) = 0 \\ {v_y}^{'} \left(-\omega^2 + k^2 {v_a}^2 \cos^2\theta\right) = 0 \\ {v_z}^{'} \left(-\omega^2 + k^2 {v_s}^2 \cos^2\theta\right) + {v_x}^{'} \left(k^2 {v_s}^2 \sin\theta\cos\theta\right) = 0 \end{cases}$$

From the second equation of the system, we obtain:

$$\frac{\omega}{k} = v_a \cos\theta = v_{shear}$$

That is, there is an Alfvén wave, called *shear Alfvén wave*, which propagates in the direction θ with respect to the direction of the magnetic field, with phase velocity equal to v_{shear}.
From the other two equations of the system we get:

$$\frac{\omega^2}{k^2} = \frac{{v_s}^2 + {v_a}^2}{2} \pm \sqrt{\left[\left({v_s}^2 + {v_a}^2\right)^2 - 4{v_s}^2 {v_a}^2 \cos^2\theta\right]}$$

There are two solutions, v_{fast} (the one obtained by the positive sign) and v_{slow} (the one obtained by the negative sign). Therefore in the case that the wave propagates in any direction with respect to the magnetic field, three different characteristic velocities are observed: v_{shear}, v_{fast} and v_{slow} which are however combinations of v_a and v_s.

1.4.0.1 Non-compressive Alfvén waves

In absence of compression (or density perturbations) $\rho' = 0 \rightarrow \rho_0 = constant$, so the system (1.14) can be rewritten:

$$\begin{cases} \nabla \cdot \mathbf{v'} = 0 \\ \rho_0 \frac{\partial \mathbf{v}^{'}}{\partial t} = \frac{1}{\mu_0} \left(\nabla \times \mathbf{b'}\right) \times \mathbf{B_0} \\ \frac{\partial \mathbf{b}^{'}}{\partial t} = \nabla \times \left(\mathbf{v}^{'} \times \mathbf{B_0}\right) \end{cases} \tag{1.20}$$

On the assumption that $\mathbf{b'} \perp$ z-axis, so that $\boldsymbol{b'} = \left(b'_x, b'_y, 0\right)$, the system (1.20) become:

$$\begin{cases} \frac{\partial \mathbf{v}^{'}}{\partial t} = \frac{B_o}{\mu_0 \rho_0} \frac{\partial \mathbf{b'}}{\partial z} \\ \frac{\partial \mathbf{b}^{'}}{\partial t} = B_0 \frac{\partial \mathbf{v'}}{\partial z} \end{cases} \tag{1.21}$$

then it can be easily obtained:

$$\left(\frac{\partial^2}{\partial t^2} - {v_a}^2 \frac{\partial^2}{\partial z^2}\right)(\mathbf{b}', \mathbf{v}') = 0 \tag{1.22}$$

that is the wave equation for Alfvén waves with velocity $v_a = \frac{B_0}{\sqrt{\mu_0 \rho_0}}$. From equation (1.19) can be found:

$$\mathbf{b}^{'} = \pm \frac{B_0}{v_a} \mathbf{v}^{'} \quad \Longrightarrow \quad \mathbf{b}^{'} = \pm \sqrt{\mu_0 \rho_0}\, \mathbf{v}^{'} \tag{1.23}$$

taking the square of this last equation (and dividing by 2 to explicit the kinetic energy), information about the energy per unit volume can be expressed as:

$$\frac{|\mathbf{b}'|^2}{2\mu_0} = \frac{1}{2}\rho_0 |\mathbf{v}'|^2 \tag{1.24}$$

Therefore the Alfvén wave fairly distributes its energy between the oscillation of the magnetic field and the kinetic energy. Moreover, from the dispersion equation for an Alfvén wave (1.18) the direction of propagation of the wave energy can be found, given by the group velocity:

$$\frac{\partial \omega}{\partial \mathbf{k}} = v_A \hat{\mathbf{z}}$$

where $\hat{\mathbf{z}}$ is the magnetic field direction; therefore, the energy propagates along field lines, independently from the $\mathbf{k}$ direction. As shown above, a linear Alfvén wave is incompressive ($\delta\rho = 0$), it is transverse because $\mathbf{b}'$ and $\mathbf{v}'$ are perpendicular to the direction of propagation (as well as perpendicular to B_0) and it is nondispersive because the perturbations propagate at the same speed at all frequencies. The previous picture is a simple way to show how an MHD fluid can sustain incompressible waves and how an Alfvén wave behaves. In the case of the solar wind, as it travels outwards, it becomes supersonic and superalfvénic (the flow speed is much higher than the magnetosonic and Alfvénic ones).

1.5 Turbulence in the solar wind

In plasmas, as in fluids, the more the Reynolds number increases, the more the flow becomes turbulent. In the limit of $R_m \to \infty$ the turbulence is said to be in a fully developed state. Therefore the plasma dynamics becomes chaotic and unpredictable when we look at the details of a sample of fluid. However, the global statistical behavior does not change going from a sample to another. At the scales where the equations of MHD can describe the plasma, we speak of magnetohydrodynamic turbulence. It plays a fundamental role in plasma dynamics, and it is essential to understand the turbulence generated by

the nonlinear plasma dynamic and magnetic fields. In this chapter are shown some remarkable results of MHD turbulence theory related to the incompressible case, using a dimensional analysis of the equations and a phenomenological treatment. Starting from Kolmogorov's fundamental results on hydrodynamic turbulence, we will include the effects due to the presence of the magnetic field. There are many similarities between hydrodynamics and magnetohydrodynamics; however, in the latter situation, the anisotropy created by the magnetic field justifies the existence of Alfvén waves.

The SW is an ideal laboratory for in situ turbulence studies because its conditions are difficult to reproduce in a laboratory. In the SW the turbulence is driven by fluctuations (such as those of the magnetic field and velocity); their characterization can tell us how energy is transferred in the plasma.

1.5.1 Heuristic derivation of Kolmogorov law

The presence of non-linear interactions during solar wind expansion in the heliosphere lead to a turbulent state of the SW itself, similar to the hydrodynamic turbulence described by Kolmogorov (1941) [19]. This phenomenology is based on the picture given by Richardson (figure 1.8): in a fluid, the turbulence is made by a collection of eddies at all scales and the energy injected at a large length scale L is transferred by non-linear interactions to small scales, where it is dissipated at characteristic scale l_d.

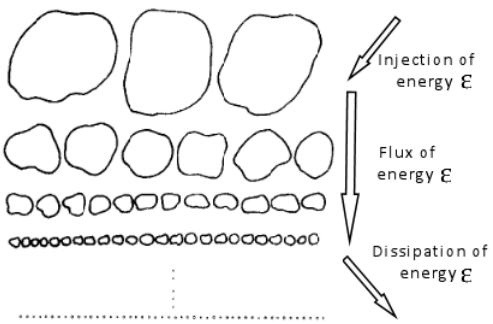

Figure 1.8: *Richardson cascade, according to the Kolmogorov 1941 theory. The blobs of decreasing sizes represent the eddies of various sizes.*

In his theory, Kolmogorov identified three different spatial ranges, in which the physical turbulence processes evolve, which are: injection range, inertial range, and dissipation range. The different ranges differ in terms of spatial scale, therefore the separation can be made in the wavenumber domain. The energy is injected in some way into the system at larger scales L (small wavenumbers), through inhomogeneity, instability, external forces, etc.; for this reason, this range is called the *injection range*. On the opposite side, at the smaller scales (l_d), with higher wavenumbers, the dissipation process due to the viscosity of the fluid dominates, and the (kinetic) energy is converted into thermal energy; for this reason, this range is called the *dissipation range*. Here the energy spectrum decreases rapidly

at the wavenumber associated with the dissipation scale (order of the mean free path). An intermediate range, called the *inertial range*, separates these two ranges; when Reynold's number (R_m) is very large, the injection scale L and the dissipative scale l_d are entirely separated, meaning that inertial range is wide. The solar wind at 1 AU falls into this case.

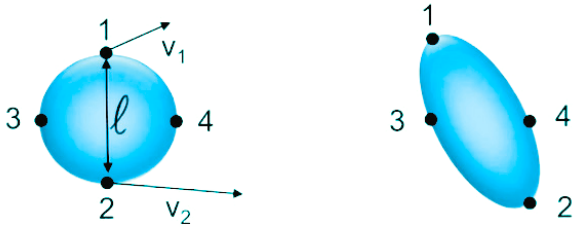

Figure 1.9: *Cross-section of a ∼spherical volume (on the left) being squeezed into elliptical shape (on the right) by fluid motion after time t_l: points 1 and 2 separate, while points 3 and 4 get closer.*

A simple scheme of what happens at a ∼ spherical bubble in a turbulent motion is shown in Figure 1.9 and explained as follows. The starting point is a basic structure of the turbulence (blob or eddy) of a certain size l. Since the motion is turbulent, the velocity of the bubble will not be the same on all points of its (spherical) surface. Suppose that point 1 has velocity v_1 and point 2 has velocity v_2. Because $v1 \neq v2$ there will be a deformation of the bubble in a characteristic time

$$t_l \sim \frac{l}{v_2 - v_1} = \frac{l}{v_l} \tag{1.25}$$

indicated as the *eddy turnover time*, where l is the scale under consideration (typically between the injection scale l_0 and the dissipation scale l_d) and v_l is the typical value of velocity associated to scales $\sim l$. Hence t_l is the typical time for a structure, of size $\sim l$, to undergo a significant distortion, due to the relative motion of its components. We can define the *energy transfer rate*, that is the energy transferred to the scale l over time t_l:

$$\epsilon_l \sim \frac{E_l}{t_l} \sim \frac{{v_l}^2}{t_l} \sim \frac{{v_l}^3}{l} \tag{1.26}$$

from which we get:

$$v_l \sim {\epsilon_l}^{1/3}\, l^{1/3} \tag{1.27}$$

Thus, the velocity fluctuation varies with the scale length as $l^{1/3}$; this is a universal scaling that does not depend on the type of flow. Replacing equation 1.27 in 1.25 it is obtained the time expressed in terms of the scale length:

$$t_l \sim {\epsilon_l}^{-1/3}\, l^{2/3} \tag{1.28}$$

Kolmogorov's basic hypothesis is that within the inertial range, there is no dissipation of energy ($\epsilon = constant$). This implies that energy is introduced on larger scales (within the injection range) and moved to smaller scales without dissipation in the inertial range. It is then dissipated to even smaller scales (of the order of the Larmor radius), heating the plasma. Note that under this hypothesis ($\epsilon = constant$) v_l (eq. 1.27) can be simply written:

$$v_l \sim l^{1/3}$$

Expressing the length of the scale l in terms of wavenumber k, where $l \sim 1/k$ and k is the wave vector modulus corresponding to some harmonics in a Fourier representation of the flux velocity field, the energy spectrum can be written as:

$$E(k) \sim \frac{{v_l}^2}{k} \sim \frac{\epsilon^{2/3}\, k^{-2/3}}{k} \sim \epsilon^{2/3}\, k^{-5/3} \tag{1.29}$$

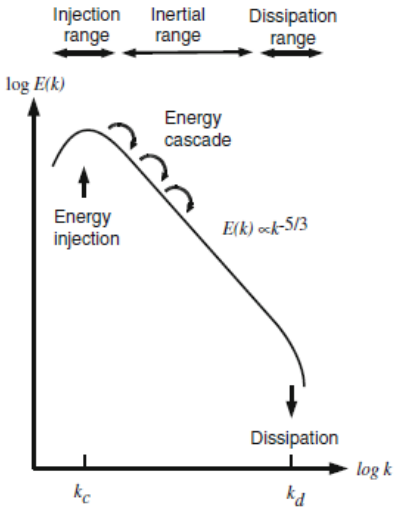

Figure 1.10: *Energy spectrum, according to Kolmogorov's scaling law.*

Equation 1.29 is one of the most relevant results of Kolmogorov's theory (1941), widely known as *-5/3 scaling Kolmogorov's law*, confirmed by numerous experimental proofs. The way the kinetic energy distributes over the multiplicity of scales is a fundamental characterization of a turbulent flow. In the inertial range, according to equation 1.29, the energy spectrum E(k) depends only on the wavenumber k, and the energy dissipation rate per unit mass. Figure 1.10 schematically shows the energy cascade dependence on the wavenumber, according to Kolmogorov's law, in a log-log scale. This so-called scaling law of the energy spectrum is universal (within the framework of the hypotheses made) and holds in systems where the Reynolds number is large. This behavior is generally observed not only in fluid turbulence but also in MHD turbulence.

Unlike neutral fluids, the solar wind is magnetized; the magnetic field introduces an anisotropy and additional forces so that Alfvén waves replace the turbulent "eddies". The development of the energy cascade in an incompressible MHD fluid, such as the solar wind, is due to non-linear terms of equation 1.36 in section 1.5.2.1. Cascade means that the energy is being transferred from one scale to another without dissipation.

1.5.2 Tools to analyze MHD turbulence

MHD approximation is a useful framework to describe large-scale solar wind properties and the turbulence that develops, because of the low-frequency domain of fluctuations, as said in section 1.3. It is good to remember that if small scales are involved, kinetic physics must also be considered. In this section it is shown how the MHD equations are described in terms of the variables introduced by Elsässer, which take his name; it is also shown how to describe the MHD turbulence with a statistical approach which will then also be used later in data analysis.

1.5.2.1 MHD incompressible equations in terms of Elsässer's variables

The basic properties of low-frequency MHD turbulence can be derived from the MHD equations (see section 1.3). In the absence of a strong magnetic field, the pressure can be considered isotropic and become scalar (trace of the tensor matrix). With these assumptions, starting from:

$$\begin{aligned} \frac{\partial \rho}{\partial t} + \nabla \cdot (\rho \mathbf{v}) &= 0 \\ \rho \left(\frac{\partial}{\partial t} + \mathbf{v} \cdot \nabla \right) \mathbf{v} &= -\nabla P + \mathbf{j} \times \mathbf{B} + \mu \nabla^2 \mathbf{v} \\ \frac{\partial \mathbf{B}}{\partial t} &= \nabla \times (\mathbf{v} \times \mathbf{B}) + \eta \nabla^2 \mathbf{B} \end{aligned} \tag{1.30}$$

the second equation of the system (1.30) can be rewritten making explicit the $\mathbf{j} \times \mathbf{B}$ term on right-hand side:

$$\rho \left(\frac{\partial}{\partial t} + \mathbf{v} \cdot \nabla \right) \mathbf{v} = \frac{1}{\mu_0} (\mathbf{B} \cdot \nabla) \mathbf{B} - \nabla \left(\frac{B^2}{2\mu_0} \right) - \nabla p + \mu \nabla^2 \mathbf{v} \tag{1.31}$$

where μ is the dynamic viscosity, the first term on the right-hand side is a magnetic tension force (per unit volume), the second one is the force related to magnetic pressure, and p is the kinetic pressure. The two pressure force terms can be rewritten in an all-inclusive term as the gradient of the total pressure

$$P = \left(p + \frac{B^2}{2\mu_0} \right)$$

as the sum of the kinetic and magnetic pressures sustained by the plasma. In the case of incompressible flow $\frac{\partial \rho}{\partial t} = 0 \implies \rho = constant$, the system (1.30) become:

$$\begin{aligned} \nabla \cdot \mathbf{v} &= 0 \\ \frac{\partial \mathbf{v}}{\partial t} + (\mathbf{v} \cdot \nabla) \mathbf{v} &= \frac{1}{\mu_0 \rho} (\mathbf{B} \cdot \nabla) \mathbf{B} - \frac{1}{\rho} \nabla P + \nu \nabla^2 \mathbf{v} \\ \frac{\partial \mathbf{B}}{\partial t} + (\mathbf{v} \cdot \nabla) \mathbf{B} &= (\mathbf{B} \cdot \nabla) \mathbf{v} + \eta \nabla^2 \mathbf{B} \end{aligned} \tag{1.32}$$

where $\nu = \mu/\rho$ is the kinematic viscosity (defined as the ratio of the dynamic viscosity μ over the density of the fluid ρ - in units m^2/s). The condition $\nabla \cdot v = 0$ simplifies the calculation and allows us to get an expression for the pressure term, simply by applying the divergence to the second equation of the system (1.32). In addition, the velocity variable for the magnetic field can be defined as $b = \frac{B}{\sqrt{\mu_0 \rho}}$ obtaining:

$$\begin{aligned} \nabla \cdot \mathbf{v} &= 0 \\ \frac{\partial \mathbf{v}}{\partial t} + (\mathbf{v} \cdot \nabla)\,\mathbf{v} &= (\mathbf{b} \cdot \nabla)\,\mathbf{b} - \frac{1}{\rho}\nabla P + \nu \nabla^2 \mathbf{v} \\ \frac{\partial \mathbf{b}}{\partial t} + (\mathbf{v} \cdot \nabla)\,\mathbf{b} &= (\mathbf{b} \cdot \nabla)\,\mathbf{v} + \eta \nabla^2 \mathbf{b} \\ \nabla^2 P &= -\rho \nabla \left[(\mathbf{v} \cdot \nabla)\,\mathbf{v} - (\mathbf{b} \cdot \nabla)\,\mathbf{v}\right] \end{aligned} \tag{1.33}$$

Introducing the *Elsässer variables* [20], which have dimensions of velocity, they are very useful to study the correlations between the velocity and magnetic fields:

$$\mathbf{z}^{\pm} = \mathbf{v} \pm \mathbf{b} \tag{1.34}$$

By taking the sum and the difference of the second and third equation of the system (1.33) and expressing the results in terms of the Elsässer variables, we get:

$$\frac{\partial \mathbf{z}^{+}}{\partial t} + \mathbf{z}^{+}\left(\mathbf{z}^{-} \cdot \nabla\right) = \left(\frac{\nu + \eta}{2}\right)\nabla^2 \mathbf{z}^{+} + \left(\frac{\nu - \eta}{2}\right)\nabla^2 \mathbf{z}^{-} - \frac{1}{\rho}\nabla P$$

$$\frac{\partial \mathbf{z}^{-}}{\partial t} + \mathbf{z}^{-}\left(\mathbf{z}^{+} \cdot \nabla\right) = \left(\frac{\nu - \eta}{2}\right)\nabla^2 \mathbf{z}^{+} + \left(\frac{\nu + \eta}{2}\right)\nabla^2 \mathbf{z}^{-} - \frac{1}{\rho}\nabla P$$

Together with the divergence of the Elsässer variable $\nabla \cdot \mathbf{z}^{\pm} = \mathbf{0}$ these last two equations can be written in a more compact form:

$$\frac{\partial \mathbf{z}^{\pm}}{\partial t} + \left(\mathbf{z}^{\mp} \cdot \nabla\right)\mathbf{z}^{\pm} = \left(\frac{\nu \pm \eta}{2}\right)\nabla^2 \mathbf{z}^{+} + \left(\frac{\nu \mp \eta}{2}\right)\nabla^2 \mathbf{z}^{-} - \frac{1}{\rho}\nabla P \tag{1.35}$$

Where ν and η are dissipative coefficients. Equation 1.35 is a very compact and symmetrical form of MHD equations in the incompressible case; furthermore, the non-linear term $(\mathbf{z}^{\mp} \cdot \nabla)\,\mathbf{z}^{\pm}$ involves at the same time both variables $\mathbf{z}^{+}$ and $\mathbf{z}^{-}$. Notice that if one of the two modes ($\mathbf{z}^{+}$ or $\mathbf{z}^{-}$) is zero then equation 1.35 becomes linear. Observe that in the absence of B, the same structure of Navier-Stokes equations is obtained; therefore, the presence of a background magnetic field makes the MHD equations intrinsically anisotropic. Because we are interested in the field fluctuations dynamics, we decompose $\mathbf{z}^{\pm}$ in an average term and a fluctuating one:

$$\mathbf{z}^{\pm} = \mathbf{z_0}^{\pm} + \delta \mathbf{z}^{\pm}$$

with

$$\mathbf{z_0}^{\pm} = \langle \mathbf{z}^{\pm} \rangle \qquad \delta \mathbf{z}^{\pm} = \delta \mathbf{v} \pm \frac{\delta \mathbf{b}}{\sqrt{\mu_0 \rho}}$$

where $\pm$ is determined by $-sign\left[\mathbf{k} \cdot \mathbf{B_0}\right]$, so that $\delta \mathbf{z}^{+}$ denotes outward propagating waves and $\delta \mathbf{z}^{-}$ denotes inward propagating waves. In this view we can write:

$$\mathbf{z_0}^{\pm} = \langle \delta \mathbf{z}^{\pm} \rangle = \langle \mathbf{v} \rangle \pm \frac{\langle \delta \mathbf{B} \rangle}{\sqrt{\mu_0 \rho}} = \langle \mathbf{v} \rangle \pm \mathbf{v_A}$$

For the velocity it is possible to realize a Galilean transformation such that $\langle \mathbf{v} \rangle = \mathbf{0}$, hence in this case $\mathbf{z_0}^{\pm} = \pm \mathbf{v_A}$ and we can write:

$$\mathbf{z}^{\pm} = \mathbf{v_A} + \delta \mathbf{z}^{\pm}$$

Replacing it in equation 1.35 we get:

$$\frac{\partial}{\partial t} \delta \mathbf{z}^{\pm} \mp (\mathbf{v_A} \cdot \nabla) \, \delta \mathbf{z}^{\pm} + \left(\delta \mathbf{z}^{\mp} \cdot \nabla\right) \delta \mathbf{z}^{\pm} = \left(\frac{\nu \pm \eta}{2}\right) \nabla^2 \delta \mathbf{z}^{+} + \left(\frac{\nu \mp \eta}{2}\right) \nabla^2 \mathbf{z}^{-} - \frac{1}{\rho} \nabla P$$

Note that non-linear coupling happens only between fluctuations propagating in opposite directions, whatever their amplitude is. Neglecting the dissipative terms and assuming $P = \left(p + \frac{B^2}{\mu_0 \rho}\right) \simeq constant$ it follows that:

$$\frac{\partial}{\partial t} \delta \mathbf{z}^{\pm} \mp (\mathbf{v_A} \cdot \nabla) \, \delta \mathbf{z}^{\pm} + \left(\delta \mathbf{z}^{\mp} \cdot \nabla\right) \delta \mathbf{z}^{\pm} = 0$$

In the end, linearizing the last equation and neglecting the terms above the first order, we get:

$$\left(\frac{\partial}{\partial t} \mp \mathbf{v_A} \cdot \nabla\right) \delta \mathbf{z}^{\pm} \simeq 0 \tag{1.36}$$

This result shows that $\delta \mathbf{z}^{-}\left(\mathbf{x} - \mathbf{v_A} \mathbf{t}\right)$ describes Alfvénic fluctuations propagating in the direction of the magnetic field and $\delta \mathbf{z}^{+}\left(\mathbf{x} + \mathbf{v_A} \mathbf{t}\right)$ describes Alfvénic fluctuations propagating opposite to the magnetic field, both with the same velocity equal to the Alfvén velocity $\mathbf{v_A}$ [21].

1.5.2.2 Statistical characterization of MHD turbulence

Using a statistical approach is advantageous to describe the MHD turbulence behavior. We can exploit the fact that for an MHD fluid, under the hypothesis of section (1.5.2.1), MHD equations have three quadratic invariants. Here we work with two of these invariants, which are the *total energy*:

$$E = \frac{1}{2} \langle v^2 + b^2 \rangle$$

and the *cross-helicity*:

$$H_c = \langle \mathbf{v} \cdot \mathbf{b} \rangle$$

where $\mathbf{v}$ and $\mathbf{b}$ are the fluctuations of velocity and magnetic field (in Alfvén units, km/s, obtained by dividing the magnetic field by $\sqrt{\mu_0 \rho}$, where μ_0 is the magnetic permeability and ρ is the plasma density). Therefore, the energy is the variance of magnetic fluctuations (in Alfvén units) and velocity fluctuations, and the cross-helicity gives us information about the correlation between velocity and magnetic fluctuations. The integrals of these quantities on the regions containing the whole plasma are the invariants of the ideal MHD equations. When velocity fluctuations are aligned to magnetic fluctuations (as for Alfvén waves, see equation 1.19 in section 1.4) the scalar product assumes maximum value, as well as H_c. Recalling the definition of Elsässer variables (equation 1.34) the velocity and magnetic fields can be redefined in terms of $\mathbf{z}^{\pm}$:

$$\mathbf{z}^{\pm} = \mathbf{v} \pm \mathbf{b}$$

$$\mathbf{v} = \frac{1}{2}\left(\mathbf{z}^{+} + \mathbf{z}^{-}\right)$$

$$\mathbf{b} = \frac{1}{2}\left(\mathbf{z}^{+} - \mathbf{z}^{-}\right)$$

that have dimensions of velocity. The second-order moments associated with these fields are:

$$e^{\pm} = \frac{1}{2}\langle \left(\mathbf{z}^{\pm}\right)^2 \rangle \qquad (energies\ related\ to\ \mathbf{z}^{+}\ and\ \mathbf{z}^{-}) \qquad (1.37a)$$

$$e^{v} = \frac{1}{2}\langle v^2 \rangle \qquad (kinetic\ energy) \qquad (1.37b)$$

$$e^{b} = \frac{1}{2}\langle b^2 \rangle \qquad (magnetic\ energy) \qquad (1.37c)$$

$$e = e^{v} + e^{b} \qquad (total\ energy) \qquad (1.37d)$$

$$e^{r} = e^{v} - e^{b} \qquad (residual\ energy) \qquad (1.37e)$$

$$e^{c} = \frac{1}{2}\langle \mathbf{v} \cdot \mathbf{b} \rangle \qquad (cross - helicity) \qquad (1.37f)$$

To describe the degree of correlation between v and b, it's convenient to use normalized quantities:

$$\sigma_c = \frac{e^{+} - e^{-}}{e^{+} + e^{-}} = \frac{2e^{c}}{e^{v} + e^{b}} \qquad (normalized\ cross - helicity) \qquad (1.38a)$$

$$\sigma_r = \frac{e^{v} - e^{b}}{e^{v} + e^{b}} = \frac{2e^{r}}{e^{+} + e^{-}} \qquad (normalized\ residual\ energy) \qquad (1.38b)$$

$$r_A = \frac{e^{v}}{e^{b}} = \frac{1 + \sigma_r}{1 - \sigma_r} \qquad (Alfven\ ratio) \qquad (1.38c)$$

$$r_E = \frac{e^{-}}{e^{+}} = \frac{1 - \sigma_c}{1 + \sigma_c} \qquad (Elsasser\ ratio) \qquad (1.38d)$$

where $-1 \leq \sigma_c \leq 1$ and $-1 \leq \sigma_r \leq 1$.
For a pure Alfvén wave the expected values are $\sigma_c \to \pm 1$, $\sigma_r \to \pm 0$ and $r_A \to 1$ (actually, r_A assume values usually lower than 1, the reason is still an open question).

The Alfvénic fluctuations occur along the magnetic field direction, which means there is a strong correlation between velocity and magnetic field fluctuations, as shown in Belcher and Davis [22], in the form:

$$\delta \mathbf{v} \simeq \pm \frac{\delta \mathbf{B}}{\sqrt{4\pi\rho}}$$

where the sign $\pm$ of correlation is determined by $-sign\,[\mathbf{k} \cdot \mathbf{B_0}]$, with $\mathbf{k}$ the wave vector and $\mathbf{B_0}$ the background magnetic field vector. They found that large-amplitude, nonsinusoidal Alfvén waves propagating outward from the Sun. The purest examples of these outwardly propagating Alfvén waves occur in high-velocity solar wind streams. In low-velocity regions, Alfvén waves are also outwardly propagating, but they usually have smaller amplitudes than in the fast streams [23]. Alfvénic fluctuations are the most frequent fluctuations observed in the solar wind. Other possible propagating modes, like compressive modes, are strongly damped, shortly after they are generated. On the contrary, Alfvènic fluctuations are difficult to be damped because of their incompressive nature; they survive much longer and dominate solar wind turbulence. There are regions where Alfvènic correlations are stronger, like the leading edge of fast streams and regions where they are weaker, like intervals of slow wind. However, the degree of these correlations fades away with increasing heliocentric distance. Additionally, as shown by Dobronwonly et al. [24], in the SW predominates outward modes. The existence of the Alfvénic critical point, where $v_{SW} = v_A$ at about $15 - 20\,R_S$ from the Sun, implies that only outward propagating waves of solar origin will be able to escape from the Sun. Hence, the inward modes observed beyond the Alfvén point cannot have a solar origin but they must be created locally. However, the majority of the Alfvén fluctuations have an outward propagation, and the best regions to observe them are the fast part of high-velocity streams.

Chapter 2

The Geomagnetic field

Earth's magnetic field, also known as the geomagnetic field, extends from Earth's interior out into space, where it interacts with the SW. The measure of the geomagnetic field is the result of the superimposition of contributions having different origins. The main field is produced by a self-sustaining dynamo mechanism (geodynamo) generated in the Earth's fluid core (at depths greater than 2900 km). To this are added other mechanisms, such as the crustal field generated by magnetized rocks in the Earth's crust; the external field generated by electric currents flowing in the ionosphere, magnetosphere, and oceans, and the magnetic field due to currents induced in the crustal layer of the Earth by the time-varying external fields.

William Gilbert in 1600 wrote one of the first treatises on magnetism, in which he extensively studied magnetism, distinguishing between magnetic and non-magnetic substances, introducing the concept of magnetic poles, and exploring the Earth's magnetic properties [25]. Two centuries later Carl Friedrich Gauss gave significant contributions to the study of Earth's magnetism. Gauss carried out a "General Theory of Terrestrial Magnetism", which he published in 1839, in which developed a mathematical framework for describing the Earth's magnetic field using potential theory [26]. He introduced the concept of magnetic potential and demonstrated how it could be employed to model the geomagnetic field by the use of spherical harmonics. The theory predicted the existence of exactly two magnetic poles on the Earth, and the experimental data allowed us to determine their location with rather good precision. It is important to stress that Gauss promoted the establishment of a network of magnetic observatories to gather systematic and accurate measurements of the Earth's magnetic field. This laid the groundwork for organized magnetic field monitoring. He also designed and improved magnetic instruments, including magnetometers, to measure the strength and direction of the Earth's magnetic field more precisely. His contributions to the development of magnetic instrumentation were crucial for advancing geomagnetic research. In addition, Gauss proposed a coordinate system for describing the Earth's magnetic field, pro-

viding a standardized way to represent magnetic data. This system, known as the geomagnetic coordinate system, is still used in geomagnetic research today. Gauss also worked on creating magnetic maps, plotting the distribution of magnetic field values across different locations. These maps helped visualize the variations in Earth's magnetic field.

The geomagnetic field model described by Gauss consists of a set of coefficients that describes the Earth's magnetic field vector $\boldsymbol{B}(t, r, \theta, \phi)$ for a given time t and position (r, θ, ϕ) in spherical coordinates, with r being the distance from the Earth's center, $\theta = 90° - \lambda$ is the geographic colatitude (λ is geographic latitude) and ϕ the geographic longitude. These coefficients are part of the solutions of the Laplace equation $\nabla^2 V = 0$ which can be searched for the geomagnetic field, in the absence of electric currents ($\nabla \times \boldsymbol{B} = 0 \rightarrow \nabla \times (\nabla V) = 0 \rightarrow \nabla^2 V = 0$).
Gauss demonstrated that the geomagnetic field can be described in a good approximation as a gradient of a scalar potential, which can be expressed as the sum of two contributions, one of internal origin (V^i) and one of external origin (V^e):

$$\boldsymbol{B} = -\boldsymbol{\nabla}(V) = -\boldsymbol{\nabla}\left(V^i + V^e\right) \tag{2.1}$$

therefore at the Earth's surface, the magnetic field due to internal (core and crust) sources can be derived as the negative gradient of the internal scalar potential $\boldsymbol{B_i} = -\boldsymbol{\nabla} V_i$, and at the same way, the magnetic field due to external sources (due to electric currents in the Earth's ionosphere and magnetosphere) can be derived as the negative gradient of the external scalar potential $\boldsymbol{B_e} = -\boldsymbol{\nabla} V_e$. Both the internal and external potential in equations 2.1 can be expanded in spherical harmonics, which are functions that oscillate over the surface of a sphere. They are the product of two functions, one that depends on latitude and one on longitude. For a spherical geocentric coordinate system, the spherical harmonic expansion of the two scalar potentials in equation 2.1 can be written as follows:

$$V^i = R_E \sum_{n=1}^{\infty} \sum_{m=0}^{n} \left(\frac{r}{R_E}\right)^{-n-1} P_n^m(\cos\theta) \left[g_n^m \cos(m\phi) + h_n^m \sin(m\phi)\right] \tag{2.2}$$

$$V^e = R_E \sum_{n=1}^{\infty} \sum_{m=0}^{n} \left(\frac{r}{R_E}\right)^{n} P_n^m(\cos\theta) \left[G_n^m \cos(m\phi) + H_n^m \sin(m\phi)\right] \tag{2.3}$$

where R_E is the radius of the Earth at the equator ($R_E \sim 6378km$). Degree n and integral order m are two integers with $m < n$ and $P_n^m(\cos\theta)$ are the associated Legendre functions, in particular

$$P_n^m(\cos\theta) = \begin{cases} P_n(\cos\theta) & m = 0 \\ \sqrt{\frac{2(n-m)!}{(n+m)!}} (1 - \cos^2\theta)^{m/2} \frac{d^m P_n(\cos\theta)}{d(\cos\theta)^m} & m > 0 \end{cases}$$

specifically, in geomagnetism $P_n(\cos\theta)$ are the Legendre's functions with the Schmidt's semi-normalization.
The coefficients g_n^m, h_n^m, G_n^m and H_n^m are the best-fitting *Gauss coefficients*, with dimension of a magnetic field, obtained via a least-squares fit to the magnetic field measurements. Clearly, the magnetic field components can be obtained by replacing equations 2.2 and 2.3 in equation 2.1.

The magnetic field components, in particular, the north, east, and vertical components of the surface magnetic field, in a spherical coordinate system, are then given by

$$X = -\frac{1}{r}\frac{\partial V}{\partial \theta}, \qquad Y = -\frac{1}{r sin\theta}\frac{\partial V}{\partial \phi}, \qquad Z = -\frac{\partial V}{\partial r} \tag{2.4}$$

In the dipolar approximation geometry, the equation of the geomagnetic field line can be written as:

$$r = r_e sin^2\theta \tag{2.5}$$

where θ is the colatitude and r_e is the distance of the line of force to the centre of the reference system in the equatorial plane. Notice that this equation is symmetric with respect to the equatorial plane.

In general, equations 2.2 and 2.3 represent the sum of infinite terms, therefore, an approximation is necessary: the order of the series expansion is given by the number of experimental simultaneous magnetic field measurements in different observatories on Earth. The $n = 1$ term determines the existence of three coefficients g_1^0, g_1^1, and h_1^1 which describe the magnetic dipole contribution, that accounts for $\sim 95\%$ of Earth's magnetic field at ground (higher degrees account for the remaining 5%), but at higher altitude, for example at 6000 km, the dipole accounts for as much as 98.7% of the total magnetic field. Terms with higher degrees, for example, coefficients describing the magnetic quadrupole ($n = 2$) or octupole ($n = 3$) attenuate more rapidly with radius. In general, low-degree *Gauss coefficients* of the expansion (with $n \leq 14$) represent wavelengths of the magnetic field that are dominated by the core field, while higher degrees ($n > 14$) are dominated by the crustal field and local contributions of superficial sources.

Since the number of variables, the *Gauss coefficients*, grows very quickly as the order of expansion increases, and this states for both internal and external terms, to facilitate the resolution of the problem, Gauss made the additional hypothesis of the absence of external contributions to the geomagnetic field; this hypothesis allows to double the order of the measurements. To date, this hypothesis is no longer followed, even if the contributions of external origin are much lower than those of internal origin. Since the mid-20^{th} century, various mathematical models were developed to represent the geomagnetic field. However, the need for a unified international model became evident with the increasing space activities and the growing importance of magnetic navigation.

The International Geomagnetic Reference Field (IGRF) is a standard mathematical description of the large-scale structure of the Earth's main magnetic field. It was created by fitting parameters of the Gauss mathematical model of the magnetic field to magnetic field data measured from surveys, observatories, and satellites across the globe. The IGRF has been produced and updated under the direction of the International Association of Geomagnetism and Aeronomy (IAGA) since 1965. After the first edition, the IGRF was periodically updated, every 5 years, to reflect new geomagnetic observations and improvements in modeling methods.

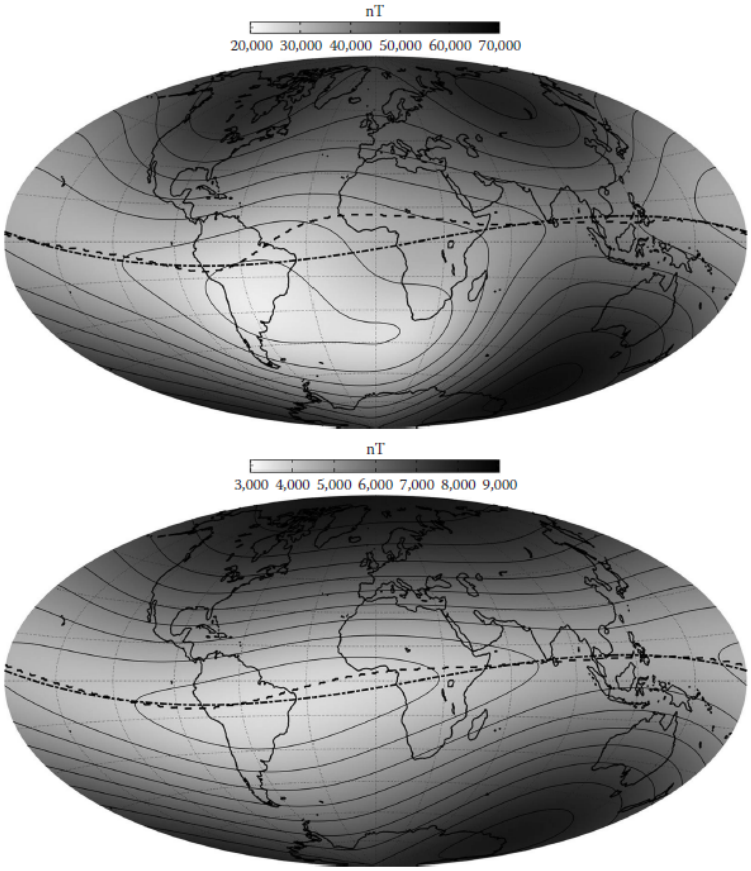

Figure 2.1: Map of the magnetic field strength F at ground (top), and at 6000 km altitude (bottom). The dashed curve represents the location of the magnetic dip equator (where the field lines are horizontal) at the respective altitude; the dash-dotted line shows the location of the dipole equator (defined as the equatorial plane of the dipole frame). Figure from [27].

The best-fitting dipole, in the *centered dipole approximation*, is tilted at an angle of about 10° with respect to the axis of terrestrial rotation, with the dipole axis passing through the Earth's center and emerging in Canada for the northern hemisphere. The g_1^0 Gauss coefficient is negative, this means that the magnetic

north pole is actually in the southern hemisphere, and vice versa, therefore the geomagnetic field has field lines entering the Northern Hemisphere and leaving from the Southern Hemisphere. A better approximation is the one of a non-centered geomagnetic dipole, which is ideally displaced around 400 km from the Earth's center towards the Northern Pacific, called *dip pole approximation* (see Figure 2.1). As well geographic latitude and longitude are defined for a geographical reference frame, in the same way, magnetic latitude and longitude can be defined for a geomagnetic reference system.

In geomagnetism, the geomagnetic field is a vectorial field denoted by $\boldsymbol{F}(\boldsymbol{r}, t)$, a function of position and time. At a fixed time t, if the position is a place on Earth's surface, the reference system can be conveniently chosen with the origin in that point of measurement (P), the $\hat{x}$ axis pointing to the geographic north, the $\hat{y}$ axis pointing to the geographic east and the $\hat{z}$ axis pointing vertically to the Earth's center. The three components of the Earth's magnetic field along such axes are called X, Y and Z, as shown in figure 2.2, and we can therefore define:

$$F = \sqrt{X^2 + Y^2 + Z^2}; \qquad H = \sqrt{X^2 + Y^2} \tag{2.6}$$

where H is the horizontal component, that is the projection of $\boldsymbol{F}$ on the horizontal plane. For simplicity, information on $\boldsymbol{F}$ is often obtained by the use of

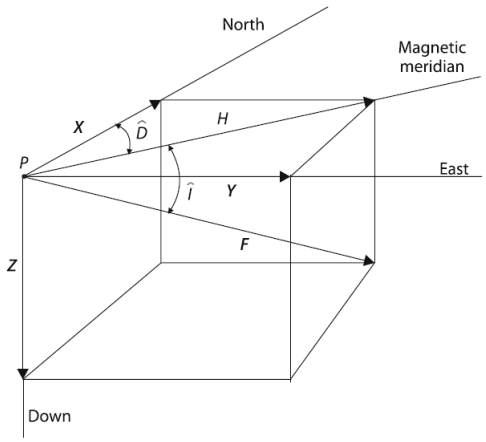

Figure 2.2: Elements of the Earth's magnetic field. At point P, on the Earth, three axes point respectively to north geographic (North), east geographic (East), and along the vertical downwards (Down). The Earth's magnetic field vector $\boldsymbol{F}$ can be projected along the three axes and three magnetic field components are obtained: X, Y and Z. $\boldsymbol{F}$ also forms an inclination angle $\hat{I}$ with the horizontal plane; H is the horizontal projection of $\boldsymbol{F}$ and declination angle $\hat{D}$ is the angle between H and X

the intensive element $|\boldsymbol{F}|$, and two angles: the inclination $\hat{I}$, that is the angle that $\boldsymbol{F}$ forms with the horizontal plane, and declination $\hat{D}$, that is the angle between the horizontal component H (projection of $\boldsymbol{F}$ on the horizontal plane)

and the direction of the geographic north. The relations among these quantities are:

$$H = F\cos\hat{I}; \quad Z = F\sin\hat{I} = H\tan\hat{I}; \quad X = H\cos\hat{D}; \quad Y = H\sin\hat{D} \quad (2.7)$$

The SI unit for measures of the geomagnetic field is the Tesla, but in practice in geophysics, it is widely used his submultiple, the nanoTesla (nT = 10^{-9}T). On the Earth's surface the geomagnetic field varies in magnitude mainly with latitude; e.g., the field varies from about 20000 nT to about 68000 nT from the equator to the poles. The quantitative determination of the Earth's magnetic field is done using magnetic instruments, called magnetometers. Over the years many kinds of magnetometers have been designed in order to improve the quality of the measurement or to reach a better portability, efficiency, or ease of use. Being the geomagnetic field a vector it is in fact self-evident that its complete determination needs the quantification of all elements of this vectorial quantity. A full knowledge of the Earth's magnetic field vector $\boldsymbol{F}$ needs at least the measurement of one of its intensive components. Gauss was the first to construct a complete set for the absolute determination of the geomagnetic field elements, in the early years of the 19^{th} century, and it was for the first time called a magnetometer.

In general, from the total field F magnitude and the angular quantities $\hat{D}$ and $\hat{I}$, the geomagnetic field components H, Z, and also X, Y can be computed. Sometimes magnetic instruments give as outputs directly the geomagnetic components; it is self-evident that once three independent elements are determined, the magnetic field measurement is considered complete. Nowadays magnetic instruments that utilize magnets for their operation are only very seldom used in magnetic observatories. Moreover, the measurement of declination and inclination angles is a procedure employed mainly for absolute magnetic measurements in magnetic observatories or at repeat magnetic stations. In geomagnetism, the term absolute measurement is still often used to indicate a procedure for the complete absolute determination of the magnetic field elements. On the other hand, relative instruments are widely utilized. An instrument is called relative when it measures the value of one element of the Earth's field as a deviation from a certain initial value not necessarily known. The use of relative instruments can be very convenient for example when only the spatial variation of the magnetic field in an investigated area is required or when, at a given place, a time variation of the Earth's magnetic field needs to be recorded.

2.1 Main interactions between Solar Wind and Geomagnetic field

When the solar wind encounters the geomagnetic field, it results in an obstacle for the wind. According to the Alfvén theorem, magnetic field lines are

frozen in the plasma. As the SW and the IMF interact with Earth's magnetic field, the geomagnetic field lines are carried along with the flow of the plasma. This interaction causes the SW to compress the geomagnetic field on the day side of Earth and stretch it into a long tail on the night side, shaping the magnetosphere. Figure 2.3 shows a cross-section through the Earth's magnetosphere in the noon-midnight meridian plane, where the black arrowed solid lines indicate geomagnetic field lines. Initially, the interaction leads to the formation of a *bow shock* on the sunward side, a region where the SW is first slowed and deflected by Earth's magnetic field.

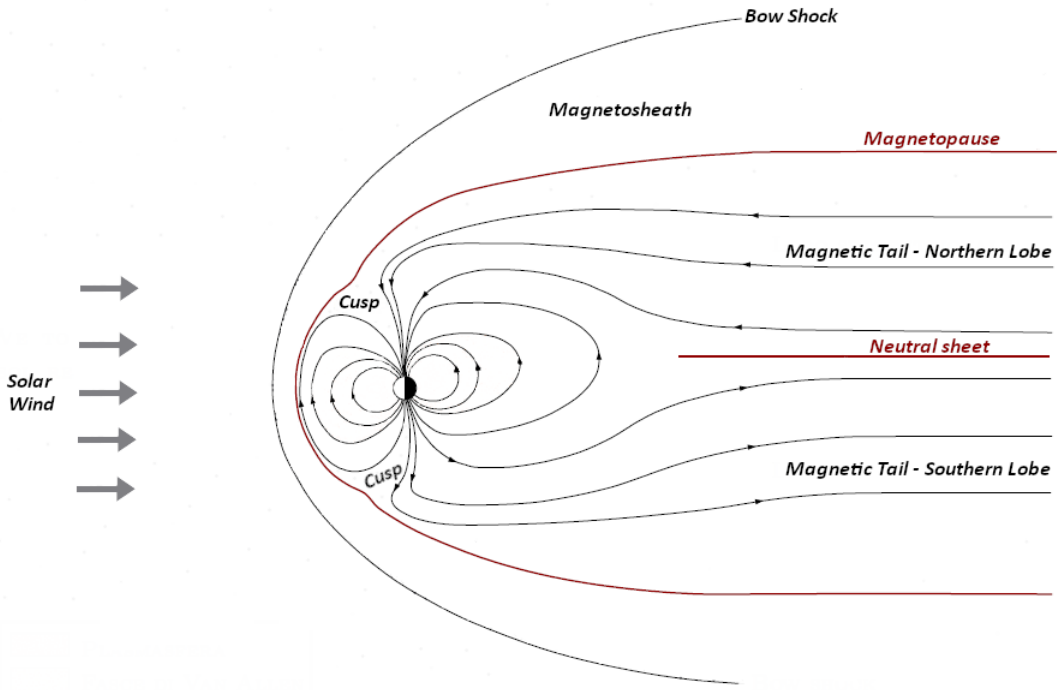

Figure 2.3: A sketch of Earth's magnetosphere in the noon–midnight meridian plane. The solar wind flows, from the left to the right, shocked by the bow shock as it encounters the Earth's magnetosphere. The black arrowed solid lines show geomagnetic field lines, which are flattened on the day side and elongated on the night side. Cusps are formed at high latitudes in both hemispheres.

The magnetopause is the outer boundary of Earth's magnetosphere, schematically represented with the red curve in Figure 2.3, where the SW and the Earth's magnetic field interact: here the pressure of the incoming SW is balanced by the pressure of the geomagnetic field (the plasma pressure inside the magnetopause can be neglected, as well as the IMF pressure outside). It is a region of significant transition between the solar wind-dominated space and the Earth's magnetosphere. Between the bow shock and the magnetopause, there is a transition region called *magnetosheath*, composed by shocked SW plasma.

The density of the particles in this region is higher than what is found outside the bow shock and within the magnetopause, and it can be considered a transitory state of turbulent plasma flow. The magnetopause on the side of the Earth facing the Sun - at the subsolar point - is typically about 10 Earth radii (R_E) away from the Earth. At the magnetopause, at a first order, the magnetosheath thermal pressure, which is proportional to the SW dynamic pressure, is is balanced by the pressure of Earth's magnetic field. The shape of the magnetopause is not static and can change based on variations in the SW and the orientation of the IMF. During periods of SW characterized by high dynamic pressure or southward IMF, the magnetopause can be compressed, bringing it closer to Earth. Conversely, during weaker solar wind or northward IMF, it can expand farther out. The region where the Earth's magnetic field prevails, enclosed by the magnetopause, is called the *magnetosphere*. Within the magnetosphere, the geomagnetic field is nearly dipolar close to the Earth and it is pulled out into a very long *magnetotail* by the solar wind flow on the nightside. The regions where the footprints of the tailward open field lines are located are called polar caps. In each hemisphere, the polar cap is surrounded by the auroral oval, a region involved in the magnetospheric dynamics described in the following paragraphs. At high latitudes in both hemispheres, there exist so-called cusps, on the dayside of the magnetosphere, that mark the separation between the closed magnetic field lines going sunward and those going tailward. The size and shape of the magnetosphere and the position of the bow shock change as the parameters of the solar wind change. The Earth's magnetosphere is a complex system where interactions between SW and the Earth's magnetic field lead to dynamic and interacting phenomena, including magnetic reconnection, plasma instabilities, and the formation of various current systems.

The magnetospheric reconnection: the Dungey cycle

The Earth's magnetosphere results from the dynamic interplay between the SW and Earth's intrinsic magnetic field. It is widely accepted that one of the major mechanisms that control SW-magnetosphere coupling is the *magnetic field line reconnection* between the IMF, with embedded the SW plasma, and the dayside magnetopause, with effects on the magnetosphere-ionosphere system.

James Dungey, in 1961, introduced the so-called *Dungey's cycle* to describe how a planet's magnetosphere, like the Earth's magnetosphere, interacts with the SW. To explain the observed dynamics within Earth's magnetosphere, Dungey proposed a recurring process of magnetic reconnection between Earth's magnetosphere and the IMF [28]. The rate of reconnection at the cycle's start depends on the orientation of the IMF and plasma conditions. The key parameter related to the SW-magnetosphere coupling is the clock angle θ_{clock} of the IMF as seen by the Earth's magnetic dipole. In the geocentric solar magnetic (GSM) coordinate system - in which the x-axis points from the center of the Earth to the Sun, the y-axis is perpendicular to both the magnetic dipole

axis and the Earth–Sun line, positive towards dusk, and the z-axis completes a right-handed system - the clock angle is given by:

$$\theta_{clock} = \cos^{-1}\left(\frac{B_z}{\sqrt{{B_y}^2 + {B_z}^2}}\right) \tag{2.8}$$

where B_z is the dipole north–south component of the IMF vector $\boldsymbol{B}$, and B_y is the dipole dawn-dusk component of $\boldsymbol{B}$. When the clock angle is 0° the IMF is purely northward, when the clock angle is 180° the IMF is purely southward.

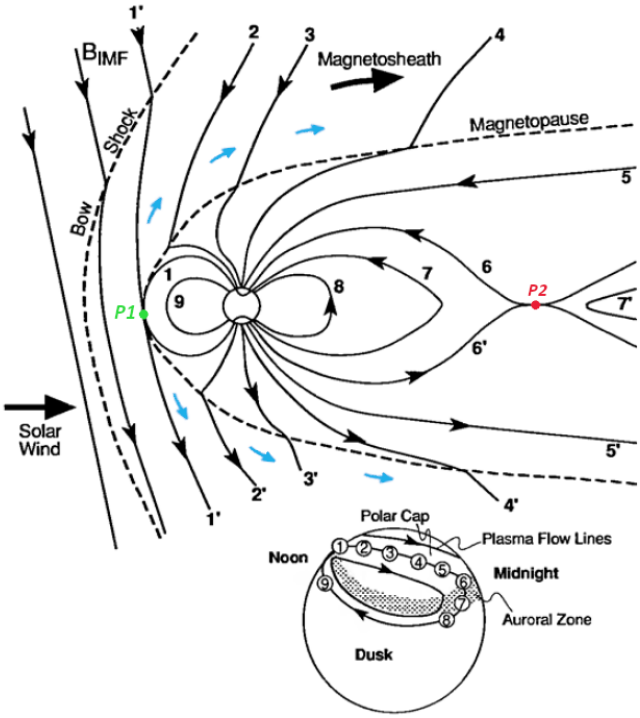

Figure 2.4: A sketch of plasma flow within the magnetosphere driven by *magnetic reconnection*, seen in the meridian plane viewed from the dusk side. Adapted from [29]. The field lines have progressive numbers following the so-called *Dungey cycle*. The numbers in ascending order, starting from 1, refer to the temporal progression of the succession of configurations of the geomagnetic field lines after reconnection with the IMF lines. The green point, P1, is the dayside neutral reconnection point. The red point, P2, is the nightside neutral reconnection point. Blue arrows represent the plasma displacement. On the bottom, it is also shown the position of the footpoints of the numbered field lines in the northern high-latitude ionosphere, and the corresponding plasma flows: antisunward flow in the polar cap and a return flow at lower latitudes.

Let's assume $\boldsymbol{B_{IMF}}$ predominantly southward ($\theta_{\text{clock}} \sim 180°$); when they make contact (as in the green point P1 in figure 2.4) with the mainly northward-

pointing geomagnetic field lines at the dayside magnetopause, IMF lines are approximately antiparallel to geomagnetic field lines, leading to a *magnetic reconnection*, like the one shown in figure 2.4 between the field lines labeled 1 and 1'. Then, instead of a purely geomagnetic field line with both ends attached to the Earth and an IMF line with both ends on the Sun, two field lines of a new type are obtained. These new field lines each have one end attached to the Earth (close to the north or south pole) and the other end stretching out into the interplanetary space. In the *Dungey's cycle* a magnetospheric magnetic field line that becomes connected on the dayside to the IMF is dragged by the moving SW plasma (blue arrows in figure 2.4), with a drift velocity $v_D = |\boldsymbol{E} \times \boldsymbol{B}|/B^2$, from the front of the magnetosphere over the poles and is laid down into the magnetotail, as shown in figure 2.4. The newly connected SW-magnetic field lines are shown passing the Earth, connecting to the polar cap in both the northern and southern polar regions. The polar cap is indeed the set of field lines that participate in magnetic reconnection. The result is a magnetosphere that is flattened on the day side and elongated on the night side. A secondary site of magnetic field line reconnection P2 (red point in figure 2.4) in the magnetotail enables the movement of magnetospheric magnetic field lines toward the Sun, from the magnetotail into the nighttime dipole region of the magnetosphere. Subsequently, magnetospheric convection shifts these field lines around either the dawn side or the dusk side of the dipole, returning them to the dayside magnetosphere, completing the cycle. Magnetic reconnection in P2 generates a release of plasma and energy both towards the Earth and towards interplanetary space. The plasma released towards Earth can lead to a geomagnetic substorm (see section 2.2.2.3) and it can interact with the Earth's atmosphere, particularly in the polar regions, giving rise to the polar aurora.
In line with the magnetospheric Dungey cycle, the point where the magnetic field line connects to the ionosphere follows a path, as shown in the bottom sketch in figure 2.4. It cycles from the high-latitude dayside area and moves anti-sunward across the polar cap to the high-latitude nightside region. Then, it either travels around the dawn or dusk side at high latitude, returning to the high-latitude dayside area. This creates the high-latitude "two-cell" convection pattern in the ionosphere [30] one of which is shown at the bottom of the figure 2.4.

The inclination of the magnetic dipole axis with respect to the ecliptic always allows the presence of an IMF component (more or less intense) which contributes to the magnetic reconnection. Furthermore, the reconnection can also occur in the horizontal direction, on the Earth's equatorial plane. Magnetic reconnection, mild or intense, occurs continuously; this means that the magnetic flux is continuously transferred from the day side to the night side.

Currents System in magnetosphere

The interaction between the SW and the geomagnetic field induces various large-scale electric currents in the Earth's magnetosphere that play a crucial role in the complex dynamics of the system and the plasma contained therein, surrounding the Earth. These currents transport charge, mass, momentum, and energy, and also create magnetic fields that alter existing fields.

Figure 2.5 shows the main currents in the magnetospheric system. The small sphere at the center of the reference system represents the Earth; the part facing the Sun is white and the part facing the night side is black. The outer shell, shaped like a paraboloid, represents the magnetopause.

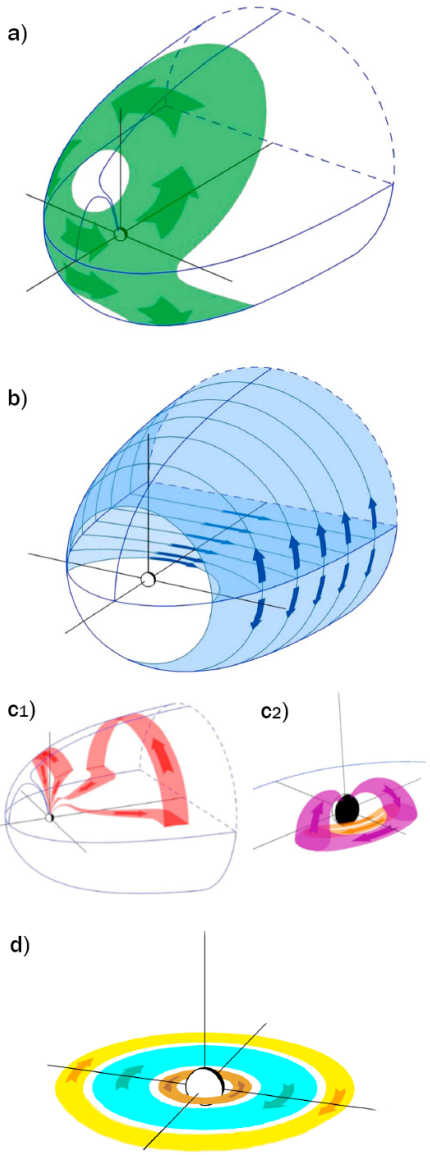

Figure 2.5: *a) Magnetopause current or Chapman-Ferraro current. b) Magnetotail currents. c) Field Aligned Currents (FACs). d) Ring current. Adapted from [31]*

Figure 2.5 a) shows the electric current flowing along the magnetopause, which is known as *magnetopause current* or *Chapman-Ferraro current*. It is formed because when SW particles encounter the Earth's magnetic field, they are bent from their paths by the Lorentz force. Due to their opposite charge sign, protons gyrate in a left-handed sense around the magnetic field lines and electrons in a right-handed sense. Since the particles are coming from the Sun toward the Earth and the direction of Earth's field around the subsolar point is upward, this gyration creates an electric current flowing from dawn to dusk across the equatorial magnetopause and from dusk to dawn across the high-latitude magnetopause. The resulting current field weakens the Earth's field outside the magnetopause and strengthens it inside. Once the current is fully developed, it occupies a thin sheet everywhere on the dayside of Earth, outside of which is canceled all the terrestrial field. Within

the thin sheet, the field is twice as strong as the main field.

On the night side, the magnetic field stretches over many tens or a few hundred of Earth's radii, creating a long magnetotail, as previously shown in Figure 2.3. Figure 2.5 b) shows the magnetopause current which closes on the night side on the tail magnetopause. Most of the volume of the tail is taken up by two large bundles of nearly parallel geomagnetic field lines of opposite directions. The geomagnetic field in the north lobe is directed toward the Earth, while the geomagnetic field in the south lobe is directed away from the Earth. Therefore, when passing from one lobe to another $\boldsymbol{\nabla} \times \boldsymbol{B} \neq 0$ meaning that an electric current must exist in the layer separating the two lobes. The interaction of the electric current with the magnetic field in turn gives rise to a force $\boldsymbol{J} \times \boldsymbol{B}$ that balances the plasma pressure gradient $\boldsymbol{\nabla} P$ which populates the magnetic tail. It follows that the current layer is populated by a plasma which, with its pressure, keeps away the field lines with opposite polarity. This current sheet lies in the center of the tail, embedded within a region of hot plasma, the plasma sheet, that separates the two tail lobes. The magnetotail is quite dynamic, large changes can take place there and ions and electrons are often energized.

The *ring current* is an electric current encircling Earth in the equatorial plane, as shown in Figure 2.5 d). It is caused by the longitudinal drift of energetic (10–200 keV) trapped charged particles, primarily ions, in the geomagnetic field. In an inhomogeneous magnetic field, such as that of the Earth, the gradient of the magnetic field and its curvature of field lines leads to a magnetic drift of charged particles, also called gradient-curvature drift. In such a configuration, ions and electrons drift in opposite directions, perpendicular to both $\boldsymbol{B}$ and $\boldsymbol{\nabla} B$. The opposing drifts of electrons and ions lead to a transverse current, which is perpendicular to the magnetic field and its curvature. In particular, the electrons drift eastwards, which corresponds to the brown current in Figure 2.5 d) whereas the ions drift westwards which corresponds to the blue current in Figure 2.5 d) giving rise to a net westward current, known as *ring current*, circulating around the Earth (yellow current in Figure 2.5 d). The ring current's radial profile, intensity, and thickness are functions of the plasma populations of ions and electrons that carry the current itself. The ring current has the effect of "weakening" the horizontal component of the geomagnetic field, therefore the magnetic field perturbation is a very good measure of the total energy of the ring current particles. In fact, there is an important geomagnetic index, called the *Dst index*, which measures the magnetic disturbances caused by the ring current, but measured at the Earth's surface. This index is used to characterize magnetic storms (see chapter 2.2.2.3) which are usually accompanied by a strong variation of the ring current and therefore of the energetic particles injected from the SW into the magnetosphere. Another important geomagnetic index is the *planetary Kp-index*, introduced by Julius Bartels in 1949 [32] to

measure solar particle radiation by its magnetic effects. It gives us an indication of the level of geomagnetic disturbance on a planetary scale. Kp index is derived by calculating a weighted average of K-indices from a network of 13 geomagnetic observatories at mid-latitude locations. The K-index quantifies disturbances in the horizontal component of Earth's magnetic field with an integer in the range 0–9 where a higher number refers to a more disturbed geomagnetic activity. It is derived from the maximum fluctuations of horizontal components observed on a magnetometer during a three-hour interval, at the given location and time compared to a calm day curve. The Kp-index also ranges from 0 to 9 where a value of 0 means that there is very little geomagnetic activity and a value of 9 means extreme geomagnetic storming. In this case, however, each unit in the 0 to 9 scale is tripartite obtaining a discrete scale of 28 values. This index is used for preliminary discrimination of quiet days.

Currents in the Earth's magnetosphere can flow not only perpendicular but also parallel to the magnetic field. In fact, *Field-aligned currents (FACs)* are electric currents, mainly carried by electrons, that flow along the magnetic field lines, which connect the magnetospheric currents with ionospheric currents. The FACs were first suggested by Birkeland (1908) [33] - this is why they are also called *Birkeland currents* - to explain the variations of the geomagnetic field measured on the ground in the polar regions. He found that electric currents are guided by field lines to a ring around the Earth's poles. These currents play a crucial role in the energy coupling between the SW and Earth's magnetosphere, influencing various magnetospheric processes. FACs can connect largely separated regions electrically, and they transfer energy and momentum almost lossless over large distances. This is because the conductivity along magnetic field lines is very high (therefore, field lines can be regarded as equipotential lines, under DC conditions). All the magnetic field lines in the magnetosphere are connected at least to one side to the ionosphere, this means that any potential difference anywhere in the magnetosphere is mapped into the ionosphere, drives currents there, and dissipates energy. FACs are therefore important because they are the connecting elements between the magnetosphere and ionosphere at high latitudes. They are usually classified into two regions: the high-latitude Region 1 or R1 (Figure 2.5 c1) which connects to the outer magnetosphere and the lower Region 2 or R2 (Figure 2.5 c2) which connects to the outer edge of the ring current. R1 FACs flow downward into the ionosphere in the dawn sector and upward out of the ionosphere in the dusk sector. R2 FACs flow in the opposite direction. Both FAC regions close on the auroral oval through electrojet currents flowing in the ionosphere at high latitudes.

2.2 Variation of geomagnetic field

The Earth's magnetic field is subject to variations on different time scales. Each of the sources of the geomagnetic field is subject to changes that produce

transient variations or disturbances in the geomagnetic field. These variations go from fractions of seconds to millions of years, due to different mechanisms, and they can be divided into two main classes: long-term and short-term variations. The long-term variations are related to deep sources inside the Earth (the same that generate the main field) with a minimum characteristic time of around 5-10 years. The short-term variations are instead related to external contributions, essentially related to solar activity and its interaction with the magnetosphere.

A way to schematize the above-mentioned variations based on time scales and related to different phenomena is as follows:

Internal Origin

$\mathbf{10^{15}}\boldsymbol{s}$ $\sim$ tens of millions of years. $\rightarrow$ Variations related to the ***geomagnetic polarity reversal*** of the geomagnetic field.

$\mathbf{10^{10}}\boldsymbol{s}$ $\sim$ hundreds of years. $\rightarrow$ ***Secular variations*** mainly associated with processes occurring in the Earth's fluid outer core and at core-mantle boundary layer.

External Origin

$\mathbf{10^{6}}\boldsymbol{s}$ $\sim$ 11-12 days $\rightarrow$ ***Geomagnetic storms***.

$\mathbf{10^{5}}\boldsymbol{s}$ $\sim$ 1 day $\rightarrow$ ***Diurnal variation***.

$\mathbf{10^{4}}\boldsymbol{s}$ $\sim$ a few hours $\rightarrow$ ***Geomagnetic substorms***.

$\mathbf{10^{2}}\boldsymbol{s}$ $\sim$ 1 minute and less $\rightarrow$ ***Pulsations***.

Below are described in a little more detail the above-mentioned variations, with more focus on those of greater interest for this thesis work.

2.2.1 Internal origin

Although variations of internal origin are not covered in this work, I describe them briefly below. Instead, I will better focus on external origin variations in section 2.2.2.

2.2.1.1 Geomagnetic polarity reversal

The inversion of geomagnetic field polarity, known as geomagnetic reversal or magnetic polarity reversal, is a phenomenon, related to the geodynamo mechanism, in which the Earth's magnetic field undergoes a substantial and systematic change in its orientation. During a reversal, the magnetic north and south poles effectively switch places. This process is revealed through the study of magnetic rocks, providing a record of the Earth's magnetic history.

The mechanisms that occur in the Earth's core and are responsible for such reversals are still under study and not completely known; it seems that a fundamental role is played by changes in physical conditions at the core-mantle separation surface. The evidence for the existence of the reverse polarity of the geomagnetic field is based on several observations and scientific studies, including magnetic recording in rocks, analysis of the polarity bands on the ocean floor and sediment, comparison with fossil record, and so on. It has been found that the verse of the dipolar part of the geomagnetic field reverses on average every $3 \cdot 10^5 - 10^6$ years. The time interval between one inversion and the other is very variable, it can go from $4 \cdot 10^4$ to $3.5 \cdot 10^6$ years and so far it has not been found periodicity or regularity in the succession of the inversions: long intervals where the field has maintained the same polarity can be followed by short intervals with opposite polarity.

2.2.1.2 Secular Variation

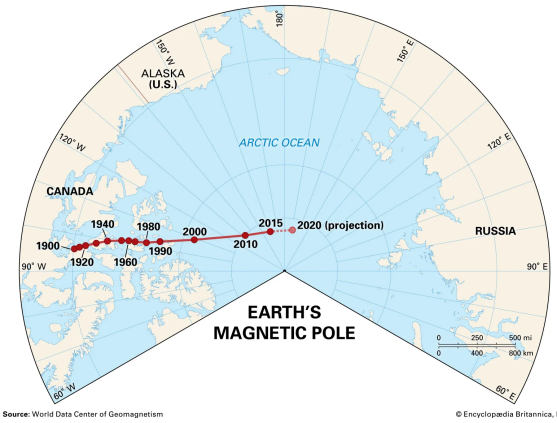

Figure 2.6: *Map of Earth's northern polar region marking known locations and times of the geomagnetic North Pole since 1900 (from Encyclopaedia Britannica, Inc.).*

The secular variation term is utilized to refer to geomagnetic variations that occur on time scales from a few years and a few tens of thousands of years. This variation can be detected when at least $5 - 10$ years, or more, magnetic data from a certain area are examined. The secular variation is due to the evolution of the deep sources within the Earth, the same sources that also generate the main field. It can be seen in geomagnetic observatory data when several years for one or more field elements (generally by their annual or monthly means) are plotted against time. For a given place of observation, the amplitude of these variations fluctuates between a few nT and a few tens of nT per year for the intensive components (X, Y, Z, H, and F) and from a few primes (or minute of arc) to a few tens of primes per year for the inclination (I) and the declination (D). Studies concerning this variation are typically divided into two parts: those concerning the dipolar approximation of the field, and those studying non-polar terms, including anomalies and multipolar components. The secular variation is a characteristic of the main field and, it is therefore representative of a planetary phenomenon, although it seems to show different trends in the various observatories all around the world. The most

important results from Geomagnetic Observations about this variation over the last 400 years are:

- A mean annual decrease of the dipole moment of the order of 0.05% of its average value with a considerable acceleration in the last 30–40 years;
- A westward precession of the dipole axis of 0.08° per year;
- A northward displacement of the dipole of the order of 2 km per year;
- A westward drift of the non-dipole field, or a part of it, of 0.2°-0.3° per year, associated with a possible but not specified southward drift;
- An intensity variation (increase or decrease) of the non-dipole field at a mean rate of about 10 nT/year.

On average magnetic field elements plotted versus time (at a geomagnetic observatory) show quasi-stable or slow-changing time variations. However, secular variation has one peculiar feature represented by a clear tendency to show at times rapid changes, observable as a variation in the slope, taking place in one or two years. This peculiar phenomenon that separates periods of reasonably steady secular variation patterns (i.e. constant slopes in the geomagnetic field time variation) is called a geomagnetic jerk. Geomagnetic jerks are thus abrupt changes in the second time derivative (secular acceleration) of the geomagnetic field. In this sense, a Geomagnetic jerk separates periods of almost steady secular acceleration of the geomagnetic field.

2.2.2 External origin

As mentioned above, the geomagnetic field on Earth's surface and in the surrounding regions results from different sources. The individual contributions exhibit a broad range of magnitudes, spatial scales, and variability, but the instantaneous state of Earth's magnetic environment largely reflects dynamic interactions between two important sources, a self-sustaining dynamo in the liquid outer core producing the dominantly dipolar internal field, and the solar wind from the Sun. The balance between the geomagnetic field pressure and the SW dynamic pressure defines the magnetopause, inside which lies the magnetosphere, a region extending to about 10-15 Earth radii and dominated by the geomagnetic field, as described in section 2.1.

The variations related to external origins are more rapid in time and are mainly connected with the Sun and solar activity. A general classification of external origin variations is the one that distinguishes among *regular variations*, *intermediate variations*, and *irregular variations*:

- Regular variations

  - Diurnal solar quiet variation
  - Diurnal lunar variation
  - Variations related to the Sun
- Intermediate variations
  - Geomagnetic pulsations
- Irregular variations
  - Geomagnetic storms
  - Subtorms
  - Pulsations

Below the characteristics of each of these phenomenologies are reported.

2.2.2.1 Regular Variations

As the name suggests, all variations that have a regularity, a characteristic period, fall into this class of variations.

Diurnal solar quiet variation

The diurnal solar quiet (Sq) variation refers to the regular, daily changes in the Earth's geomagnetic field during periods of low solar activity (quiet days). This daily variation of the geomagnetic field has been attributed to large ionospheric currents in the ionospheric dynamo region, due to the enhanced electrical conductivity in the ionosphere in that region, which does not continue in the nighttime due to the depletion of E-layer ionization. The current system is mainly a double vortex, one in the northern hemisphere and one in the southern hemisphere. The two current vortexes are centered around $\pm 40°$ of latitude in both hemispheres, on the dayside. A sketch of the Sq current system is shown in figure 2.7. Since the ionization of the ionosphere depends on the electromagnetic radiation from the Sun, it is clear that the ionospheric layers have a modulation in their ion

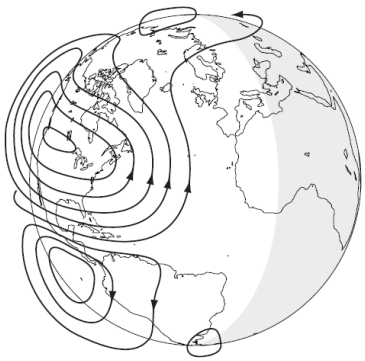

Figure 2.7: *Sketch of the Sq current system in the dayside ionosphere. The current direction is indicated by arrows. (Credit: US Geological Survey.)*

concentration and in their characteristics that depend on the time of day. The fundamental period of the diurnal variation is 24 hours, corresponding to one Earth rotation under the system of currents which is "fixed" with respect to the Sun-Earth line. The Sq variation exhibits harmonic components, which are variations at multiples of the fundamental 24-hour period, and the main of those is the semidiurnal (12 hours) variation. The amplitude of the solar quiet diurnal variation can vary depending on factors such as geographic location, season, and solar activity level. Near the equator, the diurnal variation tends to be more pronounced (of $\sim 10^2$ nT), while at higher latitudes, the variation may have different amplitude (of ~ 10 nT) and phase characteristics. Stations at the same magnetic latitude, but separated in longitude, record similar patterns but are delayed in time by the Earth's rotation.

Diurnal lunar variation

Fourier analysis of the diurnal variation at a single station reveals that it is primarily solar diurnal, with a smaller semidiurnal component. In addition, there is a weak lunar semidiurnal component at 12 h 25 min, implying that even lunar tides, which are excited by the gravitational force of the Moon, make contributions to the ionospheric dynamo. The main cause of the diurnal variation is the dynamo mechanism generated by the motion of electrons driven by winds in the ionosphere; these winds are driven by solar heating and lunar and solar tides.

Variations related to the Sun

Further regular variations in the geomagnetic field are related to the 11-year variation of the solar cycle and the relative motion of the Earth in its orbit around the Sun (seasonal variations, associated with the Earth's axial tilt and its orbit around the Sun). The geomagnetic activity reflects, for example, the 11-year periodicity of the Sun's number of sunspots.

There is also a semiannual variation of the geomagnetic activity during both active and quiet years. The maximum activity occurs near the equinoxes and the minimum activity near the solstices. This variation is related to the inclination of Earth's rotation axis at an angle of $\sim 23.5°$ with respect to the axis perpendicular to the ecliptic plane. The explanation of the semiannual variation proposed by Russell and McPherron in 1973 [34] is now widely accepted: it is based on the idea that magnetic activity occurs preferentially when the IMF is southward relative to the dipole axis and that it increases with the increasing of the southward component.

Another periodicity in geomagnetic variations is related to the equatorial rotation rate of the Sun as viewed from the moving Earth. The primary cause of the 27-day solar-rotation periodicity (as seen from Earth) regards the structures present on the Sun's surface, like coronal holes, that persist for more than one

Sun rotation becoming recurrent, as seen from Earth, with a 27-day period. As a consequence, the fast wind coming from them reaches the Earth recurrently.

2.2.2.2 Intermediate variations - Geomagnetic pulsations

Another type of geomagnetic variation, not recurring periodically, is represented by the geomagnetic pulsation. These disturbances occur in the Ultra Low Frequnecy (ULF) range, spanning from hundreds of mHz to 1 mHz. Processes in the magnetosphere and the SW produce a wide variety of ULF wave types, subsequently detected by ground magnetometers. A classification is useful to represent the variety of types of oscillations. Accordingly to IAGA, pulsations are classified based on period (or frequency) and morphology, as shown in table 2.1.

IAGA classification of geomagnetic pulsations					
Continuous Pulsations (Pc)			Irregular Pulsations (Pi)		
Type	Period (s)	Freq. (mHz)	Type	Period (s)	Freq. (mHz)
Pc1	0.2 - 5	200 - 5000	Pi1	1 - 40	25 - 1000
Pc2	5 - 10	100 - 200	Pi2	40 - 150	7 - 25
Pc3	10 - 45	20 - 100			
Pc4	45 - 150	7 - 20			
Pc5	150 - 600	1.7 - 7			

Table 2.1: Table with IAGA classification of geomagnetic continuous pulsations (Pc) in the left column and irregular pulsation (Pi) in the right column. A brief mention of irregular pulsations (Pi) will be made in the following section 2.2.2.3 regarding the irregular variations.

In addition to the *morphological classification* (based on periods, amplitudes, times of appearance, etc.), pulsations can also be classified in terms of *correlative classification*, based on the connection with other phenomena (e.g. magnetic storms, auroras, etc.), or in terms of the *genetic classification*, based on the production mechanisms. However, since the nature of some pulsations is still a subject of study, the *morphological classification* (table 2.1) is the most widespread.
Based on the morphological properties of geomagnetic pulsations, the first distinction is between continuous pulsations (Pc) and irregular pulsations (Pi). Continuous pulsations are quasi-sinusoidal signals lasting more than several cycles, therefore with a rather well-defined spectral peak; irregular pulsations are those with a wide spectral range (or short-lived pulsations). These two major classes of pulsation are split into subclasses based on the wave period or frequency, designating the subclasses by a number (see table 2.1). Figure 2.8 shows

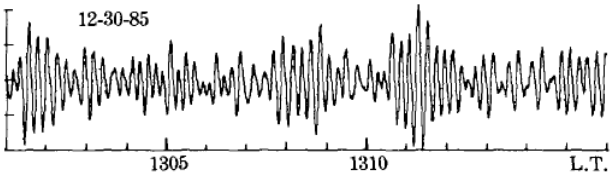

Figure 2.8: An example of continuous pulsations (Pc3 measured at L'Aquila (Italy)) for the H component, taken from [35].

an example of Pc, in particular a Pc3 for the H component of the geomagnetic field, with a period of $\sim$ 13 s and maximum amplitude of the order of $\sim$ 0.8 nT.
A more global view of the typical frequency range and characteristic amplitudes of the ULF waves can be seen in Figure 2.9. It shows the typical amplitude of the geomagnetic field intensity of pulsations in terms of the period (or the inverse: frequency). At the ground, the amplitude of the geomagnetic field pulsations varies from a few hundredth of nT to a few hundred of nT: generally the amplitude of the fluctuations increases as the period increases (or as the frequency decreases). The first to understand that the pulsations observed at the ground are related to waves propagating in the magnetosphere was Dungey in 1954. From then on, observations of ULF waves increased, with an ever-increasing number of observers reporting traces of them. In the 1960s were also reported in situ measurements of ULF oscillations at the geosynchronous orbit. In those years, many studies have been carried out using combined measurements from different devices, such as geosynchronous satellites and magnetometers on the ground.

ULF waves types depend on whether their energy source originates in the SW (external sources) or from processes within the magnetosphere (internal sources). Evidence for the former comes from the dependence of daytime power in the Pc3, Pc4, and Pc5 ranges on SW speed, density, and IMF clock angle. On the other hand, high-frequency Pc, like Pc2 and especially Pc1, are traceable to processes within the magnetosphere. ULF waves are of crucial importance in the SW-magnetosphere-ground system, because they transport and couple energy throughout the system, and may play important roles in the energization and loss of radiation belt particles [37]. Additionally, ULF waves serve as a useful tool for probing and diagnosing the magnetosphere. This work will not dwell much on all types of pulsations, which cover a very vast area of research. The following chapters will only deal with the pulsations in the Pc5 range; nonetheless, it is appropriate to briefly describe the other frequency ranges of the geomagnetic pulsations.

In terms of the *internal sources* of ULF waves in the magnetosphere, the most important is the ring current region with its energetic protons, during disturbed geomagnetic conditions. Such protons tend to thermalize via interaction

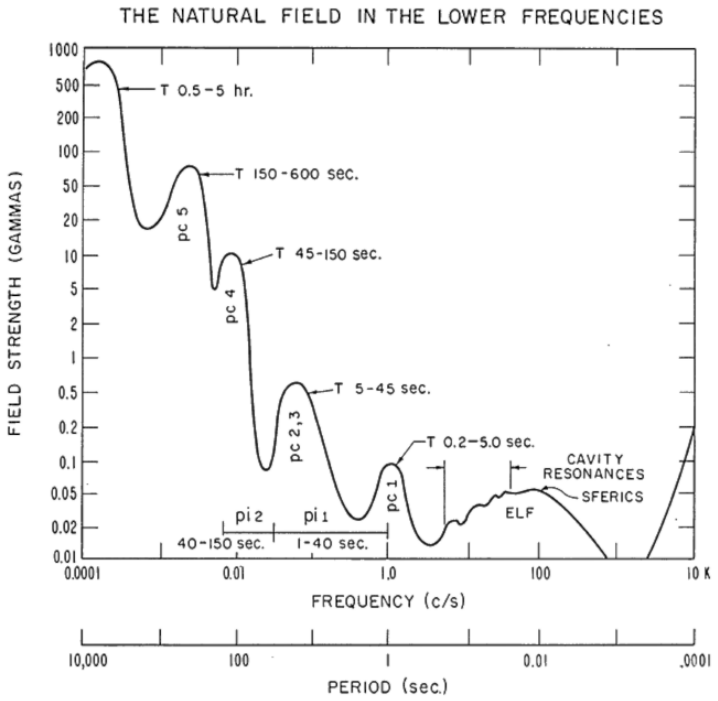

Figure 2.9: Amplitude (1 gamma = 1 nT) vs. period-frequency of geomagnetic pulsations. Amplitudes depicted in the figure are the typical sizes to be expected for moderate activity at mid-latitude locations. The "continuous" pulsation, Pc 1–5, nomenclatures are assigned the period ranges indicated near the peak amplitude positions. The "irregular" pulsation, Pi 1 and 2, nomenclatures are identified with their period ranges at the bottom. Figure from [36].

with electromagnetic waves. These waves in turn can be generated by plasma instabilities, such as the so-called bounce-resonance or drift-mirror instability that is mainly related to Pc3-5 and electromagnetic ion-cyclotron (EMIC) instability that locally generates Pc1-2 at the equatorial magnetospheric regions [37, 38].

As an *external source*, the SW provides the energy for geomagnetic pulsations, partly directly and partly indirectly. A direct energy source is plasma waves generated in the SW and penetrating the magnetopause. A major source of these waves is plasma instability in the upstream region of the near-Earth SW where protons reflected at the magnetospheric bow shock generate upstream waves, which are convected downstream toward the magnetopause and coupled through it into the magnetosphere. This mechanism is mainly related to Pc3-5. In terms of energy, only a small percentage of their energy couples to magnetosphere oscillations [38].
A more efficient SW-driven process is the impulsive excitation of plasma waves by sudden impulses from the SW. Due to its conformation, the magnetosphere is a body capable of eigenoscillations: the boundaries of the magnetosphere are

the magnetopause and the ionosphere, where the geomagnetic field lines are anchored much as strings. Due to the non-uniform distribution of plasma density in the magnetosphere, wave propagation can result in a phenomenon known as field line resonance mode coupling [39]. In this sense, the magnetosphere can behave like a resonator and Pc3-5 can be related to this mechanism.
In addition to the impulsive generation of geomagnetic pulsations, the Kelvin-Helmholtz instability plays a role in driving magnetospheric MHD waves, mainly Pc3-5. This instability arises at the magnetopause: the SW plasma flows around the magnetosphere along the magnetopause, creating shear conditions similar to atmospheric wind flowing over a water surface and generating waves. The velocity shear at the magnetopause destabilizes the boundary, giving rise to surface waves that couple into the magnetosphere. The energy for these waves is derived from the SW flow, and the maximum instability of the magnetopause is expected at the flanks of the magnetosphere, during the dawn and dusk hours. Moreover, these unstable waves should propagate tailward, moving east at dusk and west at dawn [40].

To study ULF waves, MHD approximation can be utilized when $\omega < \omega_c$ (as explained in section 1.3); in this sense, the short-period pulsations like Pc1 have frequency close to the proton cyclotron frequency (of few Hz in the magnetosphere), and do not fall within the MHD approximation. On the other hand, ULF waves from Pc2 to Pc5 have $\omega < \omega_c$, therefore long-period pulsation can be treated in the MHD wave approximation.
It is also important to underline that in trying to understand the mechanisms of generation and propagation of geomagnetic pulsations, magnetic field measurements from single-point magnetometers are usually used; therefore, the definition of wave propagation direction is ambiguous unless multipoint measurements are made [41]. In this context and in the absence of multipoint measurements, the study through various methodologies and different techniques allows for the broadening of knowledge on the mechanisms of generation and propagation of these ULF waves.

This work will focus on the lowest frequency ULF waves, specifically those in the Pc5 frequency range of 1–7 mHz, with a particular interest in how the SW, especially the Alfvénicity in HSS, controls Pc5 ULF waves. Previous studies (see [42] and reference therein) have shown the importance of the effect of the SW speed and SW dynamic pressure variation on the Pc5 pulsations, both at geosynchronous orbit and on the ground. In fact, several studies [37,42–44] suggest a good correlation between pulsations in the Pc5 band and the SW dynamic pressure. Other studies, such [45–47], found a correlation between Pc5 amplitude on the ground and the flux of energetic electrons at geosynchronous orbit. Furthermore, Pc5 waves can be excited by the Kelvin–Helmholtz instability (KHI) generated by high-speed SW flowing through the magnetopause [48,49], which gives rise to steady state oscillation of a resonant local field line that can be excited by a monochromatic surface wave at the magnetosphere [50,51]. Nu-

merous studies have found that the SW speed is a determining parameter in the control of the amplitude and occurrence of geomagnetic Pc5 pulsations on the ground [46, 52, 53], nonetheless, observations also suggest that it is insufficient to make estimates of Pc5 wave power based only on V_{sw}, but it must consider other physical factors, either intrinsic to the solar wind or related to its interaction with Earth's magnetosphere [42, 52, 54, 55]. In fact, among the external drivers for ULF waves, there can be perturbations embedded in the solar wind, or perturbations that originate near the bow shock or from magnetosheath instabilities, or perturbations arising at the magnetopause [56]. Scientific studies have investigated the potential relationship between the Alfvénicity of waves in the SW and their effects on geomagnetic activity on Earth. For example, D'Amicis et al. [57] studying the response of geomagnetic activity (through AE and SYM-H indexes) to SW turbulence during solar cycle 23, have found a statistical relationship between SW Alfvénic fluctuations and the geomagnetic response at high latitudes (mainly auroral latitudes) independent of the phase of the solar cycle, while at mid-low latitudes Alfvénic turbulence does not seem to play a relevant role. Tanskanen et al. [58] found that an increase in the amount of Alfvénic fluctuations corresponds to an increase of substorm frequency, by about 40%. In addition, periodic southward IMF intervals typical of high Alfvénic SW structures produce repeated substorms intervals, suggesting the role of Alfvénic fluctuations in modulating substorms activity. MHD wave transmissions at an open magnetopause can play a significant role in energy transport from the magnetosheath to the magnetosphere, and finally to the ground, resulting in a Pc5 power enhancement [59]. Kessel et al. [55] studied ULF fluctuations in the Pc5 range in high-speed streams, by distinguishing them in compressional and Alfvénic; they found that both compressional and Alfvénic fluctuations from SW high-speed streams are modulated at bow shock, with an enhancement of turbulence and wave power by about a factor 10. Nonetheless, the waveform of Alfvénic features is better preserved in the magnetosheath. They also showed a good correlation between the total parallel and perpendicular Pc5 SW power with the total Pc5 power of the ground-based horizontal component of the magnetic field (at KIL station, located at 69° geographic latitude). Note that the Pc5 frequency range (1-7 mHz) is comparable to the typical frequencies of Alfvénic fluctuations observed in the SW near Earth; as this thesis aims to investigate the potential effects of Alfvénic fluctuations present in HSS on geomagnetic activity, this work will focus within their typical frequency range.

Geomagnetic pulsations, once transmitted or generated in the magnetosphere, must dissipate their energy somewhere, and most of the dissipation occurs in the ionosphere. Here, the pulsation-associated electric fields induce current flow, leading to Joule heating of the ionosphere. Additionally, part of the wave energy accelerates magnetospheric particles, and these high-energy particles can hit the atmosphere, giving rise to auroras (see also 2.2.2.3).

2.2.2.3 Irregular variations

Geomagnetic storms

Geomagnetic storms are large and prolonged disturbances of the Earth's magnetosphere generated when large nonrecurrent interplanetary disturbances from the Sun, such as CME, interact with the magnetosphere. The CMEs are quite impulsive and, when approaching the Earth, they compress the magnetosphere. This compression causes a rapid increase in the magnetopause current, observed at the ground as a sudden increase in the horizontal magnetic field on the day-side of the Earth. In general, the storms result from the coupling between the IMF and the Earth's magnetosphere, with the subsequent energization of particles within the Earth's magnetosphere. Magnetic reconnection can lead to the transfer of SW energy into the Earth's magnetosphere, causing disturbances.

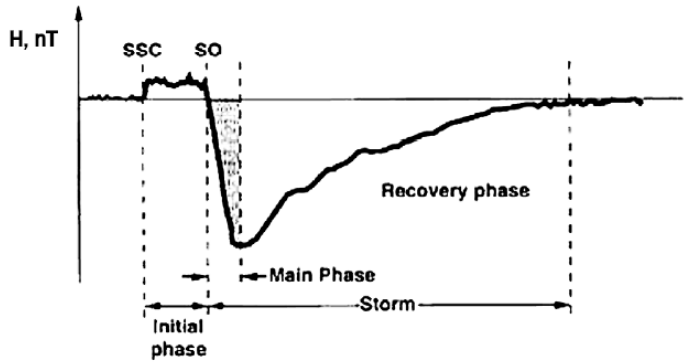

Figure 2.10: Scheme of Horizontal component variation of the geomagnetic field when a CME-generated magnetic storm occurs. The figure shows the various phases of the storm and it is adapted from [60]

As schematically shown in Figure 2.10, generally, the magnetic storm begins with a Storm Sudden Commencement (SSC) in the intensity of the horizontal component (H) of the Earth's magnetic field. Although it is a planetary phenomenon, the SSC can vary in latitude and local time. Immediately after the SSC, the initial phase of the storm occurs, characterized by a sudden increase in the intensity of the H component, up to tens of nT. Subsequently, while fluctuating, the H component maintains a high value for several hours and then decreases abruptly, reaching a value significantly lower than the starting one. This is due to the enhancement of the ring current by the increase in electrical charges penetrating the inner magnetosphere. The magnetic field produced by the ring current is horizontal and southward; thus, an increase during a magnetic storm strongly diminishes the horizontal (H) components of the main field. This is called the main phase. After that, the storm recovery phase begins, where the intensity of the horizontal component of the magnetic field

increases again, first with a time scale of a few hours, then over a few days, until it returns to the pre-storm values [60, 61]. Different magnetic storms may have different durations and intensities. The evolution of a storm can be defined statistically; examining individual storms, however, may reveal a considerable variety of patterns.

To produce a simple way of identifying a magnetic storm, the Dst index was derived. The Dst index monitors the level of magnetic storms globally. Depending on the value assumed by the index, geomagnetic storms are categorized into:

- *Super storms* $D_{st} <$ - 200 nT
- *Intense storms* - 200 nT $< D_{st} <$ - 100 nT
- *Moderate storms* - 100 nT $< D_{st} <$ - 50 nT
- *Weak storms* - 50 nT $< D_{st} <$ - 30 nT

In recent years, a higher-resolution (1 min) version of Dst was created: the SYM-H index. It utilizes 6 magnetometer stations (out of 11 observatories whose data are interchangeable depending on their availability) to compute the symmetric segment of the horizontal component of the magnetic field near the equator. The main difference between the 1 min SYM-H and the hourly Dst index is the time resolution, and the effects of the solar wind dynamic pressure variations are more clearly seen in the SYM-H than in the hourly Dst index; in fact, the higher resolution is helpful to resolve higher-frequency variations that may help study space storm trigger [62].

Substorms

A magnetospheric substorm or auroral substorm, is a brief disturbance in the Earth's magnetosphere that causes energy to be released from the geomagnetic tail and injected into the high-latitude ionosphere.

On Earth, the onset of a substorm results in the intensification of polar auroras, especially in the auroral zone around the midnight meridian. The auroral arcs intensity tends to increase and they expand to cover a significant portion of the sky. During these phenomena, magnetic disturbances become stronger, reaching up to 1000 nT. The lifetime of auroral substorm is of the order of 1-3 hours. The substorms is characterized by three phases: the growth phase, the expansion phase, and the recovery phase.

The first phase, also called *growth phase*, is characterized by the accumulation of energy from the SW in the geomagnetic tail, starting from dayside magnetic reconnection (as described in section 2.1). Afterward, the stored energy in the geomagnetic tail is impulsively released during the magnetic field dipolarization (reconfiguration from a tail-like magnetic field to a dipole-like

magnetic field), accordingly to the Dungey model of reconnection mechanism (section 2.1), giving rise to the initial phase of a substorm. This phase, lasting about 30-60 minutes, energizes particles, mainly electrons, injecting them in the inner magnetosphere up to the auroral zones. The third phase is the so-called recovery phase, during which the magnetosphere returns to its quiet configuration. The storage and release of energy in the magnetosphere during a substorm lead to changes in the auroral morphology and an increase in the intensity of currents flowing in the polar ionosphere.

Substorms differ from geomagnetic storms because, for example, storms take place over several days, are observable from anywhere on Earth, inject a large number of ions into the outer radiation belt, and occur once or twice a month during the maximum of the solar cycle and a few times a year during solar minimum. On the other hand, substorms take place for a few hours, are observable mainly in the polar regions, they can be a driver of energetic electron enhancements in the outer radiation belts, and are relatively frequent (often occurring only a few hours apart from each other). Substorms can be more intense and occur more frequently during a geomagnetic storm when one substorm may start before the previous one has been completed. While the source of the magnetic disturbances observed at the Earth's surface during geomagnetic storms is the ring current, the sources of magnetic disturbances observed on the ground during substorms are electric currents in the ionosphere at high latitudes.

Specific geomagnetic indices have been introduced to describe magnetic activity at polar latitudes. They are the AU, AL, and their combination as AO and AE indexes. They provide an overall quantitative measure of magnetic activity in the auroral zone produced by the increased ionospheric currents present at high latitudes. These indices are calculated from geomagnetic variations in the horizontal component observed at selected (10-13) observatories along the auroral zone in the northern hemisphere. For each station is first calculated a base value to normalize the data, computed for each month, by averaging all the data from the station on the five international quietest days. This base value is then subtracted from each value of data obtained at the station during that month. AU (Auroral Upper) index represents, at all times, the maximum value so selected, and AL (Auroral Lower) index represents, at all times, the minimum. The difference, AU minus AL, defines the AE (Auroral Electrojet) index. AU is a measure of the intensity of the Eastward Auroral Electrojet (EEJ) which circulates on the day side of the auroral oval and is coupled with the currents of the magnetopause. Therefore, AU is a measure of the direct response of the magnetosphere to changes in the interplanetary medium. AL is a measure of the intensity of the Western Auroral Electrojet (WEJ) which intensifies during sub-storms, therefore AL is a good way to follow the evolution of a substorm. By reflecting the integrated effect of different current systems, the AE index represents the overall activity of the electrojets. AE has been usefully employed both qualitatively and quantitatively as a correlative index

in studies of substorm morphology, and the coupling between the IMF and the Earth's magnetosphere.

Irregular Pulsations

In general, the irregular pulsations Pi1-2 are characterized by an irregular waveform, i.e. they are transient signals with a broad period or frequency range, as shown in the right column in table 2.1.

Pi2 pulsations are observed in the form of trains on the night side of the Earth. Their amplitude (on the order of ∼10 nT) is maximal near the auroral latitudes during the near-midnight hours. They are associated with the formation of substorm current wedges. The number of trains observed and their amplitude increase during the time of polar magnetic disturbances. Therefore, Pi2 are a reflection of the activity of the geomagnetic tail, mainly due to large-scale magnetic reconfiguration associated with cross-tail current disruptions.

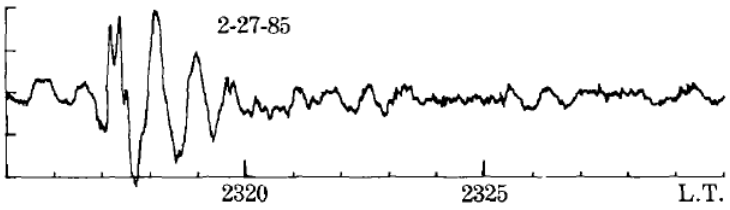

Figure 2.11: An example of Pi2 event for the H-component. Figure from [35].

Figure 2.11 shows the morphological aspect of a night-time Pi2 event, where a few cycles of irregular oscillations with periods longer than 40 s are well distinguishable. Pi1 activity observed at the ground is related to substorms and auroral activity at high latitudes. The correlation between Pi1 and auroral brightening and ionospheric current intensifications suggests that the generation mechanism for Pi1 is related to the region of precipitating auroral electrons. Pi1 may be created by some process in the topside ionosphere Alfvénic resonator [63].

Chapter 3

Data selection and dataset building

To study the effects of solar wind on the Earth's magnetosphere, a starting point is to select data appropriately. For the study of the events presented in this thesis, SW plasma and magnetic field data were acquired from interplanetary satellites, and geomagnetic field data were acquired from various ground stations at middle-high latitudes. In this chapter, you will get a quick overview of the instrumentation provided on the probes and magnetic observatories and the type of data used in the analysis. As the frequency range of interest of this work is that of Pc5 ($1 - 7$ mHz), a one-minute time resolution data is sufficient for both datasets.

3.1 Solar Wind data

Solar wind and magnetic interplanetary field data were obtained from the NASA website (Coordinated Data Analysis Web, http://cdaweb.gsfc.nasa.gov/cdaweb/), in particular from OMNI, which is a 1-minute resolution multi-source data set of near-Earth Solar Wind's magnetic field and plasma parameters, time-shifted to the Earth's bow shock subsolar point (also known as bow shock nose). OMNI provides the IMF (magnitude and vector), flow velocity (magnitude and vector), flow pressure, proton density, alpha particle to proton density ratio, and several additional parameters including geomagnetic indices (these last actually computed at WDC for Geomagnetism at U. Kyoto - https://wdc.kugi.kyoto-u.ac.jp/aeasy/). The data of spacecraft used to compile the OMNI solar wind reference include, among many, those of ACE and Wind satellites, time-shifted to the bow shock nose. This is to best support solar wind - magnetosphere coupling studies: it is desired to time-shift solar wind magnetic field and plasma data from their location of observation, which may be an hour ($\sim 240\ R_e$) upstream of the magnetosphere and up to several tens of R_e or more from the Sun-Earth line, to a point close to the magnetosphere; the NASA team that developed the database chose this point to be the bow shock nose.

About the two satellites just mentioned, *Wind* was launched on November 1, 1994, as part of NASA's contribution to the International Solar Terrestrial Program; it was designed to study radio waves and plasma in the solar wind and the Earth's magnetosphere - the scientific objectives of the Wind mission are to provide full coverage of solar wind data, energetic particles, and IMF to analyze both the phenomena occurring in the interplanetary medium and the processes of interaction with the Earth's magnetosphere. The probe follows a complex and time-varying orbit and it continues to obtain magnetic field, plasma, energetic particle, and plasma wave data. Among the various experiments mounted on Wind, the two that provided the data I worked with are SWE (Solar Wind Experiment), for measurements of fluctuations in the solar wind, and MFI (Magnetic Field Investigation) for measurements of fluctuations and large-scale structures in the IMF.

On the other hand, *ACE* (Advanced Composition Explorer) was launched on August 25, 1997, and its instrumentation contains the SWEPAM experiment that measures parameters regarding electrons, protons, and alpha particles contained in the solar wind, and the MAG experiment for magnetic field measurements. It continues to provide magnetic field, plasma, and energetic particle data.

As just said, the data obtained from these satellites are shifted to bow shock nose, very close to $\sim 1AU$, therefore in this analysis, I will not take into account the radial evolution of the SW, but I circumscribe the study to the interaction that SW has with the Earth's magnetosphere.

The data available from the OMNI database are expressed in a reference system widely utilized in space: the Geocentric Solar Ecliptic (GSE). This system is fixed with respect to the Earth-Sun line, it has its X axis towards the Sun, its Z axis perpendicular to the plane of the Earth's orbit around the Sun (positive North), and the Y axis to complete the orthogonal right-handed system. A similar frame is the Heliocentric Earth ecliptic (HEE) system, fixed with respect to the Earth-Sun line, that has its X axis towards the Earth and its Z axis perpendicular to the plane of the Earth's orbit around the Sun (positive North) - it is, basically, a rotation by 180° of GSE around the z-axis. Another widely utilized system, especially when studying the effects of IMF components on magnetospheric phenomena, is the Geocentric Solar Magnetospheric System (GSM); it has its X axis from the Earth to the Sun, the Y axis is defined to be perpendicular to the Earth's magnetic dipole so that the X-Z plane contains the dipole axis. The positive Z-axis is chosen to be in the same sense as the northern geomagnetic pole. In Chapter 4 there will be a wide treatment related to a reference system aligned to the main magnetic field that I called MEMFA (Main Electro-Magnetic Field Aligned) reference frame.

3.2 Ground data

On the ground, geomagnetic field data obtained from 6 different observatories of the INTERMAGNET network were analyzed together with data from the observatory at Terra Nova Bay (TNB, Antarctica) managed by INGV (Istituto Nazionale di Geofisica e Vulcanologia - Italy). The INTERMAGNET network (International Real-time Magnetic Observatory Network, with more than 90 observatories worldwide) is a project designed and implemented in the second half of the 1980s, whose main objective is to establish a global network of magnetic observatories scattered around the world able to exchange data "almost" in real-time. The term "almost" means that the data of an observatory is made available within 72 hours of acquisition. An INTERMAGNET Magnetic Observatory (IMO) must adopt precise standards to ensure high data quality, and compatibility with other observatories allowing an effective exchange of data. Each IMO, as well as TNB, provides one-minute averages of the magnetic field values measured by a vector magnetometer (for the three components) and an optional scalar magnetometer (for the intensity), both with 0.1 nT resolution and 5 nT accuracy on the final data. Usually, when measuring the geomagnetic field, a local reference system is established with origin at the observation point. In this system, the components of the measured magnetic field usually are the horizontal (or tangent to the Earth's surface) northward component along the local magnetic meridian, the horizontal eastward component perpendicular to the previous one, and the vertical component Z, orthogonal to the horizontal plane and directed towards the center of the Earth. From these components it is possible to calculate the total intensity, the components in the geographic reference frame as well as the angular quantities (inclination and declination) as previously shown in chapter 2 (figure 2.2 and equations 2.6, 2.7).

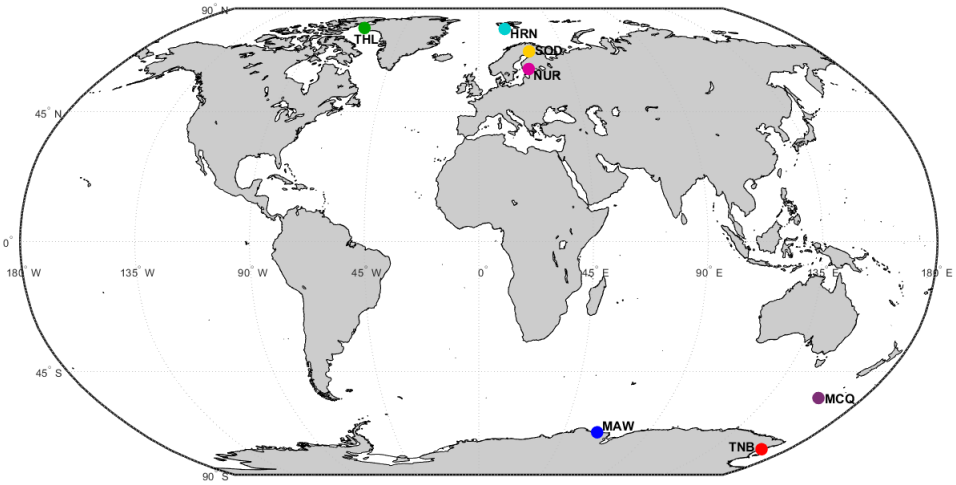

Figure 3.1: Map of geomagnetic observatories selected for the analysis.

Figure 3.1 shows the observatories selected for the analysis and table 3.1 shows their corrected geomagnetic latitude (CGM latitude) and the universal time (UT) that corresponds to the midnight in the magnetic local time (MLT). As can be seen from table 3.1, two observatories (THL and TNB) are located within the polar cap, two observatories (HRN and MAW) are at auroral latitudes and three observatories (SOD, MCQ and NUR) are at sub-auroral latitudes.

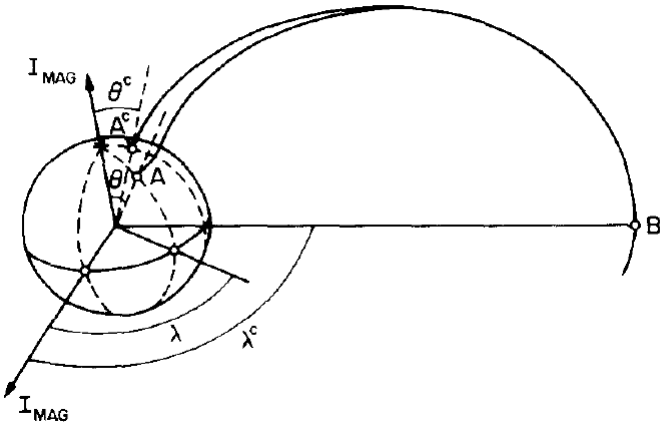

Figure 3.2: CGM coordinates definition, from [64]

The CGM coordinates (figure 3.2) were introduced to take into account the fact that the Earth's magnetic field is not perfectly dipolar ([65], [64]). They are computed starting from a realistic magnetic field model, that is the IGRF model. With this model, a geomagnetic field line can be traced starting from any point A on Earth's surface, taking into account the internal (dipole and non-dipole) sources of the magnetic field only (excluding the influence of external sources). In this sense, all the points along a single magnetic field line have the same coordinates (perhaps with opposite signs for magnetic latitude). Then, a point B can be identified where this field line crosses the dipole equatorial plane; from point B the dipole magnetic field line can be followed till going back to Earth's surface in A^c point. The angle between the straight line connecting A^c point with the center of the Earth and the dipolar axis corresponds to the CGM colatitude, the longitude instead is given by the angle formed between the plane that passes through the magnetic poles and the geographic north pole and the plane that passes through B and that contains the dipolar axis. As described in chapter 2, solar wind pressure distorts the Earth's magnetic field into the magnetosphere. This structure remains fixed with its nose towards the Sun and the tail away from it as the Earth spins within it. Hence longitude, which rotates with the Earth, is not a useful way of describing position in the magnetosphere. It is often appropriate to introduce, instead of magnetic longitude, a magnetic local time (MLT) to organize data taking into account the Earth's position

Geomagnetic observatories selected		
Observatory name	CGM latitude	MLT midnight in UT (hours)
THL	84.78 °N	03.26
TNB	80.00 °S	08.20
HRN	74.30 °N	21.00
MAW	70.39 °S	22.60
MCQ	64.26 °S	11.90
SOD	64.09 °N	21.14
NUR	57.02 °N	21.45

Table 3.1: Geomagnetic observatories selected for the analysis. First column: Name of the geomagnetic station. Second column: Corrected GeoMagnetic Latitude in the Northern (°N) or Southern (°S) hemisphere. Third column: Magnetic Local Time midnight expressed in Universal Time (in hours).

with respect to the Sun. One definition of MLT is the hour angle (1 hour is 15° magnetic longitude) from the midnight magnetic meridian, positive in the magnetic eastward direction. The midnight magnetic meridian can be defined as the meridian that is 180° magnetic longitude away from the subsolar point. The MLT/magnetic latitude coordinate system will then rotate with respect to the Earth at the rate at which the subsolar point crosses magnetic meridians. In this way, MLT can be simply described for example as value 0 (midnight) when the local field line crosses the equatorial plane in the anti-sunward direction, 12 (noon) in the sunward direction, 6 (dawn), and 18 (dusk) perpendicular to the sunward/anti-sunward line. An analogy with the geographic reference frame can be useful to better visualize the CGM reference frame: let us assume that the station is located at local geographic midnight, i.e. the local geographic meridian is at 00:00 LT (Local Time) and the station is "behind" the geographic pole with respect to the Sun. Similarly, if the Earth rotates through an angle so that the station's local CGM meridian reaches 00:00 MLT, then the station is "behind" the CGM pole with respect to the Sun; this UT instance (in hours and minutes) would be a "MLT midnight in UT", reported in table 3.1.

Chapter 4

Identification of pure Alfvén waves in the interplanetary medium in MEMFA reference frame

In chapter 1 I showed different types of SW structures and MHD waves, and in chapter 2 I explained how these SW structures interact with and affect the geomagnetic field. In this context, Alfvén waves in the SW play an important role in the stability, heating, and transport of magnetized plasmas. They are found to be ubiquitous in the SW, mainly propagating outward from the Sun, especially in HSS. When HSS impinges on the Earth's magnetosphere, the impact of Alfvénic fluctuations can cause magnetic reconnection between the intermittent southward IMF and the geomagnetic field, resulting in energy injection from the SW into the Earth's magnetosphere. Information on the quantities involved, expressed in an appropriate reference system, can help understand the dynamics of these interactions. The mathematical approach already described in section 1.5 is of fundamental importance in characterizing turbulence in the SW. However, in the study of the interaction between the turbulent SW and the Earth's magnetosphere, it may be useful to work with the SW power and its modulations, to compare them with the horizontal power of the geomagnetic field. The typical nonlinear character of the wide Alfvénic fluctuations in the SW turbulence, as highlighted in section 1.5.2.1, suggests searching for a suitable method to bring out this kind of wave from the SW signals (in situ measurements). The Empirical Mode Decomposition (EMD) technique allows the analysis of nonlinear and nonstationary signals by decomposing them into components of varying resolutions, and it is therefore suitable for the purposes of this work. In this context, it can be useful to study the MHD waves in a properly defined reference frame, which helps us to distinguish MHD wave properties mainly attributable to compressional or Alfvèn waves.

In this chapter, I described (section 4.2.1) and tested a rotation procedure from the Heliocentric Earth Ecliptic (HEE) to the Mean ElectroMagnetic Fields

Aligned (MEMFA) reference frame, identified using the Empirical Mode Decomposition (EMD), of both SW velocity and IMF at 1 AU. I aim to check the reliability of the method (section 4.2.2) and its limitations in identifying pure Alfvénic fluctuations through the spectral analysis of time series in the MEMFA coordinate system. With this procedure, the fluctuations in the main-field-aligned direction and those in the orthogonal plane to the main field can be studied. To highlight the peculiarities of each case study and be able to better identify Alfvén waves when applying this procedure to real data, I reproduced the magnetic and velocity fields of a typical corotating high-speed stream. I performed a procedure test in several cases, by adding the presence of Alfvén waves and noise (section 4.2.1.1 for the white noise case and section 4.2.1.2 for the red noise case). I performed the spectral analysis of the MEMFA components of both magnetic and velocity fields to define the power related to the two main directions: the one aligned to the ambient magnetic field and the one orthogonal to it. The efficiency of the procedure and the result's reliability are supported by Monte Carlo (MC) tests, in section 4.2.2. The method is also applied to a real case (section 4.3) represented by a selected corotating SW stream that occurred during August 2008, which falls in the solar minimum of solar cycle 23. The results are also compared with those obtained by using the Elsässer variables, as defined in sections 1.5.2.1 and 1.5.2.2, to analyze the Alfvénicity of fluctuations via the normalized cross-helicity, which is related to the degree of correlation between the SW velocity and the magnetic field fluctuations, and the normalized residual energy, which is related to the balance between magnetic and kinetic energies.

4.1 A brief background context

In the magnetosphere, where the main magnetic field is larger than its fluctuations, the Mean Field Aligned (MFA) reference frame is generally utilized (e.g., [66–69]). This system is mainly defined by identifying the ambient magnetic field, by separating long periodicity variations from small-time perturbations, using a filtering procedure. Conversely, the Minimum Variance Analysis (MVA, e.g. [70]) and the deHoffman-Teller (HT, [71]) reference frames were also used in the interplanetary medium. In the MVA, the three distinct orthogonal directions are identified by investigating the variances of the magnetic field components. It was experimentally demonstrated that the minimum variance direction does not necessarily coincide with that of the ambient magnetic field, as pointed out in [72, 73]. In the HT reference frame, the main direction is the one along which the convection electric field is minimum. In the interplanetary medium the convection electric field represents the Interplanetary Electric Field (IEF)

$$\mathbf{E} = -\mathbf{V} \times \mathbf{B} \tag{4.1}$$

where **B** and **V** represent the IMF and solar-wind velocity vectors, respectively. Traditionally, both these reference frames are used for studying the MHD wave properties as well as non-linear shock waves or discontinuities.

Here, I aim to identify a reference system that is not only able to identify the direction of the main magnetic field but also allows us to choose a second direction of physical relevance, in our case, the direction of the main IEF, which in the vicinity of the Earth's magnetosphere is the most geoeffective direction (see [74] and reference therein). I proposed a new reference frame based on both the mean directions of IEF and IMF; this new reference frame is hereafter named MEMFA reference frame. The efficiency of the MEMFA procedure in separating pure Alfvén waves from IMF and velocity fluctuations has been verified by means of Monte Carlo (MC) test simulating synthetic signals in a realistic SW corotating stream. The simulated Alfvén waves also allowed us to compute the power of Alfvénic and compressional fluctuations. The proposed method, together with the traditional adiabatic invariant computed from Elsässer variables [20, 23], helps us in better distinguishing the Alfvénicity in the SW; the Alfvénicity is a peculiar feature of SW fluctuations in the orthogonal direction with respect to the ambient magnetic field, that show a high correlation between velocity and magnetic field fluctuations at scales from a few minutes to a few hours and ideally by equipartition between kinetic and magnetic energies [22, 73].

Pure Alfvén waves propagate along the main field direction, with magnetic and velocity perturbations in the plane orthogonal to it. Therefore, a rotation procedure that enables us to identify the main magnetic field direction is a useful tool for identifying pure Alfvén waves too. I focused on the application of the MEMFA technique on SW observations during corotating streams because in its high-speed plateau, it is well known that there are Alfvén waves ([21], [14]); nonetheless, the rotation procedure is very general and can be applied to a general context.

4.2 Methodology and data

The simulated profiles of SW velocity and IMF time series in the following section of this chapter are created according to a typical SW corotating stream. The analysis has been performed by recreating magnetic field and plasma data at 1 min time resolution during the minimum of solar activity, as those provided by OMNIWeb (https://cdaweb.gsfc.nasa.gov/), time-shifted to the Earth's bow shock nose. Initial data are given in the HEE coordinate system that has its $\hat{x}$ axis towards the Earth, its $\hat{z}$ axis perpendicular to the ecliptic plane (positive North) and the $\hat{y}$ axis to complete the orthogonal right-handed frame. This system is schematically represented in Figure 4.1a.

The HEE system is fixed with respect to the Sun–Earth line. On the other hand, the use of a Lagrangian coordinate system, which is constructed with the

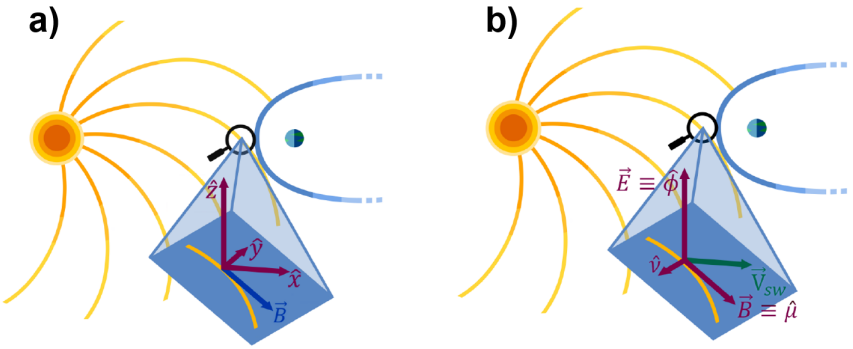

Figure 4.1: Both pictures represent the ecliptic plane in the background, with the Sun on the left and the Earth with its magnetosphere on the right, and a 3D magnification in the foreground. Panel a: the **HEE reference frame**. The $\hat{\mathbf{x}}$ axis goes from the Sun toward the Earth, the $\hat{\mathbf{z}}$ axis is perpendicular to the Ecliptic plane (positive North), and the $\hat{\mathbf{y}}$ axis completes the orthogonal right-handed frame. The yellow curve represents the IMF, with its tangent vector **B** in blue. Panel b: the **MEMFA reference frame**. The $\hat{\boldsymbol{\mu}}$ axis is aligned to the main ambient magnetic field, the $\hat{\boldsymbol{\phi}}$ axis is aligned to the main Electric field, and the $\hat{\boldsymbol{\nu}}$ axis completes the orthogonal right-handed frame. The yellow curve represents the IMF, that not necessarily lies in the ecliptic plane at the Earth's orbit. This implies that the IEF has also a component in the ecliptic plane. The solar wind velocity vector is pictured in green.

axis related to the main physical quantities I deal with, can be very useful in studying the physical phenomena that occur. The MFA (Main Field Aligned) coordinate system, widely utilized in the magnetosphere ([66], [72]), can be well applied in the solar wind because the procedure is able to reconstruct the main field by specifying the time scales of interest.

4.2.1 The MEMFA reference frame definitions and rotation procedure

This section describes the rotation procedure from the HEE coordinate system to the MEMFA (Mean ElectroMagnetic Fields Aligned) coordinate system (Figure 4.1b). Without losing generality, I refer hereafter to the HEE as the starting reference frame. To define the MEMFA reference frame, the characteristic time scale needs to be known, hereafter indicated as T_S, to separate the main magnetic field from its smaller period variations. With this assumption of time scale separation, the magnetic field can be thought of as a sum of a long period ambient magnetic field $\mathbf{B_0}(t)$, a short period (high frequency) perturbation term $\mathbf{b}(t)$ and an incoherent noise $\mathbf{n_b}(t)$:

$$\mathbf{B}(t) = \mathbf{B_0}(t) + \mathbf{b}(t) + \mathbf{n_b}(t) \tag{4.2}$$

In Equation 4.2, $\mathbf{B_0}$ corresponds to the mean IMF.

As for $\mathbf{B_0}$, also $\mathbf{V_0}$ represents the long period component of the solar wind velocity; following previous definition for $\mathbf{B}$ it follows

$$\mathbf{V}(t) = \mathbf{V_0}(t) + \mathbf{v}(t) + \mathbf{n_v}(t) \tag{4.3}$$

where, $\mathbf{v}(t)$ represents the velocity perturbation term and $\mathbf{n_v}(t)$ the incoherent noise.

The MEMFA coordinate system has the $\hat{\boldsymbol{\mu}}$ axis aligned to the main ambient magnetic field, the $\hat{\boldsymbol{\phi}}$ axis aligned to the main electric field ($\mathbf{E_0}(t) = -\mathbf{V_0}(t) \times \mathbf{B_0}(t)$), and the $\hat{\boldsymbol{\nu}}$ axis that completes the orthogonal right-handed frame ($\hat{\boldsymbol{\nu}} = \hat{\boldsymbol{\mu}} \times \hat{\boldsymbol{\phi}}$). The MEMFA unit vectors are therefore defined as follows:

$$\hat{\boldsymbol{\mu}}(t) = \frac{\mathbf{B_0}(t)}{\parallel \mathbf{B_0}(t) \parallel} \tag{4.4}$$

$$\hat{\boldsymbol{\phi}}(t) = \frac{\mathbf{B_0}(t) \times \mathbf{V_0}(t)}{||\mathbf{B_0}(t) \times \mathbf{V_0}(t)||} \tag{4.5}$$

$$\hat{\boldsymbol{\nu}}(t) = \hat{\boldsymbol{\mu}}(t) \times \hat{\boldsymbol{\phi}}(t) \tag{4.6}$$

so that the instantaneous rotation matrix from HEE to MEMFA reference frame can be computed:

$$\mathbf{R}(t) = \begin{bmatrix} \hat{\mu_x}(t) & \hat{\mu_y}(t) & \hat{\mu_z}(t) \\ \hat{\phi_x}(t) & \hat{\phi_y}(t) & \hat{\phi_z}(t) \\ \hat{\nu_x}(t) & \hat{\nu_y}(t) & \hat{\nu_z}(t) \end{bmatrix} \tag{4.7}$$

allowing us to define any vector in the new MEMFA reference frame.

Obviously, once I compute the rotation matrix from HEE to the MEMFA coordinate system, based on the magnetic field time scale separation, I can use the same $R(t)$ to rotate other vectors from HEE to MEMFA reference frame, such as the velocity vector $\mathbf{V}$. By these definitions it follows that both velocity and magnetic field vectors can be rotated as follows:

$$\mathbf{B}(t)^{'} = \mathbf{R}(t)\mathbf{B}(t) \tag{4.8}$$

$$\mathbf{V}(t)^{'} = \mathbf{R}(t)\mathbf{V}(t) \tag{4.9}$$

where $\mathbf{R}(t)$ is the rotation matrix, the vectors with the apex on the left-hand side of the Equations 4.8 and 4.9 refer to the MEMFA reference frame and the vectors without apex on the right-hand refer to the HEE reference frame.

The MEMFA reference frame gives us information about the direction of the main magnetic field (first direction), and the second direction ($\hat{\boldsymbol{\phi}}$) gives us information about the main electric field direction. As will be shown later, these quantities are important because they help us to identify the fluctuations in the

SW plasma, but they can also have other applications, such as in the proximity of the magnetosphere.

Since SW Alfvén waves manifest non-linear behavior, the time scale separation is performed by the EMD method, introduced by [75] to analyze non-linear and non-stationary signals (e.g. [72, 76, 77]). The EMD is a sifting procedure-based technique able to adaptively decompose a multiscale signal into a sum of a finite number of roughly zero mean oscillating components called Intrinsic Mode Functions, and a residue. Those functions form a complete and nearly orthogonal basis and they are identified without leaving the time domain (they have the same length as the original signal), thus preserving the varying frequencies. In this work, I am interested in applying the rotation procedure to a corotating high-speed SW stream, in order to separate its main magnetic field structure from the fluctuation within it. Clearly, physical phenomena do not change with the change of the reference system; nonetheless, a properly defined reference frame, based on the physical quantities involved, allows us to better understand the physics that occurs.

Previous studies [22, 73] showed that Alfvénic fluctuations typically have periods ranging from tens to hundredths of mHz; to efficiently take into account this time-scale separation in the MEMFA rotation procedure, I choose a time window of 6 hours, wide enough to include all Alfvénic fluctuations therein, but, at the same time, not too wide to follow the variability of the typical ambient field in a corotating stream.

Then, I assume as ambient magnetic field $\mathbf{B_0}(t)$ all variation with a time scale greater than $T_S = 6$ hours (frequencies lower than 0.005 mHz), and consequently, I consider magnetic field fluctuations all variations $\mathbf{b}(t)$ with a time scale lower than T_S (frequencies greater than 0.005 mHz), compatible with what mentioned before.

4.2.1.1 White Noise + localized Alfvén waves

In this section, I will show how the procedure works when applied to a simulated corotating SW stream with localized Alfvén waves and white noise. The basic idea is to understand if the proposed procedure is able to separate Alfvén waves from the ambient signals and project these waves in the orthogonal plane to the main field. To test this procedure, a good starting point is to create a synthetic corotating stream in the HEE reference frame, which is the reference system where we usually have the data. Then, I can apply the rotation procedure by computing the instantaneous rotation matrix $\mathbf{R_1}(t)$ from HEE to MEMFA coordinate system, in order to add the Alfvén waves to signals in the latter reference frame. As mentioned in the introduction, Alfvén waves are waves that propagate along the main magnetic field direction, with magnetic and velocity perturbation in the plane orthogonal to the main ambient field. In the MEMFA reference frame, I identify the main field direction, that is the $\hat{\boldsymbol{\mu}}$ one, therefore in this frame, I can easily introduce Alfvén waves, seen as per-

turbations to the main signal, in both velocity and magnetic field components orthogonal to the $\hat{\boldsymbol{\mu}}$ direction. In this test, I chose to add Alfvén waves in the $\hat{\boldsymbol{\phi}}$ direction, without loss of generality. Of course, the added waves, to be Alfvénic, must comply with other conditions, that are the magnetic and velocity energy equipartition, and no phase difference between magnetic and velocity perturbations. In a general sense, I can easily write the in-phase magnetic and velocity perturbations as:

$$b_\phi = A_B(t)\cos(2\pi f(t)t) \tag{4.10}$$

$$v_\phi = A_V(t)\cos(2\pi f(t)t) \tag{4.11}$$

where $A_B(t)$ and $A_V(t)$ are the fluctuations amplitudes for both magnetic and velocity $\hat{\boldsymbol{\phi}}$ component. These amplitudes are linked by the equipartition of magnetic and kinetic energy:

$$\frac{{b_\phi}^2}{2\mu_0} = \frac{1}{2} n m_p {v_\phi}^2 \tag{4.12}$$

as expected for an Alfvèn wave. I defined the amplitude of the magnetic fluctuations to 1 nT, well in accordance with real data by observing several SW corotating structures (not shown here); since the signal energy is proportional to its amplitude, I calculated the amplitude of the kinetic fluctuations accordingly, through an appropriate multiplicative constant $1/\sqrt{\mu_0 n m_p}$, where $\mu_0 = 4\pi \times 10^{-7}$ H/m is the permeability constant, n is the plasma density (here measured in counts/cm^3), and $m_p = 1.67 \times 10^{-27}$ kg is the proton mass. The frequency $f(t)$ varies in the range $0.05 - 3$ mHz, which are values well in accordance with typical Alfvén ULF in the SW at 1 AU, from tens to hundredths of mHz [22]. Then, both amplitudes are modulated by a window, i.e. a weight function or taper that smoothly goes to zero at the end points of the time series. Specifically, I used a Tukey window, whose weights are defined by a unitary amplitude cosine function at the edges of the time series, in order to restrict the fluctuations only in the HSS region and the beginning of the RR. This choice is a consequence of the well-known Alfvénic character of SW corotating streams, typically most Alfvénic in the high-speed plateau [14, 22, 23, 78], as mentioned in the introduction.

Once the Alfvén waves are added in the MEMFA coordinate system, I used the inverse of the previous rotation matrix to come back in the HEE reference frame, via $\mathbf{R_1}(t)^{-1}$. In the HEE reference system, I can easily add the white noise, that is a random signal having equal intensity at different frequencies, corresponding to a constant power spectral density, calculated according to typical real values that are available in the HEE reference system. At this point, I get magnetic and velocity components in HEE coordinate system containing Alfvén waves and noise, as a real case has. Starting from this, in order to check if the procedure is able to recognize Alfvén waves in noisy signals without loss of information, I newly apply the rotation procedure from HEE to MEMFA

by computing a new instantaneous rotation matrix $\mathbf{R_2}(t)$. If I find back the Alfvénic fluctuations (previously inserted), it means that the procedure is able to well identify them, extracting them from the overall signal.

An outline of the steps of the procedure can be the following:

1. Identify or define velocity and magnetic field component profiles in the HEE coordinate system.

2. Apply the rotation procedure from HEE to MEMFA coordinate system, using the instantaneous rotation matrix $\mathbf{R_1}(t)$.

3. In the MEMFA reference frame the Alfvén waves can be easily added (with $\mathbf{k} \parallel \mathbf{B_0}$ where $\mathbf{k}$ is the wave vector).

4. Use the inverse of the previous rotation matrix, $\mathbf{R_1}(t)^{-1}$, to come back in the HEE reference frame, knowing that there are Alfvén waves in the signals.

5. Add the noise to each component, of both $\mathbf{V}$ and $\mathbf{B}$. Now the velocity and magnetic field components within Alfvén waves and noise are expressed in the HEE reference frame.

6. Apply a new rotation procedure from HEE to MEMFA coordinate system, using the instantaneous rotation matrix $\mathbf{R_2}(t)$ and check if this procedure is able to identify Alfvén waves embedded in signals in the presence of noise.

It should be noted that the methodology and the procedure used in this work do not operate in the frequency domain, therefore the Doppler shift does not affect the results.

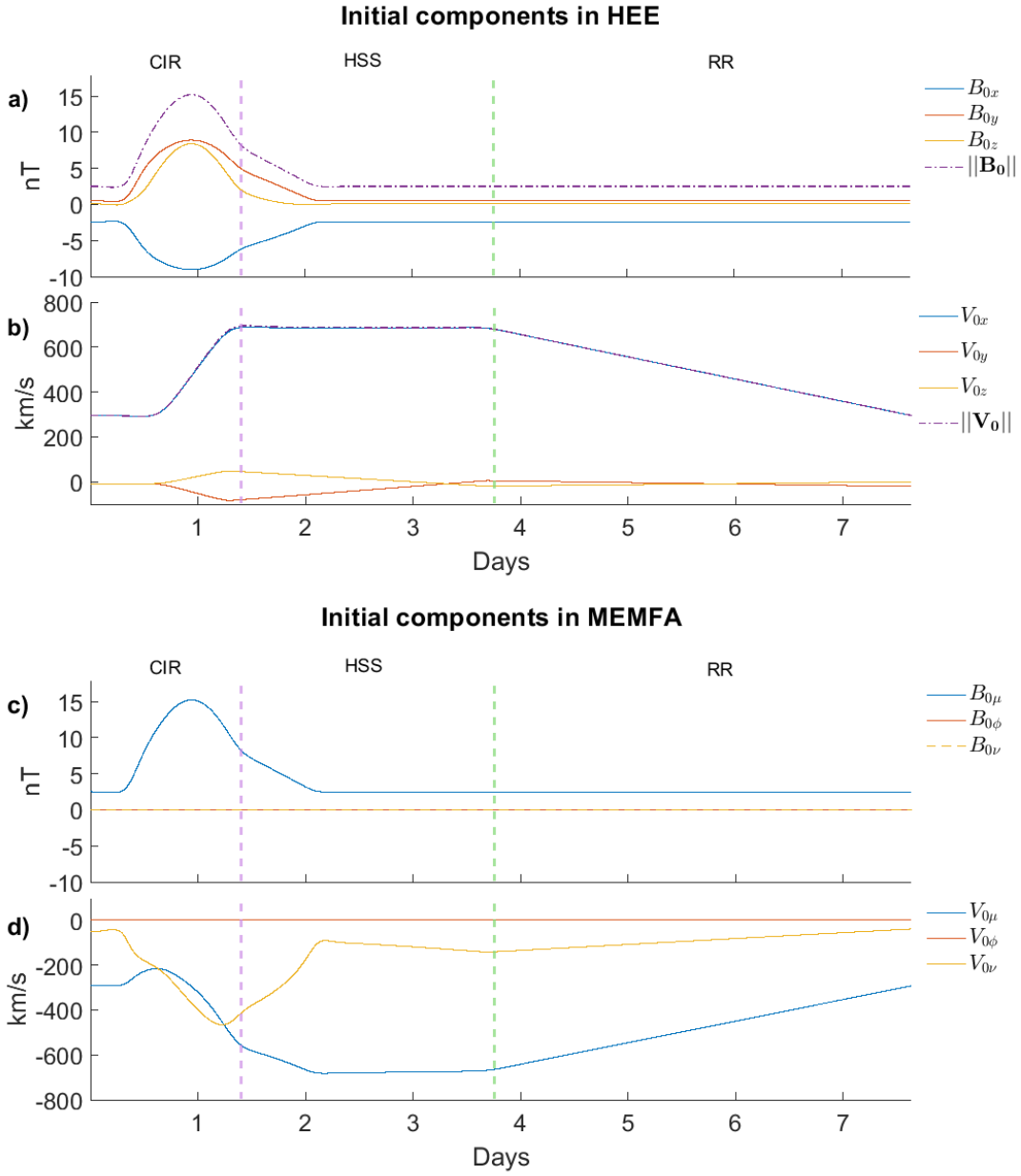

Figure 4.2: Synthetic profiles of magnetic field (panel a) and velocity (panel b) components to recreate a corotating SW stream in the HEE reference frame. Synthetic profiles of magnetic field (panel c) and velocity (panel d) components in the MEMFA reference frame, obtained by the rotation procedure from HEE to MEMFA via $\mathbf{R_1}(t)$. The x-axis refers to days in a simulated case. The vertical dashed pink line refers to the transition from the CIR to the HSS region of the simulated corotating stream. The vertical dashed green line refers to the transition from the HSS region to the RR of the simulated corotating stream.

Figure 4.2 shows the analytic profiles of the SW magnetic field (panel a) and

velocity (panel b) of a typical corotating stream, as seen in an HEE reference system. A corotating SW stream, as previously shown in Figure 1.5a, is characterized by a CIR where the compression occurs, with a consequent increase in plasma density and magnetic field; then follows a high-velocity plateau, in the so-called HSS region, where the plasma density and the magnetic field decrease; then the RR occurs, characterized by a velocity decrease. The synthetic profiles are reproduced to be representative of a typical real corotating stream. The vertical dashed pink line refers to the transition from the CIR to the HSS region of the simulated corotating stream. The vertical dashed green line refers to the transition from the HSS region to the RR. After the first rotation procedure, via $\mathbf{R_1}(t)$, $\mathbf{V_0}$ and $\mathbf{B_0}$ are rotated in the MEMFA reference frame, as shown in Figure 4.2c-d. The instantaneous rotation matrix $\mathbf{R_1}(t)$ is computed based on the magnetic field cut-off time of 6 hours, as explained in Section 4.2.1.

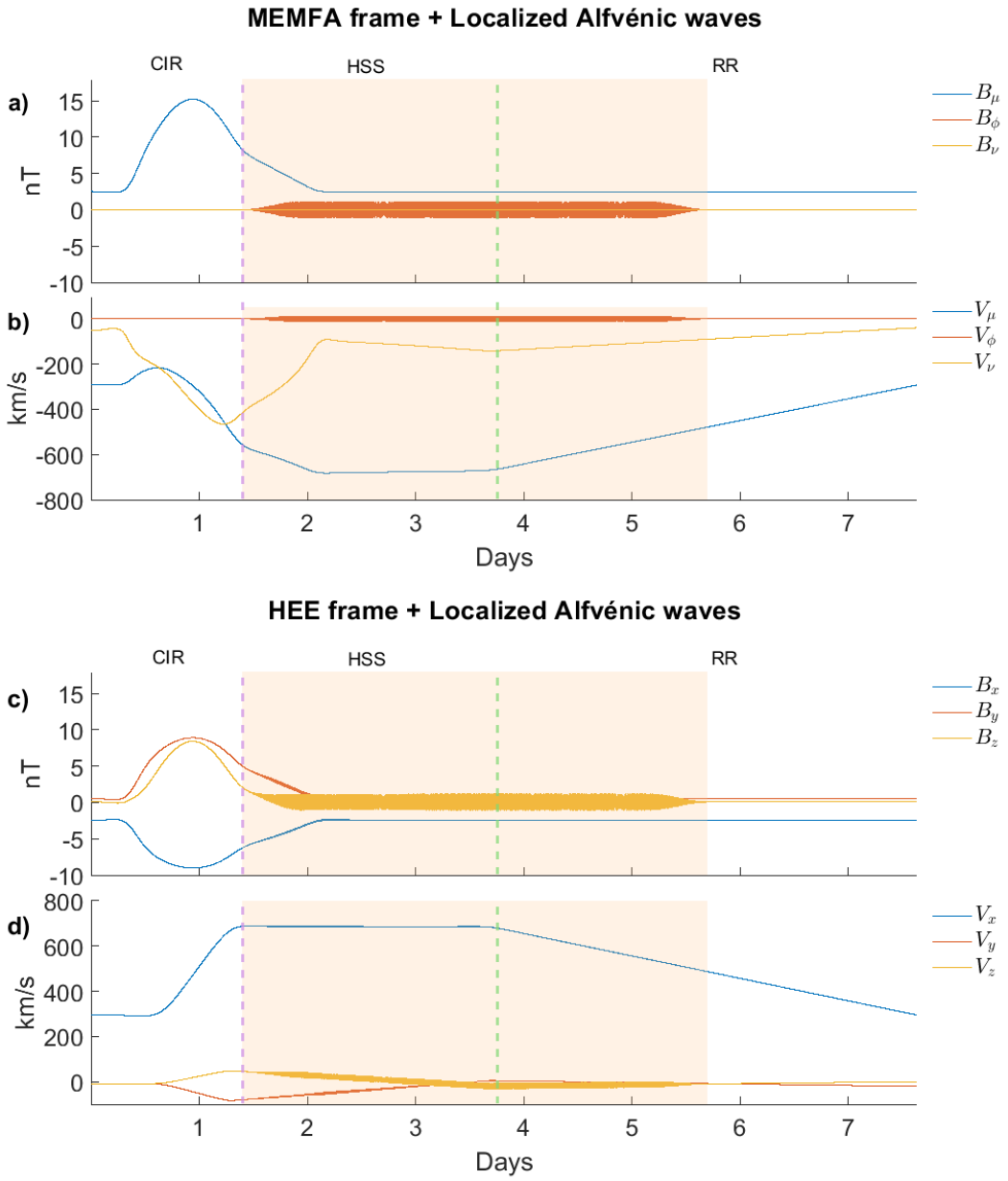

Figure 4.3: Magnetic field (panel a) and velocity (panel b) MEMFA components with the addition of Alfvén waves in the HSS region and at the beginning of RR. Magnetic field (panel c) and velocity (panel d) HEE components, containing Alfvén waves, obtained by the use of the inverse rotation matrix $\mathbf{R_1}^{-1}(t)$. The x-axis refers to days in a simulated case. The vertical dashed pink line refers to the transition from the CIR to the HSS region of the simulated corotating stream. The vertical dashed green line refers to the transition from the HSS region to the RR of the simulated corotating stream. The shaded region identify the interval with the synthetic Alfvén waves.

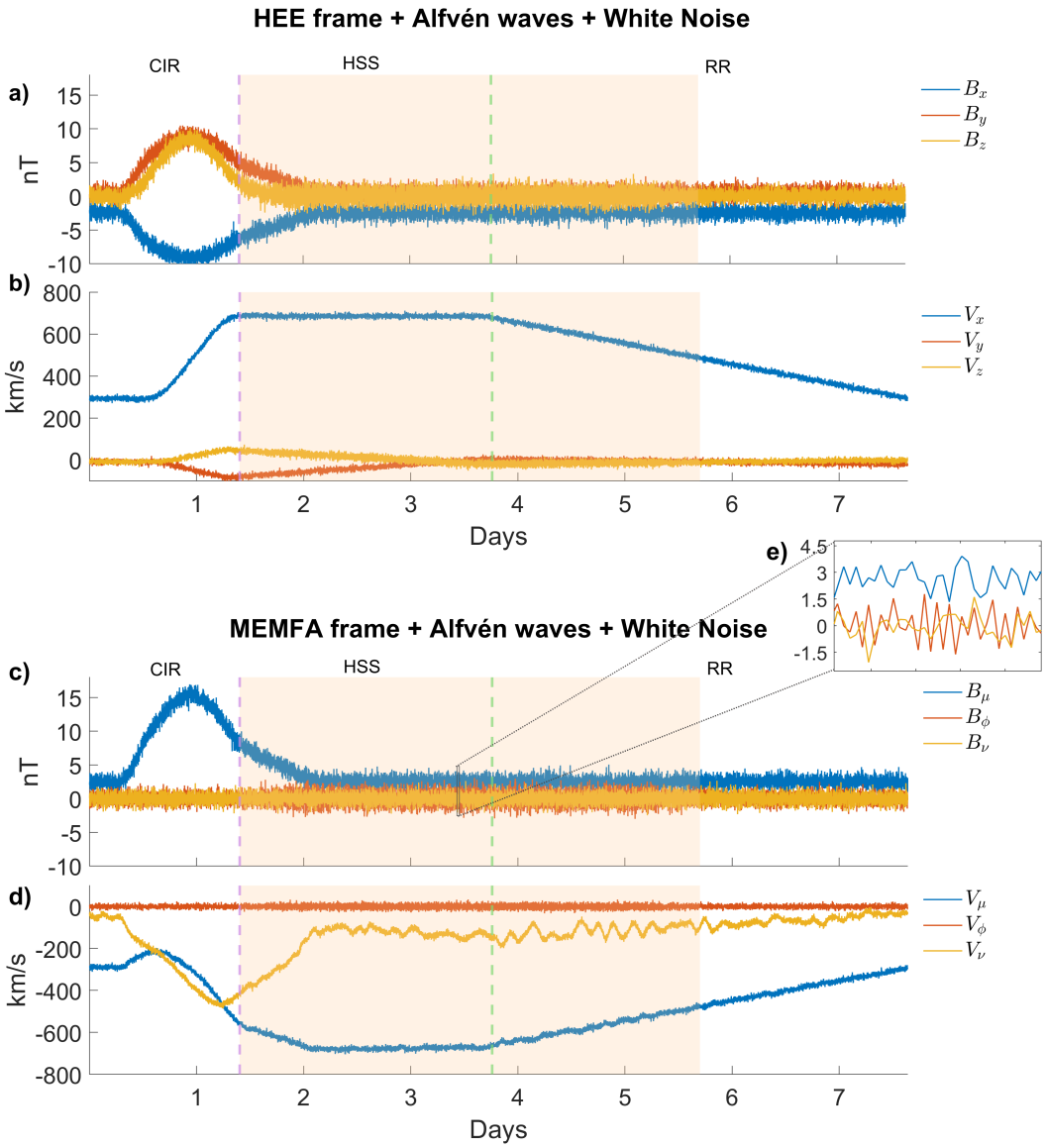

Figure 4.4: Magnetic field (panel a) and velocity (panel b) HEE components, containing Alfvén waves, with the addition of white noise. Magnetic field (panel c) and velocity (panel d) MEMFA components, obtained by a new rotation procedure from HEE to MEMFA via $\mathbf{R_2}(t)$, starting from the velocity and magnetic field HEE components containing Alfvén waves and white noise. A magnification of magnetic field fluctuations in the MEMFA reference frame is reported in panel e), as an example. The x-axis refers to days in a simulated case. The vertical dashed pink line refers to the transition from the CIR to the HSS region of the simulated corotating stream. The vertical dashed green line refers to the transition from the HSS region to the RR of the simulated corotating stream. The shaded region refers to the one with the synthetic Alfvén waves.

As shown in Figure 4.2c, the main magnetic field $B_{0\mu}$ component (in blue)

is very well identified by the procedure, while the other two magnetic field components $B_{0\phi}$ and $B_{0\nu}$, in absence of perturbations, are null. In the bottom panel of the same figure are shown the MEMFA velocity components, computed with the same rotation matrix $\mathbf{R_1}(t)$. Since the second unit vector $\hat{\boldsymbol{\phi}}(t)$ of the MEMFA system is calculated as in Equation 4.5, the $V_{0\phi}$ component (in red), in absence of perturbation, is null because $V_{0\phi}$ is perpendicular to $\mathbf{V_0}$. At this point, being in a reference system aligned to the main field, Alfvén ULF waves can be added in the $\hat{\boldsymbol{\phi}}$ direction, orthogonal to it.

The MEMFA magnetic and velocity components with the addition of Alfvén waves are shown in Figure 4.3a-b. At this point, the signal contains its main trend and Alfvén ULF waves, but not yet the noise. Because information about typical noise amplitude values can be obtained from real data in the HEE reference frame, I can apply the inversion rotation matrix $\mathbf{R_1}^{-1}(t)$ and come back in the HEE reference system (Figure 4.3c-d); in this system, I can add the noise, to resemble real observations. In this section, I reproduced white noise for both magnetic field and velocity components, whose amplitude is computed from the standard deviations of real values fluctuations, estimated from real data (obtained by removing the main trend, so they contain both waves and noise).

At this point, the noise can be added in the HEE reference frame, obtaining the signals shown in Figure 4.4 a-b. Finally, the new rotation procedure by $\mathbf{R_2}(t)$ matrix, leads to signals shown in Figure 4.4 c-d. After the rotation (via $\mathbf{R_2}(t)$) the noise remains in all components, while Alfvén waves are found only in the $\hat{\boldsymbol{\phi}}$ direction, confirming the proper functioning of the procedure (see also Figure 4.4e that is a magnification example of the magnetic field fluctuations). Further confirmation of the previous statement will be shown in Section 4.2.2, Figure 4.6. Panels a-b show an example of magnetic (top panel) and velocity components (bottom panel) with Alfvénic fluctuations (in the HSS and the beginning of the RR) and white noise embedded in the entire stream, in the HEE reference frame. This can be considered as the equivalent starting point of real data studies because when we deal with satellite data, they can generally be seen as the superposition of a main profile, some typical signals, and noise. At this point, I can apply the rotation procedure from scratch, finding a new instantaneous rotation matrix $\mathbf{R_2}(t)$, and see if the procedure can recognize not only the correct separation of the three magnetic and velocity components but also the identification of the Alfvén waves only in the $\hat{\boldsymbol{\phi}}$ direction, as previously inserted.

4.2.1.2 Red Noise + localized Alfvén waves

Both velocity and magnetic field in the SW are characterized by colored noise, particularly, red noise which shows decreasing power with increasing frequency. In order to reproduce a noise as similar as possible to the real noise embedded in the SW, I reproduced a red noise [79] with a first-order auto-

regressive process (AR1) obtained from the auto-correlation at $lag = 1$ of both magnetic and velocity components of a real case study.

In this section, I repeated the test procedure, as seen in the previous section, in the presence of red noise. The points from 1 to 4 of the outline test procedure mentioned in Section (4.2.1.1) remain the same; hereafter, I changed the kind of noise I added in point 5. Figure 4.5a-b shows magnetic and velocity components in the HEE reference frame with the embedded red noise. As said for the white noise, this can be considered as the equivalent starting point of a real data series, formed by a main trend with added signals, and a red noise typical of both magnetic and velocity components. I can then apply the rotation procedure, finding a new instantaneous rotation matrix $\mathbf{R_2}(t)$, obtaining the MEMFA magnetic and velocity components shown in Figure 4.5c-d, respectively. Also in this case, after the rotation, the noise remains in all the components, while the Alfvénic fluctuations are detected only in the $\hat{\boldsymbol{\phi}}$ component of both magnetic field and velocity (see also Figure 4.5e that is a magnification example of the magnetic field fluctuations). Further confirmation of the previous statement will be shown in Section 4.2.2, Figure 4.7.

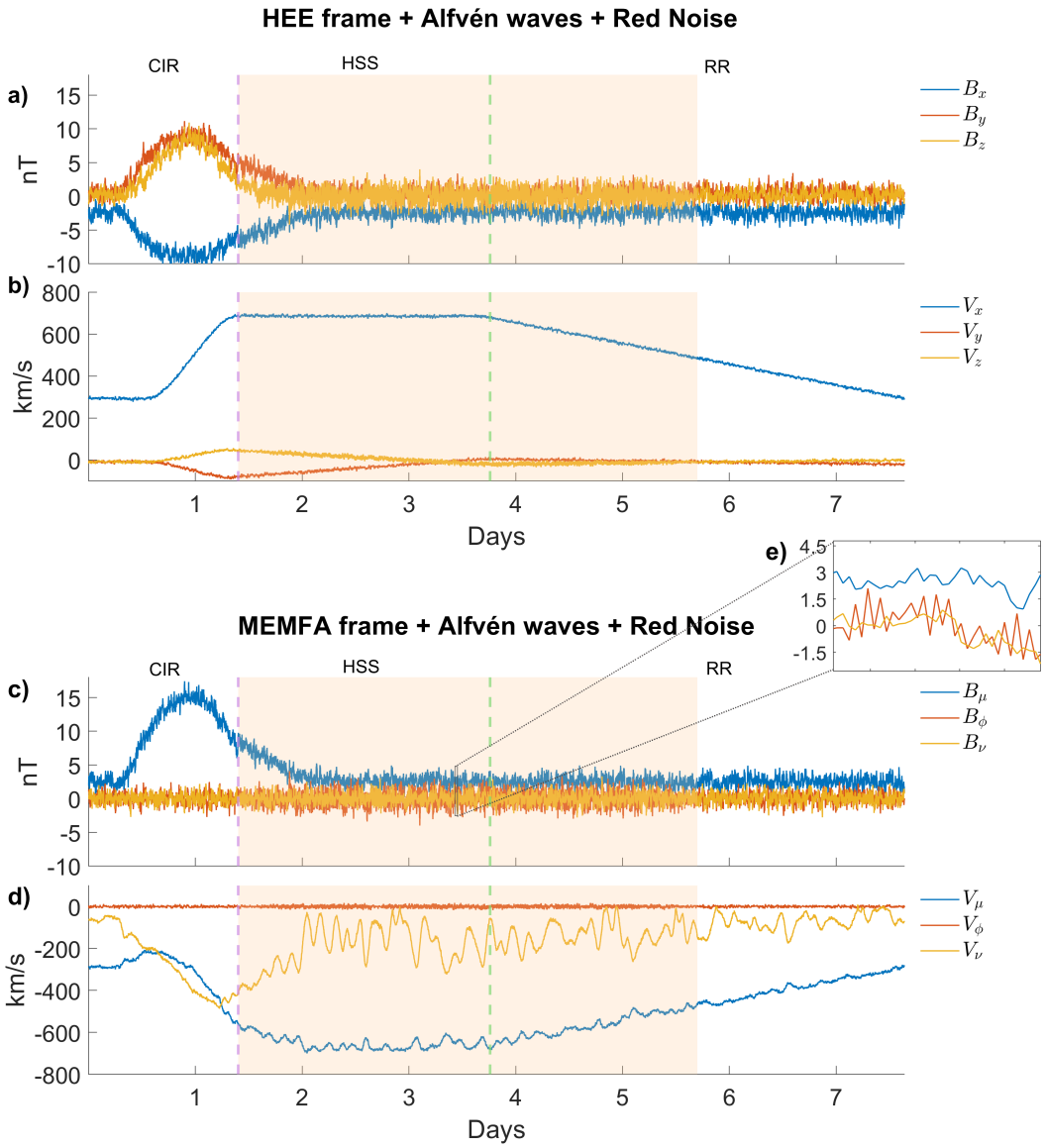

Figure 4.5: Magnetic field (panel a) and velocity (panel b) HEE components, containing Alfvén waves, with the addition of red noise. Magnetic field (panel c) and velocity (panel d) MEMFA components, obtained by a new rotation procedure from HEE to MEMFA via $\mathbf{R_2}(t)$, starting from the velocity and magnetic field HEE components containing Alfvén waves and red noise. A magnification of magnetic field fluctuations in the MEMFA reference frame is reported in panel e), as an example. The x-axis refers to days in a simulated case. The vertical dashed pink line refers to the transition from the CIR to the HSS region of the simulated corotating stream. The vertical dashed green line refers to the transition from the HSS region to the RR of the simulated corotating stream. The shaded region is the one containing Alfvén ULF waves.

4.2.2 MC test and reliability

To check the reliability of the procedure, I made a MC test by generating surrogates of both white and red noise, with different amplitudes, in order to compute the Signal-to-Noise Ratio (SNR_A), in terms of amplitude, and calculate the correlation coefficient between the MEMFA components (obtained via $\mathbf{R_1}(t)$ matrix) with only the localized Alfvén waves and the MEMFA components (obtained via $\mathbf{R_2}(t)$ matrix) in the presence of both localized Alfvén waves and noise.

The SNR_A is the ratio between the signal amplitude and the noise amplitude, therefore it gives us an idea of how much the signal prevails over the noise and vice versa. In the MC test, I decided to vary the noise amplitudes in order to vary the SNR_A. I defined the amplitudes of the noise of both magnetic field and velocity as $N_B = A_N \sigma_B$ and $N_V = A_N \sigma_V / C$ where A_N is the varying dimensionless amplitude, σ_B and σ_V are the standard deviations of real values fluctuations (obtained by removing the main trend), and C (see Equation 4.14) is a dimensionless multiplicative constant that links the amplitude of the magnetic noise with that of the velocity noise, while maintaining the uncorrelated noise between them, in the case of white noise. Imposing equality between the

$$SNR_A(B) = \frac{A_B}{N_B} = \frac{A_B}{A_N \sigma_B} \quad , \quad SNR_A(V) = \frac{A_V}{N_V} = \frac{A_v}{A_N \sigma_V / C} \tag{4.13}$$

the proportionality constant between noise amplitudes can be found:

$$C = \frac{A_B \sigma_V}{A_V \sigma_B} \tag{4.14}$$

Figure 4.6 shows the correlation coefficient computed between each MEMFA component with only localized Alfvén waves in the absence of noise and the equivalen MEMFA component in the presence of both Alfvén waves and white noise. Recall that, in the test procedure, the Alfvén wave was added only in the $\hat{\boldsymbol{\phi}}$ component, orthogonal to that ($\hat{\boldsymbol{\mu}}$) aligned to the ambient magnetic field. Each panel shows the mean correlation trend computed by averaging over 40 surrogates at each fixed SNR_A (colored dots) and its confidence interval at 95% (shaded area). In addition, for each SNR_A I computed the corresponding average correlation r_{mean}. It can be seen that these correlations computed between $\hat{\boldsymbol{\mu}}$ and $\hat{\boldsymbol{\nu}}$ components, of both magnetic field and velocity, are basically zero, whereas the correlation computed between $\boldsymbol{B_\phi}$ (obtained via $\mathbf{R_1}(t)$) with only Alfvén waves and $\boldsymbol{B_\phi}$ (obtained via $\mathbf{R_2}(t)$) with Alfvén waves and white noise, reach a value of $r = 0.7$ in correspondence with $SNR_A = 2.04$ for both the magnetic and the velocity component; it means that the signal (total signal - noise) in terms of amplitude is greater than 2/3 ($\sim 66\%$) of the total signal.

Figure 4.7 shows the correlation coefficient computed between each MEMFA component with only localized Alfvén waves in the absence of noise and the

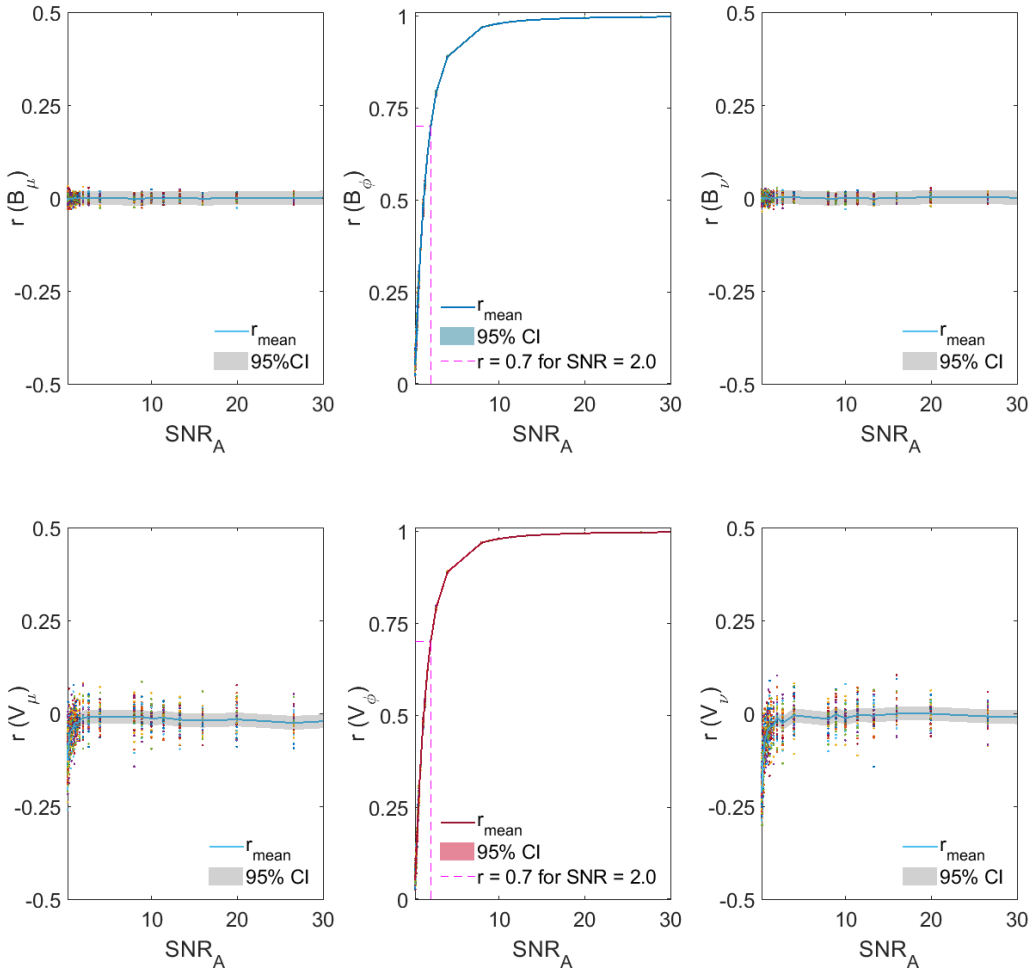

Figure 4.6: Correlation coefficient computed between each MEMFA component with only localized Alfvén waves in the absence of noise and the homonym MEMFA component in the presence of both Alfvén waves and white noise (dots). The first row shows the correlation coefficient related to the three magnetic field components, in terms of the SNR_A, where SNR_A is the Signal-to-Noise Ratio evaluated with the Amplitudes of signals and noise. The second row shows the correlation coefficient related to the three velocity components, in terms of the SNR_A. r_{mean} refers to the average correlation coefficient, while CI refers to the Confidence Interval, shown at 95%. Only for the $\hat{\phi}$ component, I reported the extrapolated SNR_A in correspondence to a correlation value of $r = 0.7$ (pink dashed lines).

homonym MEMFA component in the presence of both Alfvén waves and red noise. For each magnetic and velocity component the red noise was computed with an auto-regressive coefficient obtained from real data, respectively. Again, in the presence of red noise, the correlation coefficient is basically zero for components that do not contain ULF waves (obviously, the non-zero correlation

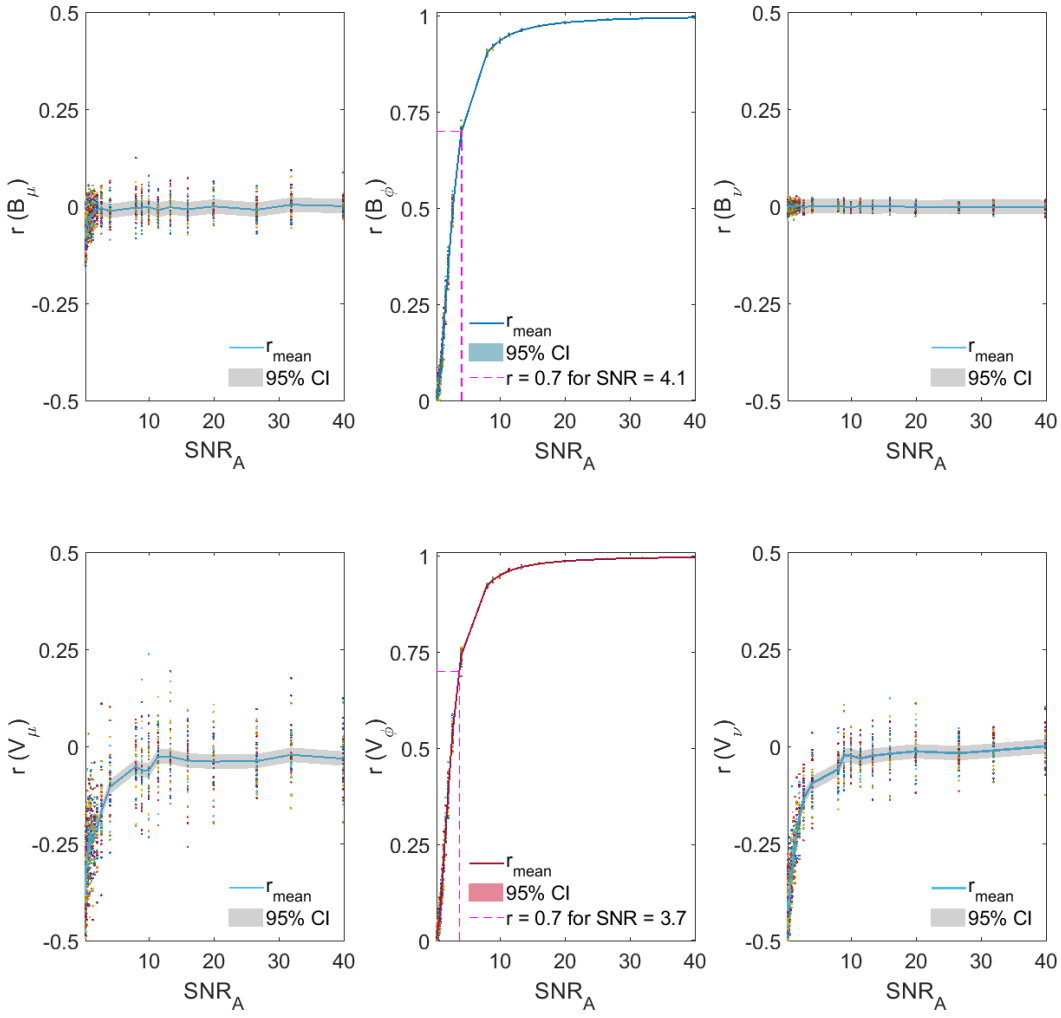

Figure 4.7: Correlation coefficient computed between each MEMFA component with only localized Alfvén waves in the absence of noise and the homonym MEMFA component in the presence of both Alfvén waves and red noise (dots). The first row shows the correlation coefficient related to the three magnetic field components, in terms of the SNR_A, where SNR_A is the Signal-to-Noise Ratio evaluated with the Amplitudes of signals and noise. The second row shows the correlation coefficient related to the three velocity components, in terms of the SNR_A. r_{mean} refers to the average correlation coefficient, while CI refers to the Confidence Interval, shown at 95%. Only for the $\hat{\phi}$ component, I reported the extrapolated SNR_A in correspondence to a correlation value of $r = 0.7$ (pink dashed lines).

when the signal is negligible compared to the noise is characteristic of red noise); on the other hand, the correlation coefficient grows rapidly towards 1 for the $\hat{\boldsymbol{\phi}}$ component, where I have previously added ULF Alfvén waves, that are well found back after the second rotation procedure.

The correlation computed between $\boldsymbol{B_\phi}$ (obtained via $\mathbf{R_1}(t)$) with only Alfvén waves and $\boldsymbol{B_\phi}$ (obtained via $\mathbf{R_2}(t)$) with Alfvén waves and red noise, reach a value of $r = 0.7$ in correspondence with $SNR_A = 4.1$ for the magnetic component and a value of $r = 0.7$ in correspondence with $SNR_A = 3.7$ for the velocity component; it means that, if the SNR_A is approximated to 4 for both components, the signal (total signal - noise) in terms of amplitude is greater than 4/5 ($\sim 80\%$) of the total signal for both the magnetic and velocity $\hat{\boldsymbol{\phi}}$ components. In both cases, the procedure is able to recognize the Alfvénic fluctuations in the presence of white noise and red noise. Furthermore, the procedure is as well able to identify the main component's profiles, giving a high correlation value for all three components of both magnetic field and velocity (not shown here). Notice that the ULF fluctuations that were present only in the $\hat{\boldsymbol{\phi}}$ component are found, after the second rotation, only in the same $\hat{\boldsymbol{\phi}}$ component and not in the others components.

4.3 SW Analysis: a dual approach

As shown in chapter 1.5.2.2, to study the Alfvénicity in the inertial range in the SW turbulence, adiabatic invariants are widely used, in particular, the normalized cross helicity σ_c and the normalized residual energy σ_r ([80] and references therein), which are reported below for convenience :

$$\sigma_c = \frac{e^+ - e^-}{e^+ + e^-} \tag{4.15}$$

$$\sigma_r = \frac{e^v - e^b}{e^v + e^b} \tag{4.16}$$

where e^+ and e^- are the variances related to Elsässer variables $\mathbf{z}^+$ and $\mathbf{z}^-$ (see section 1.5.2.1), whereas e^v is the velocity variance and e^b is the magnetic field variance in Alfvén units. It is recalled that for a pure Alfvén wave, as shown in section 1.4.0.1 we expect $\sigma_r \to 0$ and $\sigma_c \to \pm 1$.

4.3.1 Application to Synthetic Data

Therefore, to check the Alfvénicity, I computed these quantities both in the absence and in the presence of Alfvén waves. In the absence of Alfvén waves (see red and blue dashed curves in panel a of Figure 4.8) $\sigma_c \to 0$ and $\sigma_r \to 1$ as expected in absence of Afvén waves. When Alfvén waves are added, localized in the shaded region, there is the opposite scenario: $\sigma_c \to 1$ and $\sigma_r \to 0$ as expected for Alfvén waves.

The behavior of these variables in the compressive region is the result of the wide stream variability in this region. Indeed, while for a purely Alfvén wave in a homogeneous plasma, the method using the Elsässer variables is strictly

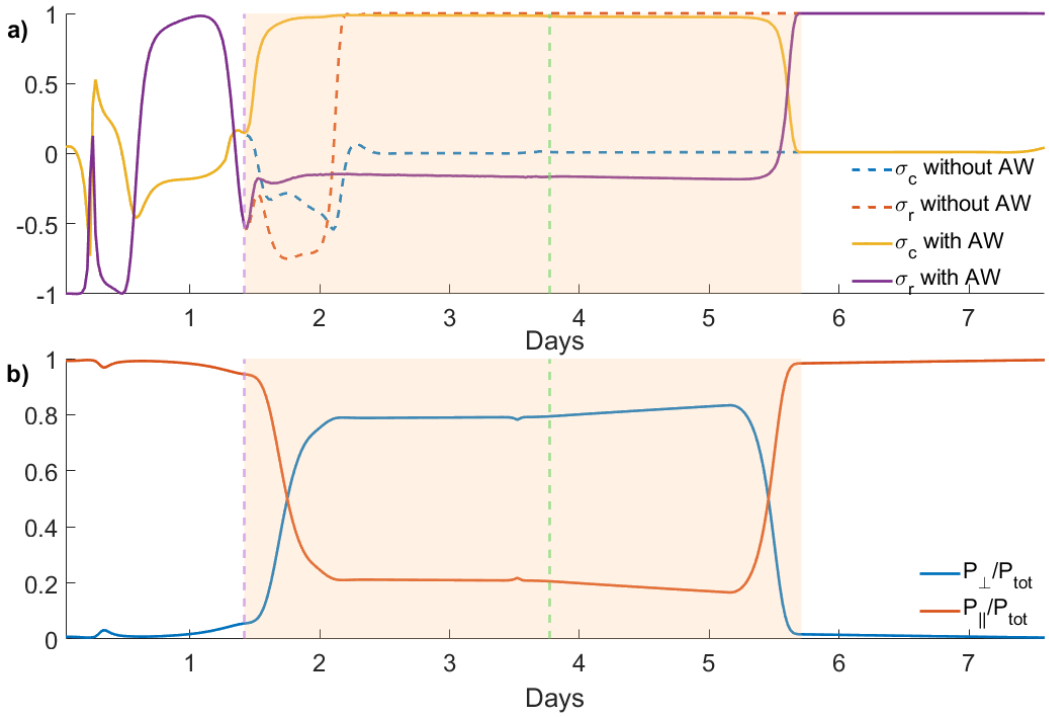

Figure 4.8: Panel a shows the normalized cross helicity σ_c and the normalized residual energy σ_r computed in the absence of Alfvén waves (AW) (dashed lines) and the same quantities computed in the presence of AW (solid line). Panel b shows the normalized power $P_\parallel$ aligned to the main magnetic field and the one orthogonal to it $P_\perp$. The vertical dashed pink line refers to the transition from the CIR to the HSS region of the simulated corotating stream. The vertical dashed green line refers to the transition from the HSS region to the RR. The shaded region is the one containing Alfvén ULF waves.

valid, for a compressible and inhomogeneous plasma pure MHD waves are no longer normal modes, but the waves become coupled or show a mixed nature between the Alfvénic and the magnetosonic one. In this case, magnetosonic waves are described by both z+ and z-, and cannot be separated inward and outward from the background field [81].

In the test, I can compute two quantities that can be compared with σ_c and σ_r, to get more information about the characteristics of fluctuations. I performed the spectral analysis of both magnetic and velocity components in the MEMFA reference frame, to define the normalized power related to the main two directions: the one aligned to the main ambient field and the one orthogonal to it. Obviously, power is a scalar quantity, hence subscriptions $\parallel$ and $\perp$ refer to the components used to calculate the power itself. I defined $P_\perp = P_{V_\perp} + P_{B_\perp|_V}$ where $P_{V_\perp}$ is the sum of powers of V_ϕ and V_ν, and $P_{B_\perp|_V}$ is the sum of powers of B_ϕ and B_ν both re-scaled to velocity dimensions. At

the same way, I defined $P_{\parallel} = P_{V_{\parallel}} + P_{B_{\parallel}|V}$ where $P_{V_{\parallel}}$ is the power of V_{μ} and $P_{B_{\parallel}|V}$ is the power of B_{μ} re-scaled to velocity dimensions. Alfvén waves are characterized by perturbations in the direction orthogonal to the main field, therefore a prevalence of $P_{\perp}$ in their presence is expected.

In panel b of Figure 4.8 are shown $P_{\perp}/P_{Tot}$ in blue and $P_{\parallel}/P_{Tot}$ in red (where P_{Tot} is the total power), both defined in the range $[0, 1]$. In the shaded region, which corresponds to the one with Alfvén waves, $P_{\perp}/P_{Tot}$ is greater than $P_{\parallel}/P_{Tot}$, as expected. There is a well-foundend correspondence ($r = 0.95$) between σ_c and $P_{\perp}/P_{Tot}$ and also ($r = 0.88$) between σ_r and $P_{\parallel}/P_{Tot}$, in the MEMFA reference frame.

4.3.2 Application to Real Event

I applied the same procedure to a real event, for a high-velocity stream from 9^{th} to 15^{th} August 2008 (solar minimum activity).

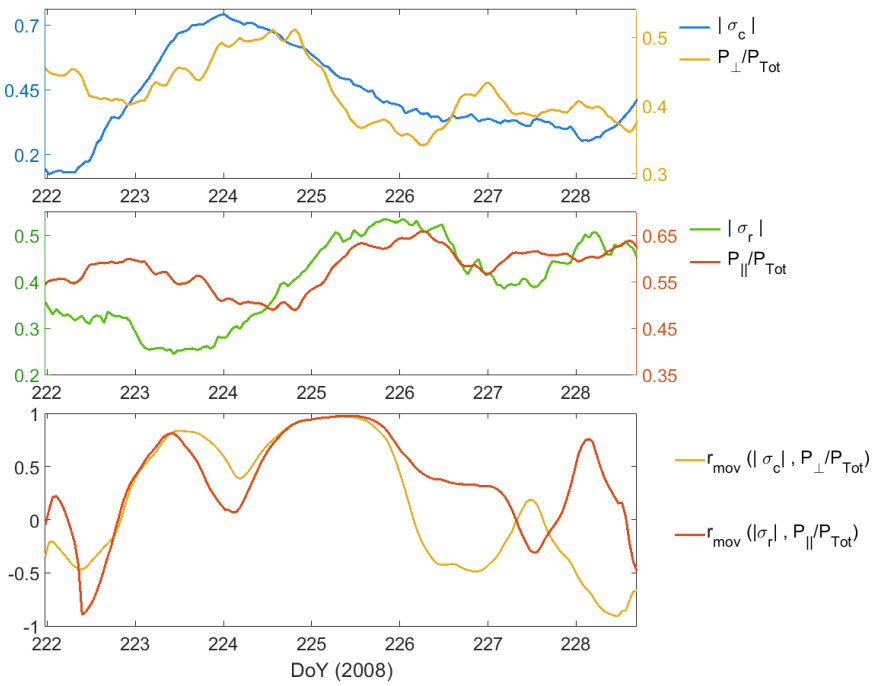

Figure 4.9: Top panel: smoothed $|\sigma_c|$ in blue and $P_{\perp}/P_{Tot}$ in yellow. Middle panel: smoothed $|\sigma_r|$ in green and $P_{\parallel}/P_{Tot}$ in red. Bottom panel: moving correlation (r_{mov}) between $|\sigma_c|$ and $P_{\perp}/P_{Tot}$ in yellow, and moving correlation between $|\sigma_r|$ and $P_{\parallel}/P_{Tot}$ in red.

Figure 4.9 shows the results (smoothed over 36 hours) obtained with the procedure applied to a real case study. In the top panel are plotted the normalized

cross helicity $|\sigma_c|$ (in blue) and the normalized SW power $P_\perp/P_{Tot}$ (in yellow) orthogonal to the main field. In the middle panel are plotted the normalized residual energy $|\sigma_r|$ (in green) and the normalized SW power $P_\parallel/P_{Tot}$ (in red) aligned to the main field. In the bottom panel, is shown the moving correlations (over 48 hours) between the two quantities ($|\sigma_c|$ and $P_\perp/P_{Tot}$) shown in the top panel (in yellow) and between the two quantities ($|\sigma_r|$ and $P_\parallel/P_{Tot}$) shown in the middle panel (in red). Without loss of generality, the use of the absolute value of σ_c and σ_r has been chosen so that the range of variability of these two quantities is comparable with that of the normalized powers, that is between 0 and 1. The correlation gives us an idea of how well the two procedures are in agreement. From the beginning of DoY 223 to the end of DoY 225 can be observed that both correlations have similar trends and both correlations have quite high values (except for a quick decrease at the beginning of DoY 224) suggesting a good accordance between the two methods used. After DoY 226 the correlations decrease, suggesting that the two methods give different information. When there is accordance between the two methods and $|\sigma_c|$ and $P_\perp/P_{Tot}$ reach high values and $|\sigma_r|$ and $P_{||}/P_{Tot}$ reach low values, I am confident that there are Alfvén waves. When there is still accordance between the two methods and σ_c and $P_\perp/P_{Tot}$ values are low, I am confident that there are no Alfvén waves. When the two methods are not in agreement, there could be the presence of isotropic waves also in the orthogonal direction.

Chapter 5

Identification of the geomagnetic re-scaling *composite quiet background* (CQB)

As shown in chapter 2.2, the geomagnetic field shows variations on different scales related to different phenomena. In this work, I am interested in studying the effect of SW fluctuations found in the corotating high-speed streams on the geomagnetic field variation in the Pc5 range. Despite the Pc5 waves having a maximum period of 10 minutes, these fluctuations are immersed in a background power that contains in itself even variations of a larger period.

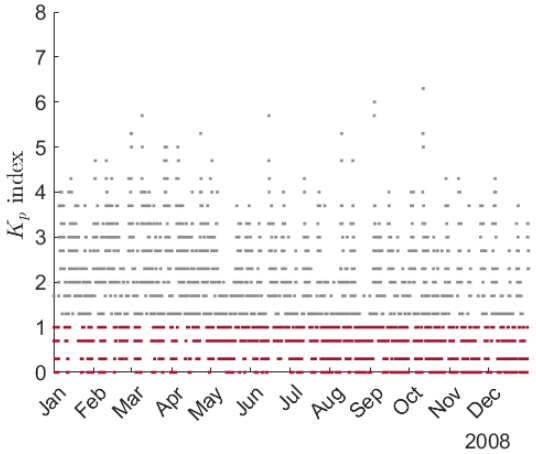

Figure 5.1: Kp index selection for quiet periods.

To highlight small-scale variations, particularly fluctuations in the Pc5 range, I initially identified a background associated with periods of quiet geomagnetic activity, with which I subsequently scaled the ground power before proceeding with the joint analysis, shown in chapter 6, with fluctuations observed in the solar wind during HSS.

To begin, I selected a year of data (2008) corresponding to a declining phase of the solar cycle, to which the events subsequently studied belong. From the geomagnetic horizontal components measured at the selected stations reported in table 3.1 of section

3.2, I calculated the horizontal dynamic power spectra. The spectral analysis has been performed for the ground power, at different latitudes, of the horizontal components with a moving window for the dynamic spectrum of 2 hours overlapped by 75 %; within the two hours, the spectra were computed using a running Welch's method with a 1-hour Hamming-tapered window and 75% overlap. Then the spectra were frequency smoothed over 3 adjacent bands by using a triangular window, so that the final frequency resolution is 0.6 mHz. Then the power P has been integrated over the whole frequency range [0.6 - 8.3] mHz, that is between the minimum frequency resolved according to the chosen Welch window (1h), the frequency smoothing, and the Nyquist frequency related to sampling.

For this year, I selected the quiet periods corresponding to low geomagnetic activity, by imposing a threshold on Kp $\leq$ 1. As mentioned in section 2.1, this index measures the disturbance of the horizontal component of the Earth's magnetic field, on a planetary scale. Figure 5.1 shows in gray the Kp index for the whole year, and in red the values corresponding to Kp $\leq$ 1 which cover the 48.7% of the whole year.

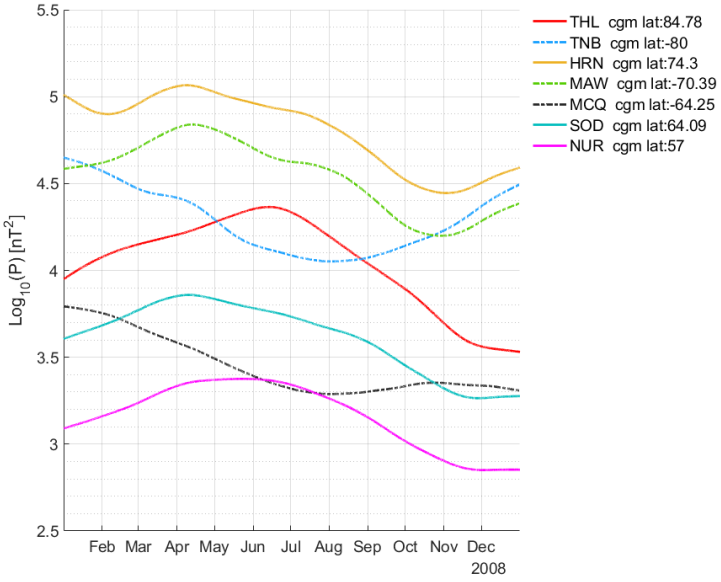

Figure 5.2: Each curve shows the trend over the whole year found for the corresponding station specified in the legend. Solid lines refer to the northern hemisphere; dashed lines refer to the southern hemisphere.

In order to determine the background power, I proceeded to identify the main trend over the whole year of the log(P) at each observatory in correspondence to quiet periods, shown in figure 5.2. The highest power is observed for stations at auroral latitudes in both hemispheres, such as HRN (in yellow) at 74.3° magnetic latitude and MAW (in green) at -70.39° magnetic latitude. These two curves show a maximum (minimum) at the spring (autumn) equinox for the northern

hemisphere and at the autumn (spring) equinox for the southern hemisphere. Then follow the stations in the polar cap of both hemispheres, such as THL (in red) at 84.78° magnetic latitude and TNB (in blue) at -80° magnetic latitude, both with a maximum at the local summer solstice and a minimum at the local winter solstice. Finally, in terms of power, there are the stations at sub-auroral latitudes; here too, there is a broad maximum at the local summer equinox and a broad minimum at the local winter equinox. This suggests that the power of the horizontal component in the Pc5 range is higher in auroral regions, where there is greater activity and a more intense and direct effect of solar activity on the geomagnetic field.
For each station, I subtracted from the integrated power the corresponding trend over the whole year. From the resulting power, I proceeded to identify the semiannual periodicity and its sub-harmonic, by fitting them with the superposition of sinusoidal functions at their corresponding periodicities, shown by the red curve in figure 5.3. At this point, I also removed the semiannual contribution and, from the remaining power, I further identified the synodic periodicity (at 27 days) and its two sub-harmonics (at 13.5 days and 9 days), shown in yellow in figure 5.3.

After subtracting the contributions shown in Figure 5.3 from the Log(P) identified during quiet periods, I proceeded to separate the remaining power based on the four local seasons. Then, for each station and each season, I calculated the average of the Log(P), net of the previous contributions, corresponding to the same UT time of the day. This identifies the diurnal variation for each station and for each season corresponding to periods of low geomagnetic activity, shown in black in figures 5.4, 5.5, 5.6, 5.7, 5.8, 5.9, and 5.10. Seasonal division is done because the diurnal variation for each season changes based on the inclination of the Earth's magnetic axis relative to the ecliptic, and therefore on the solar illumination to which each hemisphere is subjected during different periods of the year. Consequently, this leads to different ionization levels in the ionosphere, affecting the geomagnetic field power, as can be seen from the figures.

A comparison between the average profiles of the logarithm of quiet power and the total power P_T (obtained without removing any contributions and any condition on Kp), separated by local seasons for each observatory, is shown in figure 5.11. Here, each row corresponds to a different local season: spring in the first row, summer in the second row, then autumn in the third row, and finally the local winter in the last row. Each column corresponds to a different magnetic observatory, sorted from left to right by decreasing absolute geomagnetic latitude. All daily profiles are shown as a function of MLT.
The average of the logarithm of total power (black curves in figure 5.11) shows a peak around noon MLT and a minimum around midnight MLT, for both THL and TNB. This effect is associated with the station approaching the magnetic

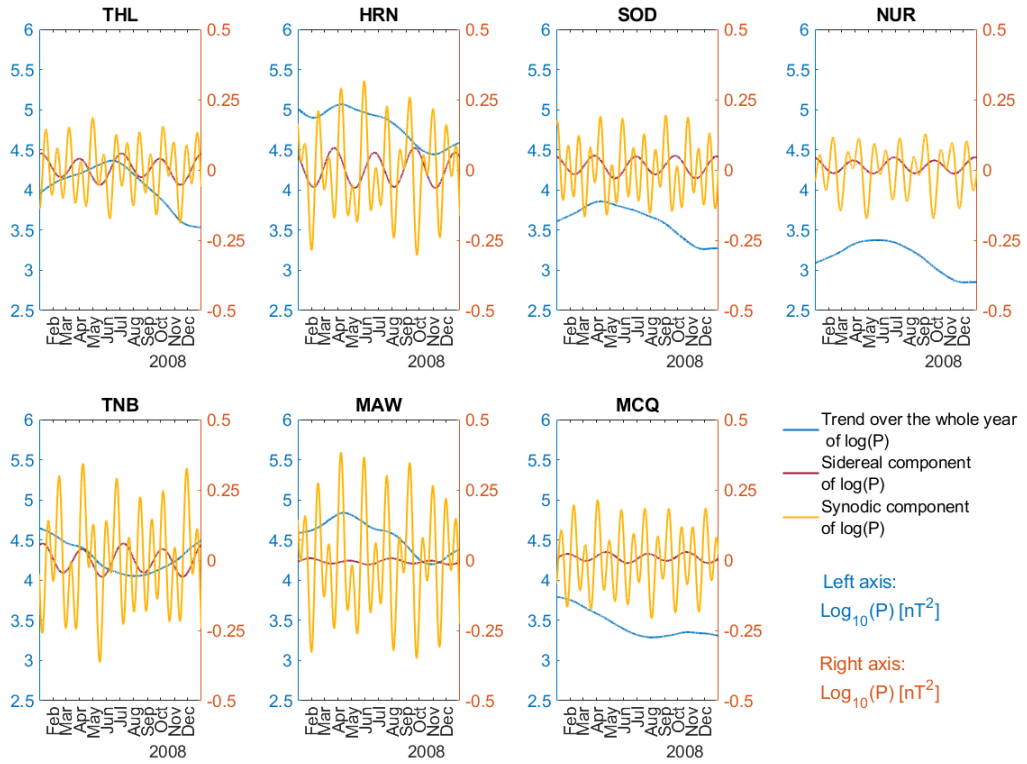

Figure 5.3: The blue curve represents the power trend over the whole year (blue scale on the left axis of each panel). The red curve represents the sidereal contribution (orange scale on the right axis of each panel). The yellow curve represents the synodic contribution (orange scale on the right axis of each panel). Each plot refers to a different geomagnetic observatory, in particular: on the first row those of the northern hemisphere, on the second row those of the southern hemisphere.

cusp at the sunward side. For the same stations, the diurnal profile associated with quiet periods sees the peak shifted towards the morning side and the minimum shifted towards the evening side. This behavior highlights an asymmetry between the morning and afternoon sides.
For stations at auroral latitudes (HRN and MAW), the average diurnal total powers exhibit two relative peaks: one in the morning and one at local midnight. The morning peak could be linked to Kelvin-Helmholtz instability, while the midnight one could be associated with phenomena related to the geomagnetic tail activity, typical of auroral latitudes. For the same stations, the daily profiles associated with quiet periods show a pronounced peak in the early morning and, conversely, a second peak in the late afternoon.
For stations at lower latitudes, the average diurnal power profile undergoes fewer variations compared to the previous cases. This holds both when considering the total power on average and when considering the power associated with quiet periods, and it is indicative of the fact that stations at lower latitudes,

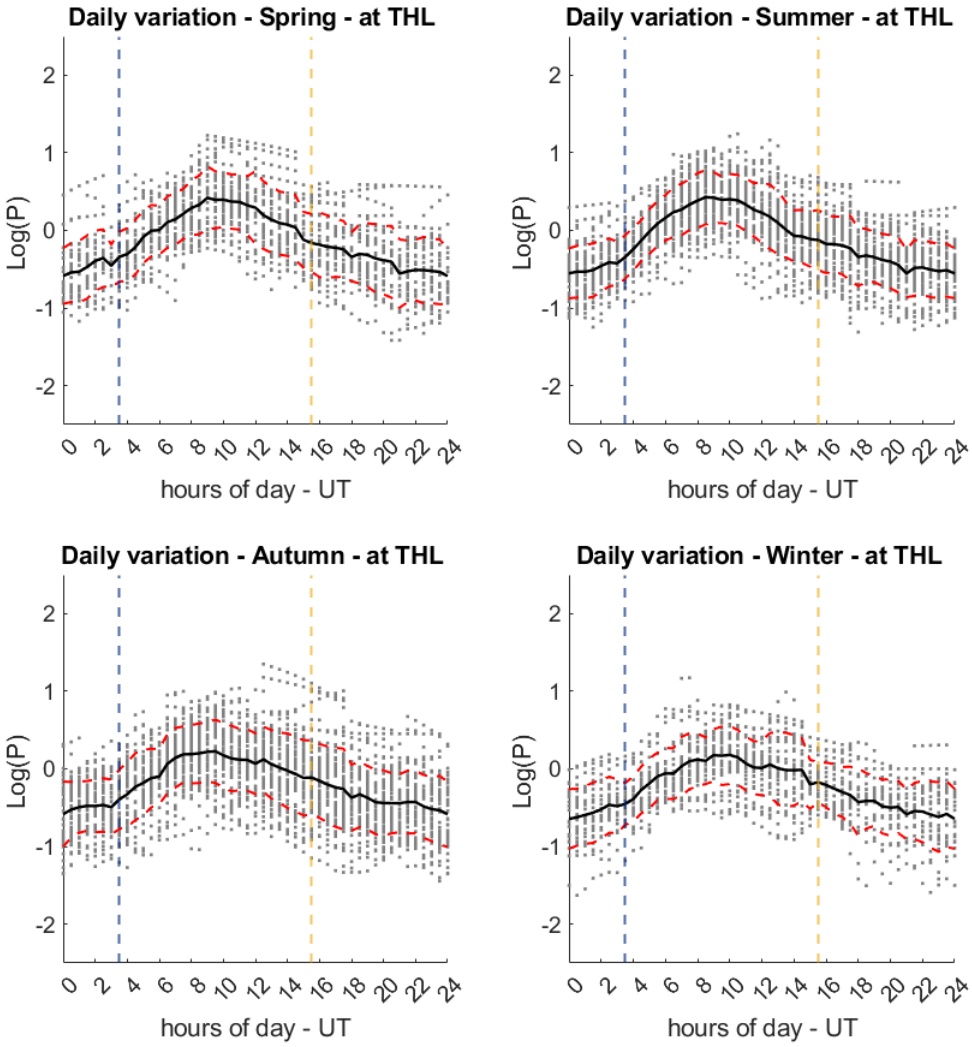

Figure 5.4: The black curve is the quiet diurnal variation at THL (average of gray points), separated into the four seasons. The red dashed curves represent the standard deviation of the mean. The yellow and blue dashed vertical lines represent the MLT noon and the MLT midnight, respectively.

connected to more internal magnetic shells, experience external disturbances less intensely on average.
For all seasons, the power level at the auroral observatories (HRN and MAW) is definitely higher than at the other latitudes.

Once all the contributions during quiet periods (low geomagnetic activity) were identified, including the trend over the whole year, the semiannual, the sidereal and synodic variations (shown in figure 5.3), and finally the diurnal variations (separated by season), I proceeded to construct the Composite Quiet

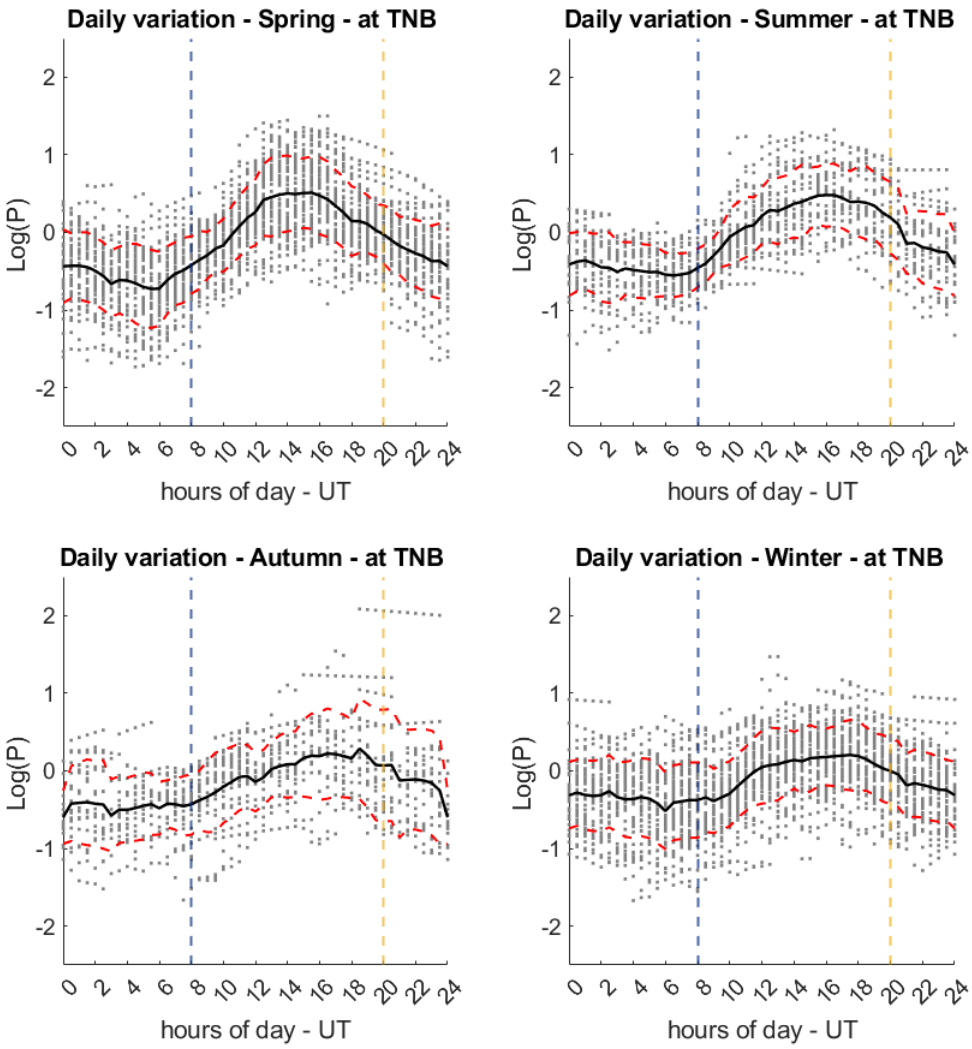

Figure 5.5: The black curve is the quiet diurnal variation at TNB (average of gray points), separated into the four seasons. The red dashed curves represent the standard deviation of the mean. The yellow and blue dashed vertical lines represent the MLT noon and the MLT midnight, respectively.

Background (CQB) for each observatory. This was obtained by combining all the aforementioned contributions. The result is shown in figure 5.12.

The CQB power represents the background power associated with periods of very low geomagnetic activity. It is used to scale the power of a specific period of the year, an event under investigation, allowing the fluctuations (that we are interested in studying) to stand out more prominently compared to the background itself. Therefore, in the joint analysis (chapter 6), the power computed on the ground for various stations corresponding to an event will be

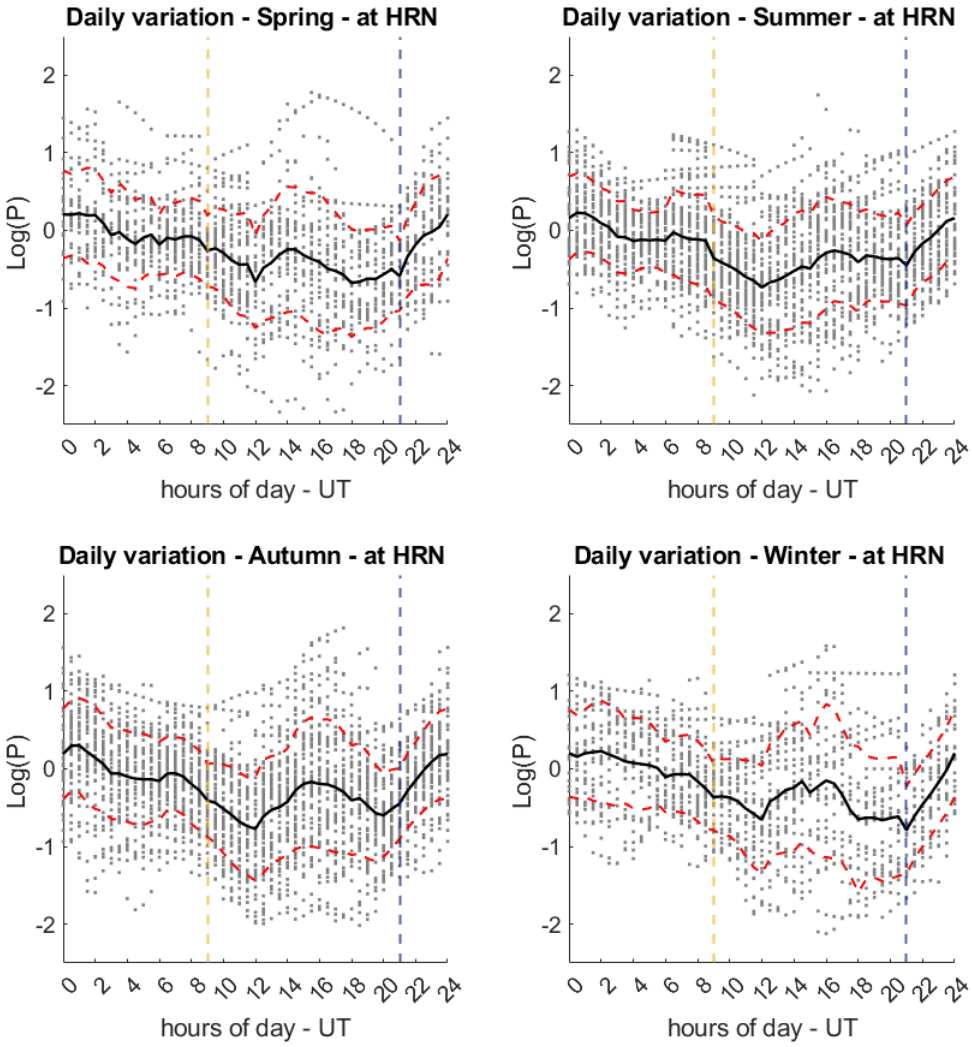

Figure 5.6: The black curve is the quiet diurnal variation at HRN (average of gray points), separated into the four seasons. The red dashed curves represent the standard deviation of the mean. The yellow and blue dashed vertical lines represent the MLT noon and the MLT midnight, respectively.

scaled to the CQB extracted for the respective station at the selected event's temporal correspondence.

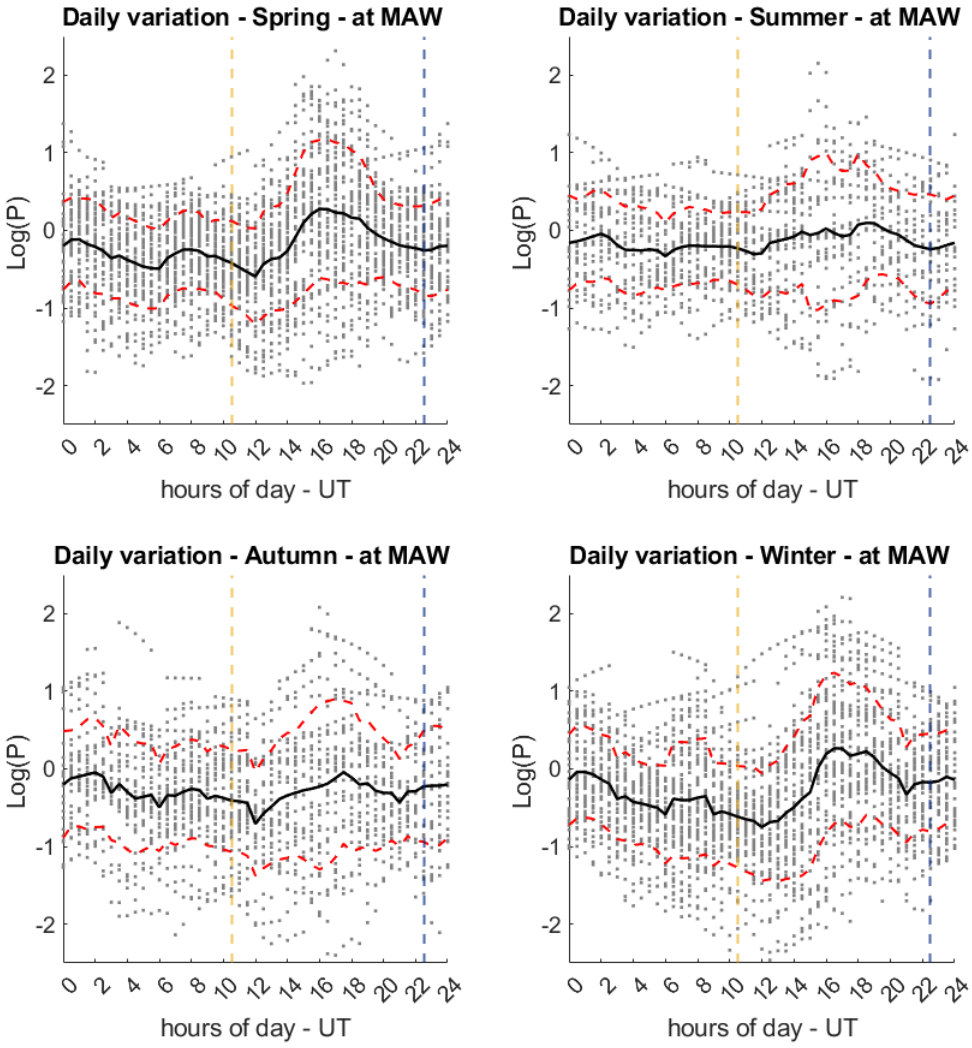

Figure 5.7: The black curve is the quiet diurnal variation at MAW (average of gray points), separated into the four seasons. The red dashed curves represent the standard deviation of the mean. The yellow and blue dashed vertical lines represent the MLT noon and the MLT midnight, respectively.

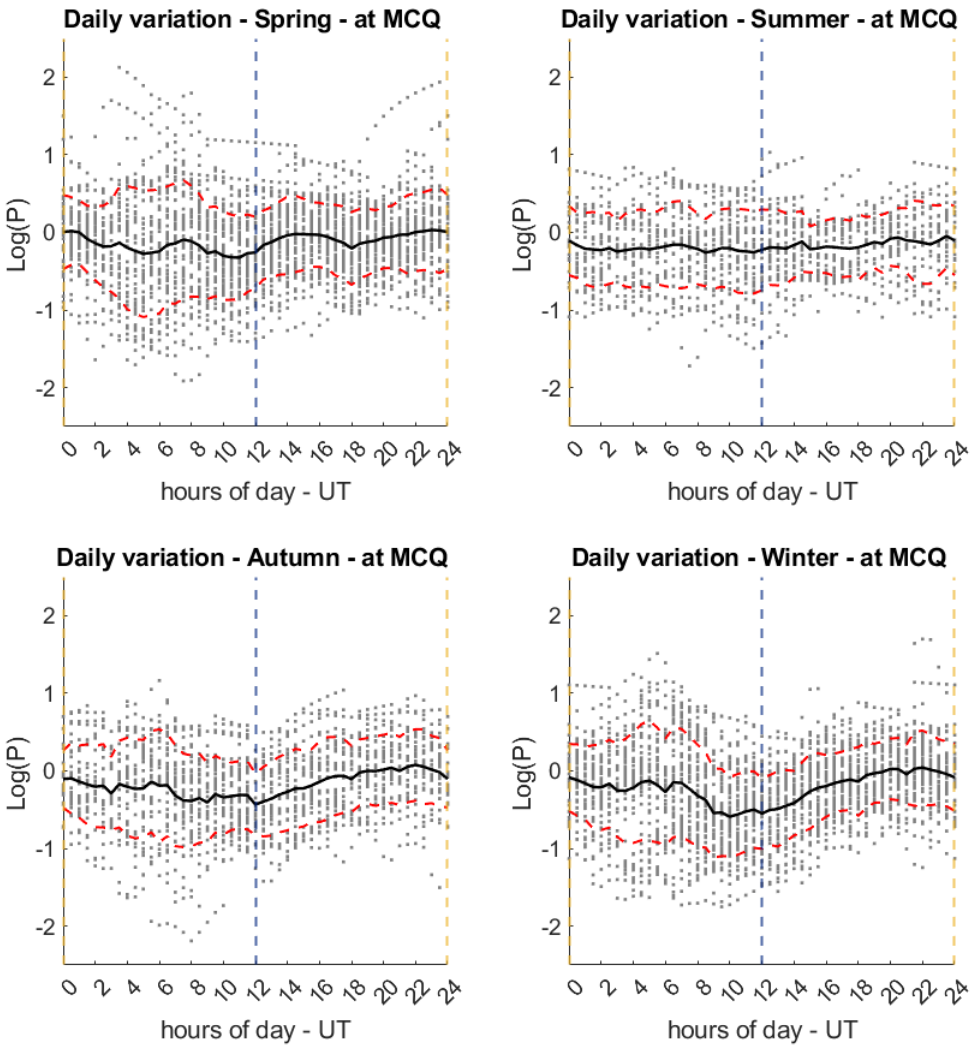

Figure 5.8: The black curve is the quiet diurnal variation at MCQ (average of gray points), separated into the four seasons. The red dashed curves represent the standard deviation of the mean. The yellow and blue dashed vertical lines represent the MLT noon and the MLT midnight, respectively.

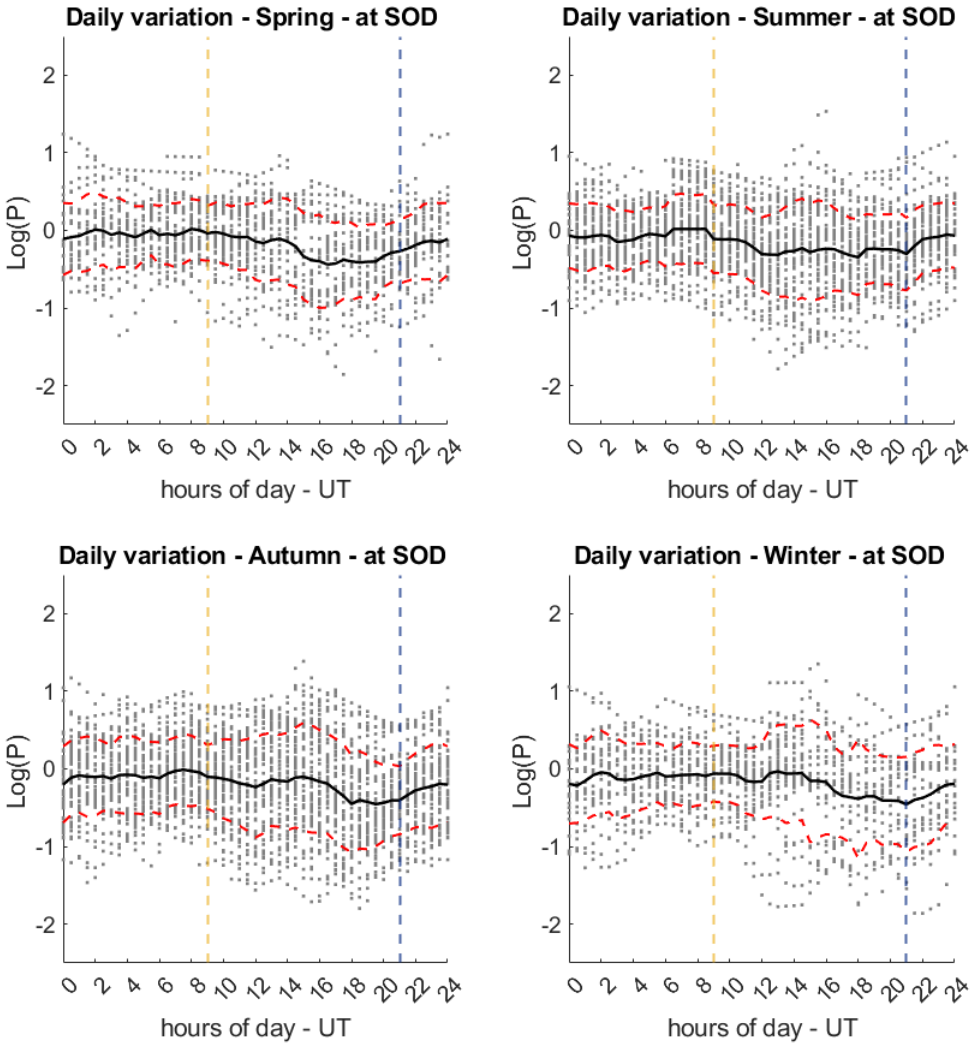

Figure 5.9: The black curve is the quiet diurnal variation at SOD (average of gray points), separated into the four seasons. The red dashed curves represent the standard deviation of the mean. The yellow and blue dashed vertical lines represent the MLT noon and the MLT midnight, respectively.

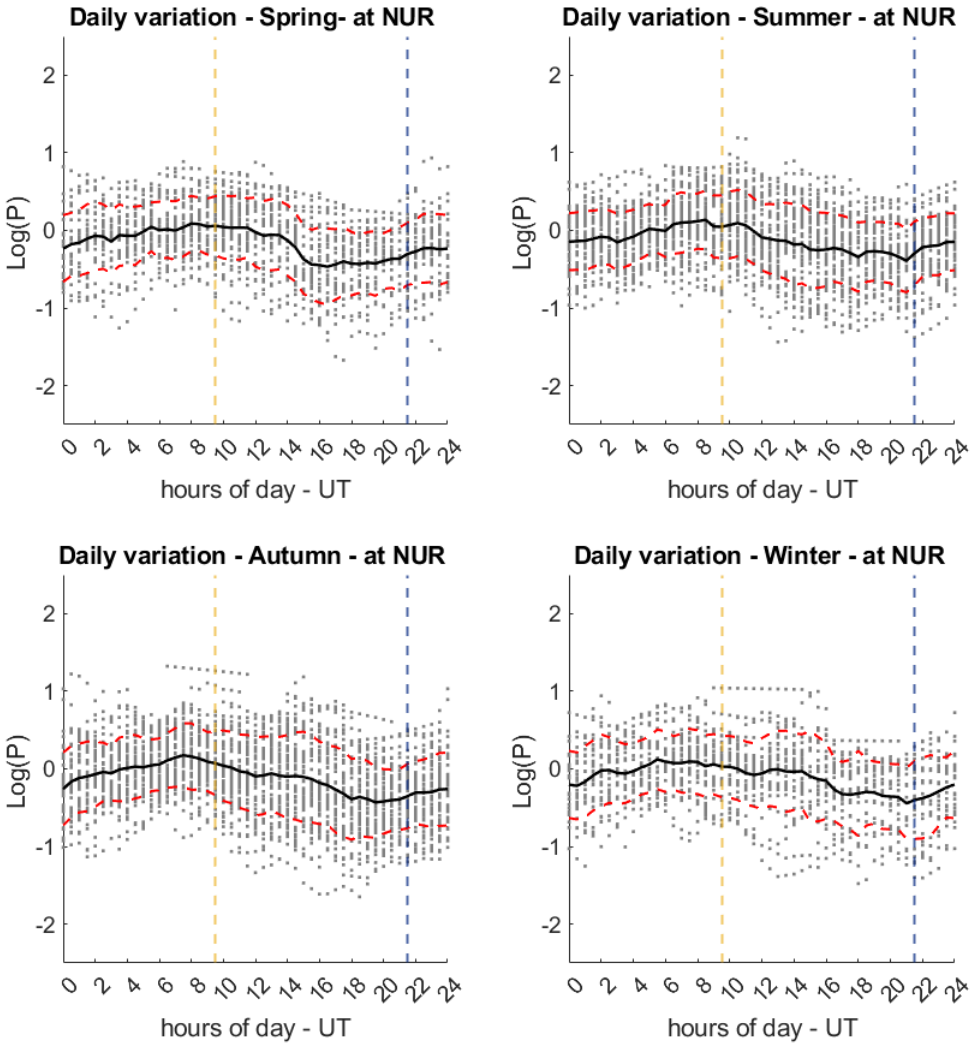

Figure 5.10: The black curve is the quiet diurnal variation at NUR (average of gray points), separated into the four seasons. The red dashed curves represent the standard deviation of the mean. The yellow and blue dashed vertical lines represent the MLT noon and the MLT midnight, respectively.

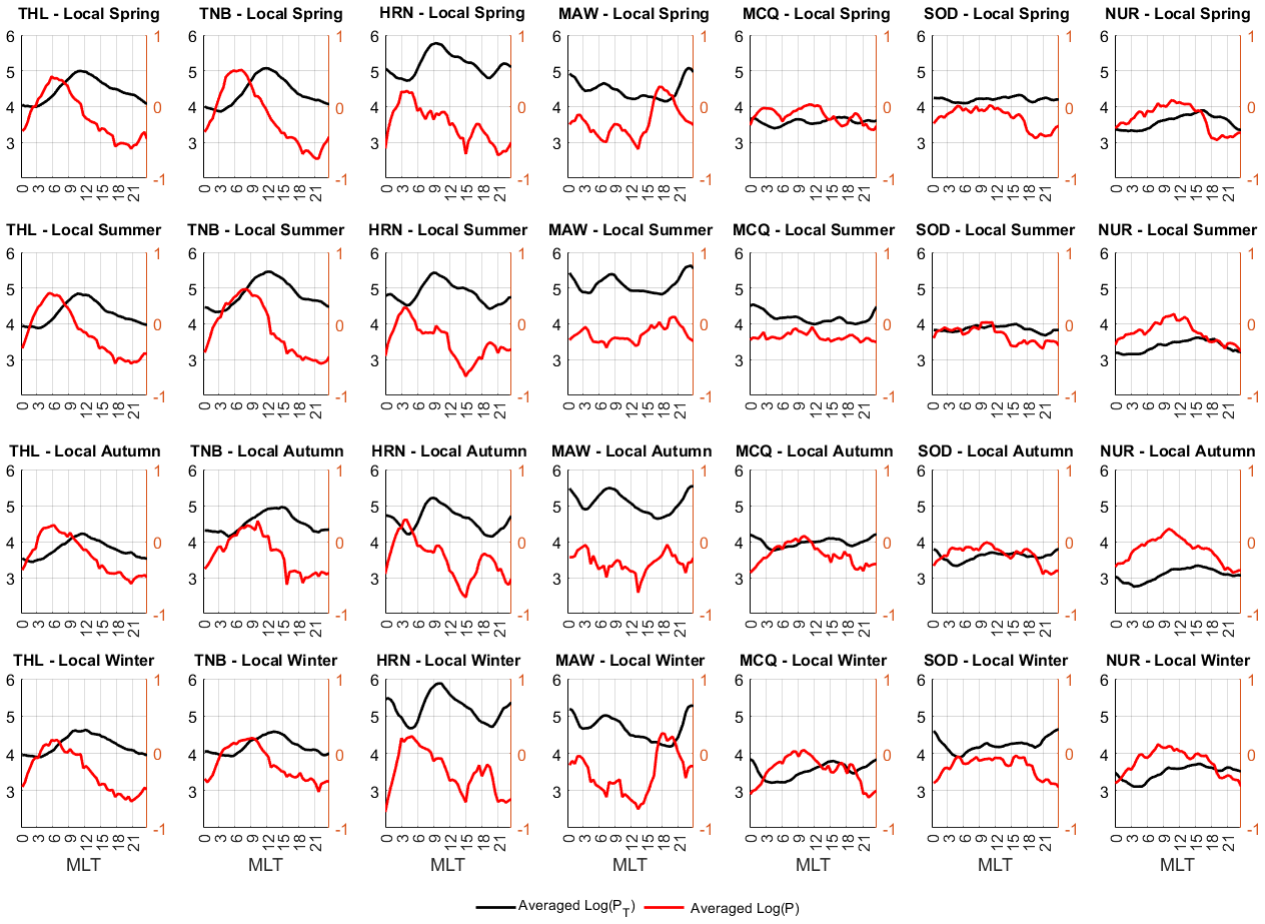

Figure 5.11: The red curve is the quiet diurnal variation. The black curve is the average of the total power at the corresponding observatory, without removing any contributions and without any threshold on Kp. Each row corresponds to a different local season: spring in the first row, summer in the second row, then autumn in the third row, and finally the local winter in the last row. Each column corresponds to a different geomagnetic station, sorted in descending order in terms of |CGM lat|, from the higher latitude on the left-hand column (THL) to the lower latitude on the right-hand column (NUR). The x-axis denotes the MLT.

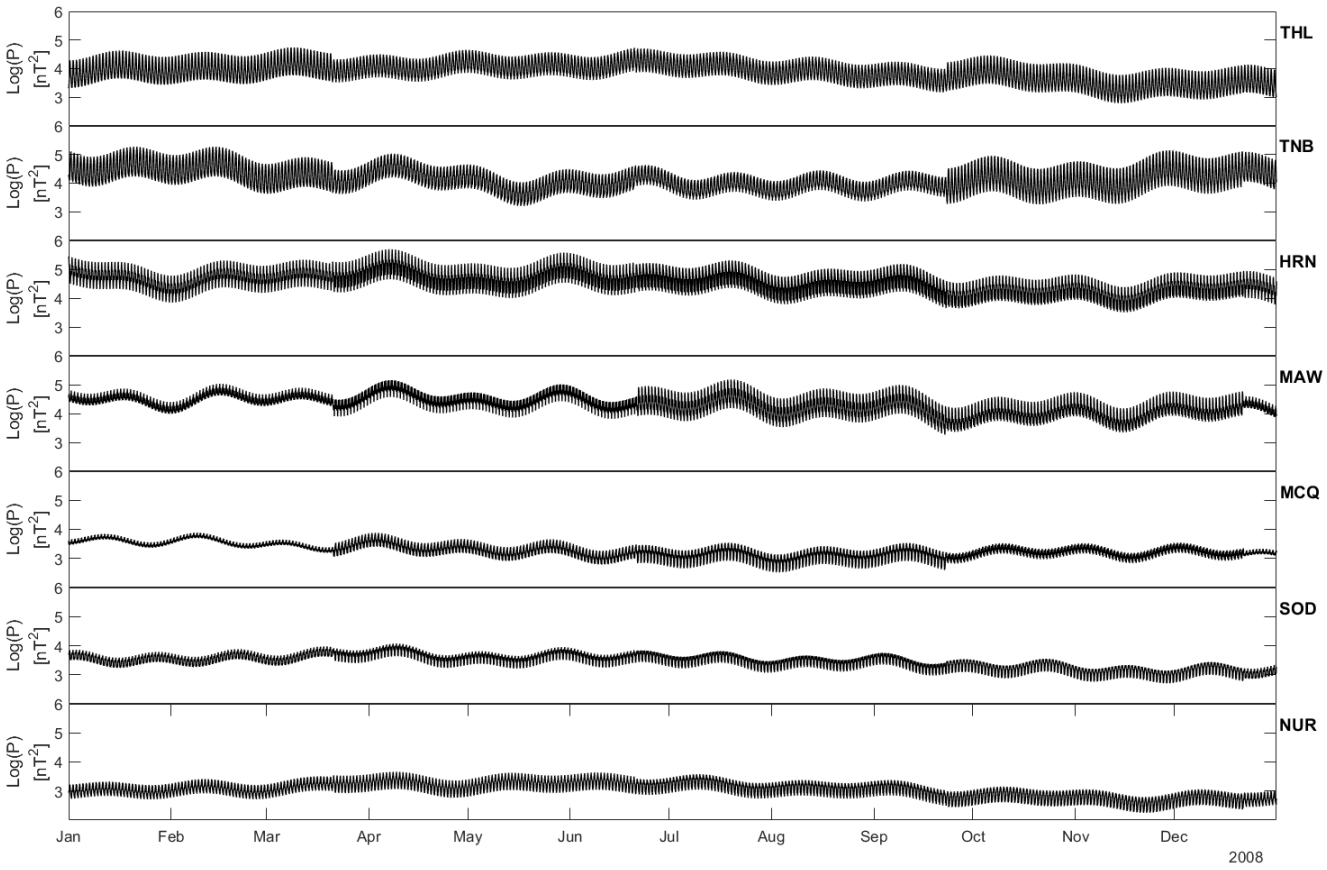

Figure 5.12: The CQB power during 2008 for each observatory, in order of geomagnetic latitude decreasing from top to bottom.

Chapter 6

Joint analysis and events

This chapter aims to investigate the potential effects of Alfvénic fluctuations present in corotating high-speed streams on geomagnetic activity at high latitudes (at the geomagnetic stations shown in chapter 3). The regions at medium-high latitude are those more affected by the external magnetic structures present in the solar wind. The work focuses on the Pc5 ULF frequency range (1-7 mHz) because it is a range of frequency comparable to the typical frequencies of Alfvénic fluctuations observed in the corotating SW streams near Earth. To investigate the possible effects of geomagnetic fluctuations, in this frequency range, present in the SW corotating streams, I selected 4 SW high-speed streams on the declining phase of Solar Cycle 23. As said in Section 1.2.1, the declining phase of the solar cycle is where these recurring structures are most observed. This chapter has a section for each of the events analyzed. In each section, there is a subsection for the event characterization, a subsection for the joint analysis distinguishing between Alfvénic populations and their geoeffectiveness, a subsection for a joint correlation analysis, and a subsection for a joint wavelet coherence analysis.

6.1 5-12 January 2008

6.1.1 Characterization

The first event studied, in the declining phase of solar cycle 23, is that of a corotating stream observed in January 2008, with the HSS (High-Speed Stream) and the RR (Rarefaction Region) spanning from January 5th to January 12th, 2008. Figure 6.1 shows the velocity (in red) and magnetic (in blue) components in the first three panels, the proton number density in the fourth panel, and the proton temperature in the last panel. Figure 6.1 refers to the HSS and the RR of the selected corotating stream, which correspond to the light blue and pink regions in Figure 1.5b, respectively. The vertical green line in Figure 6.1 approximately marks the boundary between these two regions. At the beginning

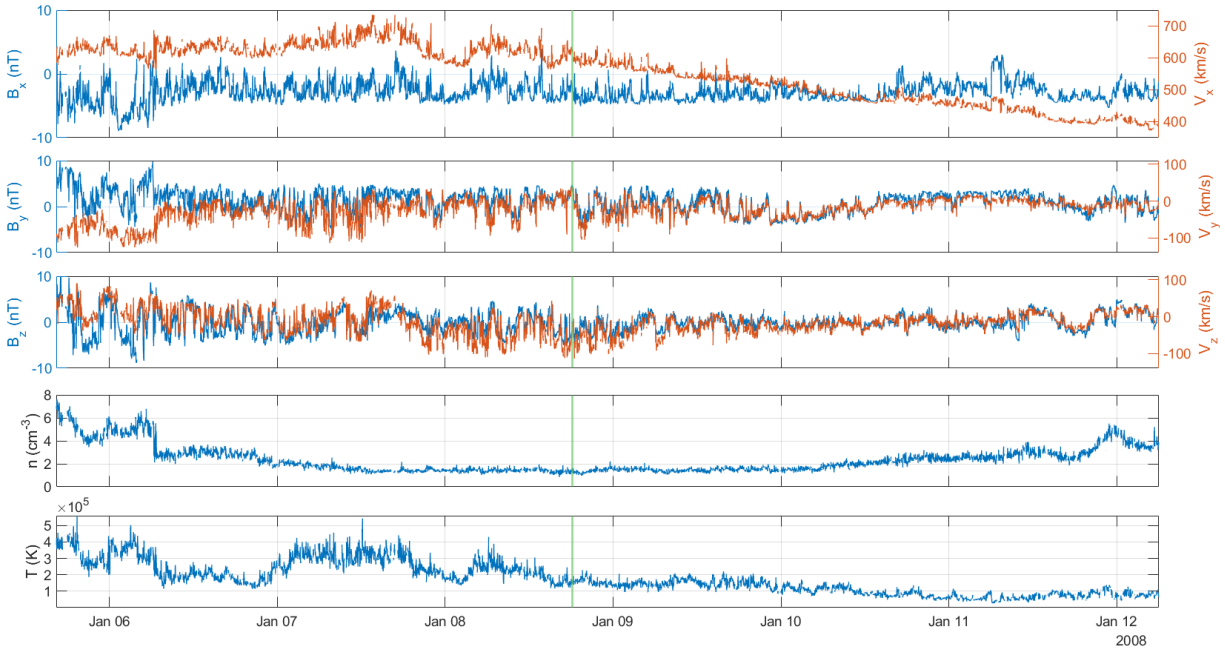

Figure 6.1: January event. From top to bottom, the first three panels: velocity components V_x, V_y, V_z (in red) and magnetic field components B_x, B_y, B_z (in blue) in the HEE reference frame. Fourth panel: the proton number density. Fifth panel: the proton temperature. The vertical green line identifies the separation between HSS and RR of the corotating stream.

of the HSS, there is a decrease in both density and temperature, after experiencing an increase in the preceding compression region (not shown here). Within the HSS, there are large fluctuations in both magnetic and kinetic components, typically of Alfvénic nature, as shown in the following figure 6.2. The RR starts at the velocity knee, where there is a transition from the high-speed plateau of the SW to a decreasing velocity trend, usually together with a decrease in the amplitude of magnetic and kinetic fluctuations. In both HSS and RR, the proton density and temperature remain quite low.

The top panel of Figure 6.2 shows the SYM-H index, which is at a higher time resolution (1 min) than the Dst index (1 hour), as stated in section 2.2.2.3. The SYM-H index does not even reach values of -50 nT, indicating the presence of a very weak geomagnetic storm. The second panel of Figure 6.2 shows the AE index, which reaches values of 750 nT in correspondence with the HSS region of the stream; these values are associated with modest substorms. The third and the fourth panel show the normalized cross-helicity σ_c (in red) and the normalized residual energy σ_r (in yellow), respectively, both computed as described in section 1.5.2.2, using a 1-hour moving window with 50% of overlap. The use of a one-hour moving window, as widely employed in the literature, allows for the good tracking of low-frequency variations typical of Alfvénic turbulence. The

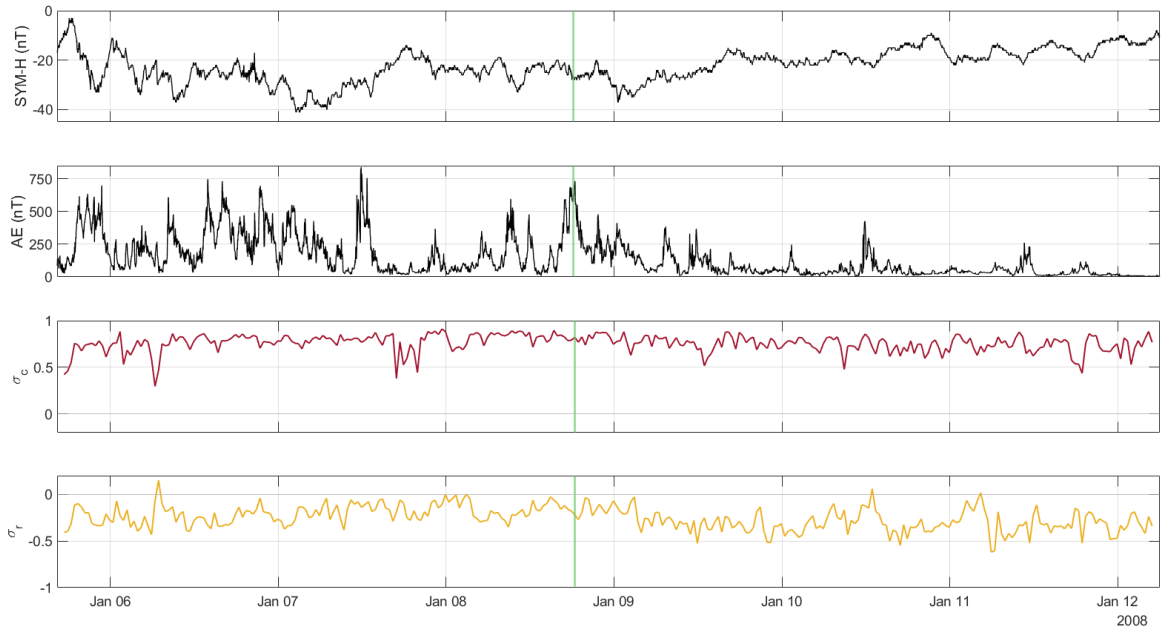

Figure 6.2: January event. From top to bottom: the horizontal symmetric (SYM-H) disturbance index, the Auroral Electrojet (AE) index, the normalized cross-helicity, and the normalized residual energy. The green vertical line corresponds to the velocity knee location, separating HSS from RR.

more $\sigma_c \to \pm 1$ and $\sigma_r \to 0$, the more Alfvénic the SW is. In this case, σ_c tends to 1, denoting the presence of outward modes, mainly in the HSS region, with more variability in the RR, despite maintaining high values even in this region. Accordingly, σ_r assumes values close to zero, albeit consistently slightly negative, indicating an almost balance between magnetic and kinetic energy, with a slight prevalence of magnetic energy, a phenomenon typically observed in the SW, still under investigation. This corotating stream is peculiar because it contains highly Alfvénic fluctuations for almost its entire duration, not only in the HSS but also in the RR.

6.1.2 Joint analysis: Alfvénic and non-Alfvénic populations and geomagnetic effectiveness

A first approach for the joint analysis between SW and ground-based data involved examining how ground power is distributed across various latitudes as a function of two external parameters: the geoeffective component of the electric field and the normalized cross-helicity in the SW. To achieve this, the ground power of the horizontal H and D components was computed for each observatory with a moving window for the dynamic spectrum of 2 hours overlapped for 75%; within the two hours, the spectra were computed using a running

Welch's method with a 1-hour window and 75% overlap. A frequency triangular smoothing over 3 bands is applied (this control spreads the noise reduction into the specified number of neighboring bands , and the triangular shape has the advantage of reducing the random fluctuations while maintaining a reasonable spectral resolution [82]). This setup ensures that the minimum detectable frequency is 0.55 mHz and the temporal resolution of the dynamic spectrum is 30 minutes. I then calculated ratio between the logarithm of the power integrated on the entire frequency range, that of Pc5 waves, and the logarithm of the corresponding background power (CQB), as described in chapter 5; from this point onwards, concerning ground-based power, I refer to this quantity as re-scaled power or Log(P) ♦, for the sake of notation brevity.

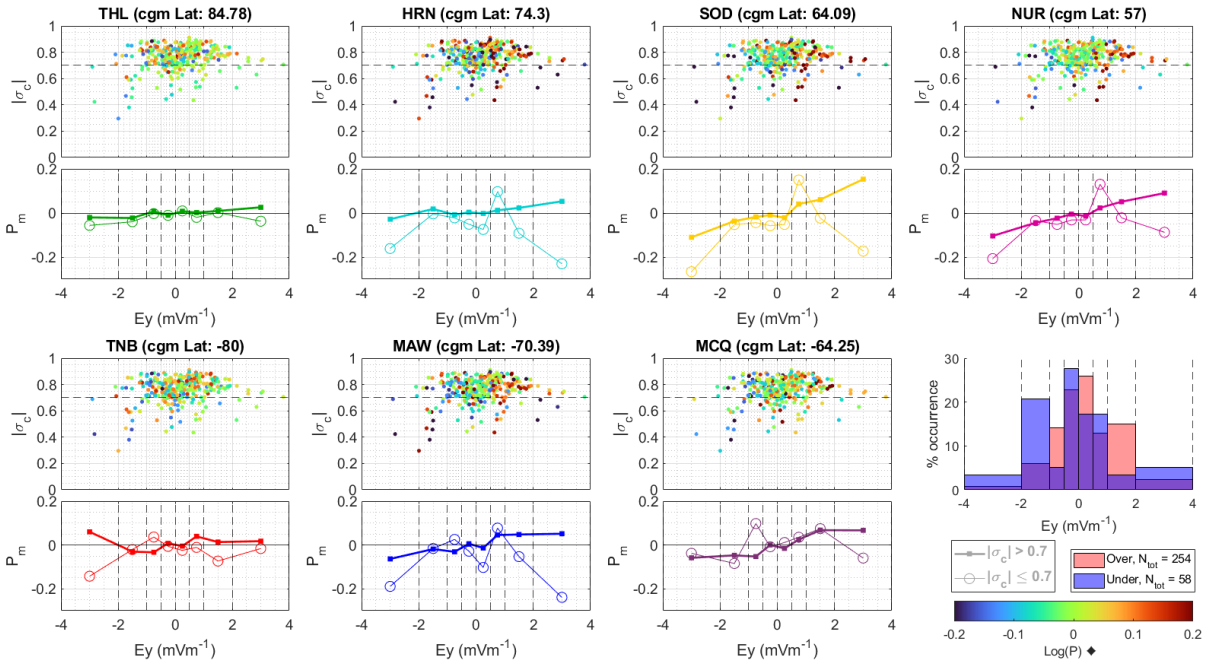

Figure 6.3: January event. First and third rows: scatter plots of the rescaled geomagnetic power at different geomagnetic observatories in terms of Ey in the GSM reference frame and the normalized cross-helicity. The horizontal black dashed line refers to $|\sigma_c| = 0.7$. Under each scatterplot, the average power is calculated for each bin of Ey values, distinguishing between the more Alfvénic cases (thick line and solid points) from the less Alfvénic ones (thin line and empty circles). The first two rows refer to the northern hemisphere, the second two rows refer to the southern hemisphere. The bottom-right panel shows the percentage occurrence of points falling into each bin both above and below threshold conditions of $|\sigma_c| = 0.7$. More details in the text.

Figure 6.3 shows, for each observatory, the scatterplot of the rescaled geomagnetic power (Log(P) ♦) in terms of the geoeffective component of the interplanetary electric field $E_y = v_x B_z$, in the GSM reference frame, and the

absolute value of the normalized cross-helicity σ_c. The horizontal dashed black line refers to $|\sigma_c| = 0.7$, which is a threshold set to discriminate between two different populations of the distribution: the one with high Alfvénicity ($|\sigma_c| > 0.7$) and the one with low Alfvénicity ($|\sigma_c| \leq 0.7$). The distribution of points in the Ey-σ_c plane is the same for each observatory and depends solely on quantities external to the magnetosphere and on the characteristics of the corotating stream; what varies for each observatory is the ground-based power (color of the points). Under each scatterplot, there is a panel where the abscissa refers to Ey values binned in a non-equidistant manner, with narrower bins around zero and wider bins as one moves away from zero; this is because Ey is a highly fluctuating quantity around zero, where most of the values cluster. On the y-axis is reported the average ground power (Pm) falling within each bin for two distinct groups: the lines marked with solid dots refer to points corresponding to σ_c values above 0.7, while the thin line with empty circles refers to those corresponding to σ_c values below 0.7. The bottom-right panel shows a bar plot of the percentage occurrence of points falling into each bin, both above (pink) and below (purple) the σ_c threshold. The number of points falling into the two main populations is also displayed, in this case, there are 254 points corresponding to high values of σ_c and 58 points corresponding to low values of σ_c. Understanding how densely populated each bin is gives us an idea of the significance of the mean computed for each bin. The two stations in the polar cap, THL and TNB, exhibit a rather flat trend of power with respect to Ey, especially THL, which is at a higher latitude. However, moving from auroral to sub-auroral latitudes, there is an increase in average power at positive Ey values for the more Alfvénic population, where the average power remains generally slightly higher compared to the average power corresponding to the less Alfvénic population.

The average power associated with the less Alfvénic population appears to be more variable, exhibiting a sort of double peak, with one peak particularly pronounced for observatories in the northern hemisphere (excluding the one in the polar cap) around the Ey bin between 0.5 and 1 mVm^{-1}.
To provide an overview of the average power profiles for the two distinct populations, Figure 6.4, shows the average power for each bin associated with $\sigma_c > 0.7$ in the left column, for all observatories, and in the right column for $\sigma_c \leq 0.7$, for all observatories. In this figure, are shown values for which at least 3 points contributed to the average calculation since fewer points correspond to greater statistical uncertainty. It is interesting to note that in the case of $\sigma_c > 0.7$, the power at different latitudes exhibits similar behavior, with a tendency to increase for positive Ey values, i.e. in correspondence to a dawn-dusk electric field, in open magnetospheric conditions. In addition, the geomagnetic power increase is generally higher at the lowest latitudes, corresponding to the sub-auroral region, resulting in the highest power levels for the highest positive Ey values at NUR, SOD, and MCQ. In the case of $\sigma_c \leq 0.7$, the average power

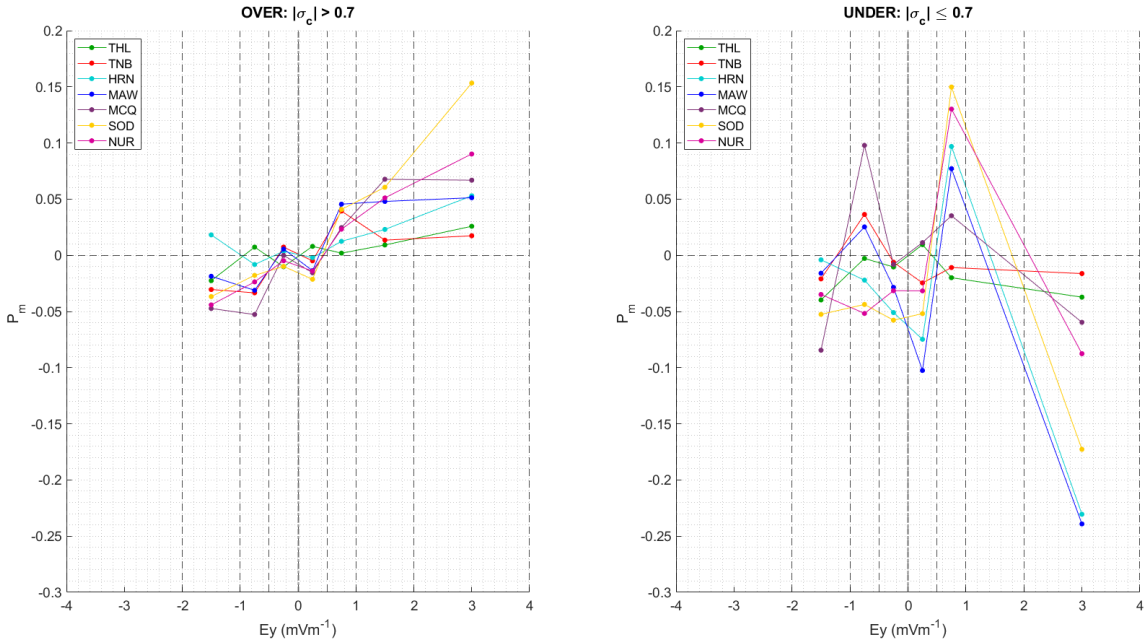

Figure 6.4: January event. Average of the rescaled power falling into each Ey bin, for all selected observatories (different colors): on the left for the more Alfvénic population of the SW, and on the right for the less Alfvénic population of the SW. The legend lists the observatories in descending order based on the absolute value of their magnetic latitude.

exhibits more variable trends, probably due to the lower number of points involved in the statistics. Nonetheless, for auroral and sub-auroral latitudes, the average power shows a peak corresponding to the Ey bin ranging from 0.5 to 1 mVm^{-1}, with a more pronounced peak for the stations at lower latitudes (SOD and NUR).

6.1.3 Joint analysis with parallel and perpendicular power

In the literature, there is the hypothesis that fluctuations in the solar wind, present in the high-speed streams, directly drive ULF power in the magnetosphere [43]. As adopted by Kessel et al. [55], one way to analyze compressive and Alfvénic fluctuations in the solar wind is to study parallel (compressional) and perpendicular (transverse) power. Kessel et al. [55] found that Alfvénic fluctuations maintain similar characteristics when crossing the bow shock, and upon crossing the shock, their power increases by slightly less than a factor of 10. Based on this information, a further approach was to compare the power of fluctuations present in the solar wind with the geomagnetic power observed on the ground, scaled to the background level (CQB) as shown earlier. Specifically for solar wind data, I rotated the velocity and magnetic field components from the HEE reference frame (top row of Figure 6.5) to the MEMFA reference

frame (second row of Figure 6.5), following the procedure described in chapter 4. As specified in chapter 4, I choose a 6 hours time window for the rotation procedure, wide enough to include all Alfvénic fluctuations therein, but, at the same time, short enough to follow the variability of the typical ambient field in a corotating stream. By doing so, the direction of the main ambient magnetic field has been identified. This was done to distinguish two main directions: one aligned with the main magnetic field where isotropic perturbations of compressive nature will be present, and the other perpendicular to the main magnetic field where Alfvénic fluctuations will be present, as described in section 1.4.

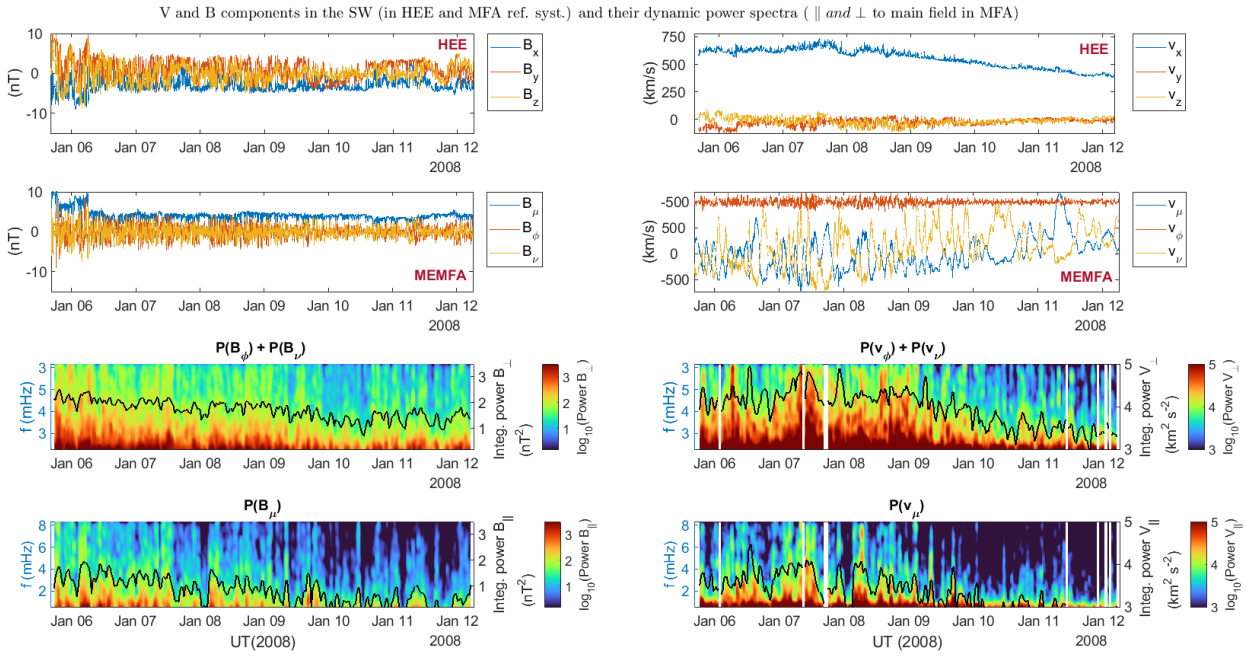

Figure 6.5: January event. First row: magnetic (left) and velocity (right) components in the HEE reference frame. Second row: magnetic (left) and velocity (right) components in the MEMFA reference frame. Third row: dynamic spectrum of the two magnetic (left) and velocity (right) components orthogonal to the main field direction. Fourth row: dynamic spectrum of the magnetic (left) and velocity (right) components aligned to the main field direction. The black overlaid curve on each dynamic spectrum is the corresponding integrated power in the Pc5 range.

The two panels at the bottom left of Figure 6.5 show, respectively, the dynamic spectra associated with the two magnetic field components in the plane orthogonal to the main field direction ($P(B_\phi) + P(B_\nu)$) and the dynamic spectrum associated with the magnetic component aligned with the main field direction ($P(B_\mu)$). The black curve corresponds to the integrated power in the Pc5 frequency range. It can be noticed that the power in this frequency range is greater in the plane orthogonal to the field, with respect to the one in the field-aligned direction. Similarly, the two panels at the bottom on the right show,

respectively, the dynamic spectra associated with the two velocity components in the plane orthogonal to the main field ($P(V_\phi) + P(V_\nu)$) and the dynamic spectrum associated with the velocity component aligned with the main field ($P(V_\mu)$). In this case, as well, the power is greater in the direction orthogonal to the main magnetic field, especially in the HSS region, corresponding to the high-velocity plateau, where the most Alfvénic fluctuations are observed.

To compare the powers in the SW with those on the ground at various latitudes, I defined the total power in the direction aligned with the main magnetic field ${P_{||}}^{SW}$, and the total power in the plane perpendicular to it ${P_{\perp}}^{SW}$, as specified in equations 6.1 and 6.2. This can be done by summing the velocity power with the magnetic one, suitably scaled to have quantities that are dimensionally homogeneous and comparable (for more details see A):

$$ {P_{\perp}}^{SW} = P(V_{\perp}) + P(B_{\perp}\ scaled\ to\ V) \tag{6.1} $$

$$ {P_{||}}^{SW} = P(V_{||}) + P(B_{||}\ scaled\ to\ V) \tag{6.2} $$

Figure 6.6 shows in yellow the total SW power (log) obtained from the sum of the logarithm of the velocity power (in blue) and the one of the magnetic power (in red, properly scaled to V) in the plane orthogonal to the main magnetic field (top panel) and in the direction aligned to the main magnetic field (bottom panel). The integrated total power, as argument of logarithm, has dimensions of km^2/s^2. Below, I will improperly refer to the two quantities plotted in yellow in Figure 6.6 as *orthogonal power* and *aligned* or *parallel power*, aware that they refer to both velocity and magnetic field, and that the direction they refer to is associated with the fields and not the power, which is a scalar.

Once the SW powers associated with the two directions of interest (aligned to the main magnetic field and orthogonal to it) were calculated, I proceeded to perform a correlation analysis between these two powers and the geomagnetic power measured on the ground at various latitudes, appropriately scaled to the CQB. I then removed their own 12-hour moving average to compensate for any possible residual diurnal effects. I calculated the correlation coefficient separately for the HSS region and the RR region. This is because the linear correlation coefficient is greatly affected by long-term variability, and in a corotating stream, the trend is different in these two regions (mainly due to the significant variation in the velocity profile).

Figure 6.7 shows in each panel the logarithm of the SW power related to the direction perpendicular (in blue) to the main field, the logarithm of the SW power related to the direction aligned (in green) with the main field, and the logarithm of the ground power (in red). The vertical pink line denotes the separation between HSS and RR, corresponding to the SW velocity knee. Each panel also includes the correlation coefficient between the solar wind power and the ground power measured at the observatory specified in the panel's title:

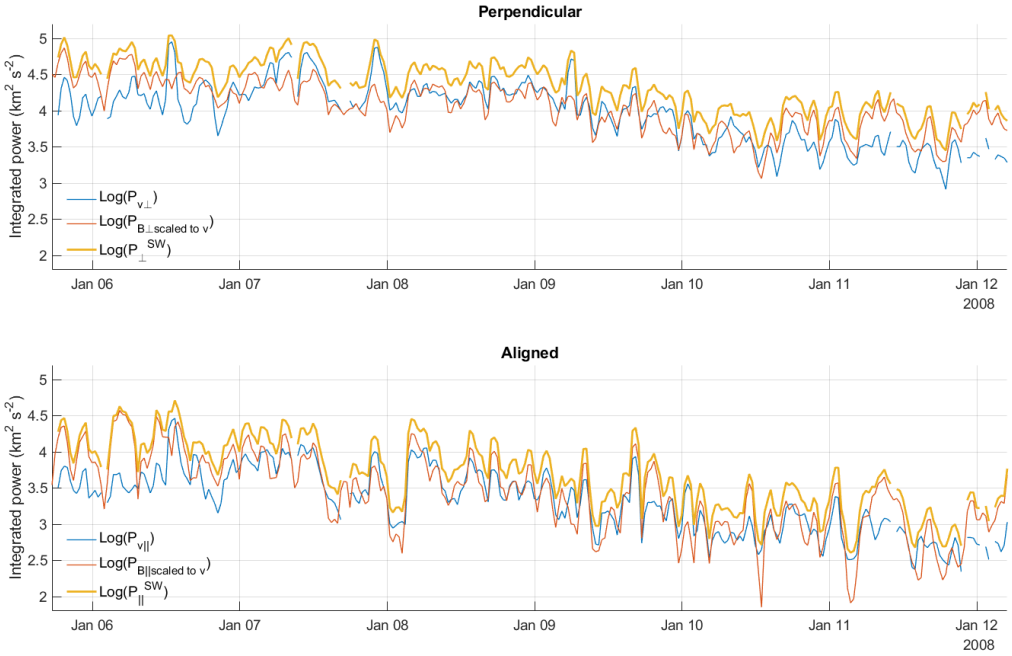

Figure 6.6: January event. Top panel: in blue is the logarithm of the integrated power of velocity in the orthogonal direction to the main field, in red is the logarithm of the integrated power of the magnetic field in the orthogonal direction to the main field, rescaled to velocity power dimensions, and in yellow is their sum, the total SW power related to the orthogonal direction to the main magnetic field. Bottom panel: in blue is the logarithm of the integrated power of velocity in the direction aligned to the main field, in red is the logarithm of the integrated power of the magnetic field in the direction aligned to the main field, rescaled to velocity power dimensions, and in yellow is their sum, the total SW power related to the direction aligned to the main magnetic field.

in blue for the correlation $r_{p\perp}$ between ground power and perpendicular SW power, in green for the correlation $r_{p||}$ between ground power and aligned SW power. For instance, for the HRN observatory at 74.3° magnetic latitude, the correlation coefficient between Log($P_\perp{}^{SW}$) and Log(P$_{HRN}$)♦$|_{dm}$ in the HSS region is $r_{\perp HSS} = 0.3$, and a practically null correlation coefficient, $r_{\perp RR} = -0.01$, between the same quantities in the RR. In general, especially in the HSS region, the correlation coefficient associated with the power of the components perpendicular to the main magnetic field is greater than the correlation coefficient associated with the power of the aligned components.
To observe how these coefficients vary with latitude in both hemispheres, I plotted, separately for the two regions HSS and RR, the correlation coefficients as a function of the absolute value of the magnetic latitude, as shown in Figure 6.8. Here, the correlation coefficient between the ground power and the SW power in the orthogonal plane is shown in blue, on the left panel for the HSS region and on the right panel for the RR; on the other hand, the correlation coefficient

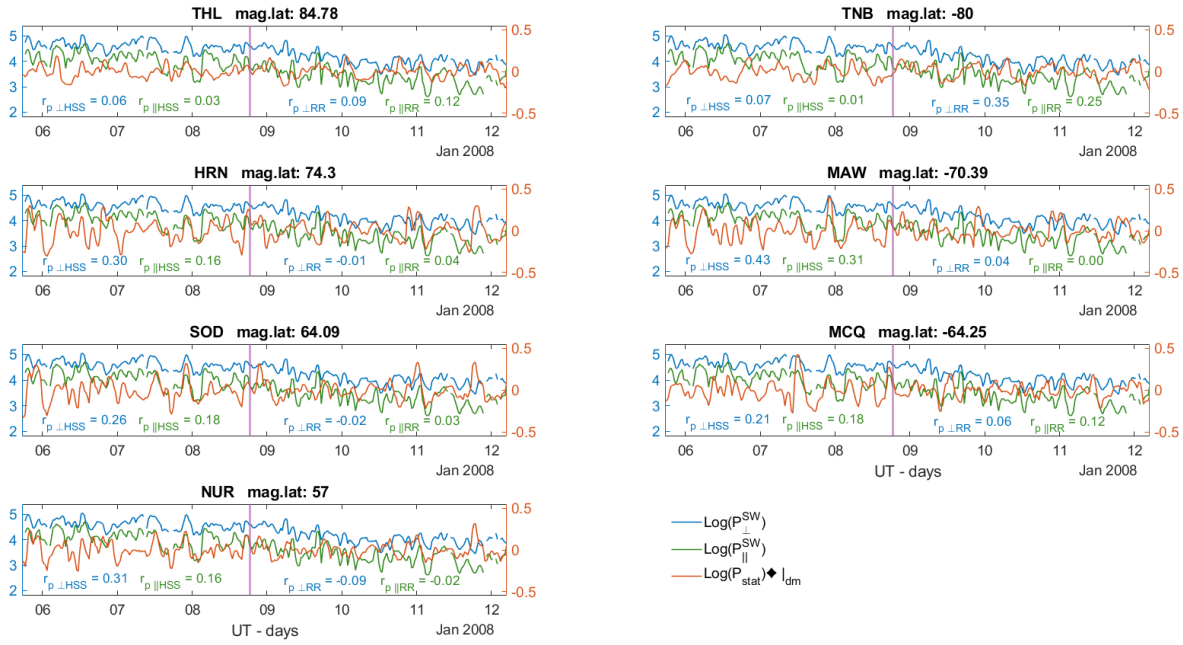

Figure 6.7: January event. In each panel, in blue the logarithm of the velocity and magnetic power in the orthogonal plane to the main field; in green the logarithm of the velocity and magnetic power in the direction aligned to the main field; in red the logarithm of the geomagnetic power rescaled to CQB, excluding a 12-hour moving average, for the observatory/geomagnetic latitude specified on the panel's title. The vertical pink line separates the HSS region from the RR. In the two regions (HSS and RR), the correlation coefficients between the ground powers and those in the two solar wind directions are also specified.

between the ground power and the SW power in the aligned direction is shown in green. Both panels have two dashed lines indicating the 95% significance level. Despite the correlation coefficients are not high, from this figure can be observed a peak in the correlation coefficient at auroral latitudes in the HSS region, for both directions of interest, while a peak (single significant value) is observed at the near cusp latitude in the RR.
From the linear correlation analysis, which does not distinguish in the frequency domain, in the next section I moved to a more detailed analysis, both in frequency and time domain, specifically a wavelet coherence analysis between the profiles of the logarithm of the SW power (perpendicular and parallel) and the profiles of the logarithm of the ground power.

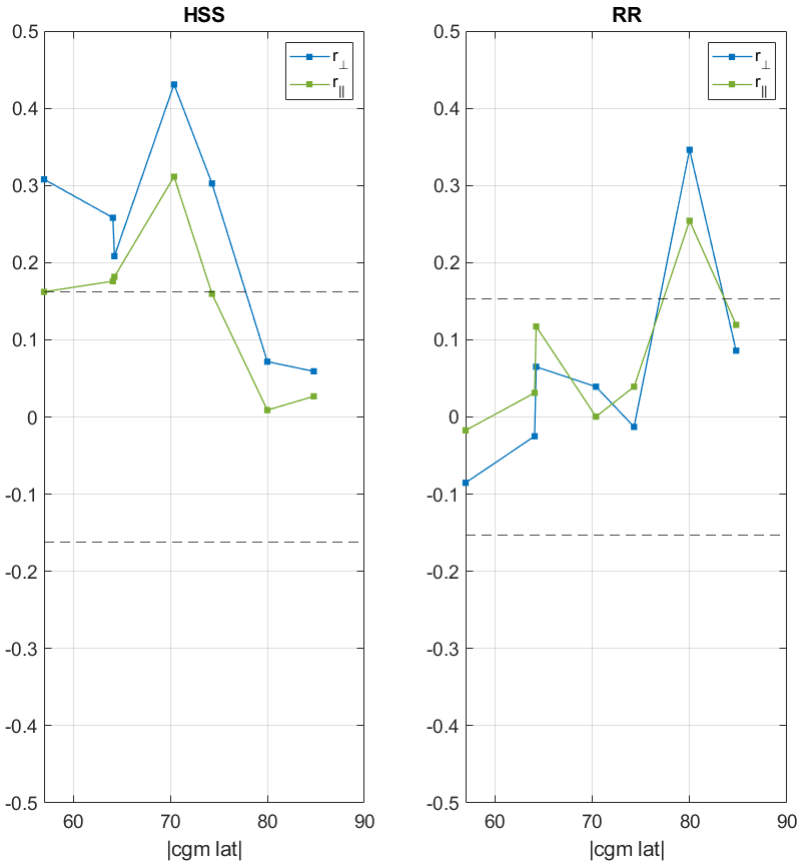

Figure 6.8: January event. The correlation coefficient (r) vs. the CGM latitude; in blu is r computed between the logarithm of the geomagnetic power rescaled to CQB (and without a 12h moving average) and the logarithm of the SW total power related to the plane orthogonal to the main field, in green is r computed between the logarithm of the geomagnetic power rescaled to CQB (and without a 12h moving average) and the logarithm of the SW total power related to the direction aligned to the main field. The left panel refers to HSS, and the right panel refers to RR. The horizontal dashed black lines represent the significance level at 95 % (which is ± 0.16 for the HSS data and ± 0.15 for the RR data)

.

6.1.4 Wavelet coherence analysis

Coherence analysis is a statistical method used to measure the degree of correlation between two signals in the frequency domain. It quantifies the extent to which the phase and amplitude of one signal correspond to those of another signal across different frequencies. The coherence function is defined as:

$$\gamma^2{}_{xy}(f) = \frac{|S_{xy}(f)|^2}{S_{xx}(f)S_{yy}(f)} \qquad 0 \leq \gamma^2{}_{xy}(f) \leq 1 \tag{6.3}$$

where $S_{xy}(f)$ is the cross-spectral density of the two generic signals $x(t)$ and $y(t)$; $S_{xx}(f)$ and $S_{yy}(f)$ are the power spectral density functions of $x(t)$ and $y(t)$, respectively. It is possible to use the wavelet transform instead of the common Fourier transform to calculate the cross-spectral density function. The wavelet is a wave-like oscillation with an amplitude modulation and is localized in time. In this work the continuous complex wavelet (Morlet) has been utilized. Wavelet transform offers advantages over Fourier transform, especially when dealing with non-stationary signals or signals with localized features in the time-frequency domain. Using wavelet as a spectral technique for calculating cross-spectral density, we refer to it as wavelet coherence. Wavelet coherence involves decomposing each time series into wavelet components at different scales or frequencies, and then computing the cross-wavelet spectrum to measure the similarity in their time-frequency representations. Wavelet coherence is therefore a method for evaluating the correlation at each scale (or frequency) between two signals in the time-frequency domain. This approach is suitable for analyzing nonstationary relationships in time series data, because it offers an advantage over traditional correlation and cross-spectrum techniques: it provides more detailed and comprehensive information about the relationship between signals, considering both their temporal and spectral structure. There is a correspondence between wavelet scales and frequency (or period): a smaller scale corresponds to a compressed wavelet, which is high in frequency (lower in period), while larger scales correspond to a stretched wavelet, representing lower frequency (higher period).

In this case, in equation 6.3, $x(t)$ will be represented by the logarithm of the power in the solar wind (referred separately to the direction orthogonal or parallel to the main field), and $y(t)$ will be represented by the logarithm of the ground power, as defined previously. In addition, the phase of the cross-spectrum values can be utilized to identify the relative time delay (lag) between the input signals:

$$\delta T = \frac{\delta\theta}{2\pi f}$$

where θ is the phase angle of the complex spectrum.

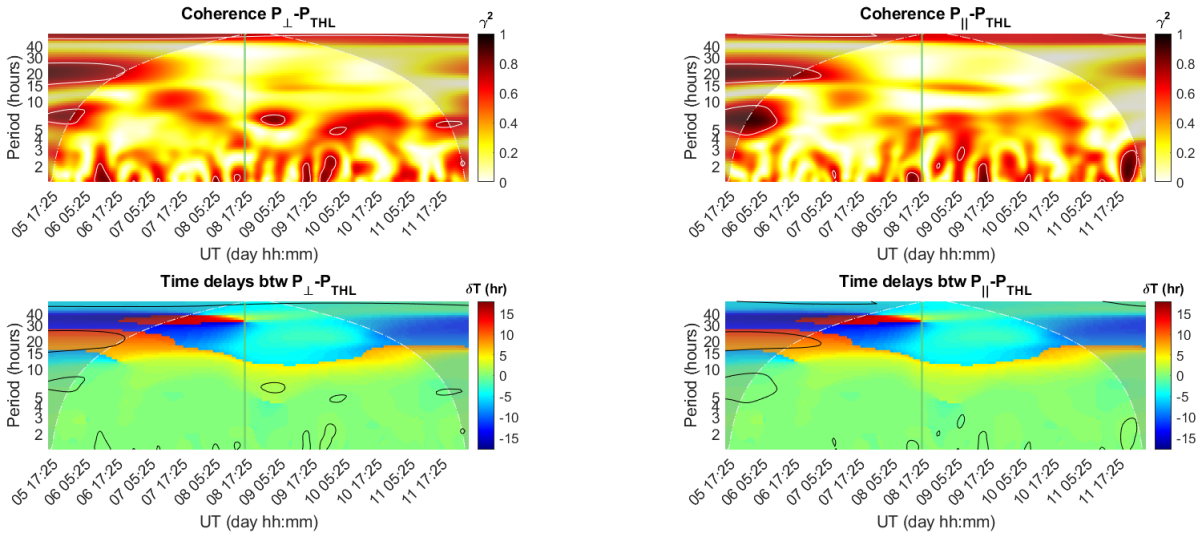

Figure 6.9: January event. Wavelet coherence between $\mathrm{Log}(P_{\perp}{}^{SW})$ and $\mathrm{Log}(P_{THL})\blacklozenge|_{dm}$ in the left and $\mathrm{Log}(P_{||}{}^{SW})$ and $\mathrm{Log}(P_{THL})\blacklozenge|_{dm}$ on the right. The x-axis represents time while the y-axis represents period (or scales) in hours. In the first row, the color coding indicates coherence, with lighter and darker colors representing low and high coherence, respectively. The regions enclosed by a white contour shape represent the coherence peaks found for $\gamma^2 \geq 0.7$. In the second row, the color coding indicates the time delay, in hours, between the two signals. The regions enclosed by a black contour shape are those of the coherence peaks identified in the coherence plot above. The shaded region in all panels is the one external to the cone of influence. The green vertical line corresponds to the velocity knee location, separating HSS from RR.

Figures from 6.9 to 6.15 show the wavelet coherograms obtained for the 7 different magnetic observatories (from THL to NUR). Each of them has, on the left column, the coherogram referring to $\mathrm{Log}(P_{\perp}{}^{SW})$ and $Log(P_{Station})\blacklozenge|_{dm}$, and on the right column, the coherogram referring to $\mathrm{Log}(P_{||}{}^{SW})$ and $Log(P_{Station})\blacklozenge|_{dm}$. The x-axis represents time, the y-axis represents period (or scales) in hours and the color coding indicates coherence, ranging from 0 or white (no coherence) to 1 or dark red (maximum coherence). In the coherograms, the regions enclosed by a white contour shape represent the coherence peaks found for $\gamma^2 \geq 0.7$, which can be considered a threshold for a high level of coherence between the two input signals. On the second row of each figure, the x and y axes are the same, while the color scale represents the phase difference, expressed in terms of time delay. The regions enclosed by a black contour shape are the same as the white contour shape identified in white, for the coherence peaks, on the coherogram above. The shaded region in both coherograms and time-delay panels is the one external to the cone of influence, and shows areas in the coherograms potentially affected by edge-effect artifacts: within the unshaded region, the information provided by the scalogram is an accurate time-frequency representation of the

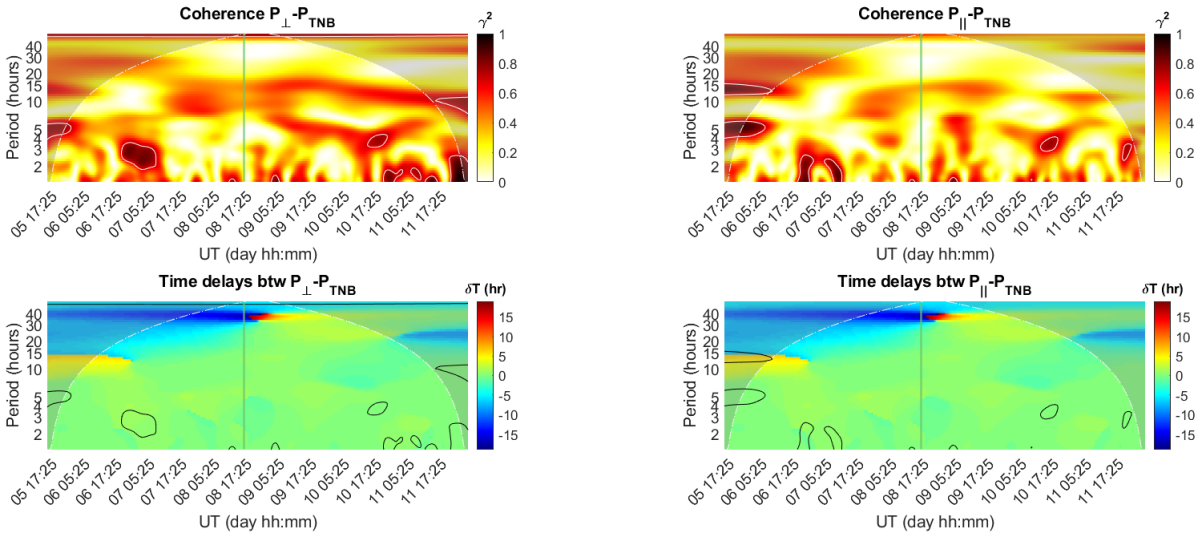

Figure 6.10: January event. Wavelet coherence between Log($P_{\perp}{}^{SW}$) and $Log(P_{TNB})\blacklozenge|_{dm}$ in the left and Log($P_{||}{}^{SW}$) and $Log(P_{TNB})\blacklozenge|_{dm}$ on the right. The x-axis represents time while the y-axis represents period (or scales) in hours. In the first row, the color coding indicates coherence, with lighter and darker colors representing low and high coherence, respectively. The regions enclosed by a white contour shape represent the coherence peaks found for $\gamma^2 \geq 0.7$. In the second row, the color coding indicates the time delay, in hours, between the two signals. The regions enclosed by a black contour shape those of the coherence peaks identified in the coherence plot above. The shaded region in all panels is the one external to the cone of influence. The green vertical line corresponds to the velocity knee location, separating HSS from RR.

data. These figures show that there are intervals of high coherence between the SW powers (orthogonal/parallel) and the ground power, in correspondence of timescales of a few hours, indicating a coherent fluctuation between the powers compared on scales of a few hours. This suggests that solar wind power fluctuations are efficiently transmitted to Earth in high-latitude regions.

An enlarged detail corresponding to a coherence peak identified at HRN between Log($P_{\perp}{}^{SW}$) and $Log(P_{HRN})$ is shown on the left of Figure 6.16 (the right column shows the same time and frequency interval for Log($P_{||}{}^{SW}$)). The third row displays the two signals filtered in the selected time and frequency interval, and the last panel also shows the corresponding σ_c values. It can be noticed the close correspondence between the two powers, indicating that this type of analysis effectively highlights the coherence between the two signals.

After the coherence peaks were identified for each latitude (i.e., the regions identified by the white curves in the coherograms), I checked the corresponding time-delay values. Since the response between an external and internal signal typically does not exceed one hour, I selected as actual coherence peaks those with a maximum delay of 1.5 hours. Once this was done, I plotted each co-

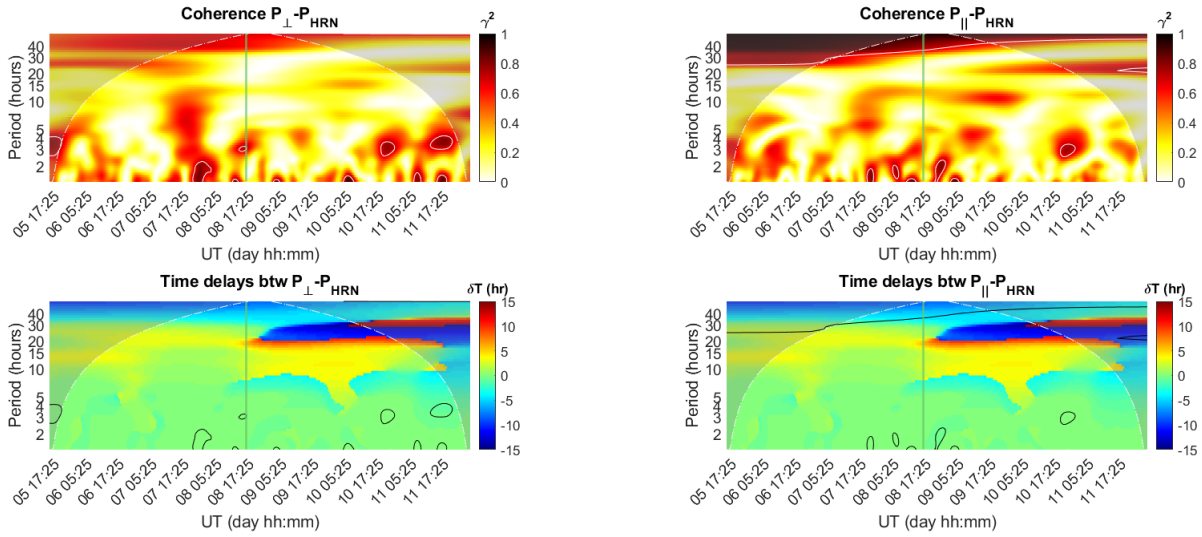

Figure 6.11: January event. Wavelet coherence between Log($P_{\perp}{}^{SW}$) and $Log(P_{HRN})\blacklozenge|_{dm}$ in the left and Log($P_{||}{}^{SW}$) and $Log(P_{HRN})\blacklozenge|_{dm}$ on the right. The x-axis represents time while the y-axis represents period (or scales) in hours. In the first row, the color coding indicates coherence, with lighter and darker colors representing low and high coherence, respectively. The regions enclosed by a white contour shape represent the coherence peaks found for $\gamma^2 \geq 0.7$. In the second row, the color coding indicates the time delay, in hours, between the two signals. The regions enclosed by a black contour shape those of the coherence peaks identified in the coherence plot above. The shaded region in all panels is the one external to the cone of influence. The green vertical line corresponds to the velocity knee location, separating HSS from RR.

herence peak identified on a polar plot, as a function of MLT, as shown in the circular plots in Figure 6.17 (midnight MLT on the right, noon MLT on the left). Here each circular graph shows the coherence peaks related to the magnetic observatory in the northern or southern hemisphere, associated with either the parallel or orthogonal direction in the SW (as specified in each subtitle). The color code in the top row corresponds to the average ground power at the identified coherence peak. The color code in the bottom row corresponds to the average value of σ_c at the identified coherence peak. The two bar plots on the right show the average temporal coverage percentage for each latitude or observatory (on the x-axis) associated with the two main directions in the solar wind: perpendicular (top) and parallel (bottom) to the main magnetic field. As a first observation from Figure 6.17, it can be noticed that the percentage of coherence times is higher in the case of the direction perpendicular to the main field, with a slight prevalence around 70° latitude. Regarding the average power, it varies across latitudes and magnetic sectors, without showing a particular pattern between the two hemispheres and the two main directions in the solar wind. The average values of σ_c identified at the selected coherence peaks

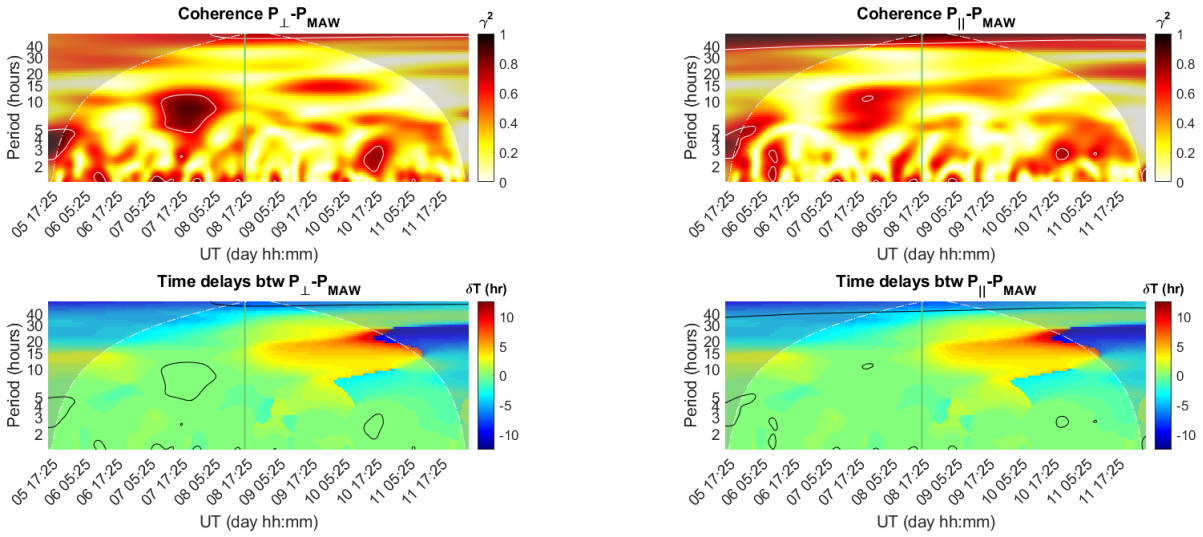

Figure 6.12: January event. Wavelet coherence between Log($P_{\perp}{}^{SW}$) and $Log(P_{MAW})\blacklozenge|_{dm}$ in the left and Log($P_{||}{}^{SW}$) and $Log(P_{MAW})\blacklozenge|_{dm}$ on the right. The x-axis represents time while the y-axis represents period (or scales) in hours. In the first row, the color coding indicates coherence, with lighter and darker colors representing low and high coherence, respectively. The regions enclosed by a white contour shape represent the coherence peaks found for $\gamma^2 \geq 0.7$. In the second row, the color coding indicates the time delay, in hours, between the two signals. The regions enclosed by a black contour shape those of the coherence peaks identified in the coherence plot above. The shaded region in all panels is the one external to the cone of influence. The green vertical line corresponds to the velocity knee location, separating HSS from RR.

are generally high, which is due to the high Alfvénicity characterizing the entire stream. However, each arc in the figure corresponds to a high coherence value (above 0.7) between the power in the solar wind and the power on the ground, both for the perpendicular and parallel directions to the main magnetic field. This confirms the results obtained by Kessel et al. 2004, stating that "Both the total parallel and perpendicular Pc5 power in the solar wind correlate well with the total Pc5 power of the ground-based H-component magnetic field." In the same manner, our results from wavelet analysis could be formulated as follows: fluctuating SW powers are efficiently transmitted to high-latitude regions.

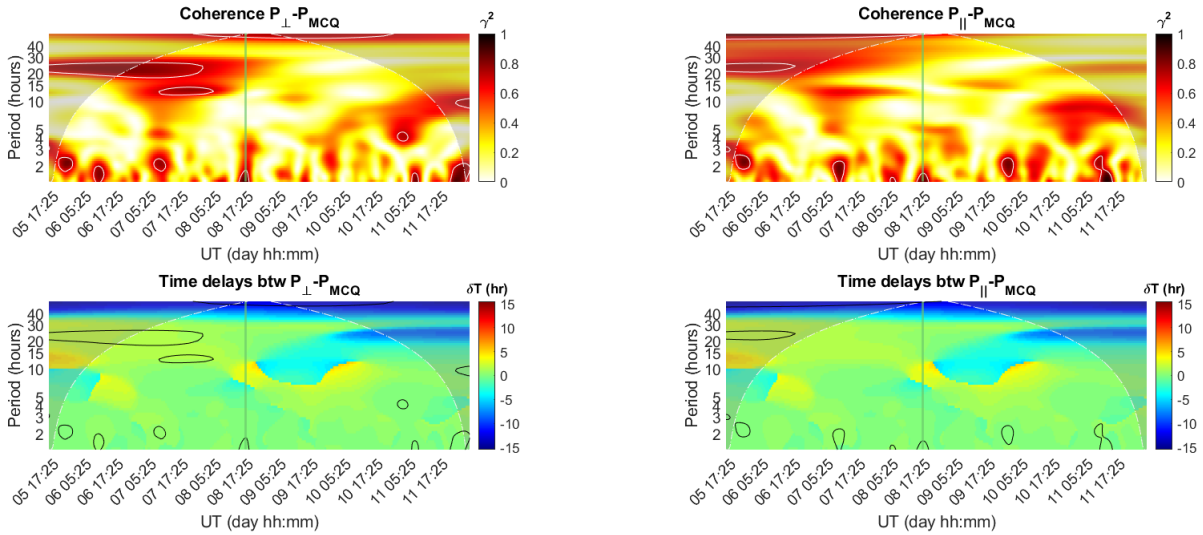

Figure 6.13: January event. Wavelet coherence between Log($P_{\perp}{}^{SW}$) and $Log(P_{MCQ})\blacklozenge|_{dm}$ in the left and Log($P_{||}{}^{SW}$) and $Log(P_{MCQ})\blacklozenge|_{dm}$ on the right. The x-axis represents time while the y-axis represents period (or scales) in hours. In the first row, the color coding indicates coherence, with lighter and darker colors representing low and high coherence, respectively. The regions enclosed by a white contour shape represent the coherence peaks found for $\gamma^2 \geq 0.7$. In the second row, the color coding indicates the time delay, in hours, between the two signals. The regions enclosed by a black contour shape those of the coherence peaks identified in the coherence plot above. The shaded region in all panels is the one external to the cone of influence. The green vertical line corresponds to the velocity knee location, separating HSS from RR.

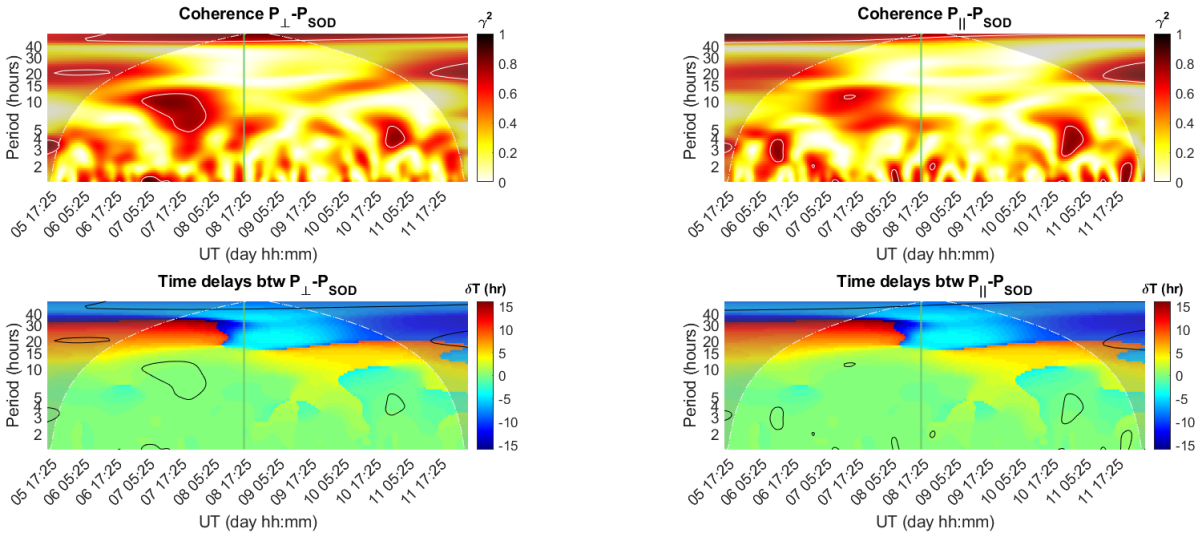

Figure 6.14: January event. Wavelet coherence between Log($P_{\perp}{}^{SW}$) and $Log(P_{SOD})\blacklozenge|_{dm}$ in the left and Log($P_{||}{}^{SW}$) and $Log(P_{SOD})\blacklozenge|_{dm}$ on the right. The x-axis represents time while the y-axis represents period (or scales) in hours. In the first row, the color coding indicates coherence, with lighter and darker colors representing low and high coherence, respectively. The regions enclosed by a white contour shape represent the coherence peaks found for $\gamma^2 \geq 0.7$. In the second row, the color coding indicates the time delay, in hours, between the two signals. The regions enclosed by a black contour shape those of the coherence peaks identified in the coherence plot above. The shaded region in all panels is the one external to the cone of influence. The green vertical line corresponds to the velocity knee location, separating HSS from RR.

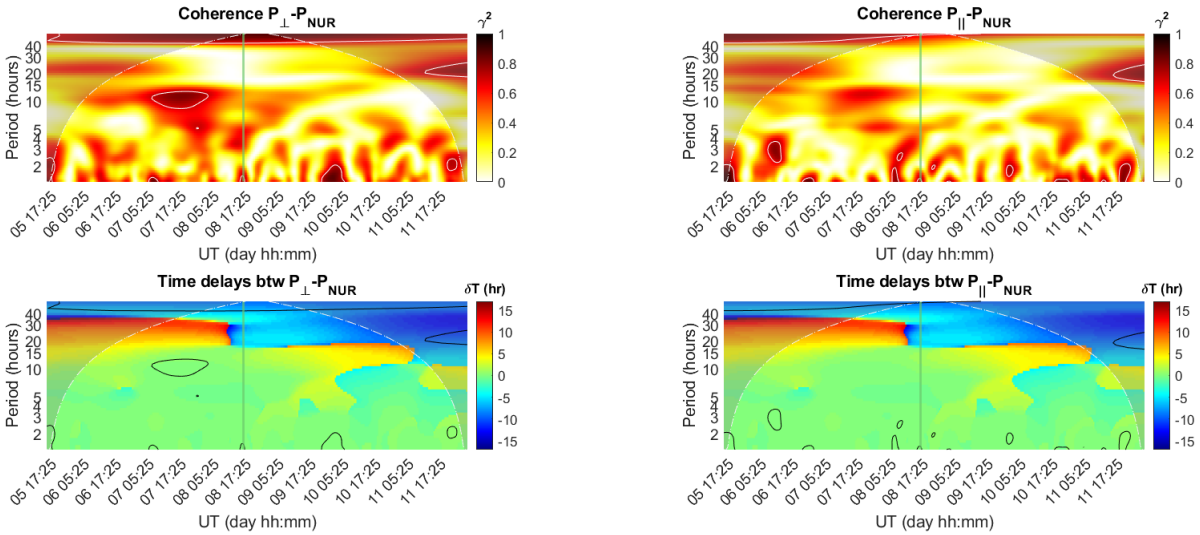

Figure 6.15: January event. Wavelet coherence between Log($P_{\perp}{}^{SW}$) and $Log(P_{NUR})\blacklozenge|_{dm}$ in the left and Log($P_{||}{}^{SW}$) and $Log(P_{NUR})\blacklozenge|_{dm}$ on the right. The x-axis represents time while the y-axis represents period (or scales) in hours. In the first row, the color coding indicates coherence, with lighter and darker colors representing low and high coherence, respectively. The regions enclosed by a white contour shape represent the coherence peaks found for $\gamma^2 \geq 0.7$. In the second row, the color coding indicates the time delay, in hours, between the two signals. The regions enclosed by a black contour shape those of the coherence peaks identified in the coherence plot above. The shaded region in all panels is the one external to the cone of influence. The green vertical line corresponds to the velocity knee location, separating HSS from RR.

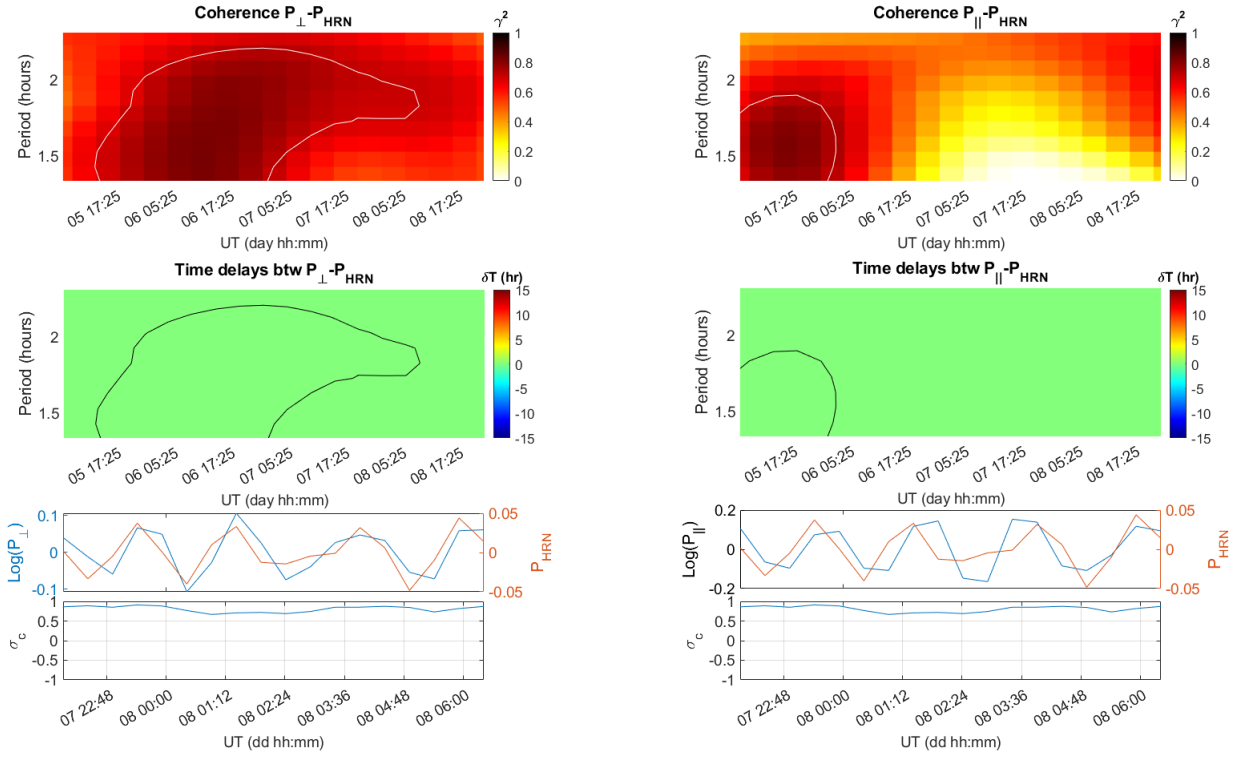

Figure 6.16: An enlargement of figure 6.11 in correspondence of a coherence peak (a time-period region characterized by high coherence) for the orthogonal direction. The third row shows the signals filtered in the time and frequency domains, from which the coherence shown above was calculated. The bottom panels show the σ_c corresponding to the same time interval.

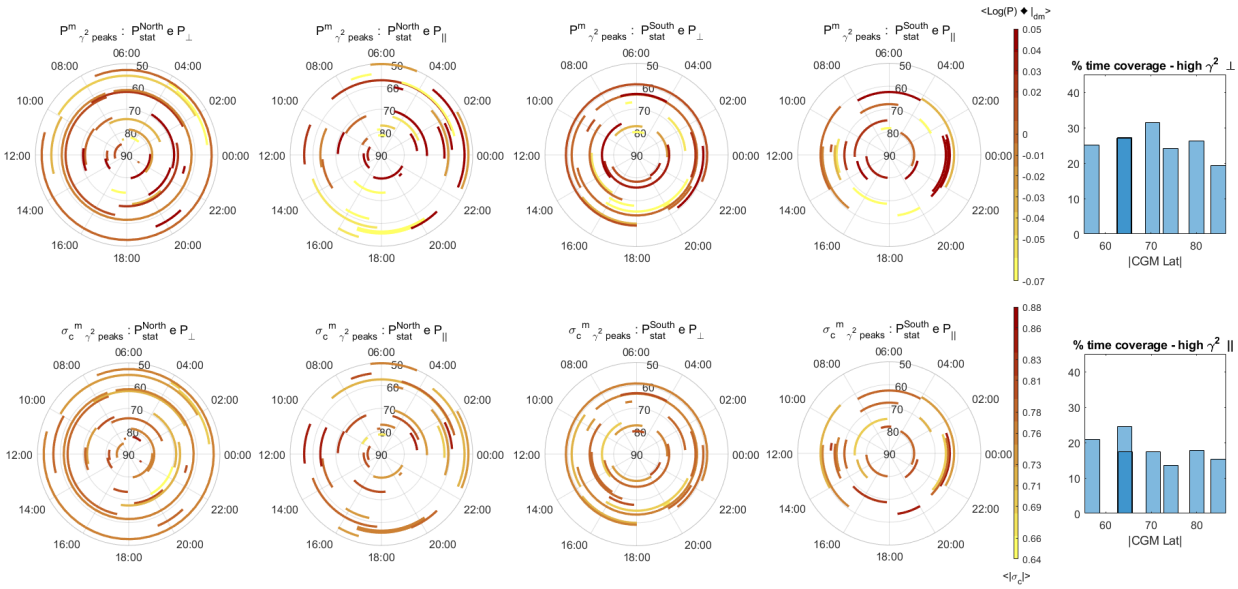

Figure 6.17: January event. Polar plot of the coherence peaks in terms of MLT. The color code in the top row corresponds to the average ground power at the identified coherence peak. The color code in the bottom row corresponds to the average value of σ_c at the identified coherence peak. The first column refers to observatories in the northern hemisphere and SW power related to the orthogonal plane to the main field. The second column refers to observatories in the northern hemisphere and SW power related to the parallel direction to the main field. The third column refers to observatories in the southern hemisphere and SW power related to the orthogonal plane to the main field. The fourth column refers to observatories in the southern hemisphere and SW power related to the parallel direction to the main field. The fifth column shows the bar plots of the average temporal coverage percentage for each latitude or observatory (on the x-axis) associated with the two main directions in the solar wind: perpendicular (top) and parallel (bottom) to the main magnetic field.

6.2 10-19 February 2008

6.2.1 Characterization

A second corotating stream selected is the one spanning from February 10th to February 19th. For this event, as for those that followed, I repeated the analysis procedure performed for the January event. Also in this case, there is the typical structure of the HSS and RR of the corotating stream.

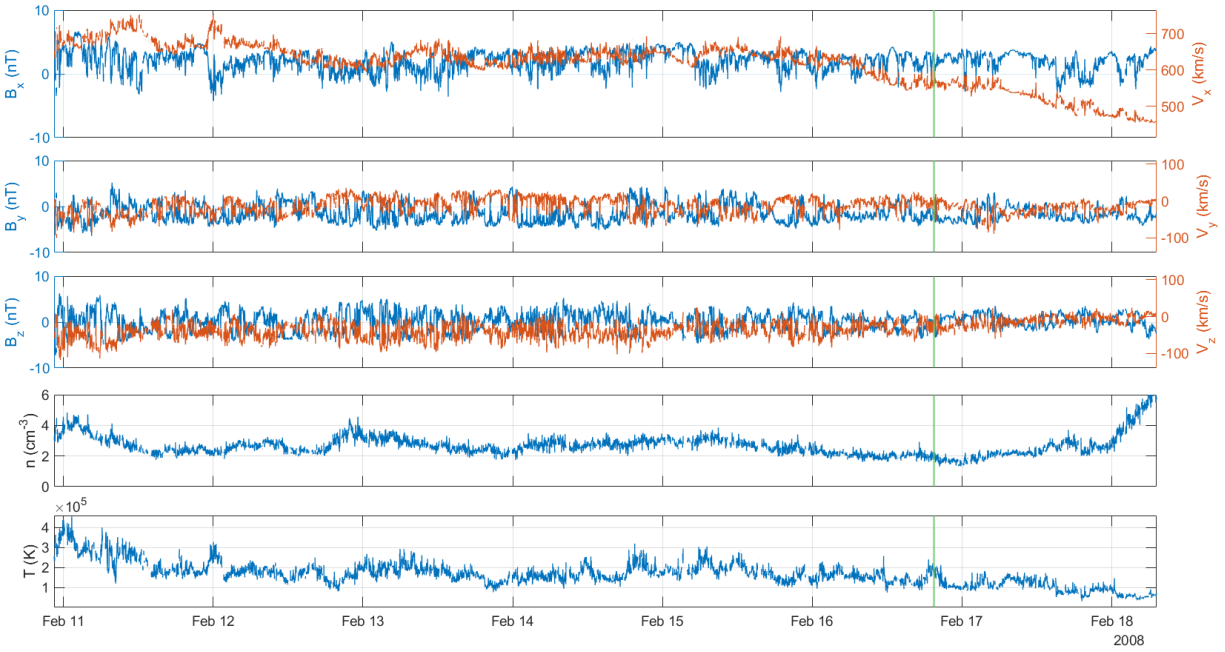

Figure 6.18: February event. From top to bottom, the first three panels: velocity components V_x, V_y, V_z (in red) and magnetic field components B_x, B_y, B_z (in blue) in the HEE reference frame. Fourth panel: the proton number density. Fifth panel: the proton temperature. The vertical green line identifies the separation between HSS and RR of the corotating stream.

Looking at Figure 6.19, it can be noticed that also in this case there are Alfvénic fluctuations throughout the stream, especially in the HSS region, where on the ground a wide variability of the AE index is observed. It falls within the category of modest substorms, throughout the entire HSS region. Here, the SYM-H index is highly variable, although the range of variability (orders of magnitude) is comparable to the previous case. Its profile is initially characterized by a slow rise, followed by a rapid decrease, then a rapid rise again, and finally a profile similar to that of a weak storm. Looking at the last two panels in the figure, it can be noticed that this stream is also characterized by high Alfvénicity in the HSS, which then decreases in the short subsequent RR.

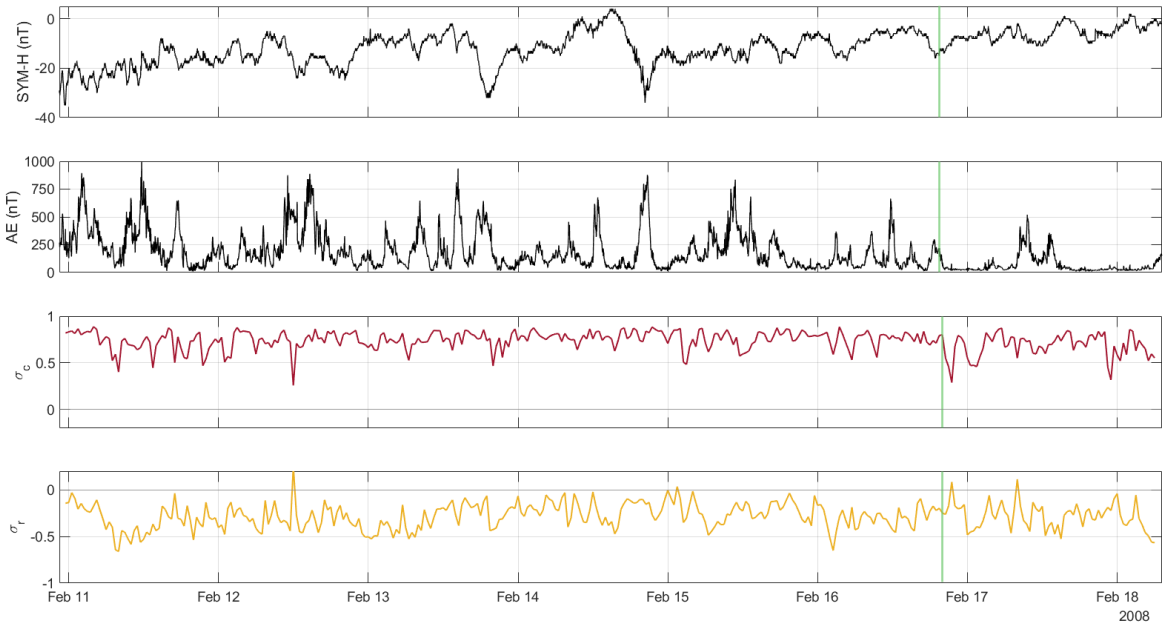

Figure 6.19: February event. From top to bottom: the horizontal symmetric (SYM-H) disturbance index, the Auroral Electrojet (AE) index, the normalized cross-helicity, and the normalized residual energy. The green vertical line corresponds to the velocity knee location, separating HSS from RR.

6.2.2 Joint analysis: Alfvénic and non-Alfvénic populations and geomagnetic effectiveness

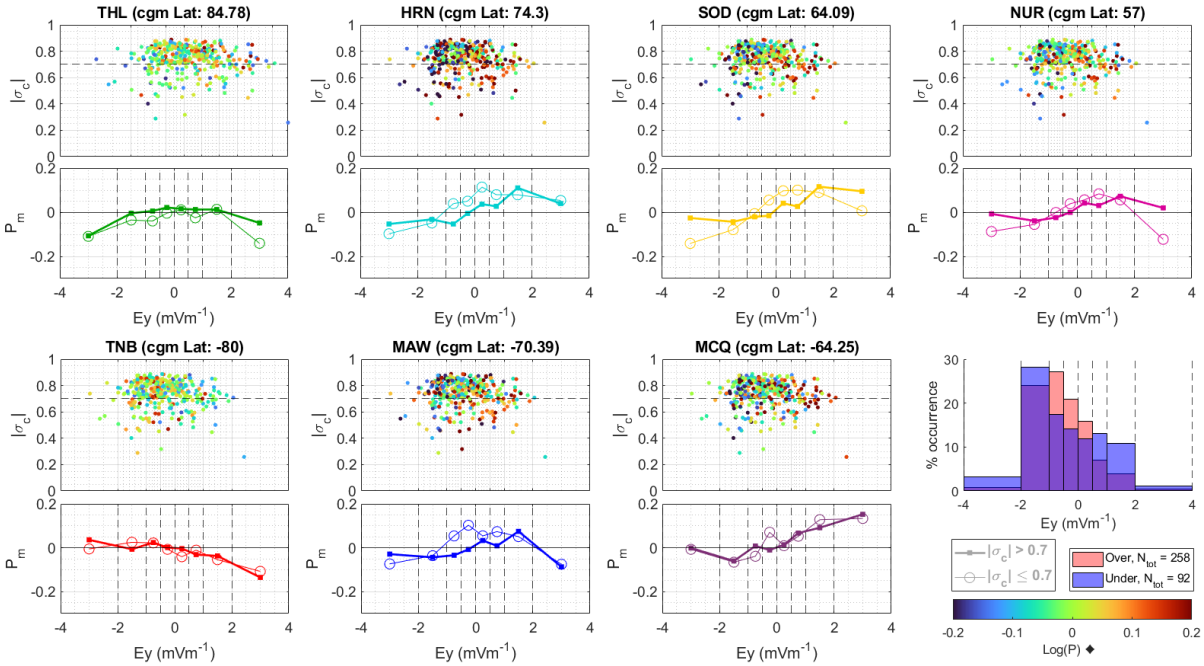

Figure 6.20: February event. First and third rows: scatter plots of the rescaled geomagnetic power at different geomagnetic observatories in terms of Ey in the GSM reference frame and the normalized cross-helicity. The horizontal dashed black line refers to $|\sigma_c| = 0.7$. Under each scatterplot, the average power is calculated for each bin of Ey values, distinguishing between the more Alfvénic cases (thick line and solid points) from the less Alfvénic ones (thin line and empty circles). The first two rows refer to the northern hemisphere, the second two rows refer to the southern hemisphere. The bottom-right panel shows the percentage occurrence of points falling into each bin both above and below threshold conditions of $|\sigma_c| = 0.7$. More details in the text.

Figure 6.20 shows, for each observatory, the scatterplot of the rescaled geomagnetic power (Log(P) ♦) (color of the points) in terms of the geoeffective component of the interplanetary electric field $E_y = v_x B_z$, in the GSM reference frame, and the absolute value of the normalized cross-helicity σ_c. Under each scatterplot, there is a panel where the abscissa refers to Ey values binned in a non-equidistant manner, with narrower bins around zero and wider bins as one moves away from zero; this is because Ey is a highly fluctuating quantity around zero, where most of the values cluster. In this case, the distribution of points in Ey is skewed more toward negative Ey values, as can be seen in the histograms at the right-bottom panel. However, looking at the subplot reporting the average ground power (Pm) falling within each bin for the two distinct

populations (thin lines with open circles for the low Alfvénic one and thick lines with closed points for the high Alfvénic one) there are still an increase in the mean of the logarithm of the ground power at auroral and sub-auroral latitudes for positive Ey values, regardless of the two populations with low and high Alfvénicity. Figure 6.21, shows the average power for each bin associated with $\sigma_c > 0.7$ in the left column, for all observatories, and in the right column for $\sigma_c \leq 0.7$, for all observatories. In this figure, are shown values for which at least 3 points contributed to the average calculation.

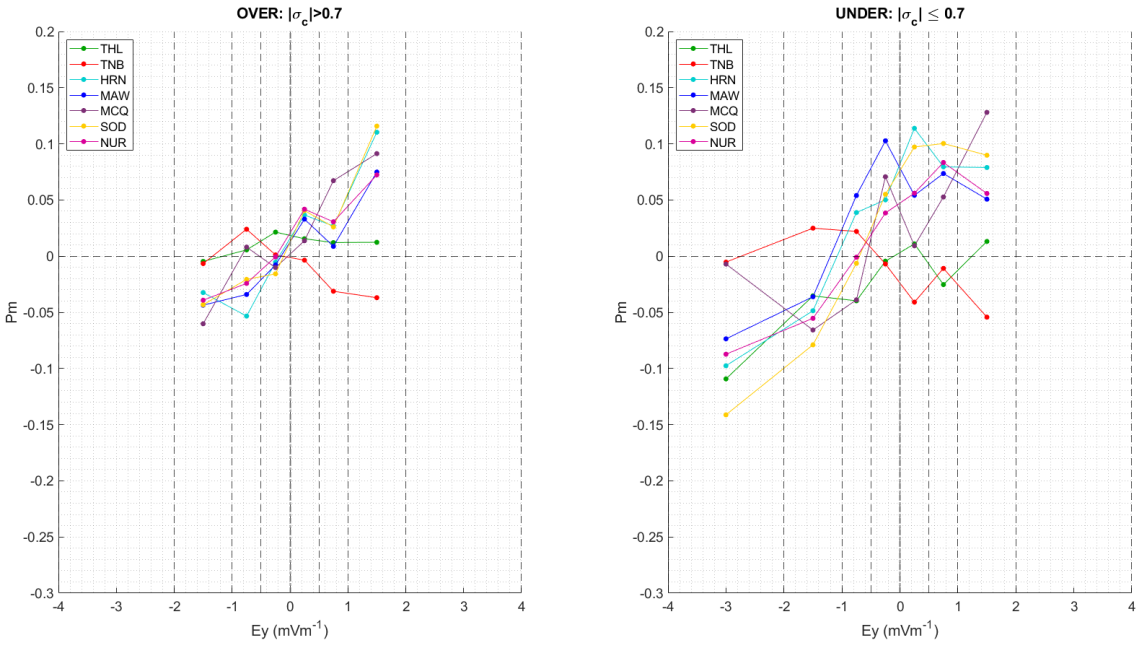

Figure 6.21: February event. Average of the rescaled power falling into each Ey bin, for all selected observatories (different colors): on the left for the more Alfvénic population of the SW, and on the right for the less Alfvénic population of the SW. The legend lists the observatories in descending order based on the absolute value of their magnetic latitude.

For this event, the increasing trend for the increasing Ey values is found for both Alfvénic and less Alfvénic populations, confirming a higher power in correspondence with open magnetospheric conditions. A different behavior is observed for polar cap latitudes where the power level trend is less defined. Furthermore, the average power values are more compact (showing less variability) for the Alfvénic population and are slightly more scattered for the less Alfvénic population.

6.2.3 Joint analysis with parallel and perpendicular power

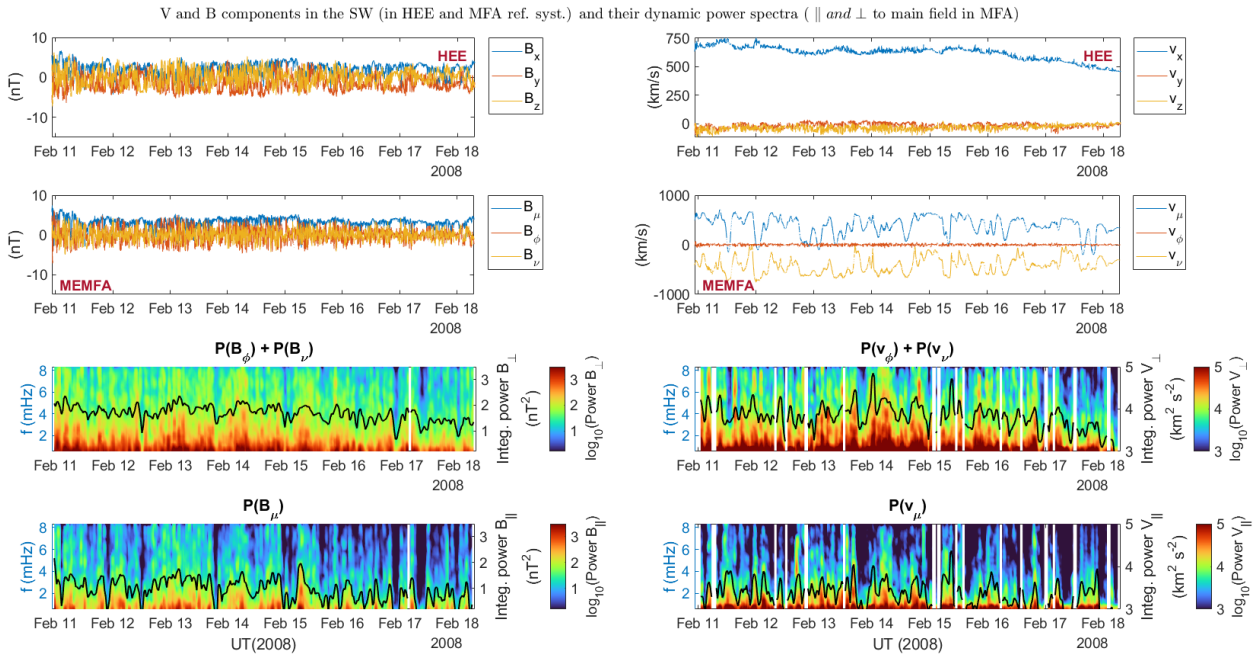

Figure 6.22: February event. First row: magnetic (left) and velocity (right) components in the HEE reference frame. Second row: magnetic (left) and velocity (right) components in the MEMFA reference frame. Third row: dynamic spectrum of the two magnetic (left) and velocity (right) components orthogonal to the main field direction. Fourth row: dynamic spectrum of the magnetic (left) and velocity (right) components aligned to the main field direction. The black overlaid curve on each dynamic spectrum is the corresponding integrated power in the Pc5 range.

As done in previous section, I proceeded to rotate the SW velocity and magnetic field components from the HEE reference frame to the MEMFA reference frame, as shown in Figure 6.22 where I also included the dynamic spectra associated with both the magnetic (on the left) and velocity (on the right) components perpendicular to the direction of the main magnetic field (third row) and the component aligned with the field (fourth row). In this case, as in the previous stream, the magnetic power fluctuations decrease along the stream, while the velocity fluctuations are maximum in the HSS region, especially corresponding to the power associated with the components perpendicular to the field direction.

To compare the powers in the SW with those on the ground at various latitudes, I defined the total power in the direction aligned with the main magnetic field ${P_{||}}^{SW}$, and the total power in the plane perpendicular to it ${P_{\perp}}^{SW}$, according to equations 6.1 and 6.2.

Once the SW powers associated with the two directions of interest (aligned with the main magnetic field and orthogonal to it) were calculated, I proceeded

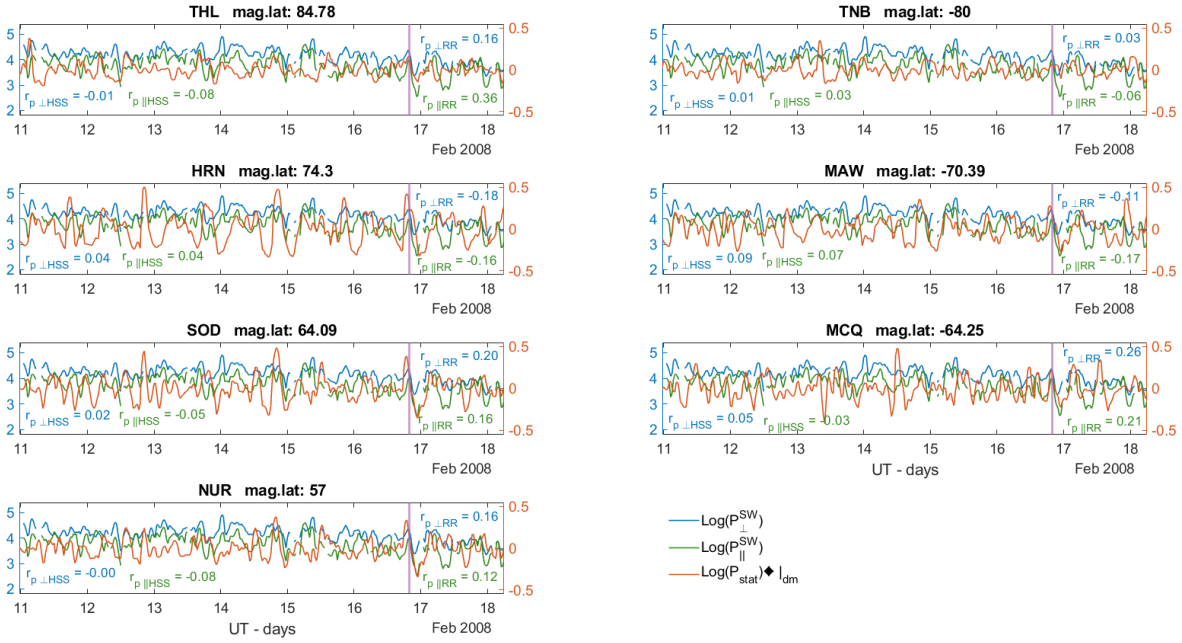

Figure 6.23: February event. In each panel, in blue the logarithm of the velocity and magnetic power in the orthogonal plane to the main field; in green the logarithm of the velocity and magnetic power in the direction aligned to the main field; in red the logarithm of the geomagnetic power rescaled to CQB, after removing a 12-hour moving average, for the observatory/geomagnetic latitude specified on the panel's title. The vertical pink line separates the HSS region from the RR. In the two regions (HSS and RR), the correlation coefficients between the ground powers and those in the two solar wind directions are also specified.

to perform a correlation analysis between these two powers and the geomagnetic power measured on the ground at various latitudes, appropriately scaled to the CQB. As before, I then removed its 12-hour moving average to compensate for any possible diurnal effects. Figure 6.23 shows in each panel the logarithm of the SW power related to the direction perpendicular (in blue) to the main field, the logarithm of the SW power related to the direction aligned (in green) with the main field, and the logarithm of the ground power (in red). The vertical pink line line denotes the separation region between HSS and RR, corresponding to the SW velocity knee. Each panel also includes the correlation coefficient between the solar wind power and the ground power measured at the observatory specified in the panel's title: in blue for the correlation $r_{p\perp}$ between ground power and perpendicular SW power, in green for the correlation $r_{p||}$ between ground power and aligned SW power. This time the linear correlation coefficients are very low and even below the significance threshold. Although very low, on average, the correlation coefficients are higher for the perpendicular direction compared to those for the parallel direction. Even more so, a

subsequent analysis of coherence at various scales is deemed important.

6.2.4 Wavelet coherence analysis

As done for the January event, I proceeded with a wavelet coherence analysis between the logarithms of the SW powers (in both directions, $\perp$ and $||$ to the main field) and the logarithm of the ground power, at various latitudes, suitably scaled. Figures from 6.24 to 6.30 show the coherograms for the February stream. Following the same procedure described for the January event, I identified the peaks of high coherence, above 0.7, between Log($P_{\perp}{}^{SW}$) and $Log(P_{Station})\blacklozenge|_{dm}$, and between Log($P_{||}{}^{SW}$) and $Log(P_{Station})\blacklozenge|_{dm}$.

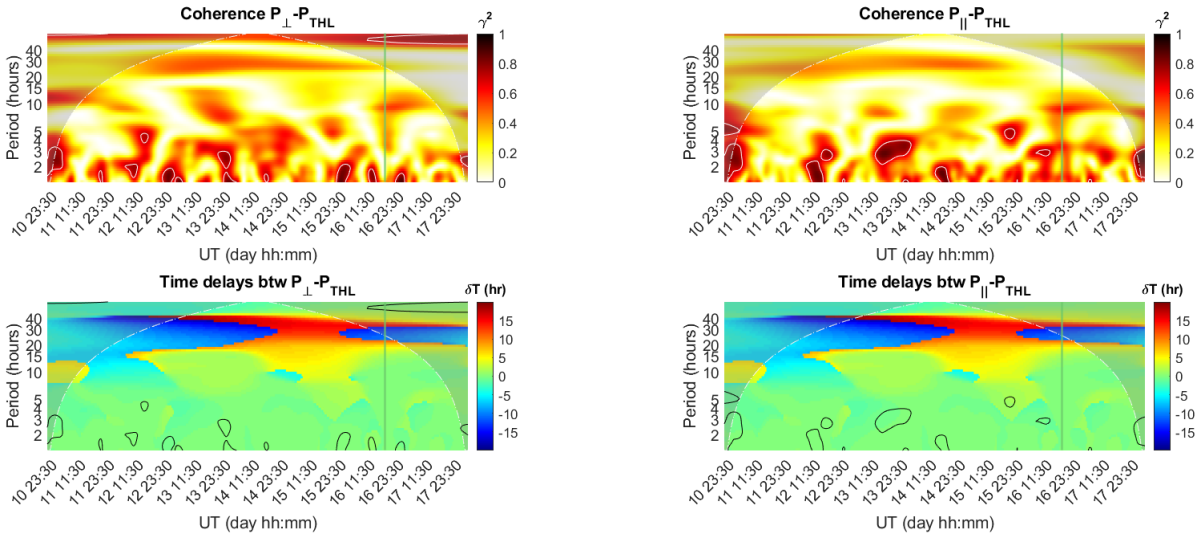

Figure 6.24: February event. Wavelet coherence between Log($P_{\perp}{}^{SW}$) and $Log(P_{THL})\blacklozenge|_{dm}$ in the left and Log($P_{||}{}^{SW}$) and $Log(P_{THL})\blacklozenge|_{dm}$ on the right. The x-axis represents time while the y-axis represents period (or scales) in hours. In the first row, the color coding indicates coherence, with lighter and darker colors representing low and high coherence, respectively. The regions enclosed by a white contour shape represent the coherence peaks found for $\gamma^2 \geq 0.7$. In the second row, the color coding indicates the time delay, in hours, between the two signals. The regions enclosed by a black contour shape are those of the coherence peaks identified in the coherence plot above. The shaded region in all panels is the one external to the cone of influence. The green vertical line corresponds to the velocity knee location, separating HSS from RR.

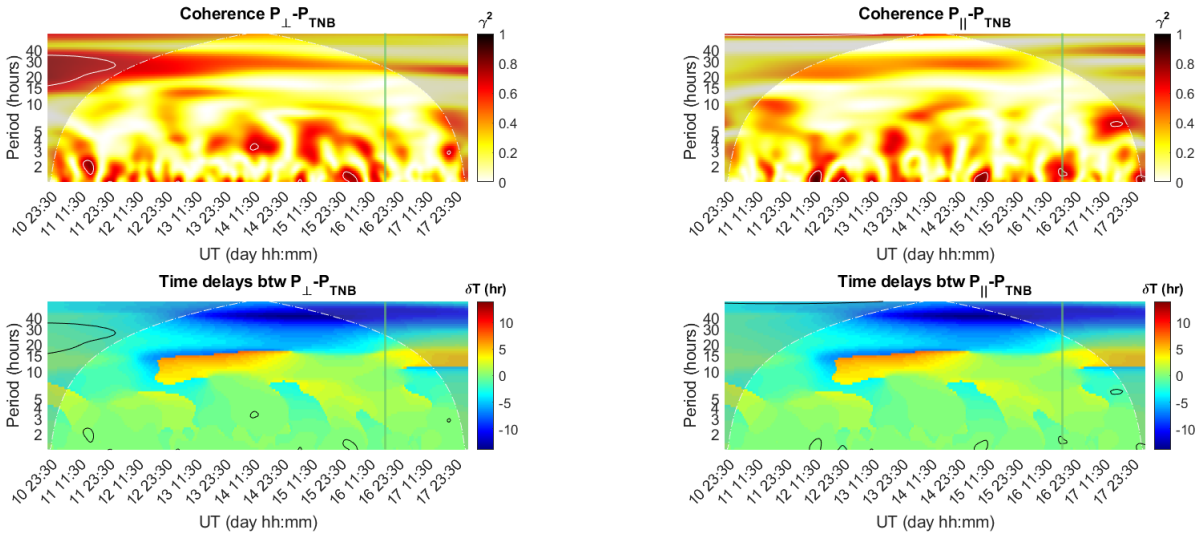

Figure 6.25: February event. Wavelet coherence between Log($P_{\perp}{}^{SW}$) and $Log(P_{TNB})\blacklozenge|_{dm}$ in the left and Log($P_{||}{}^{SW}$) and $Log(P_{TNB})\blacklozenge|_{dm}$ on the right. The x-axis represents time while the y-axis represents period (or scales) in hours. In the first row, the color coding indicates coherence, with lighter and darker colors representing low and high coherence, respectively. The regions enclosed by a white contour shape represent the coherence peaks found for $\gamma^2 \geq 0.7$. In the second row, the color coding indicates the time delay, in hours, between the two signals. The regions enclosed by a black contour shape those of the coherence peaks identified in the coherence plot above. The shaded region in all panels is the one external to the cone of influence. The green vertical line corresponds to the velocity knee location, separating HSS from RR.

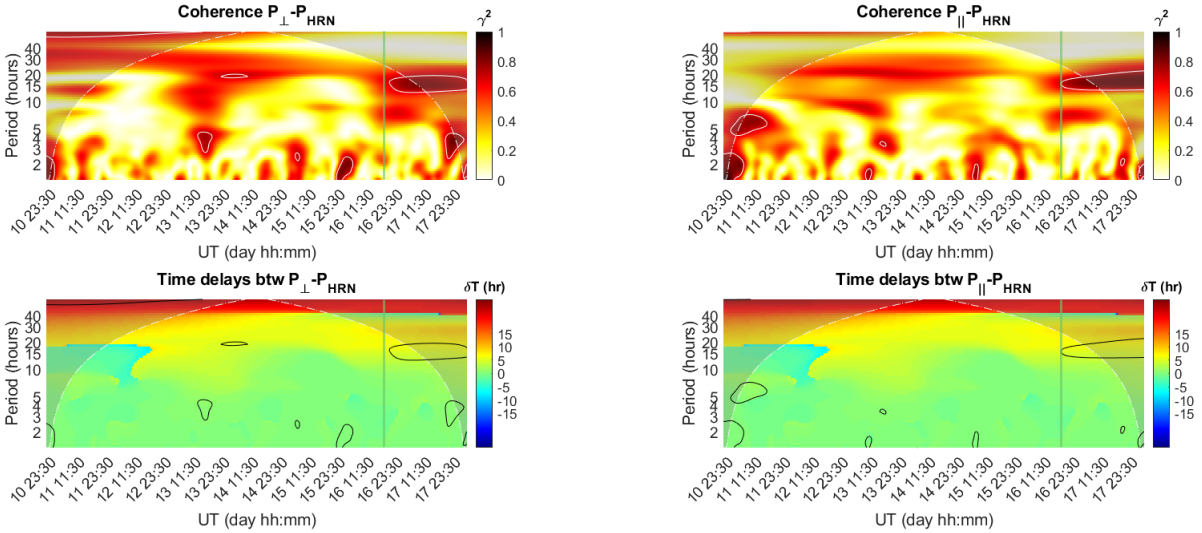

Figure 6.26: February event. Wavelet coherence between Log($P_{\perp}{}^{SW}$) and $Log(P_{HRN})\blacklozenge|_{dm}$ in the left and Log($P_{||}{}^{SW}$) and $Log(P_{HRN})\blacklozenge|_{dm}$ on the right. The x-axis represents time while the y-axis represents period (or scales) in hours. In the first row, the color coding indicates coherence, with lighter and darker colors representing low and high coherence, respectively. The regions enclosed by a white contour shape represent the coherence peaks found for $\gamma^2 \geq 0.7$. In the second row, the color coding indicates the time delay, in hours, between the two signals. The regions enclosed by a black contour shape those of the coherence peaks identified in the coherence plot above. The shaded region in all panels is the one external to the cone of influence. The green vertical line corresponds to the velocity knee location, separating HSS from RR.

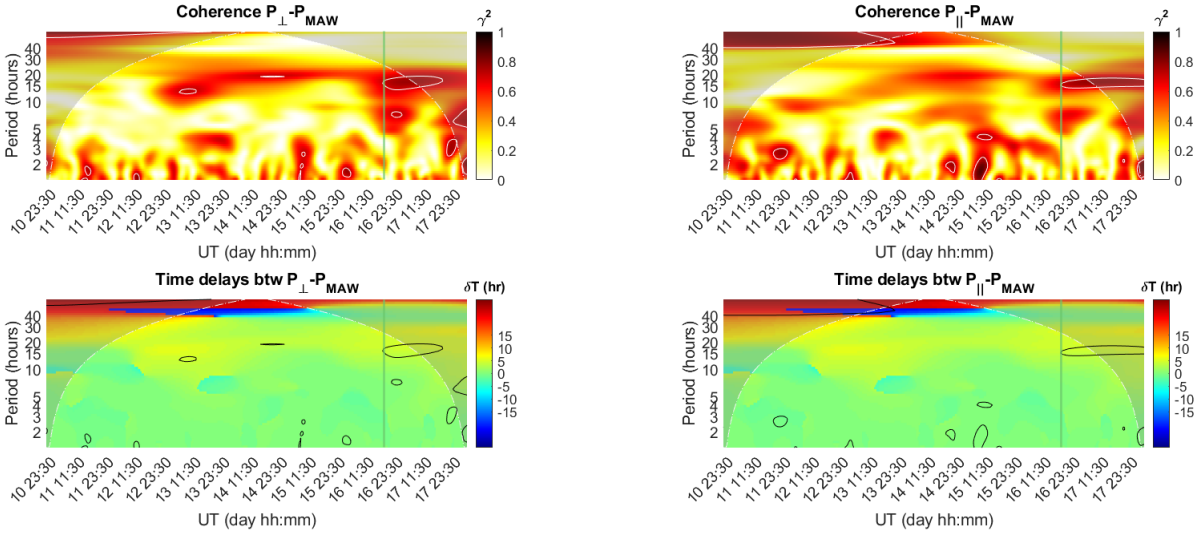

Figure 6.27: February event. Wavelet coherence between Log($P_{\perp}{}^{SW}$) and $Log(P_{MAW})\blacklozenge|_{dm}$ in the left and Log($P_{||}{}^{SW}$) and $Log(P_{MAW})\blacklozenge|_{dm}$ on the right. The x-axis represents time while the y-axis represents period (or scales) in hours. In the first row, the color coding indicates coherence, with lighter and darker colors representing low and high coherence, respectively. The regions enclosed by a white contour shape represent the coherence peaks found for $\gamma^2 \geq 0.7$. In the second row, the color coding indicates the time delay, in hours, between the two signals. The regions enclosed by a black contour shape those of the coherence peaks identified in the coherence plot above. The shaded region in all panels is the one external to the cone of influence. The green vertical line corresponds to the velocity knee location, separating HSS from RR.

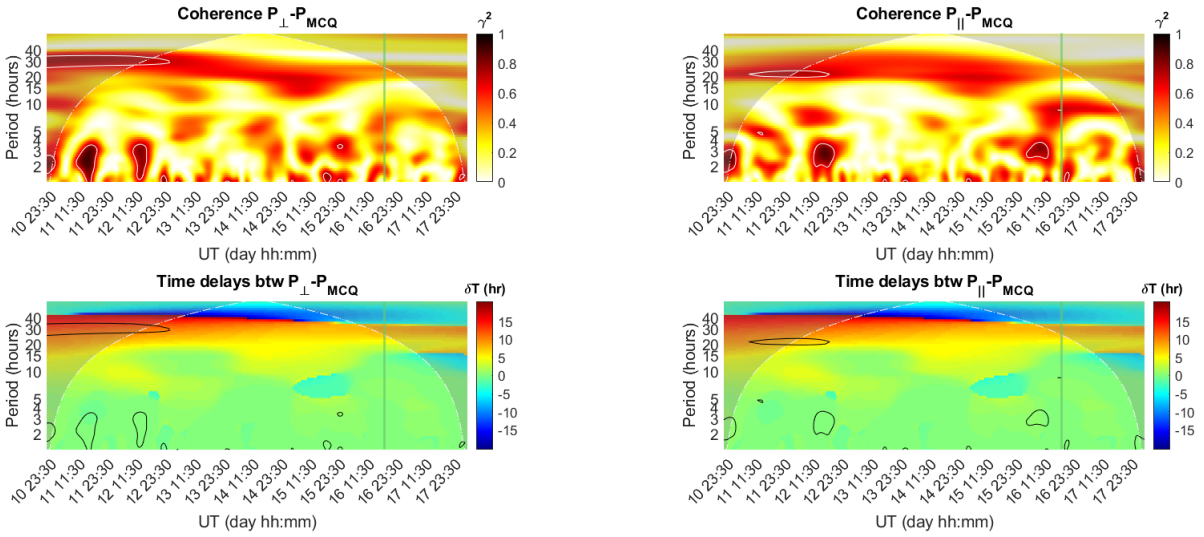

Figure 6.28: February event. Wavelet coherence between Log($P_{\perp}{}^{SW}$) and $Log(P_{MCQ})\blacklozenge|_{dm}$ in the left and Log($P_{||}{}^{SW}$) and $Log(P_{MCQ})\blacklozenge|_{dm}$ on the right. The x-axis represents time while the y-axis represents period (or scales) in hours. In the first row, the color coding indicates coherence, with lighter and darker colors representing low and high coherence, respectively. The regions enclosed by a white contour shape represent the coherence peaks found for $\gamma^2 \geq 0.7$. In the second row, the color coding indicates the time delay, in hours, between the two signals. The regions enclosed by a black contour shape those of the coherence peaks identified in the coherence plot above. The shaded region in all panels is the one external to the cone of influence. The green vertical line corresponds to the velocity knee location, separating HSS from RR.

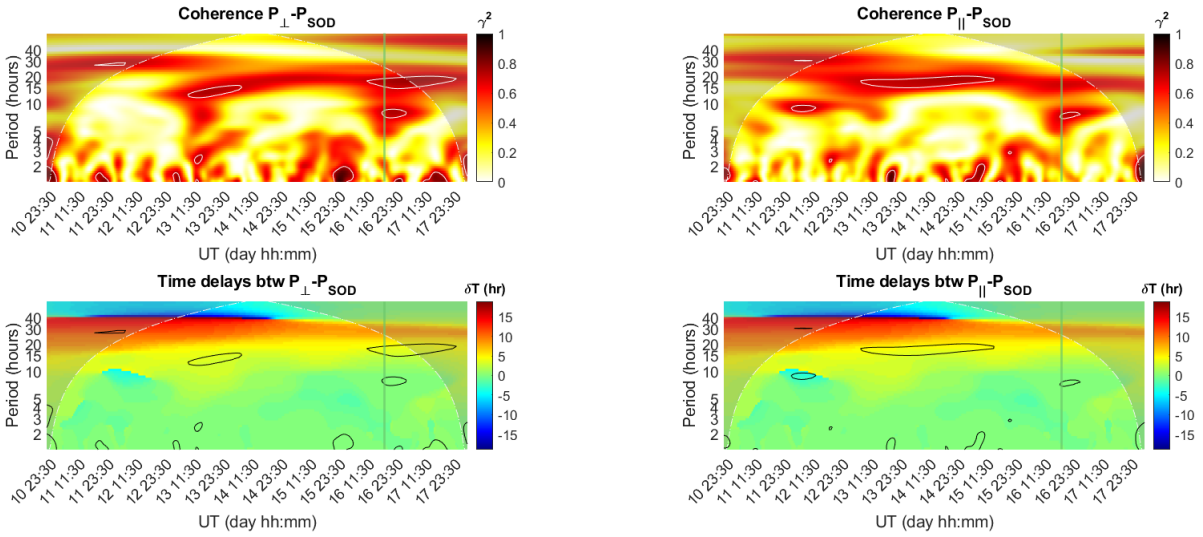

Figure 6.29: February event. Wavelet coherence between Log($P_{\perp}{}^{SW}$) and $Log(P_{SOD})\blacklozenge|_{dm}$ in the left and Log($P_{||}{}^{SW}$) and $Log(P_{SOD})\blacklozenge|_{dm}$ on the right. The x-axis represents time while the y-axis represents period (or scales) in hours. In the first row, the color coding indicates coherence, with lighter and darker colors representing low and high coherence, respectively. The regions enclosed by a white contour shape represent the coherence peaks found for $\gamma^2 \geq 0.7$. In the second row, the color coding indicates the time delay, in hours, between the two signals. The regions enclosed by a black contour shape those of the coherence peaks identified in the coherence plot above. The shaded region in all panels is the one external to the cone of influence. The green vertical line corresponds to the velocity knee location, separating HSS from RR.

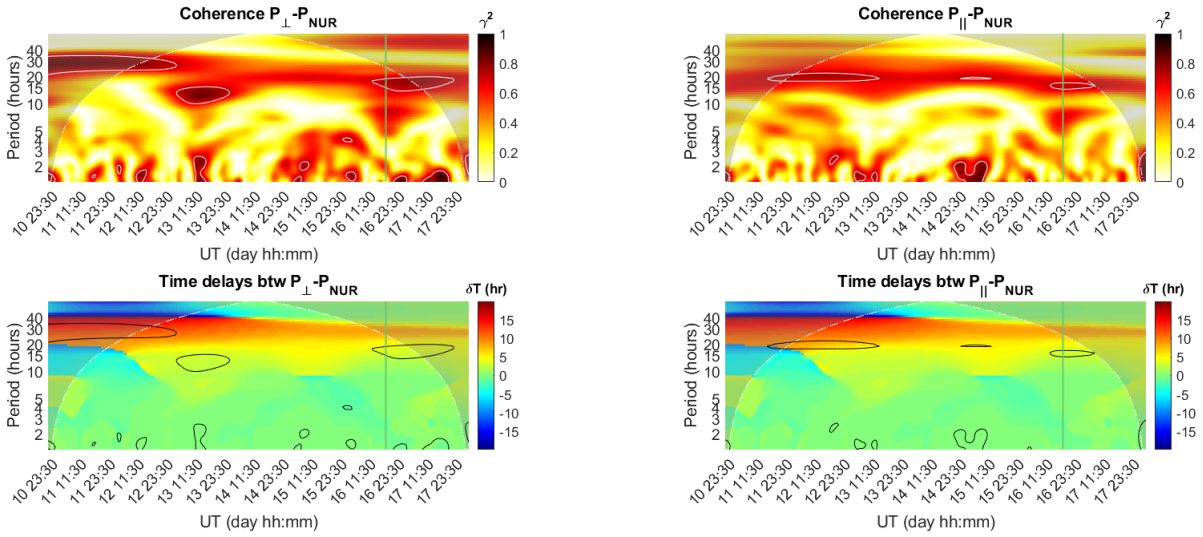

Figure 6.30: February event. Wavelet coherence between Log($P_{\perp}{}^{SW}$) and $Log(P_{NUR})\blacklozenge|_{dm}$ in the left and Log($P_{||}{}^{SW}$) and $Log(P_{NUR})\blacklozenge|_{dm}$ on the right. The x-axis represents time while the y-axis represents period (or scales) in hours. In the first row, the color coding indicates coherence, with lighter and darker colors representing low and high coherence, respectively. The regions enclosed by a white contour shape represent the coherence peaks found for $\gamma^2 \geq 0.7$. In the second row, the color coding indicates the time delay, in hours, between the two signals. The regions enclosed by a black contour shape those of the coherence peaks identified in the coherence plot above. The shaded region in all panels is the one external to the cone of influence. The green vertical line corresponds to the velocity knee location, separating HSS from RR.

Once the coherence peaks for all geomagnetic latitudes and both SW main directions have been identified, these peaks are then plotted on polar plots as a function of MLT, with separate plots for different directions in the solar wind and different geomagnetic latitudes, as shown in Figure 6.31. As can be seen in the last right-hand column, the temporal coverage percentage still prevails (as in the previous case) for the orthogonal component of the solar wind: however, in this case, there is a higher temporal coverage percentage at THL (84.7°) and the stations at sub-auroral latitudes, with a minimum coverage percentage at auroral latitudes. In this case, as well, several intervals of coherence between the SW power and the power on the ground have been found; at these intervals, the average power on the ground varies heterogeneously. Additionally, the arrangement of high-coherence intervals does not exhibit a clear distribution in terms of MLT.

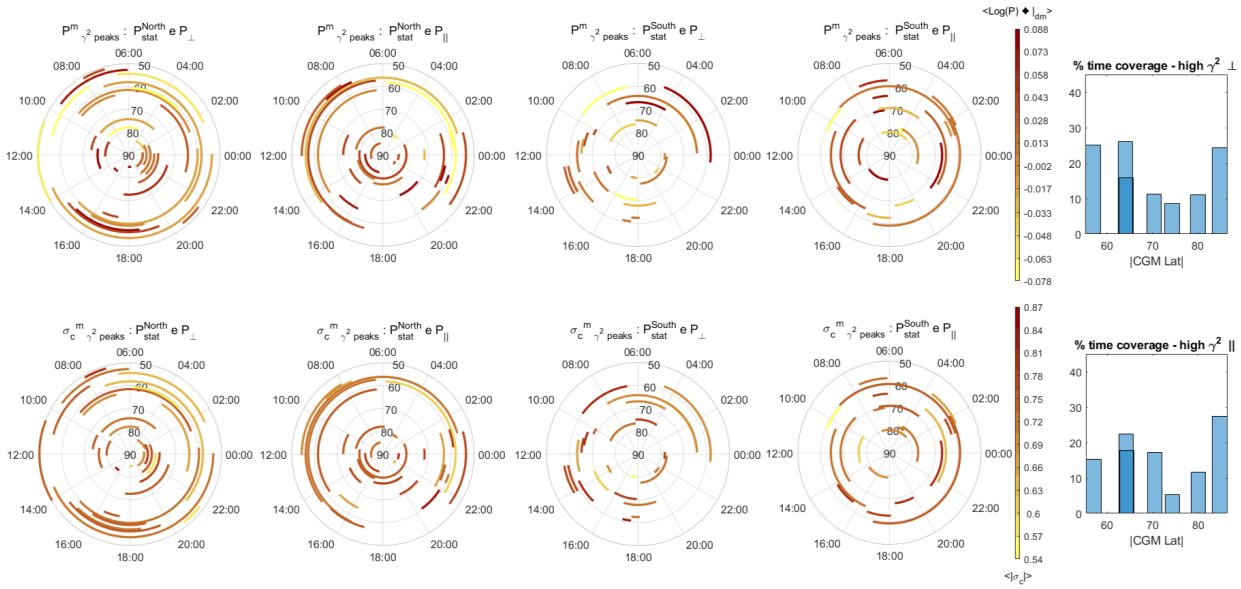

Figure 6.31: February event. Polar plot of the coherence peaks in terms of MLT. Coherence peaks at the same latitude/observatory are slightly shifted in latitude to avoid overlapping. The color code in the top row corresponds to the average ground power at the identified coherence peak. The color code in the bottom row corresponds to the average value of σ_c at the identified coherence peak. The first column refers to observatories in the northern hemisphere and SW power related to the orthogonal plane to the main field. The second column refers to observatories in the northern hemisphere and SW power related to the parallel direction to the main field. The third column refers to observatories in the southern hemisphere and SW power related to the orthogonal plane to the main field. The fourth column refers to observatories in the southern hemisphere and SW power related to the parallel direction to the main field. The fifth column shows the bar plots of the average temporal coverage percentage for each latitude or observatory (on the x-axis) associated with the two main directions in the solar wind: perpendicular (top) and parallel (bottom) to the main magnetic field.

6.3 9-16 August 2008

6.3.1 Characterization

A third corotating stream selected is the one spanning from August 9th to August 16th. For this event, as for the previous, I repeated the analysis procedure performed for the January and February events. In this case, the typical structure of the HSS is shorter in time and the RR of the corotating stream lasts for more days.

Looking at Figure 6.33, it can be noticed that Alfvénic fluctuations are mainly present in the HSS region lasting for less than two days, shorter than the previous cases. On the other hand, in the RR the Alfvénicity is reduced.

Figure 6.32: August event. From top to bottom, the first three panels: velocity components V_x, V_y, V_z (in red) and magnetic field components B_x, B_y, B_z (in blue) in the HEE reference frame. Fourth panel: the proton number density. Fifth panel: the proton temperature. The vertical green line identifies the separation between HSS and RR of the corotating stream.

The AE index shows high values in correspondence with the very beginning of the HSS and of an isolated peak corresponding to the middle of the RR. The SYM-H index values are comparable to those of previous events, although in this case, similar to January and unlike February, the profile seems more akin to that of a weak storm, characterized by a rapid initial decrease and a slow rise thereafter.

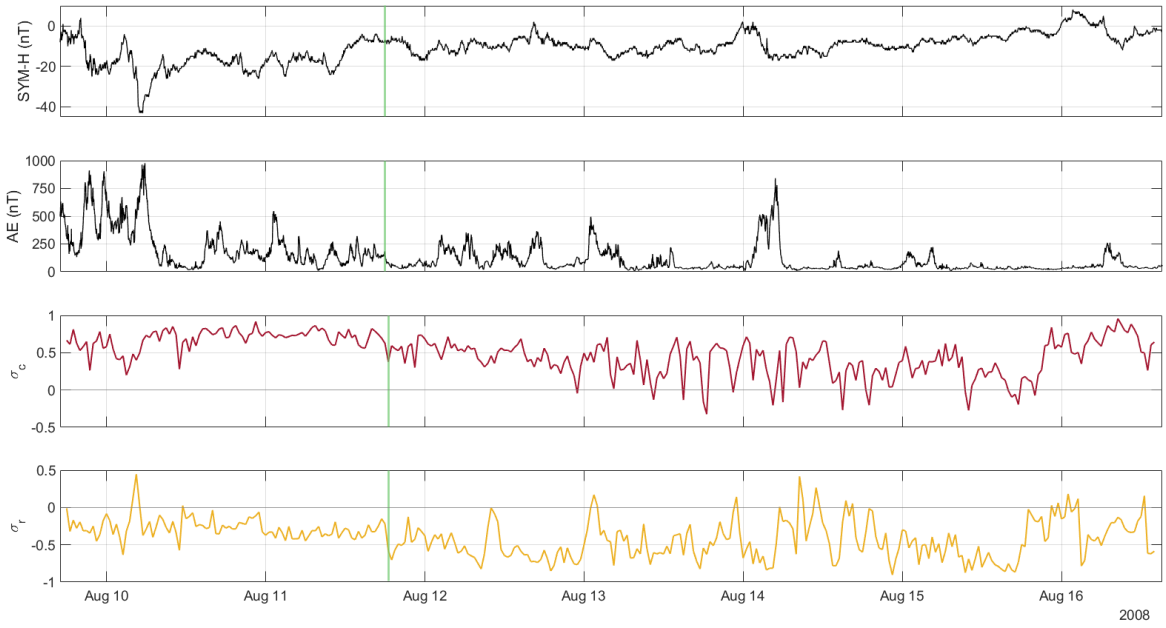

Figure 6.33: August event. From top to bottom: the horizontal symmetric (SYM-H) disturbance index, the Auroral Electrojet (AE) index, the normalized cross-helicity, and the normalized residual energy. The green vertical line corresponds to the velocity knee location, separating HSS from RR.

6.3.2 Joint analysis: Alfvénic and non-Alfvénic populations and geomagnetic effectiveness

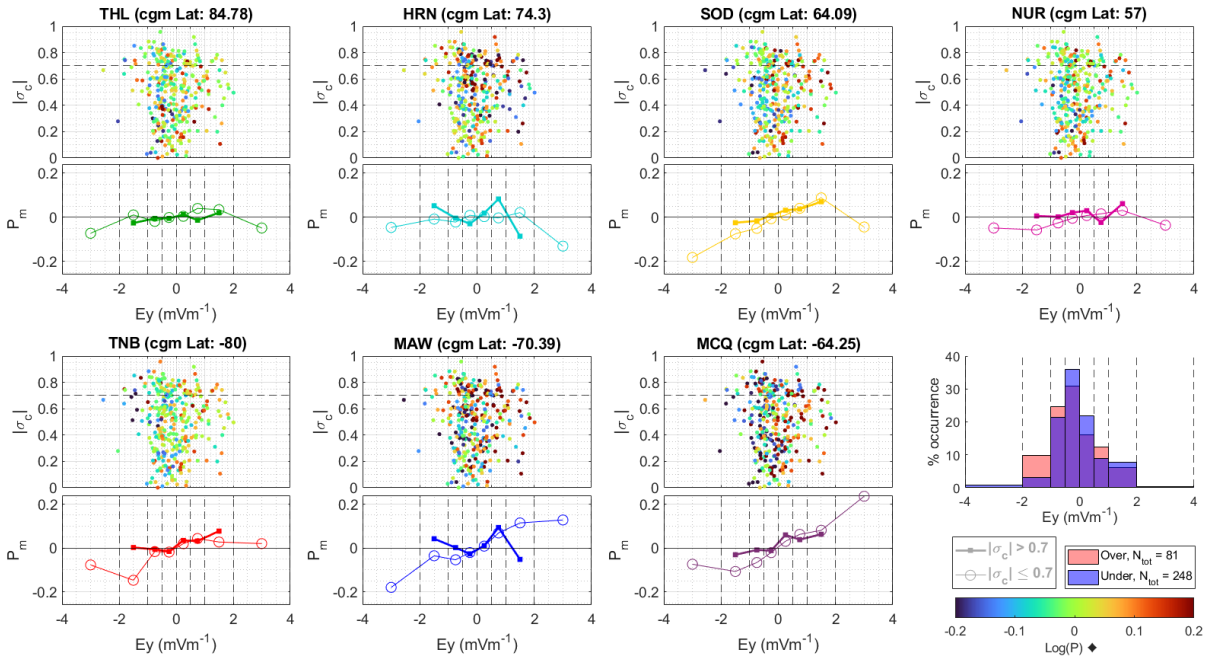

Figure 6.34: August event. First and third rows: scatter plots of the rescaled geomagnetic power at different geomagnetic observatories in terms of Ey in the GSM reference frame and the normalized cross-helicity. The horizontal dashed black line refers to $|\sigma_c| = 0.7$. Under each scatterplot, the average power is calculated for each bin of Ey values, distinguishing between the more Alfvénic cases (thick line and solid points) from the less Alfvénic ones (thin line and empty circles). The first two rows refer to the northern hemisphere, the second two rows refer to the southern hemisphere. The bottom-right panel shows the percentage occurrence of points falling into each bin both above and below threshold conditions of $|\sigma_c| = 0.7$. More details in the text.

Regarding the Alfvénic and non-Alfvénic populations in terms of geoeffectiveness, Figure 6.34 shows, for each observatory, the scatterplot of the rescaled geomagnetic power (Log(P) ♦) (color of the points) in terms of the geoeffective component of the interplanetary electric field $E_y = v_x B_z$, in the GSM reference frame, and the absolute value of the normalized cross-helicity σ_c. The distribution of points in Ey is centered around zero values of Ey, as can be seen in the histograms at the right-bottom panel, similar to the January event. In the panel under each scatterplot, the abscissa refers to Ey bins while the y-axis refers to the average ground power (Pm) falling within each bin for the two distinct populations (thin lines with open circles for the low Alfvénic one and thick lines with closed points for the high Alfvénic one). Here, there is still

an increase in the mean of the logarithm of the ground power at auroral and sub-auroral latitudes for positive Ey values, regardless of the two populations with low and high Alfvénicity. The stations at auroral latitudes show a local maximum for the geomagnetic power in correspondence of Ey between 0.5 and 1 mVm^{-1} for the Alfvénic population. Figure 6.35, shows the average power for each bin associated with $\sigma_c > 0.7$ in the left column, for all observatories, and in the right column for $\sigma_c \leq 0.7$, for all observatories. In this figure, are shown values for which at least 3 points contributed to the average calculation.

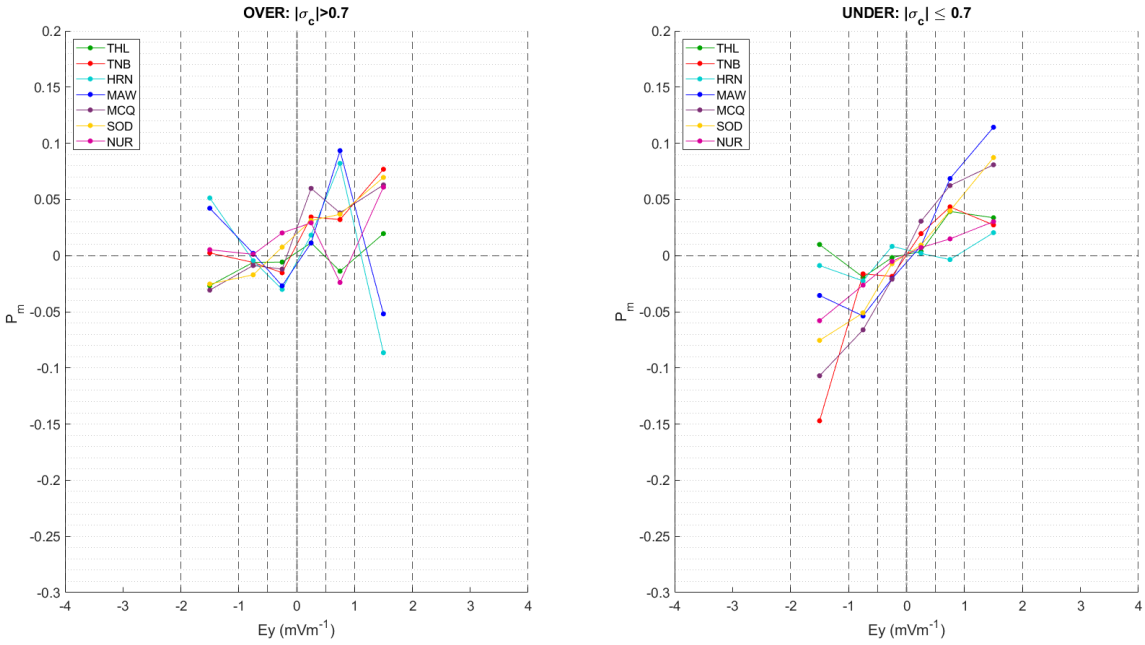

Figure 6.35: August event. Average of the rescaled power falling into each Ey bin, for all selected observatories (different colors): on the left for the more Alfvénic population of the SW, and on the right for the less Alfvénic population of the SW. The legend lists the observatories in descending order based on the absolute value of their magnetic latitude.

For this event, for $\sigma_c > 0.7$ the average power exhibits more variable trends, probably due to the lower number of points involved in the statistics. Nonetheless, the general behavior of increasing power for increasing Ey emerges, except for the auroral latitudes (HRN and MAW), although the general variability is quite low. Regarding the average power values for $\sigma_c \leq 0.7$, they exhibit an increasing trend with increasing Ey, over a wider range of variability, for all observatories/latitudes.

6.3.3 Joint analysis with parallel and perpendicular power

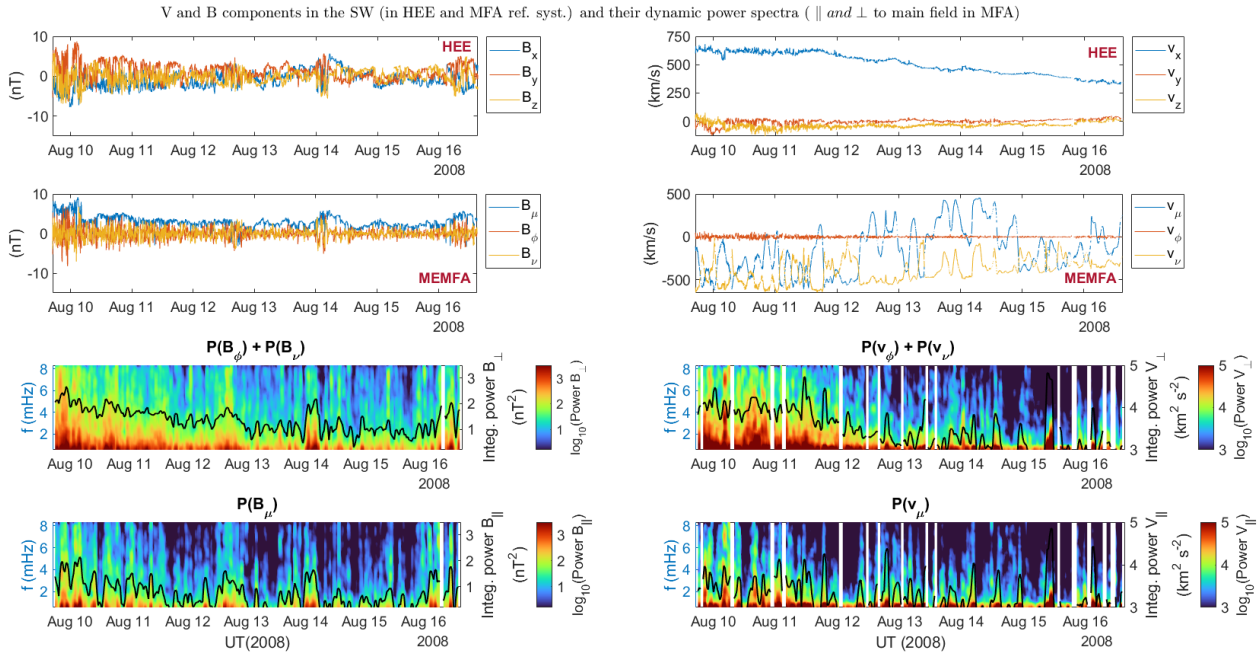

Figure 6.36: August event. First row: magnetic (left) and velocity (right) components in the HEE reference frame. Second row: magnetic (left) and velocity (right) components in the MEMFA reference frame. Third row: dynamic spectrum of the two magnetic (left) and velocity (right) components orthogonal to the main field direction. Fourth row: dynamic spectrum of the magnetic (left) and velocity (right) components aligned to the main field direction. The black overlaid curve on each dynamic spectrum is the corresponding integrated power in the Pc5 range.

As done for the previous events studied, I proceeded to rotate the SW velocity and magnetic field components from the HEE reference frame to the MEMFA reference frame, as shown in Figure 6.36. Here, the integrated power associated with the orthogonal components of velocity undergoes a rapid decrease immediately after the velocity knee. Also, the power associated with the magnetic field decreases from the HSS region to the RR, but in a more gradual manner. In both cases, for both the magnetic field (on the left) and velocity (on the right), the power is greater in the direction orthogonal to the main field (third row) with respect to the aligned one (fourth row).

After defining the total SW power in the direction aligned with the main magnetic field $P_{||}{}^{SW}$ and in the plane perpendicular to it $P_{\perp}{}^{SW}$, as seen in equations 6.1 and 6.2, I proceeded to perform a correlation analysis between these two powers and the geomagnetic power measured on the ground at various latitudes, appropriately scaled to the CQB. As before, I then removed its 12-hour moving average to compensate for any possible diurnal effects. Figure

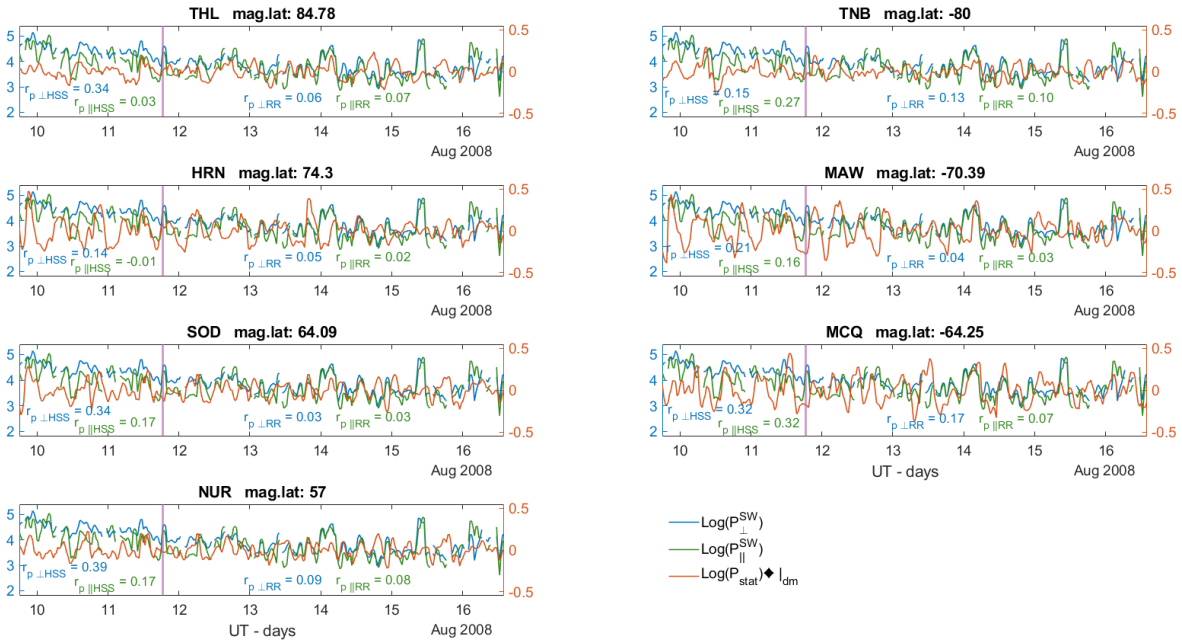

Figure 6.37: August event. In each panel, in blue the logarithm of the velocity and magnetic power in the orthogonal plane to the main field; in green the logarithm of the velocity and magnetic power in the direction aligned to the main field; in red the logarithm of the geomagnetic power rescaled to CQB, excluding a 12-hour moving average, for the observatory/geomagnetic latitude specified on the panel's title. The vertical pink line separates the HSS region from the RR. In the two regions (HSS and RR), the correlation coefficients between the ground powers and those in the two solar wind directions are also specified.

6.37 shows in each panel the logarithm of the SW power related to the direction perpendicular (in blue) to the main field, the logarithm of the SW power related to the direction aligned (in green) with the main field, and the logarithm of the ground power (in red). The vertical pink line line denotes the separation region between HSS and RR, corresponding to the SW velocity knee. Each panel also includes the correlation coefficient between the solar wind power and the ground power measured at the observatory specified in the panel's title. The linear correlation coefficients associated with the direction perpendicular to the main field $r_{p\perp}$ (in blue) are greater than those associated with the aligned direction $r_{p||}$ (in green); however, their value is very low for the RR (below the significance level), while it is higher for the HSS region, although here it is not significant for auroral latitudes.

6.3.4 Wavelet coherence analysis

As done for the January and February events, I proceeded with a wavelet coherence analysis between the logarithms of the SW powers (in both direc-

tions, $\perp$ and || to the main field) and the logarithm of the ground power, at various latitudes, suitably scaled. Figures from 6.38 to 6.44 show the cohero-grams for the August stream. Following the same procedure described before, I identified the peaks of high coherence, above 0.7, between Log($P_{\perp}{}^{SW}$) and $Log(P_{Station})\blacklozenge|_{dm}$, and between Log($P_{||}{}^{SW}$) and $Log(P_{Station})\blacklozenge|_{dm}$.

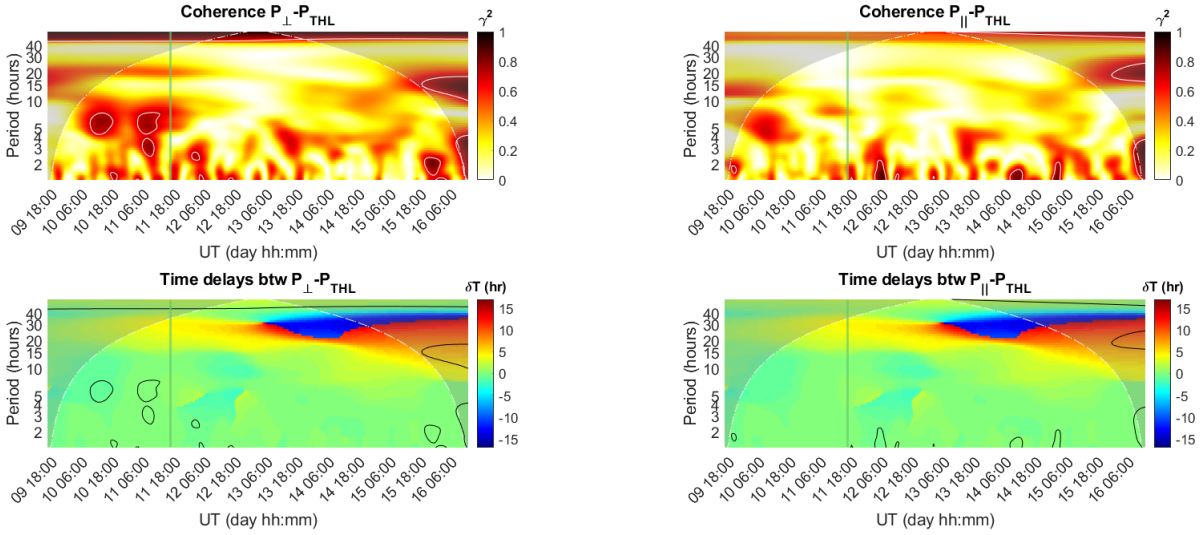

Figure 6.38: August event. Wavelet coherence between Log($P_{\perp}{}^{SW}$) and $Log(P_{THL})\blacklozenge|_{dm}$ in the left and Log($P_{||}{}^{SW}$) and $Log(P_{THL})\blacklozenge|_{dm}$ on the right. The x-axis represents time while the y-axis represents period (or scales) in hours. In the first row, the color coding indicates coherence, with lighter and darker colors representing low and high coherence, respectively. The regions enclosed by a white contour shape represent the coherence peaks found for $\gamma^2 \geq 0.7$. In the second row, the color coding indicates the time delay, in hours, between the two signals. The regions enclosed by a black contour shape are those of the coherence peaks identified in the coherence plot above. The shaded region in all panels is the one external to the cone of influence. The green vertical line corresponds to the velocity knee location, separating HSS from RR.

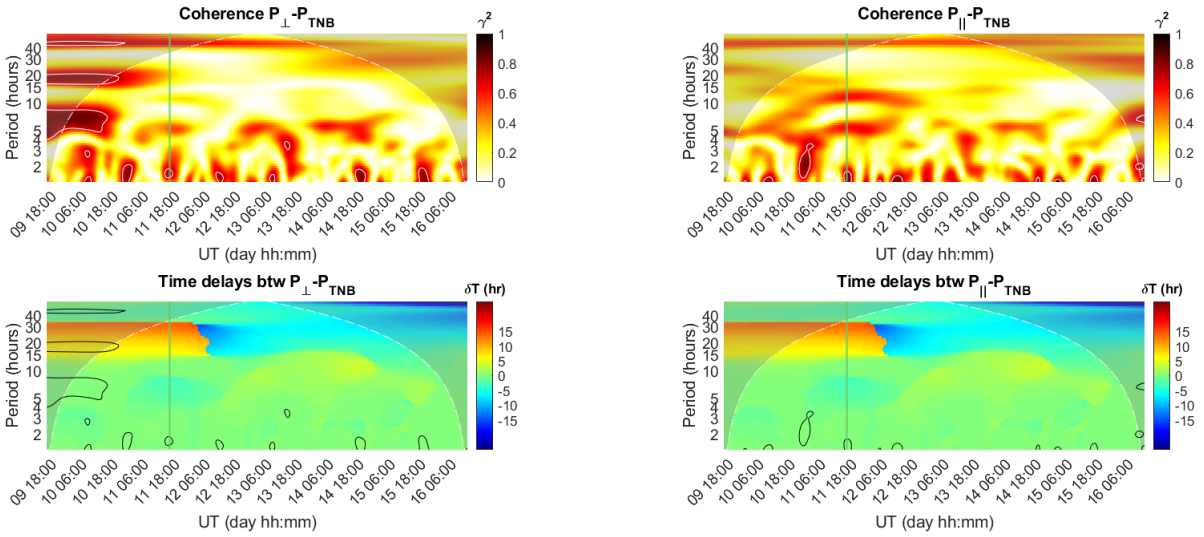

Figure 6.39: August event. Wavelet coherence between Log($P_{\perp}{}^{SW}$) and $Log(P_{TNB})\blacklozenge|_{dm}$ in the left and Log($P_{||}{}^{SW}$) and $Log(P_{TNB})\blacklozenge|_{dm}$ on the right. The x-axis represents time while the y-axis represents period (or scales) in hours. In the first row, the color coding indicates coherence, with lighter and darker colors representing low and high coherence, respectively. The regions enclosed by a white contour shape represent the coherence peaks found for $\gamma^2 \geq 0.7$. In the second row, the color coding indicates the time delay, in hours, between the two signals. The regions enclosed by a black contour shape those of the coherence peaks identified in the coherence plot above. The shaded region in all panels is the one external to the cone of influence. The green vertical line corresponds to the velocity knee location, separating HSS from RR.

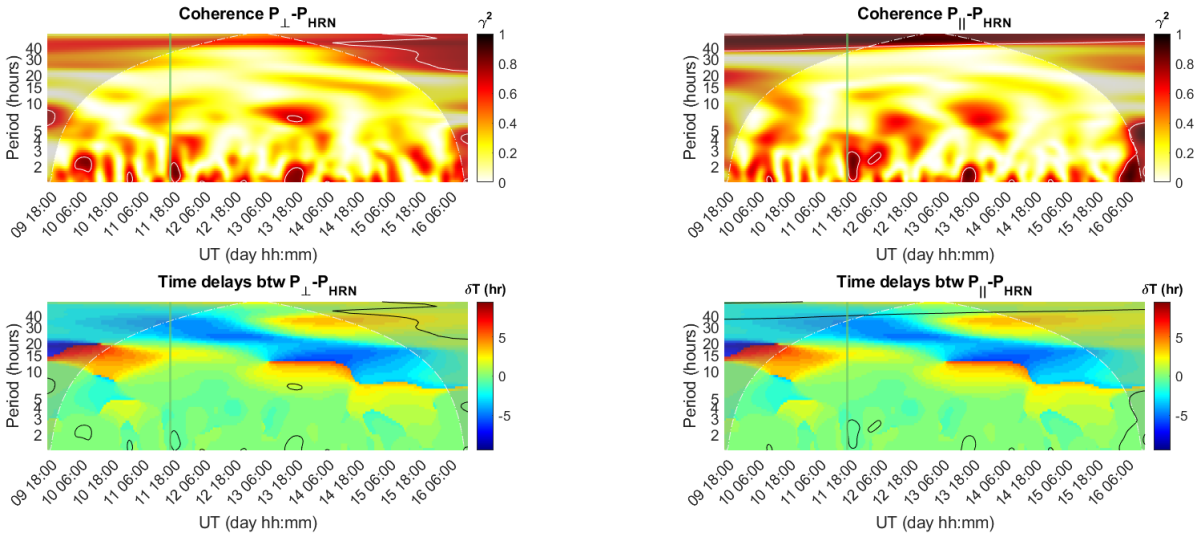

Figure 6.40: August event. Wavelet coherence between Log($P_{\perp}{}^{SW}$) and $Log(P_{HRN})\blacklozenge|_{dm}$ in the left and Log($P_{||}{}^{SW}$) and $Log(P_{HRN})\blacklozenge|_{dm}$ on the right. The x-axis represents time while the y-axis represents period (or scales) in hours. In the first row, the color coding indicates coherence, with lighter and darker colors representing low and high coherence, respectively. The regions enclosed by a white contour shape represent the coherence peaks found for $\gamma^2 \geq 0.7$. In the second row, the color coding indicates the time delay, in hours, between the two signals. The regions enclosed by a black contour shape those of the coherence peaks identified in the coherence plot above. The shaded region in all panels is the one external to the cone of influence. The green vertical line corresponds to the velocity knee location, separating HSS from RR.

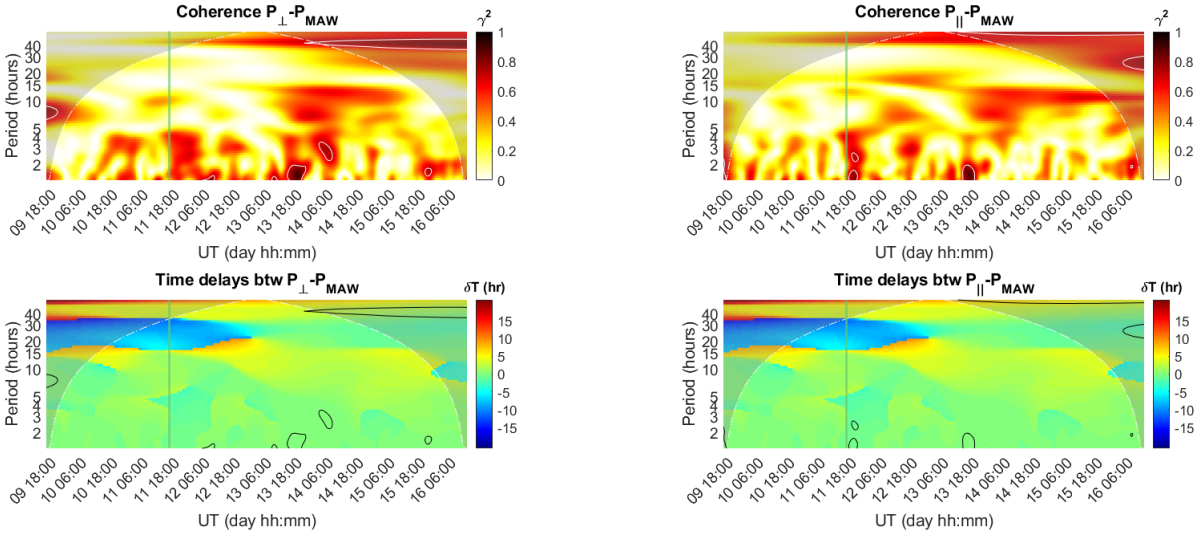

Figure 6.41: August event. Wavelet coherence between Log($P_{\perp}{}^{SW}$) and $Log(P_{MAW})\blacklozenge|_{dm}$ in the left and Log($P_{||}{}^{SW}$) and $Log(P_{MAW})\blacklozenge|_{dm}$ on the right. The x-axis represents time while the y-axis represents period (or scales) in hours. In the first row, the color coding indicates coherence, with lighter and darker colors representing low and high coherence, respectively. The regions enclosed by a white contour shape represent the coherence peaks found for $\gamma^2 \geq 0.7$. In the second row, the color coding indicates the time delay, in hours, between the two signals. The regions enclosed by a black contour shape those of the coherence peaks identified in the coherence plot above. The shaded region in all panels is the one external to the cone of influence. The green vertical line corresponds to the velocity knee location, separating HSS from RR.

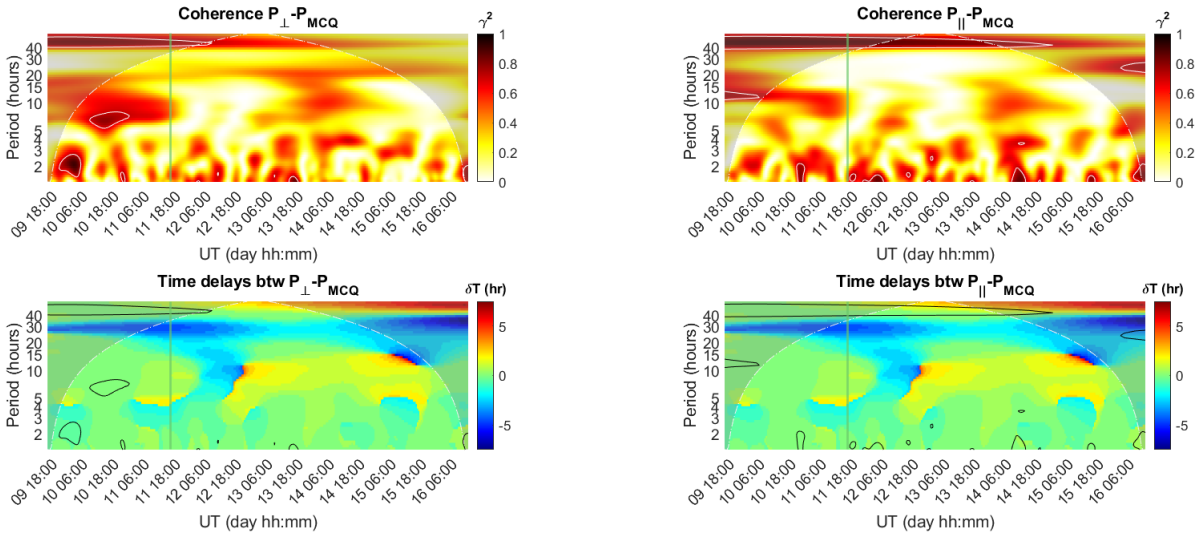

Figure 6.42: August event. Wavelet coherence between Log($P_{\perp}{}^{SW}$) and $Log(P_{MCQ})\blacklozenge|_{dm}$ in the left and Log($P_{||}{}^{SW}$) and $Log(P_{MCQ})\blacklozenge|_{dm}$ on the right. The x-axis represents time while the y-axis represents period (or scales) in hours. In the first row, the color coding indicates coherence, with lighter and darker colors representing low and high coherence, respectively. The regions enclosed by a white contour shape represent the coherence peaks found for $\gamma^2 \geq 0.7$. In the second row, the color coding indicates the time delay, in hours, between the two signals. The regions enclosed by a black contour shape those of the coherence peaks identified in the coherence plot above. The shaded region in all panels is the one external to the cone of influence. The green vertical line corresponds to the velocity knee location, separating HSS from RR.

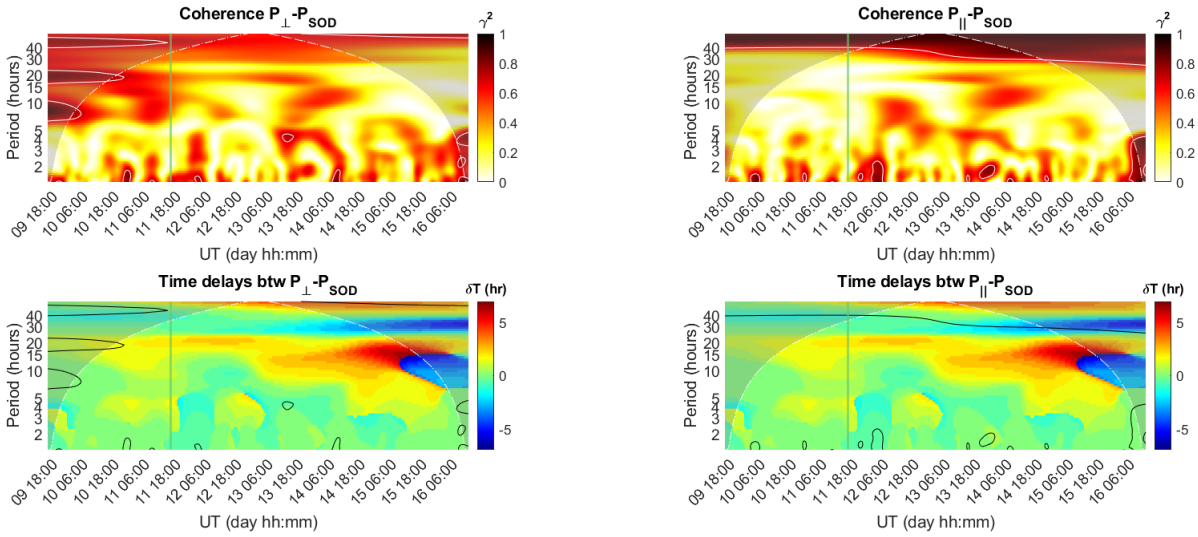

Figure 6.43: August event. Wavelet coherence between Log($P_{\perp}{}^{SW}$) and $Log(P_{SOD})\blacklozenge|_{dm}$ in the left and Log($P_{||}{}^{SW}$) and $Log(P_{SOD})\blacklozenge|_{dm}$ on the right. The x-axis represents time while the y-axis represents period (or scales) in hours. In the first row, the color coding indicates coherence, with lighter and darker colors representing low and high coherence, respectively. The regions enclosed by a white contour shape represent the coherence peaks found for $\gamma^2 \geq 0.7$. In the second row, the color coding indicates the time delay, in hours, between the two signals. The regions enclosed by a black contour shape those of the coherence peaks identified in the coherence plot above. The shaded region in all panels is the one external to the cone of influence. The green vertical line corresponds to the velocity knee location, separating HSS from RR.

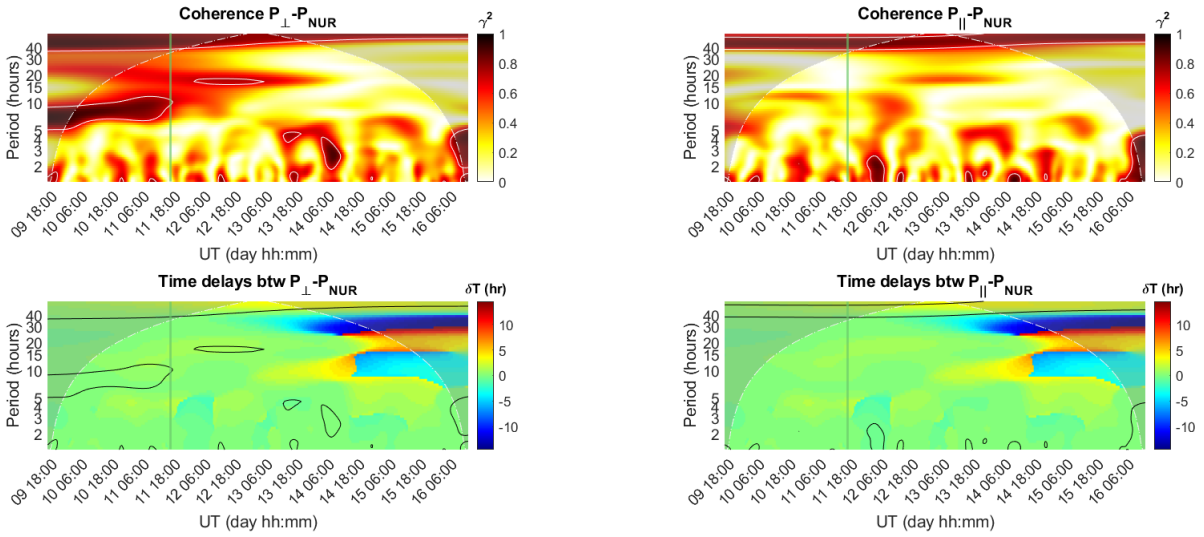

Figure 6.44: August event. Wavelet coherence between Log($P_{\perp}{}^{SW}$) and $Log(P_{NUR})\blacklozenge|_{dm}$ in the left and Log($P_{||}{}^{SW}$) and $Log(P_{NUR})\blacklozenge|_{dm}$ on the right. The x-axis represents time while the y-axis represents period (or scales) in hours. In the first row, the color coding indicates coherence, with lighter and darker colors representing low and high coherence, respectively. The regions enclosed by a white contour shape represent the coherence peaks found for $\gamma^2 \geq 0.7$. In the second row, the color coding indicates the time delay, in hours, between the two signals. The regions enclosed by a black contour shape those of the coherence peaks identified in the coherence plot above. The shaded region in all panels is the one external to the cone of influence. The green vertical line corresponds to the velocity knee location, separating HSS from RR.

The coherence peaks identified for all geomagnetic latitudes and both SW main directions are then plotted on polar plots as a function of MLT, with separate plots for different directions in the SW and different geomagnetic latitudes, as shown in Figure 6.45. Also this time, the temporal coverage percentage prevails for the orthogonal component of the SW, as can be seen in the last right-hand column of figure 6.45. As fot the February event, the higher temporal coverage percentage is found at THL. Numerous peaks of high coherence between ground power and SW power have also been identified for this event. The higher power is observed on the pre-noon and pre-midnight sides for the orthogonal power in the northern hemisphere, mainly at higher latitudes, and only on the pre-noon side for the parallel power in the same hemisphere at auroral and sub-auroral latitudes. In the southern hemisphere, higher powers are observed at auroral and sub-auroral latitudes, mostly on the daytime side for orthogonal power and mostly on the nighttime side for aligned power. This time, the range of variability of σ_c is much greater than in previous cases, as it also assumes values around zero, observed mainly in correspondence with the coherence peaks found for the parallel power at the stations in the southern hemisphere.

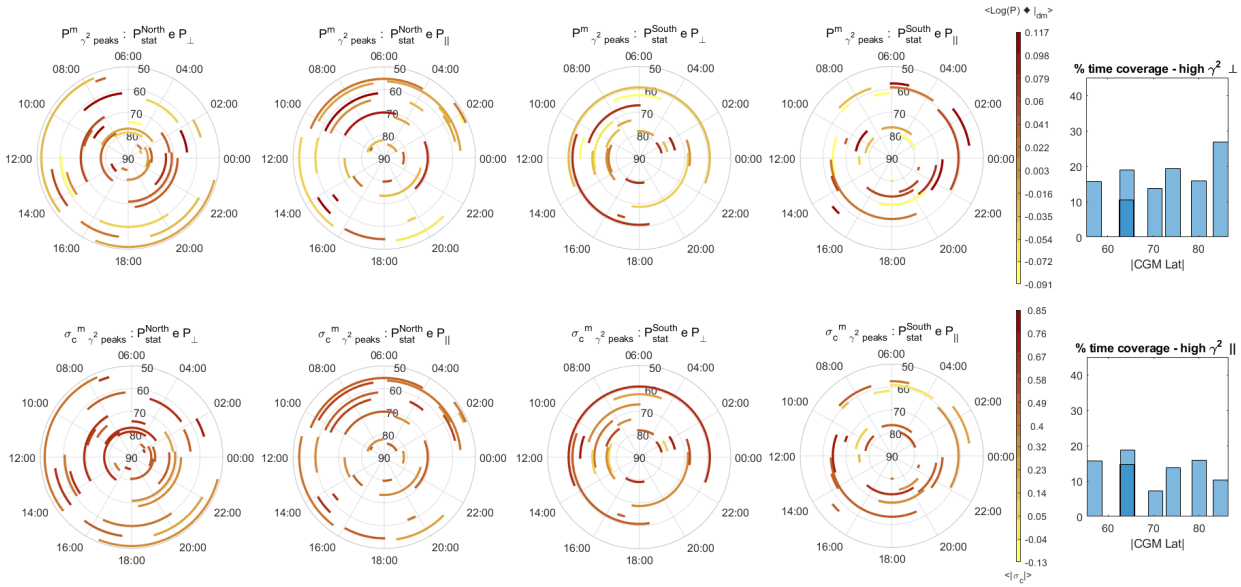

Figure 6.45: August event. Polar plot of the coherence peaks in terms of MLT. The color code in the top row corresponds to the average ground power at the identified coherence peak. The color code in the bottom row corresponds to the average value of σ_c at the identified coherence peak. The first column refers to observatories in the northern hemisphere and SW power related to the orthogonal plane to the main field. The second column refers to observatories in the northern hemisphere and SW power related to the parallel direction to the main field. The third column refers to observatories in the southern hemisphere and SW power related to the orthogonal plane to the main field. The fourth column refers to observatories in the southern hemisphere and SW power related to the parallel direction to the main field. The fifth column shows the bar plots of the average temporal coverage percentage for each latitude or observatory (on the x-axis) associated with the two main directions in the solar wind: perpendicular (top) and parallel (bottom) to the main magnetic field.

6.4 25 November - 1st December 2008

6.4.1 Characterization

A further corotating stream selected is the one spanning from November 25th to December 1st. As for the previous events, I repeated the analysis procedure. As in the previous cases, the HSS region is characterized by large fluctuations in velocity and magnetic field components (Figure 6.46), which are subsequently reduced in amplitude in the RR. The duration of the two regions this time is similar.

From the two bottom panels of Figure 6.47, it can be noticed that there are Alfvénic fluctuations mainly in the HSS region of the stream (except around the 27 November), while the Alfvénicity is reduced in the RR. This time, the AE index (second panel of figure 6.47) is lower and less variable compared to

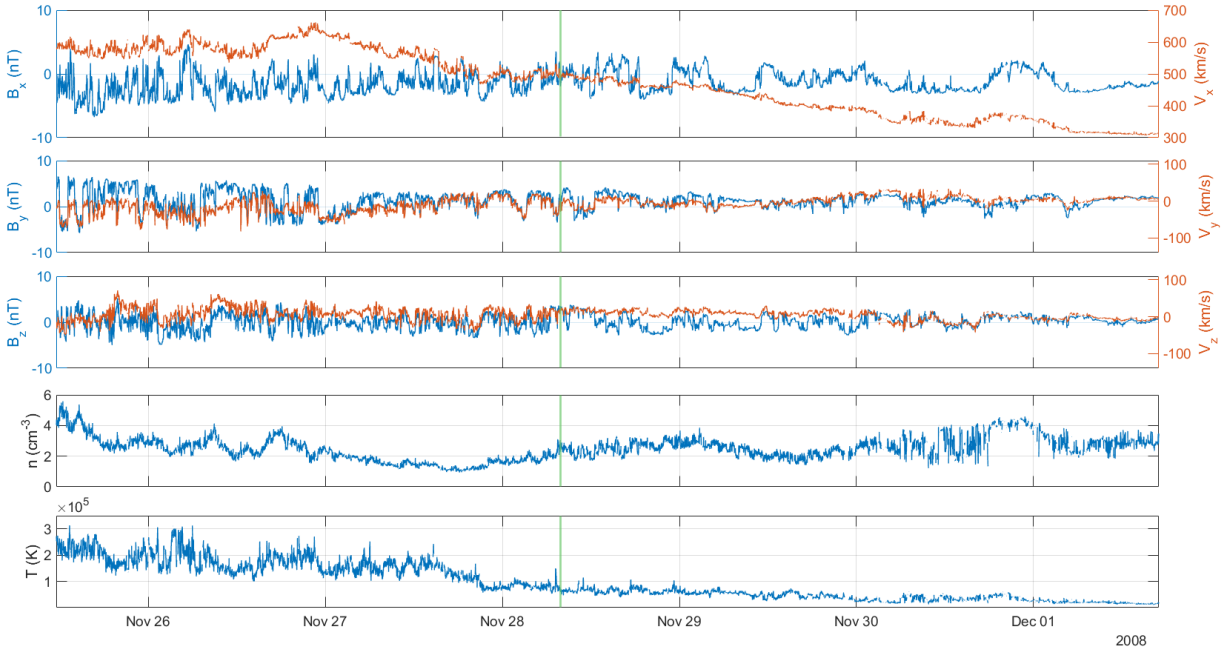

Figure 6.46: November event. From top to bottom, the first three panels: velocity components V_x, V_y, V_z (in red) and magnetic field components B_x, B_y, B_z (in blue) in the HEE reference frame. Fourth panel: the proton number density. Fifth panel: the proton temperature. The vertical green line identifies the separation between HSS and RR of the corotating stream.

the previous cases. The SYM-H index (first panel of figure 6.47) is lower, in magnitude, compared to all the previous cases, reaching a minimum value of -20 nT at the beginning of the HSS, gradually returning towards zero in the RR.

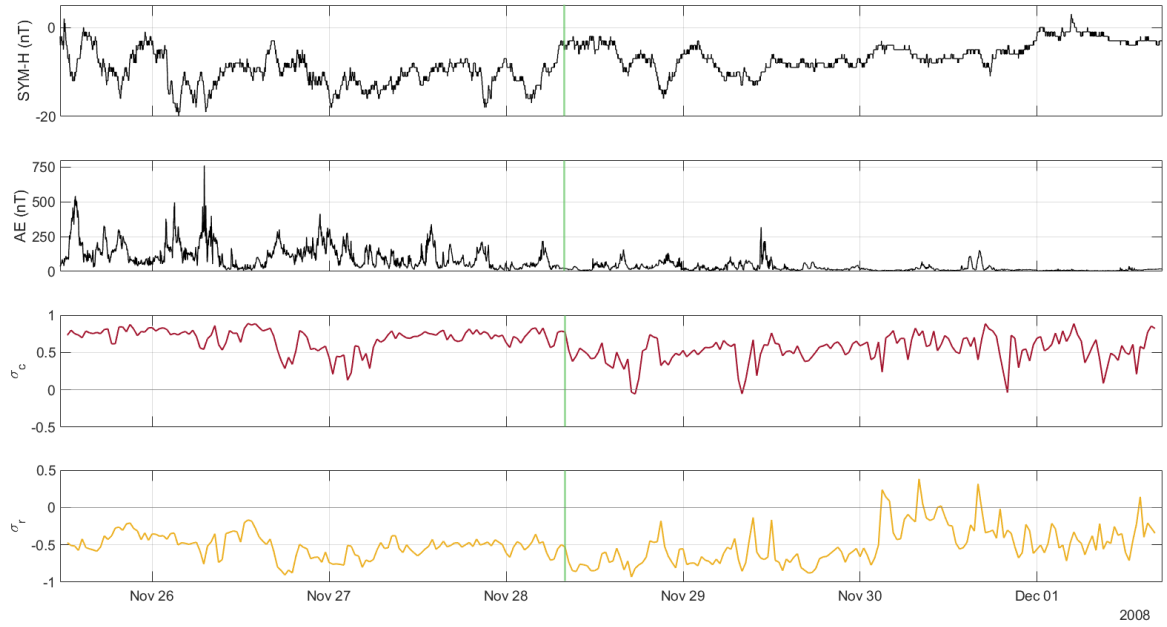

Figure 6.47: November event. From top to bottom: the horizontal symmetric (SYM-H) disturbance index, the Auroral Electrojet (AE) index, the normalized cross-helicity, and the normalized residual energy. The green vertical line corresponds to the velocity knee location, separating HSS from RR.

6.4.2 Joint analysis: Alfvénic and non-Alfvénic populations and geomagnetic effectiveness

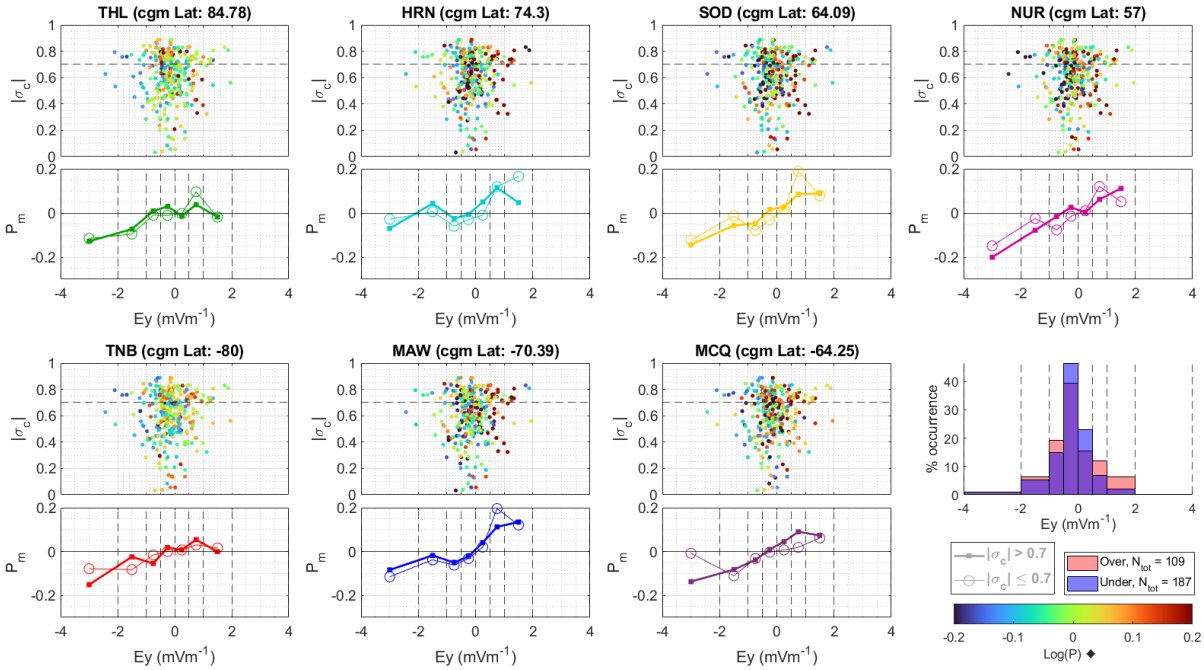

Figure 6.48: November event. First and third rows: scatter plots of the rescaled geomagnetic power at different geomagnetic observatories in terms of Ey in the GSM reference frame and the normalized cross-helicity. The horizontal dashed black line refers to $|\sigma_c| = 0.7$. Under each scatterplot, the average power is calculated for each bin of Ey values, distinguishing between the more Alfvénic cases (thick line and solid points) from the less Alfvénic ones (thin line and empty circles). The first two rows refer to the northern hemisphere, the second two rows refer to the southern hemisphere. The bottom-right panel shows the percentage occurrence of points falling into each bin both above and below threshold conditions of $|\sigma_c| = 0.7$. More details in the text.

Figure 6.48 shows, for each observatory, the scatterplot of the rescaled geomagnetic power (Log(P) ♦) (color of the points) in terms of the geoeffective component of the interplanetary electric field $E_y = v_x B_z$, in the GSM reference frame, and the absolute value of the normalized cross-helicity σ_c. Because Ey is a highly fluctuating quantity around zero, the Ey values are binned in a non-equidistant manner, with narrower bins around zero and wider bins as one moves away from zero. The distribution of points in the scatterplots is centered around the zero value of Ey, as can be also seen in the histograms at the right-bottom panel, for both the Alfvénic and less Alfvénic populations. The panel under each scatterplot shows the average ground power (Pm) falling within each bin for the two distinct populations (thin lines with open circles for the low Alfvénic

one and thick lines with closed points for the high Alfvénic one). Figure 6.49 shows the average power for each bin (with at least 3 points contributed to the average calculation) associated with $\sigma_c > 0.7$ in the left column, for all observatories, and in the right column for $\sigma_c \leq 0.7$, for all observatories. Also in this case, there is a general trend of growth for increasing Ey values, very similar for both populations, which are characterized by a similar number of points in statistical terms and by a similar power level and variability. The stations at auroral and sub-auroral latitudes reach the highest power values, with a very pronounced difference between open and closed magnetospheric conditions.

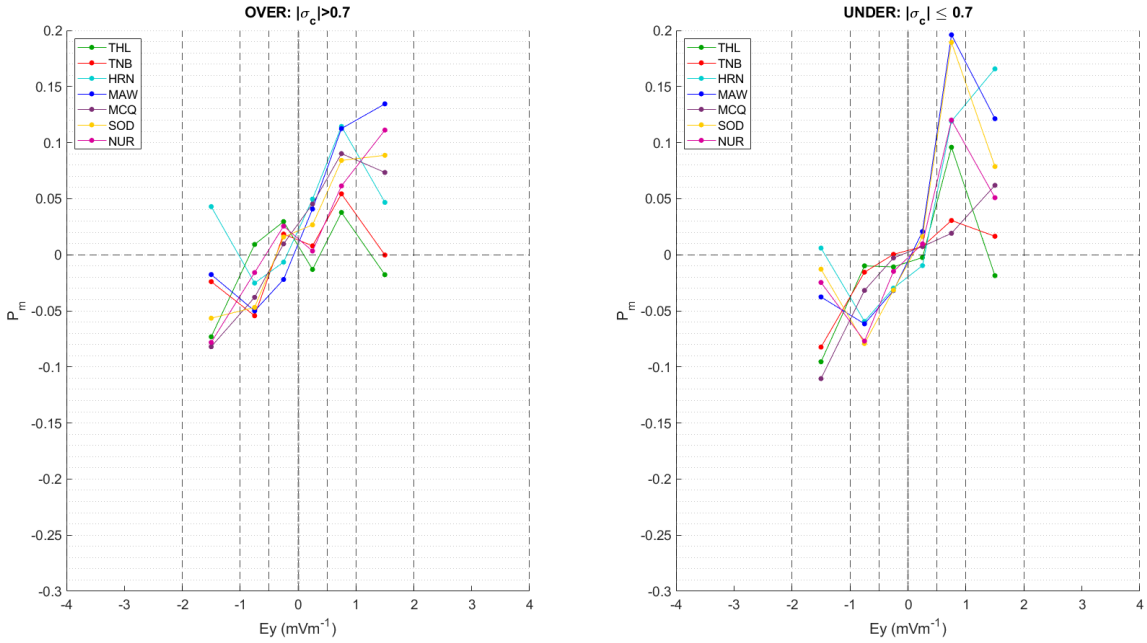

Figure 6.49: November event. Average of the rescaled power falling into each Ey bin, for all selected observatories (different colors): on the left for the more Alfvénic population of the SW, and on the right for the less Alfvénic population of the SW. The legend lists the observatories in descending order based on the absolute value of their magnetic latitude.

6.4.3 Joint analysis with parallel and perpendicular power

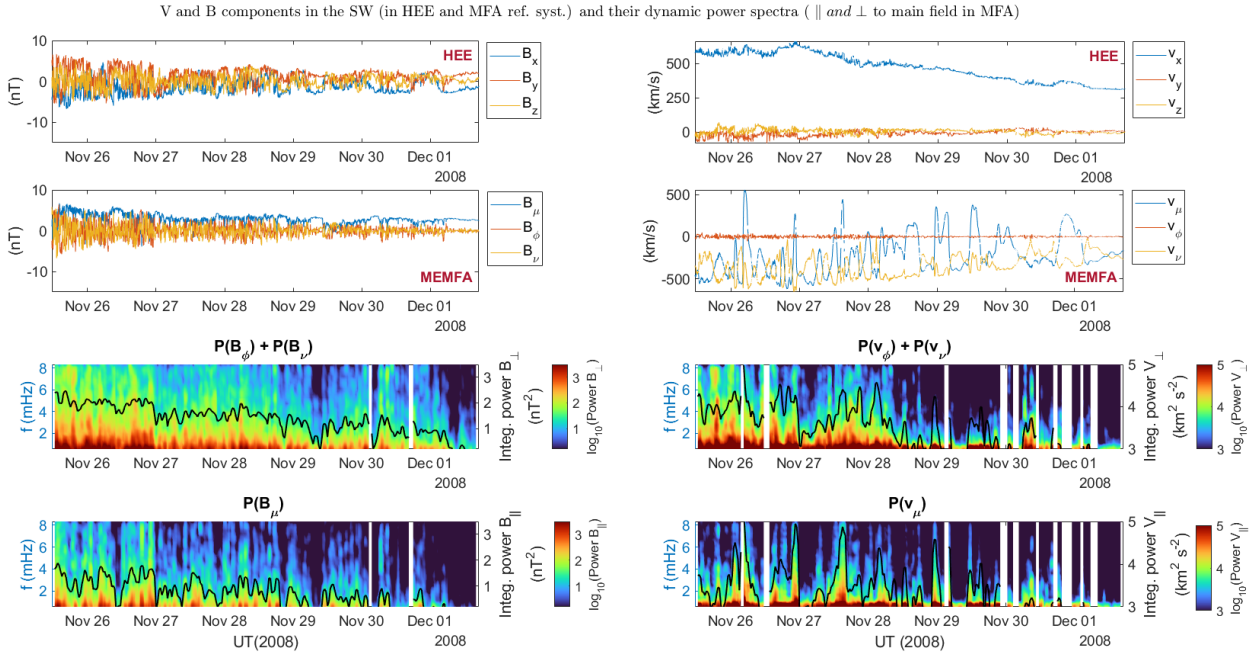

Figure 6.50: November event. First row: magnetic (left) and velocity (right) components in the HEE reference frame. Second row: magnetic (left) and velocity (right) components in the MEMFA reference frame. Third row: dynamic spectrum of the two magnetic (left) and velocity (right) components orthogonal to the main field direction. Fourth row: dynamic spectrum of the magnetic (left) and velocity (right) components aligned to the main field direction. The black overlaid curve on each dynamic spectrum is the corresponding integrated power in the Pc5 range.

In Figure 6.50 are showed the SW velocity and magnetic field components both in the HEE and MEMFA reference frame (first and second row, respectively) and the dynamic spectra associated with both the magnetic (on the left) and velocity (on the right) components perpendicular to the direction of the main magnetic field (third row) and the component aligned with the field (fourth row). The power of magnetic fluctuations decreases along the stream, and it is greater in the direction perpendicular to the main field. Similarly, the power of kinetic fluctuations is higher in the perpendicular direction compared to the one aligned with the main field. When observing the power associated with the perpendicular direction, it exhibits higher intensity at the beginning of the stream and around November 28, corresponding to an increase in σ_c, as can be seen in the third panel of Figure 6.47. Once defined the total power in the direction aligned with the main magnetic field ${P_{||}}^{SW}$, and the total power in the plane perpendicular to it ${P_{\perp}}^{SW}$, according to equations 6.1 and 6.2, I proceeded to perform a correlation analysis between these two powers and the

geomagnetic power measured on the ground at various latitudes.

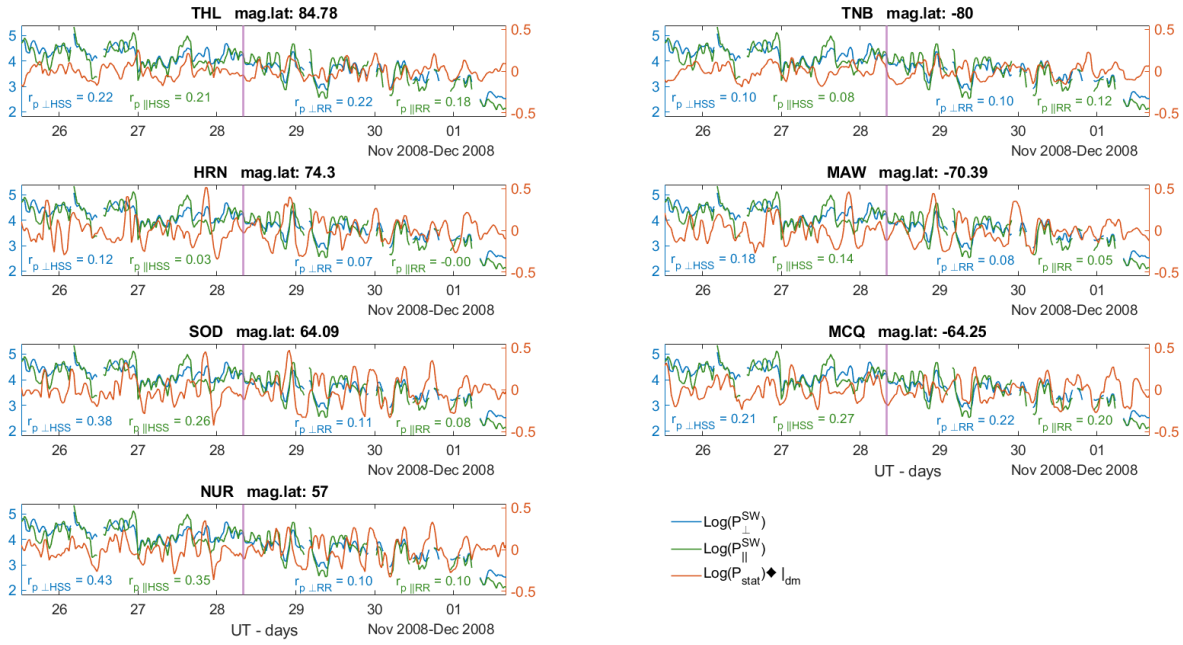

Figure 6.51: November event. In each panel, in blue the logarithm of the velocity and magnetic power in the orthogonal plane to the main field; in green the logarithm of the velocity and magnetic power in the direction aligned to the main field; in red the logarithm of the geomagnetic power rescaled to CQB, excluding a 12-hour moving average, for the observatory/geomagnetic latitude specified on the panel's title. The vertical pink line separates the HSS region from the RR. In the two regions (HSS and RR), the correlation coefficients between the ground powers and those in the two solar wind directions are also specified.

Each panel in Figure 6.51 shows the logarithm of the SW power related to the direction perpendicular (in blue) to the main field, the logarithm of the SW power related to the direction aligned (in green) with the main field, and the logarithm of the ground power (in red). The vertical pink line line denotes the separation region between HSS and RR, corresponding to the SW velocity knee. Each subplot also includes the correlation coefficient between the SW power and the ground power measured at the observatory specified in the panel's title: in blue for the correlation $r_{p\perp}$ between ground power and perpendicular SW power, in green for the correlation $r_{p||}$ between ground power and aligned SW power. This time, the correlation coefficients beyond the significance threshold are mainly in the HSS region, for sub-auroral latitudes, with the highest value found for NUR in both cases, $r_{\perp HSS}$ and $r_{||HSS}$, with the perpendicular one higher than the aligned one. As before, I proceeded with the wavelet coherence analysis between the SW powers in the two identified directions, and the ground powers at various latitudes.

6.4.4 Wavelet coherence analysis

As for the previous events, here is the wavelet coherence analysis performed between the logarithms of the SW powers (in both directions, $\perp$ and $||$ to the main field) and the logarithm of the ground power, at various latitudes, suitably scaled. Figures from 6.52 to 6.58 show the coherograms for the November stream. Following the same procedure described for the previous events, I identified the peaks of high coherence, above 0.7, between Log($P_{\perp}{}^{SW}$) and $Log(P_{Station})\blacklozenge|_{dm}$, and between Log($P_{||}{}^{SW}$) and $Log(P_{Station})\blacklozenge|_{dm}$.

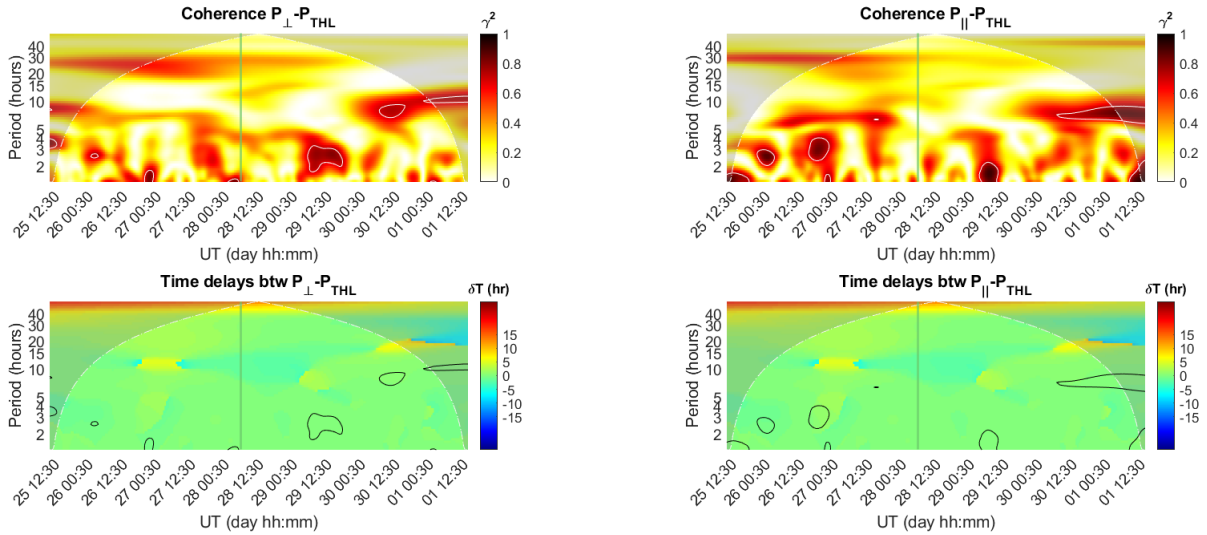

Figure 6.52: November event. Wavelet coherence between Log($P_{\perp}{}^{SW}$) and $Log(P_{THL})\blacklozenge|_{dm}$ in the left and Log($P_{||}{}^{SW}$) and $Log(P_{THL})\blacklozenge|_{dm}$ on the right. The x-axis represents time while the y-axis represents period (or scales) in hours. In the first row, the color coding indicates coherence, with lighter and darker colors representing low and high coherence, respectively. The regions enclosed by a white contour shape represent the coherence peaks found for $\gamma^2 \geq 0.7$. In the second row, the color coding indicates the time delay, in hours, between the two signals. The regions enclosed by a black contour shape are those of the coherence peaks identified in the coherence plot above. The shaded region in all panels is the one external to the cone of influence. The green vertical line corresponds to the velocity knee location, separating HSS from RR.

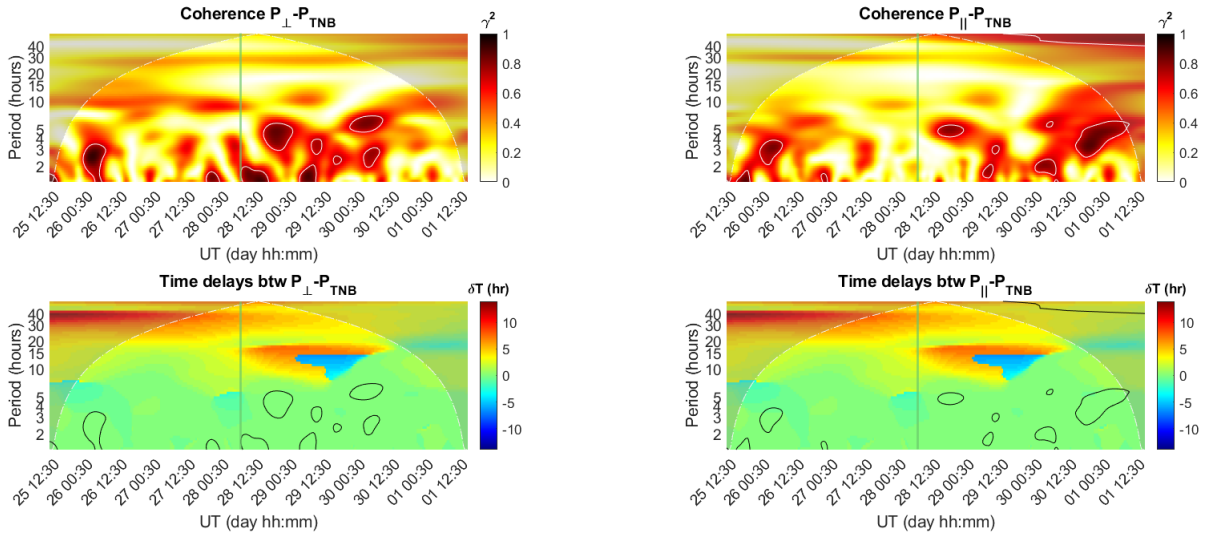

Figure 6.53: November event. Wavelet coherence between Log($P_{\perp}{}^{SW}$) and $Log(P_{TNB})\blacklozenge|_{dm}$ in the left and Log($P_{||}{}^{SW}$) and $Log(P_{TNB})\blacklozenge|_{dm}$ on the right. The x-axis represents time while the y-axis represents period (or scales) in hours. In the first row, the color coding indicates coherence, with lighter and darker colors representing low and high coherence, respectively. The regions enclosed by a white contour shape represent the coherence peaks found for $\gamma^2 \geq 0.7$. In the second row, the color coding indicates the time delay, in hours, between the two signals. The regions enclosed by a black contour shape those of the coherence peaks identified in the coherence plot above. The shaded region in all panels is the one external to the cone of influence. The green vertical line corresponds to the velocity knee location, separating HSS from RR.

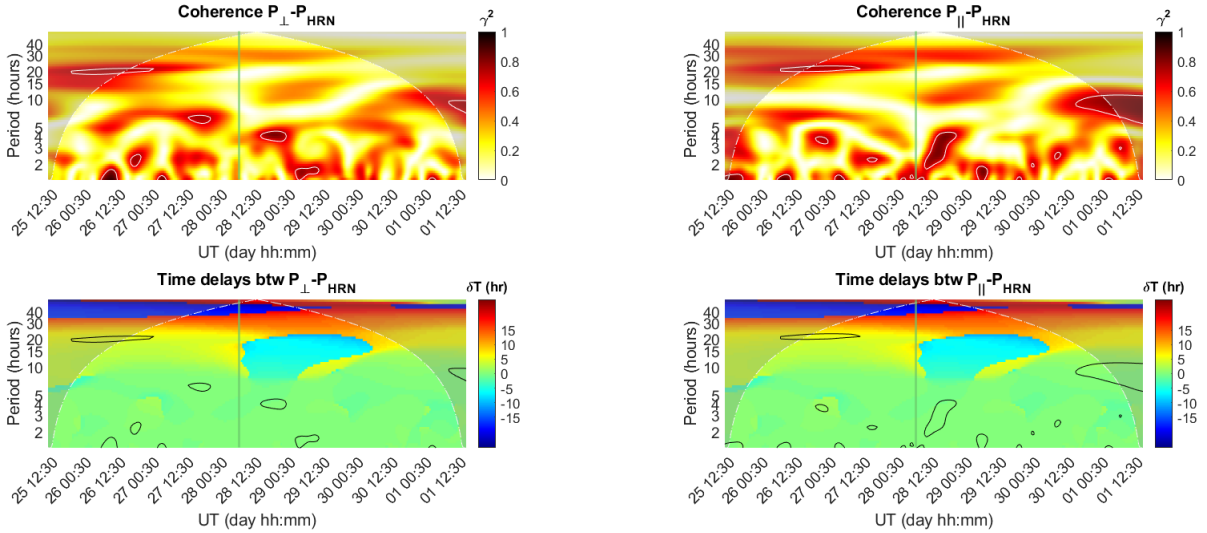

Figure 6.54: November event. Wavelet coherence between Log($P_{\perp}{}^{SW}$) and $Log(P_{HRN})\blacklozenge|_{dm}$ in the left and Log($P_{||}{}^{SW}$) and $Log(P_{HRN})\blacklozenge|_{dm}$ on the right. The x-axis represents time while the y-axis represents period (or scales) in hours. In the first row, the color coding indicates coherence, with lighter and darker colors representing low and high coherence, respectively. The regions enclosed by a white contour shape represent the coherence peaks found for $\gamma^2 \geq 0.7$. In the second row, the color coding indicates the time delay, in hours, between the two signals. The regions enclosed by a black contour shape those of the coherence peaks identified in the coherence plot above. The shaded region in all panels is the one external to the cone of influence. The green vertical line corresponds to the velocity knee location, separating HSS from RR.

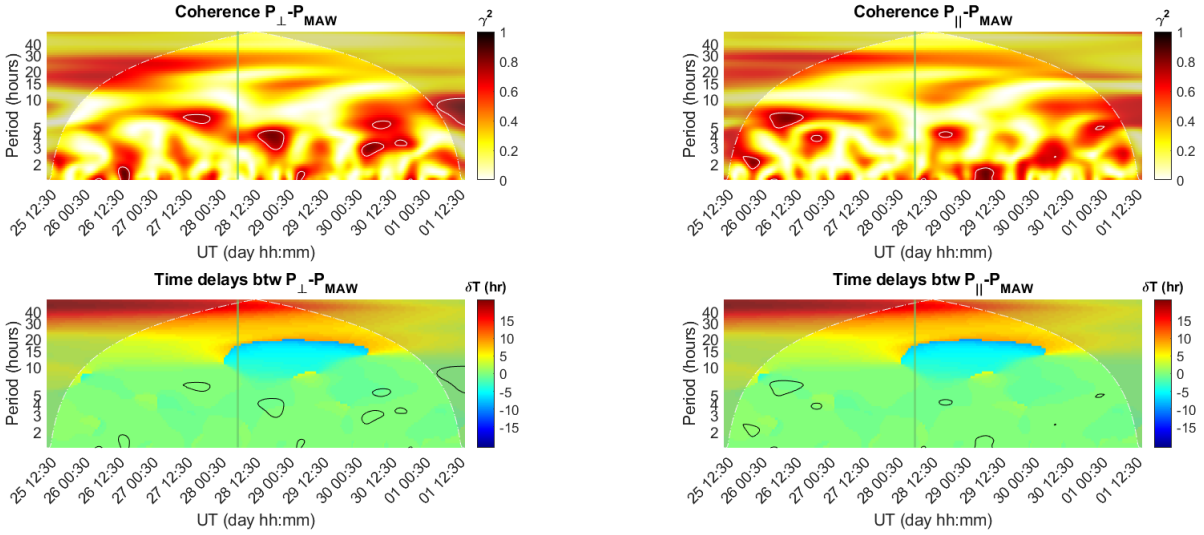

Figure 6.55: November event. Wavelet coherence between Log($P_{\perp}{}^{SW}$) and $Log(P_{MAW})\blacklozenge|_{dm}$ in the left and Log($P_{||}{}^{SW}$) and $Log(P_{MAW})\blacklozenge|_{dm}$ on the right. The x-axis represents time while the y-axis represents period (or scales) in hours. In the first row, the color coding indicates coherence, with lighter and darker colors representing low and high coherence, respectively. The regions enclosed by a white contour shape represent the coherence peaks found for $\gamma^2 \geq 0.7$. In the second row, the color coding indicates the time delay, in hours, between the two signals. The regions enclosed by a black contour shape those of the coherence peaks identified in the coherence plot above. The shaded region in all panels is the one external to the cone of influence. The green vertical line corresponds to the velocity knee location, separating HSS from RR.

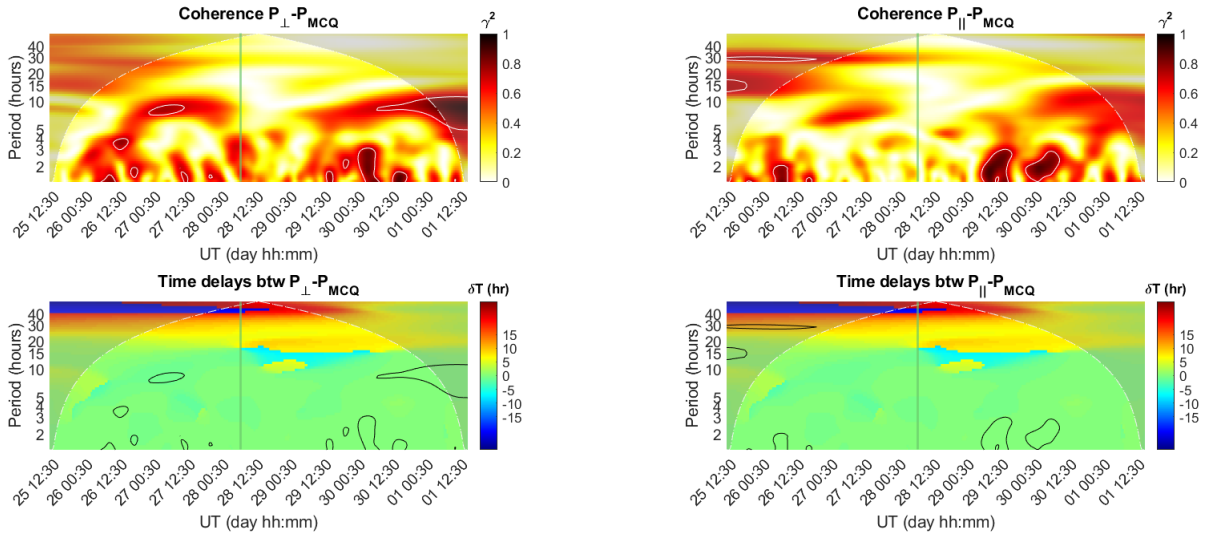

Figure 6.56: November event. Wavelet coherence between Log($P_{\perp}{}^{SW}$) and $Log(P_{MCQ})\blacklozenge|_{dm}$ in the left and Log($P_{||}{}^{SW}$) and $Log(P_{MCQ})\blacklozenge|_{dm}$ on the right. The x-axis represents time while the y-axis represents period (or scales) in hours. In the first row, the color coding indicates coherence, with lighter and darker colors representing low and high coherence, respectively. The regions enclosed by a white contour shape represent the coherence peaks found for $\gamma^2 \geq 0.7$. In the second row, the color coding indicates the time delay, in hours, between the two signals. The regions enclosed by a black contour shape those of the coherence peaks identified in the coherence plot above. The shaded region in all panels is the one external to the cone of influence. The green vertical line corresponds to the velocity knee location, separating HSS from RR.

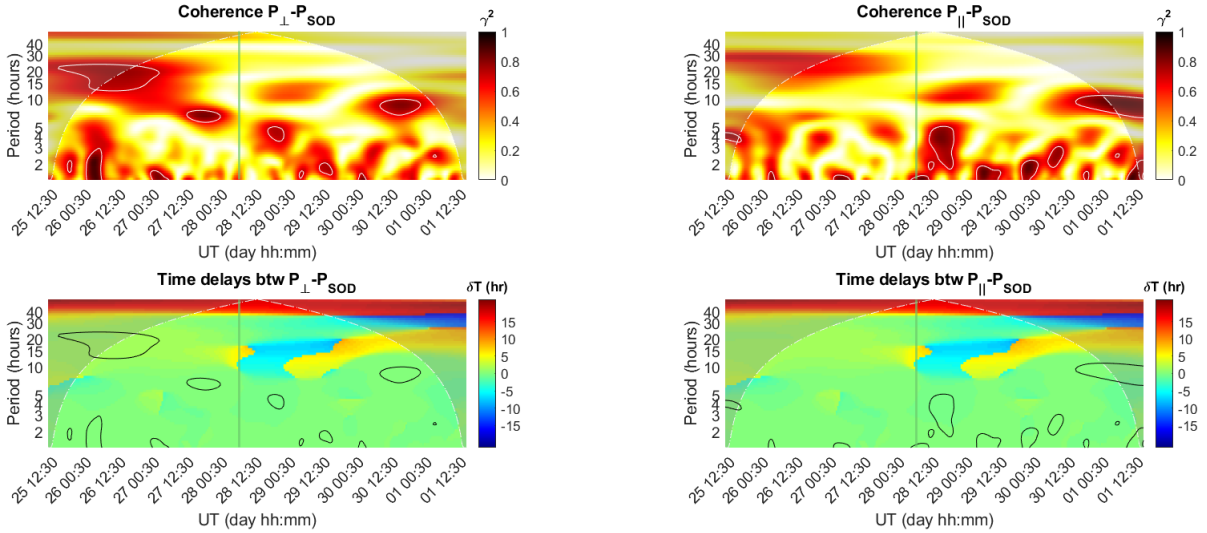

Figure 6.57: November event. Wavelet coherence between Log($P_{\perp}{}^{SW}$) and $Log(P_{SOD})\blacklozenge|_{dm}$ in the left and Log($P_{||}{}^{SW}$) and $Log(P_{SOD})\blacklozenge|_{dm}$ on the right. The x-axis represents time while the y-axis represents period (or scales) in hours. In the first row, the color coding indicates coherence, with lighter and darker colors representing low and high coherence, respectively. The regions enclosed by a white contour shape represent the coherence peaks found for $\gamma^2 \geq 0.7$. In the second row, the color coding indicates the time delay, in hours, between the two signals. The regions enclosed by a black contour shape those of the coherence peaks identified in the coherence plot above. The shaded region in all panels is the one external to the cone of influence. The green vertical line corresponds to the velocity knee location, separating HSS from RR.

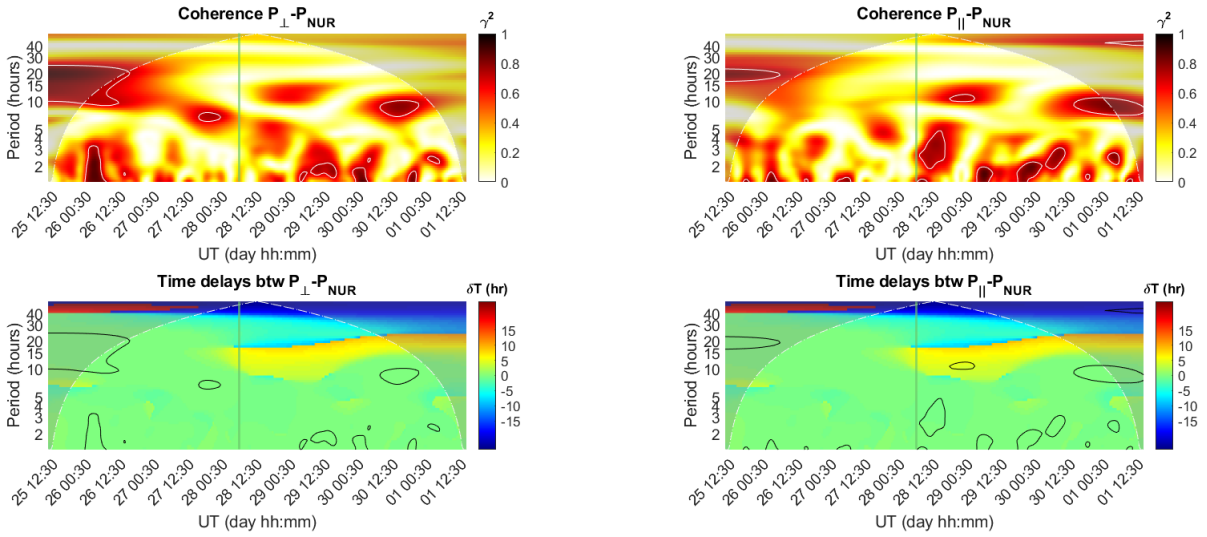

Figure 6.58: November event. Wavelet coherence between Log($P_{\perp}{}^{SW}$) and $Log(P_{NUR})\blacklozenge|_{dm}$ in the left and Log($P_{||}{}^{SW}$) and $Log(P_{NUR})\blacklozenge|_{dm}$ on the right. The x-axis represents time while the y-axis represents period (or scales) in hours. In the first row, the color coding indicates coherence, with lighter and darker colors representing low and high coherence, respectively. The regions enclosed by a white contour shape represent the coherence peaks found for $\gamma^2 \geq 0.7$. In the second row, the color coding indicates the time delay, in hours, between the two signals. The regions enclosed by a black contour shape those of the coherence peaks identified in the coherence plot above. The shaded region in all panels is the one external to the cone of influence. The green vertical line corresponds to the velocity knee location, separating HSS from RR.

After identifying the coherence peaks for all geomagnetic latitudes and both SW main directions, these peaks are then plotted on polar graphs as a function of MLT. Separate plots refer to different directions in the solar wind and different hemispheres, as shown in Figure 6.59 and explicitly stated in each title within the figure.

Looking at the bar plots in the right column, it can be observed that, once again, the percentage of temporal coverage with high coherence is higher for the perpendicular direction; it increases as the magnetic latitude decreases, except for the peak at TNB. In general, also in this case, there is a significant number of intervals identified for high coherence in both cases. In this case, as well, the distribution of high-coherence peaks is very heterogeneous in terms of MLT, the geomagnetic latitude, and the wide variability of σ_c values.

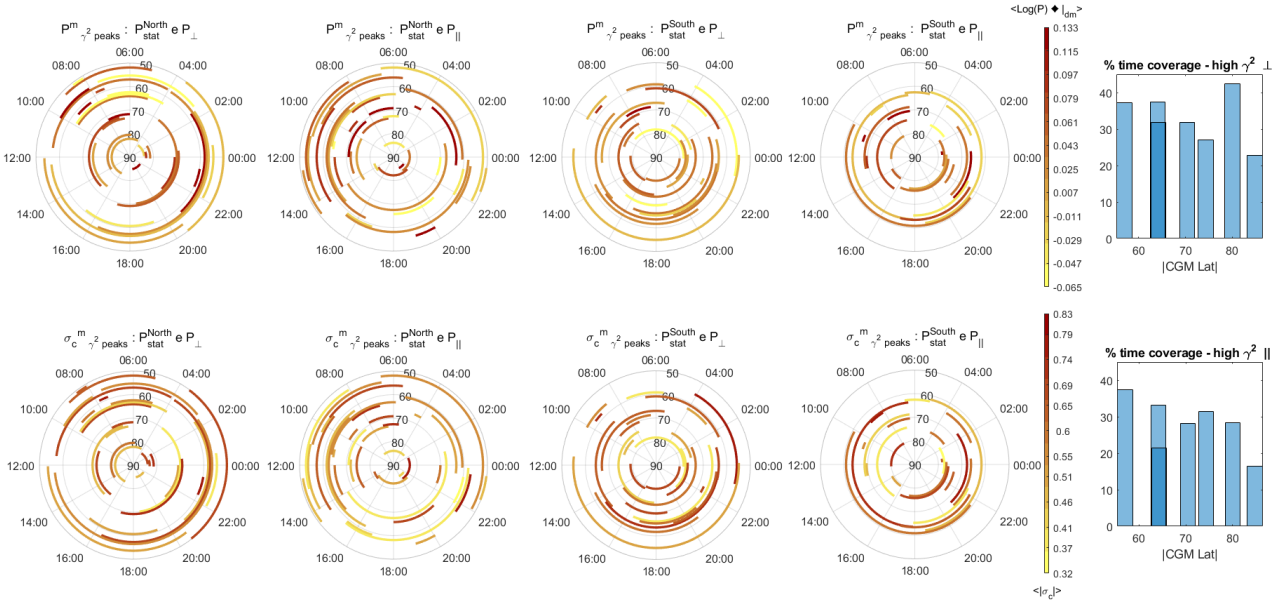

Figure 6.59: November event. Polar plot of the coherence peaks in terms of MLT. The color code in the top row corresponds to the average ground power at the identified coherence peak. The color code in the bottom row corresponds to the average value of σ_c at the identified coherence peak. The first column refers to observatories in the northern hemisphere and SW power related to the orthogonal plane to the main field. The second column refers to observatories in the northern hemisphere and SW power related to the parallel direction to the main field. The third column refers to observatories in the southern hemisphere and SW power related to the orthogonal plane to the main field. The fourth column refers to observatories in the southern hemisphere and SW power related to the parallel direction to the main field. The fifth column shows the bar plots of the average temporal coverage percentage for each latitude or observatory (on the x-axis) associated with the two main directions in the solar wind: perpendicular (top) and parallel (bottom) to the main magnetic field.

6.5 Discussion

In the previous sections of this chapter, I investigated the effects of fast Alfvénic solar wind streams on geomagnetic power at mid to high latitudes. The selected streams all belong to the same year, 2008, which is a year of the declining phase of the solar cycle 23. During the studied events, geomagnetic activity shows low negative values of SYM-H, related to weak storms, and high values for the AE index, associated with substorm occurrence. The AE index assumes quite high values in correspondence with the HSS region and is highly variable, especially for the January and February streams. These two events are those characterized by higher Alfvénicity in the solar wind, then follows the November event, and finally, the August event, which is the least Alfvénic. Indeed, distinguishing between Alfvénic and non-Alfvénic populations based on the chosen σ_c threshold (0.7), we have the following characterization, in terms

of Alfvénicity, for the analyzed events:

Stream	Alfvénic	Non-Alfvénic
January	81,4 %	18,6 %
February	73,7 %	26,3 %
August	24,6 %	75,4 %
November	36,8 %	63,2 %

Once the two populations were separated, I examined the average ground power at various latitudes corresponding to the different values (bins) of Ey to understand if there was greater geoeffectiveness for one population or the other. For the January, August and November events the Ey distribution is almost symmetrically centered around zero value, due to its intrinsic intermittent behavior, while the February event is characterized by a non-symmetric distribution with the Ey values clustered in the negative range, corresponding to more intervals of closed magnetosphere. For most Alfvénic streams, the average ground power has an increasing trend for increasing Ey related to $\sigma_c > 0.7$, less clear for stations in the polar cap, whose field lines are stretched in the geomagnetic tail. For the August stream, the least Alfvénic one, the average ground power for $\sigma_c > 0.7$ shows an increasing trend for increasing Ey values for stations at lower latitudes, and instead, it exhibits a local minimum at negative Ey and a local maximum at positive Ey for stations at auroral latitudes.
Regarding the non-Alfvénic population, streams with a lower percentage of non-Alfvénic population show a more scattered trend of ground power at various latitudes. Streams with a higher non-Alfvénic population, especially the August one, show an increasing trend of average power at various latitudes with increasing Ey.
Generally, all streams exhibit a higher average power for positive Ey values, for both Alfvénic and non-Alfvénic populations, at all latitudes except in the polar cap where the behavior is less defined. Therefore, for the events selected, the open magnetosphere seems to transmit more power to the ground at auroral and sub-auroral latitudes, regardless of the Alfvénicity present in the solar wind.

I then utilized an approach, through a rotation in the MEMFA reference system, that involves defining power in the SW associated with the velocity and magnetic component aligned to the main magnetic field, and power associated with velocity and magnetic component in the plane orthogonal to the main magnetic field. This has been made because Alfvén waves propagate in the direction aligned to the main magnetic field, with fluctuations orthogonal to it; therefore, in terms of power, they can only be found in the direction orthogonal to the main magnetic field. By applying the rotation in the MEMFA reference system, it is possible to identify these directions and work with the powers, improperly defined as "orthogonal" and "parallel," referring to these two main directions in the SW and inclusive of both velocity and magnetic field

fluctuations. Observing the integrated SW power in the Pc5 frequency range, associated with the selected events, it is noted that the most powerful one is the most Alfvénic stream, that is the one in January. In all selected events, it is observed higher power in the components orthogonal to the main magnetic field and lower power associated with the component aligned with the main field. This applies to both velocity and magnetic field components. Additionally, the power associated with both magnetic field and velocity fluctuations is higher in the HSS region than in the RR.

After scaling the ground power at various selected stations with respect to the previously identified background power (CQB), I conducted a correlation analysis between these ground powers and the powers in the SW associated with the two identified directions, distinguishing between the HSS and RR regions. In general, a higher correlation coefficient is observed for the "orthogonal power" compared to the "parallel power," across all latitudes, and it is higher in the HSS region compared to the RR. However, the values of these coefficients are generally low and sometimes below the significance threshold.

I then proceeded to conduct a more in-depth analysis using wavelet coherence between the geomagnetic powers at different latitudes and SW powers in the two main directions identified with respect to the main field (parallel and orthogonal to it). From this analysis, various peaks of high coherence (above 0.7) were identified at different temporal scales and time intervals. In particular, there is a higher percentage of temporal coverage of high coherence corresponding to the SW power associated with the direction orthogonal to the ambient field, compared to the aligned one. Moreover, the ground power coherently related to the SW power in the perpendicular direction is generally higher than the one coherently related to the SW power in the parallel direction, especially in correspondence of high σ_c values. The high coherence found for both "orthogonal power" and "parallel power" is consistent with findings reported by Kessel et al [55]. It is worth noting that the coherence peaks are mostly observed at periodicities at the order of a few hours. This is also in accordance with the IMF Bz/IEFy periodicity found by [83] during HILDCAA (High-Intensity Long-Duration Continuous AE Activity) events associated with corotating high-speed streams and fluctuating IMF Bz within.

Bringing together the information obtained from the four studied events, Figure 6.60 shows the distribution of coherence peaks as a function of MLT. Each panel corresponds to a latitudinal range, as specified at the top. The panels are arranged from top to bottom in order of decreasing |CGM lat|. The left column, in red, refers to the coherence peaks identified between the ground power and the SW perpendicular power. The right column, in blue, refers to the coherence peaks identified between the ground power and the SW parallel power. Looking at the left column of Figure 6.60, referring to the perpendicular direction in the SW, it is noticed that the distribution of coherence peaks for stations in the polar cap has higher values corresponding to the local magnetic

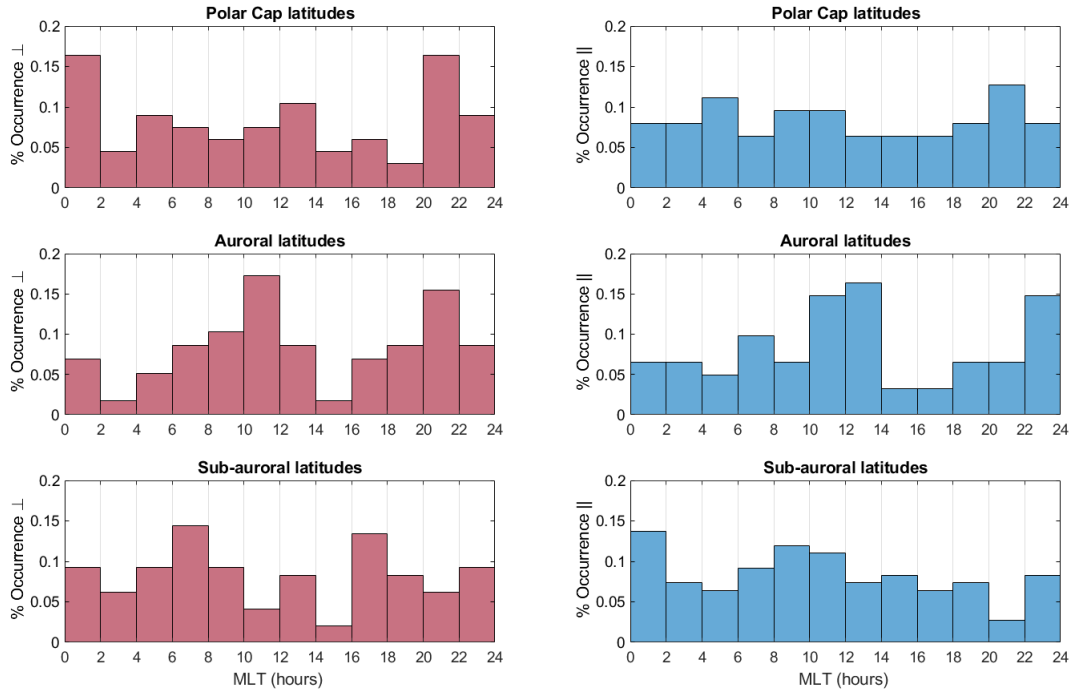

Figure 6.60: This figure refers to the four streams shown in the previous sections. Each panel displays the relative occurrence of coherence peaks falling within the MLT bin for three latitudinal regions. The panels are arranged in order of decreasing |CGM latitude| from top to bottom. The left column (in red) refers to the coherence peaks found between the ground power and the SW power in the direction perpendicular to the main magnetic field. The right column (in blue) refers to the coherence peaks found between the ground power and the SW power in the direction aligned with the main magnetic field.

midnight sector. At auroral latitudes, two local peaks are observed, one between 10 and 12 MLT and one in the evening hours (20-22 MLT). At sub-auroral latitudes, two peaks emerge, one in the morning around 6-8 MLT and the other in the afternoon at 16-18 MLT. Looking at the right column of Figure 6.60, referring to the parallel direction in the SW, the MLT dependence is generally less clear; there is a shift of the peaks toward later hours, with respect to the orthogonal direction, for the auroral and sub-auroral latitudes. In general, in the polar cap the occurrence peak around the midnight sector could be related to the processes occurring in the geomagnetic tail, such as reconnection phenomena, at open/closed boundary at the tail magnetopause; the higher peak in the orthogonal SW power, with respect to the aligned one, is probably due to the occurrence of Alfvénic fluctuations, causing an intermitted reconnection. At auroral latitudes, the two main peaks in the pre-noon and pre-midnight sectors, more explicit for the orthogonal direction, could be related to the Region 1 FAC system, also connected with substorm phenomena. At sub-auroral latitudes, the

morning and afternoon sector peaks observed for the orthogonal direction can be related to KHI on the flanks of the magnetopause. Indeed, it is well known that high SW speed is associated with higher geomagnetic Pc5 power through the KHI and, on the other hand, HSS is characterized by high Alfvénicity, which corresponds to higher SW orthogonal power.

Chapter 7

Conclusions

This work focuses on the study of the effects of Alfvénic SW high-speed streams on geomagnetic activity at high latitudes. The first approach has been the definition of an appropriate SW reference frame which allows the identification of the direction of the main IMF, in order to define the SW powers of velocity and magnetic field components related both to the aligned and orthogonal directions. This allows us to associate the compressional waves with fluctuations in the direction aligned with the main magnetic field, and Alfvén waves with fluctuations in the plane orthogonal to the main magnetic field. The MEMFA reference frame, in addition to the MFA system, imposes a constraint on the second direction, aligning it with the main IEF. This may be relevant in SW studies related to dayside magnetic reconnection phenomena, guided by the interplanetary electric field direction at the magnetopause. In this context, in chapter 4, after defining the rotation procedure, it was tested for its ability to separate waves by selecting a reasonable time scale, in the presence of noises. The procedure easily allows the simulation of waves with specific characteristics, such as Alfvén waves. In chapter 4, I reproduced an analytic corotating SW stream profile, with Alfvén waves, to test the procedure and its reliability with a MC test. Based on MC test results, a high correlation ($r > 0.7$) has been found for $SNR_A > 2.0$ for both the magnetic and the velocity component in the case of white noise; it means that the signal (total signal–noise), in terms of amplitude, is greater than 2/3 ($\sim 66\%$) of the total signal. In the case of red noise, which represents the realistic noise spectrum, a high correlation ($r>0.7$) has been found as well for $SNR_A>4.1$ for the magnetic component and $SNR_A>3.7$ for the velocity component; the corresponding signal percentage, in terms of amplitude, is $\sim 80\%$ of the total one. The presence of red noise does not change the result much. It introduces only a small slowdown in the growth rate of the correlation of V_ϕ, which however is well recognized by the rotation procedure as the only component containing Alfvén waves. The higher extrapolated SNR_A in correspondence to the same $r = 0.7$, for the red noise case, is clearly due to the auto-regressive process, whose coefficient of the first

order (AR1) is greater than 0.
To further check the reliability of the proposed procedure, the results have been compared with those found via the two invariants, σ_c and σ_r, computed via Elsässer variables, widely utilized to study SW Alfvénicity. A good correspondence has been found between σ_c and $P_\perp/P_{Tot}$ and between σ_r and $P_{||}/P_{Tot}$, both in the simulated case ($r(\sigma_c, P_\perp) = 0.95$ and $r(\sigma_r, P_{||}) = 0.88$, related to HSS+RR) and in a real case study, carefully estimated by moving correlation. In the real case study (on August 2008), a correlation between the two invariants and the powers in the MEMFA reference frame reaches values ∼0.9 related to the long-term variation. The method based on the normalized cross helicity and normalized residual energy can be well-supported by the new proposed procedure, making clearer the identification of Alfvén waves in the experimental data. This aspect is particularly evident in the case study reported during the HSS region, which is the one where Alfvén waves are mostly present. A less clear correspondence between the two methods is found in the RR. This could be possibly attributed to a different spectral content of the two invariants in the HSS and the RR, with a significant content in the RR in the frequency range cutted out from the powers due to the filtering within the rotation procedure.

Once the rotation procedure in the MEMFA reference system was verified, it was applied to the selected events for solar wind data. In order to compare the SW powers related to the two main directions with the high-latitude ground-based power, I first identified a background power associated with quiet periods in order to rescale the ground-based power measured at each of the selected geomagnetic observatories (latitudes). This procedure is described in Chapter 5. The composite quiet background (CQB) power associated with quiet periods (Kp<1) is calculated for an entire year. It takes into account all periodicities typical of geomagnetic field variations, such as the semi-annual periodicity related to seasonality (the Earth's position on the ecliptic relative to the Sun); the synodic periodicity related to the Sun's rotation (and thus to structures present on it) as seen from Earth; and the diurnal variation, separated according to seasons, related to the Earth's rotation under the fixed magnetospheric current system. These well known effects are present in the geomagnetic field variations regardless of a specific event, and are not of interest in the present study focused on the Pc5 frequency range. Therefore the re-scaling procedure well mitigates them.

The impact of solar wind fluctuations on the interaction between the SW and the Earth's magnetosphere is a topic covered in several scientific papers. The existence of Alfvén waves within the SW streams is found to cause weak to moderate geomagnetic storms and high AE activity; continuous magnetic reconnection is followed by shallow injections of plasma into the magnetosphere [60]. D'Amicis et al. [57] investigate the role of SW turbulence and its impact on the geomagnetic activity during solar cycle 23. The study presents a statistical analysis of the relationship between SW MHD turbulence and geomagnetic activity

at high and low latitudes as measured by the AE and SYM-H indices, respectively. For the solar cycle 23 they found good correlations between Alfvénic fluctuations and auroral activity, even during solar activity maximum. This finding suggests the relevance of SW turbulence in driving the geomagnetic response at high latitudes. However, at low latitudes, SW turbulence does not seem to play a significant role in the geomagnetic response.
Tanskanen et al. [58] examine variations in SW intervals with Alfvénic fluctuations during 1995-2011. They find that the annual number, total annual duration, and average length of Alfvénic fluctuations vary over the solar cycle: Alfvénic fluctuations are most frequent in the declining phase of the solar cycle (in 2003) and less frequent in the minimum of solar activity (2009). In addition, they find that the annual number of substorms closely follows the annual cross helicity, emphasizing the role of Alfvénic fluctuations in modulating substorm activity.
Han et al. [84] investigate the characteristics of interplanetary Alfvén waves and their connection to geomagnetic responses near 1 AU over a 10-year period. The study explores the spectra of Alfvén waves and their correlation with geomagnetic activity. They find that Alfvén waves are associated with moderate geomagnetic response and that flatter spectra correspond to stronger responses in geomagnetic indices compared to steeper spectra. The authors suggest that Alfvénic fluctuations with periods of 30–90 minutes, related to flatter power spectra, are important in the intensification of the symmetric ring-current and auroral electrojets.
Kessel et al. [55, 59] investigate the relationship between SW fluctuations and ground and magnetospheric Pc5 fluctuations. They find that both the parallel and perpendicular Pc5 SW power are at comparable levels in the central region of high-speed streams; moreover, they correlate well with the Pc5 ground power. They also find that the power of fluctuations just inside the dayside magnetopause is higher than that of compressional fluctuations at the dayside geostationary orbits, suggesting evanescent propagation of compressional fluctuations inward from the magnetopause.
Borovsky [85] explores the impact of SW fluctuations on the interaction between the SW and the Earth's magnetosphere. The study uses 11 years of data to demonstrate that geomagnetic activity statistically increases with the amplitude of upstream fluctuations and Alfvénicity, even when solar-wind reconnection on the dayside magnetopause is weak or vanishes. In addition, he finds that the fluctuation amplitude effect appears to be stronger on the geomagnetic activity than the Alfvénicity effect.

In this context, the present thesis investigates the effects on the ground at high latitudes of various SW streams identified during the declining phase of the solar cycle 23. Consistent with the studies by [60], [57] and [58], elevated values of the AE index, associated with substorms, are observed for the events studied in this work, particularly in correspondence with the HSS region characterized

by higher Alfvénicity.
In addition to previous studies that correlate solar wind fluctuations with geomagnetic activity indices, this study focuses on ground-based Pc5 power to highlight variations driven by periods of enhanced SW fluctuations, in particular in the HSS region. The four events studied in this work are characterized by different percentages of Alfvénicity. By separating the SW data in two populations, the Alfvénic one (for $|\sigma_c| > 0.7$) and the non Alfvénic one (for $|\sigma_c| \leq 0.7$), the geomagnetic power in terms of the geoeffective interplanetary electric field component $E_y(GSM)$ has similar behavior: it tends to increase for increasing E_y, at all latitudes, except in the polar cap, where the trend is less clear. For the events selected, the open magnetosphere seems to transmit more power to the ground at auroral and sub-auroral latitudes, regardless of the Alfvénicity present in the solar wind. The importance of the geoeffective component of the IEF on the Pc5 geomagnetic activity is examined in a recent work by [86]. They suggest that high latitude Pc5 activity is driven by velocity fluctuations in the fast SW flowing over the polar cap, through Region 1 FACs (whose footpoints are at auroral latitudes) driven by the geoeffective component of the IEF time-modulated by the velocity fluctuations.

From a direct comparison between the SW perpendicular and parallel power with the ground power, there are some intervals where the visual inspection and the correlation coefficients indicate a good correspondence; however, the correlation computed over the whole HSS and RR regions is generally low, with the exception of the January event, which is the most Alfvénic one, where the correlation is more significative for HSS region at sub-auroral and auroral latitudes.
The coherence analysis shows clearer results; in particular, the coherence computed between the SW powers, respectively associated with the orthogonal and parallel directions to the main IMF, and the ground power at various latitudes reveals the presence of various intervals of high coherence for both directions. This means that there are signals modulated with similar periodicity both in the SW perpendicular/parallel power and in the geomagnetic Pc5 power. These results are in line with observations by Kessel et al. [55], who find that both the parallel and perpendicular Pc5 SW power correlate well with the Pc5 power of the ground magnetic field. The present results are also consistent with those of Borovsky [85], who suggests that geomagnetic activity in the Pc5 range is more related to the amplitude of SW fluctuations than to their Alfvénicity. Nonetheless, Alvénicity seems to play an important role in the temporal duration of periods characterized by high coherence: the temporal duration of these time intervals are generally greater in the directions orthogonal to the main magnetic field, where Alfvénic fluctuations take place. The MLT distribution of high coherence intervals associated with the orthogonal direction, examined for the different latitudinal ranges, exhibits a peak for latitudes within the polar cap in the MLT midnight sector; for auroral latitudes are observed two peaks,

in the pre-noon and pre-midnight MLT sectors, more explicit for the orthogonal direction, probably related to the time-modulated Region 1 FAC system [86]; for sub-auroral latitudes are found two peaks, in the morning and afternoon, probably related to KHI on the flanks of the magnetopause.

This work denotes that, for the selected events, the Alfvénicity in the HSS region drives the substorm activity, as demonstrated by the correspondence with high values of the AE index. The increase of Pc5 geomagnetic power does not seem to be strictly dependent on Alfvénicity. The Pc5 activity is indeed related to the geoeffective IEF component (dawn-dusk component), associated with open magnetospheric conditions. In addition, the Pc5 geomagnetic power is coherent with the SW powers for both orthogonal and parallel directions, denoting a similar modulation, but with more persistence and a clearer MLT dependence for the orthogonal one, associated with Alfvénic fluctuations.

Potential future directions for this research could include exploring additional datasets extending the analysis to other ground stations, and increasing the number of events for a statistical investigation. Additionally, characterizing events by the average speed of high-speed streams could be analyzed to investigate potential relationships with KHI contributions; furthermore, analyzing magnetospheric satellite data can help to have a more complete view of the SW/magnetosphere coupling.

Appendix A

Comparison on how to properly scale the magnetic power to the velocity one

To find a scaling function between P(v) and P(B), I compared the following two procedures.

Method 1: linear regression with the fit function

First, I linearly fit the relationship between P(v), on the y-axis, and P(B), on the x-axis. The fit was conducted using the least squares method, which is a form of linear regression in this case. The power of B rescaled to V dimension, for example for the orthogonal direction, will therefore be:

$$\mathrm{P}(\mathrm{B}_\perp \text{ scaled to v}) = \mathrm{P}(\mathrm{B}_\perp)\,\alpha_{\mathrm{fit}} + \beta_{\mathrm{fit}}$$

Method 2: Linear regression with average slope

In this case, I compute the slope of each line passing through every pair of points in the P(v) vs P(B) plane, imposing that the line passes through the origin (intercept is zero). This is equivalent to calculating the ratio $\alpha_i = P(V)_i/P(B)_i$ for each i^{th} pair. Finally, I compute the average of the obtained α_i coefficients to find α_{mean}, which is used to scale the power:

$$\mathrm{P}(\mathrm{B}_\perp \text{ scaled to v}) = \mathrm{P}(\mathrm{B}_\perp)\,\alpha_{\mathrm{mean}}$$

▶ A comparison of the two methods is shown in figure A.1. In both panels are shown $P(B_\perp)$ in blue (referring to the left axis) and $P(V_\perp)$ in red (referring to the right axis); in addition, in the top panel $P(B_\perp)$ rescaled to velocity is shown in black, and the yellow curve contains the sum of the two homogeneous powers $\mathrm{P}(V_\perp)$ + $\mathrm{P}(B_\perp$ scaled to v). In the bottom panel, $\mathrm{P}(B_\perp)$ rescaled to velocity is shown in green, and the purple curve contains the sum of the two homogeneous

powers P($V_\perp$) + P($B_\perp$ scaled to v). Once scaled, the power of B will have the same dimensions as P(v), in km^2/s^2 (to be read on the right-hand axis for both methods). Even at a visual level, the black curve in the first panel (method 1) is different from the green one in the second panel (method 2), and therefore also the sum of each one with P(v) will be different.

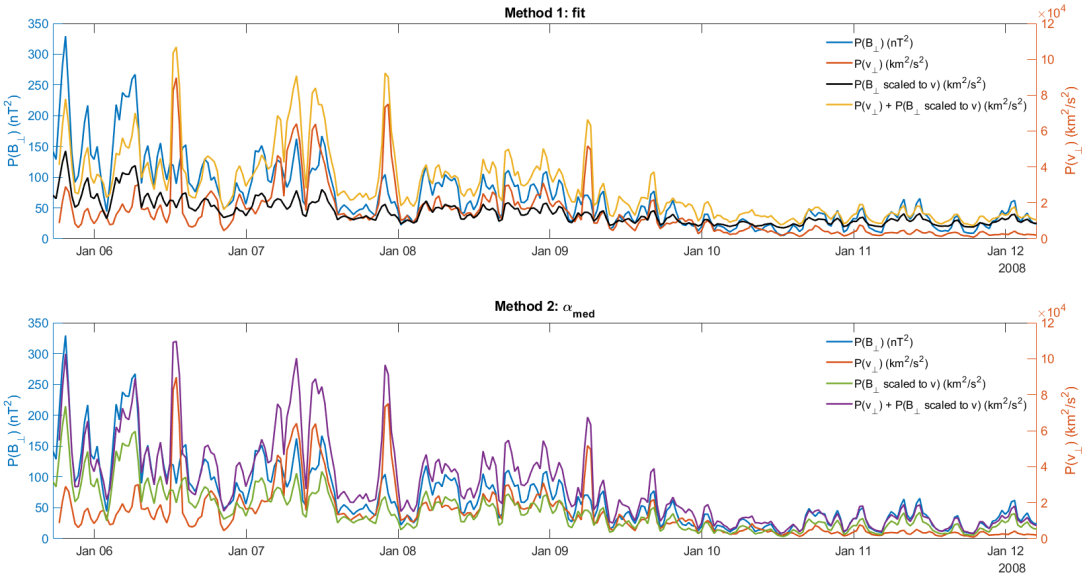

Figure A.1: Top panel: in blue P($B_\perp$) in nT^2, in red P($V_\perp$) in km^2/s^2, in black P($B_\perp$ scaled to v) in km^2/s^2 computed via method 1, in yellow the sum of black and red curves. Bottom panel: in blue P($B_\perp$) in nT^2, in red P($V_\perp$) in km^2/s^2, in green P($B_\perp$ scaled to v) in km^2/s^2 computed via method 2, in purple the sum of green and red curves.

To decide which method to use, I plotted the distribution of the two scaled powers and compared it with the initial distribution. Figure A.2 shows on the left the distribution of P(B) (in nT^2), in the center that of P($B_\perp$ scaled to v) obtained with method 1, and on the right that of P($B_\perp$ scaled to v) with method 2. Since the latter distribution is closer to the original one, I used method 2 in the analysis to scale the power of B to that of v, for both directions in the analysis.

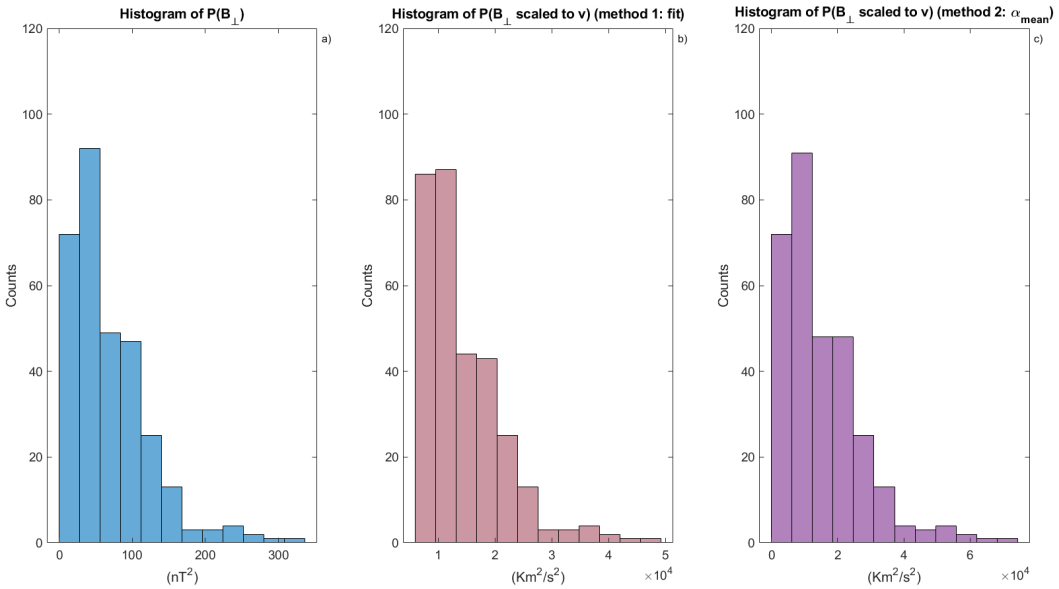

Figure A.2: Left panel: distribution of P($B_\perp$). Middle panel: distribution of P($B_\perp$ scaled to v) via method 1. Right panel: distribution of P($B_\perp$ scaled to v) via method 2.

Bibliography

[1] L. Biermann. Kometenschweife und solare korpuskularstrahlung. *zap*, 29:274, jan 1951.

[2] L. Biermann. Über den schweif des kometen halley im jahre 1910. *Zeitschrift für Naturforschung A*, 7(1):127–136, 1952.

[3] H. Alfvén. On the theory of comet tails. *Tellus A: Dynamic Meteorology and Oceanography*, Jan 1957.

[4] Sydney Chapman and Harold Zirin. Notes on the Solar Corona and the Terrestrial Ionosphere. *Smithsonian Contributions to Astrophysics*, 2:1, January 1957.

[5] E.N. Parker. Dynamics of the Interplanetary Gas and Magnetic Fields. *Astrophysical Journal*, 128:664, 11 1958.

[6] John D. Richardson, John W. Belcher, Paula Garcia-Galindo, and Leonard F. Burlaga. Voyager 2 plasma observations of the heliopause and interstellar medium. *Nature Astronomy*, 3:1019 – 1023, 2019.

[7] D. J. McComas, H. A. Elliott, N. A. Schwadron, J. T. Gosling, R. M. Skoug, and B. E. Goldstein. The three-dimensional solar wind around solar maximum. *Geophysical Research Letters*, 30(10), 2003.

[8] M.C. Kelley and R.A. Heelis. *The Earth's Ionosphere: Plasma Physics and Electrodynamics*. International geophysics series. Academic Press, 1989.

[9] Hannes Alfvén. Electric currents in cosmic plasmas. *Reviews of Geophysics*, 15(3):271–284, 1977.

[10] V Bothmer. Solar corona, solar wind structure and solar particle events. In *Proc. of ESA Workshop on Space Weather Nov. 1998, ESA WPP-155, ISSN 1022-6656, 117-126*, 1999.

[11] Donald M. Hassler, Ingolf E. Dammasch, Philippe Lemaire, Pål Brekke, Werner Curdt, Helen E. Mason, Jean-Claude Vial, and Klaus Wilhelm. Solar wind outflow and the chromospheric magnetic network. *Science*, 283(5403):810–813, 1999.

[12] A.R. Breen, C.F. De Forest, B.J. Thompson, J.F. McKenzie, A. Modigliani, P.J. Moran, and P.J.S. Williams. Comparisons of interplanetary scintillation and optical measurements of solar wind acceleration with model results. *Advances in Space Research*, 26(5):781–784, 2000. Coupling of the High and Low Latitude Heliosphere and its Relation to the Corona.

[13] Giannina Poletto. Sources of solar wind over the solar activity cycle. *Journal of Advanced Research*, 4(3):215–220, 2013. Special Issue on "Heliospheric Physics during and after a deep solar minimum".

[14] Carnevale, G., Bruno, R., Marino, R., Pietropaolo, E., and Raines, J. M. Sudden depletion of alfvénic turbulence in the rarefaction region of corotating solar wind high-speed streams at 1 au: Possible solar origin? *A&A*, 661:A64, 2022.

[15] A. J. Hundhausen. *Coronal Expansion and Solar Wind*. Springer-Verlag Berlin Heidelberg, 1972.

[16] J. T. Gosling and V. J. Pizzo. Formation and Evolution of Corotating Interaction Regions and their Three Dimensional Structure. *ssr*, 89:21–52, July 1999.

[17] Anthony Peratt. *Physics of the plasma universe, second edition*. Springer New York, NY, 01 2015.

[18] James M. Weygand, W. H. Matthaeus, S. Dasso, M. G. Kivelson, and R. J. Walker. Taylor scale and effective magnetic reynolds number determination from plasma sheet and solar wind magnetic field fluctuations. *Journal of Geophysical Research: Space Physics*, 112(A10), 2007.

[19] Uriel Frisch. *Turbulence: The Legacy of A.N. Kolmogorov*. Cambridge University Press, 11 1995.

[20] Walter M. Elsasser. Hydromagnetic Dynamo Theory. *Reviews of Modern Physics*, 28(2):135–163, apr 1956.

[21] Roberto Bruno and Vincenzo Carbone. The solar wind as a turbulence laboratory. *Living Reviews in Solar Physics*, 10(1):2, May 2013.

[22] J. W. Belcher and Leverett Davis Jr. Large-amplitude alfvén waves in the interplanetary medium, 2. *Journal of Geophysical Research (1896-1977)*, 76(16):3534–3563, 1971.

[23] Roberto Bruno and Vincenzo Carbone. The Solar Wind as a Turbulence Laboratory. *Living Reviews in Solar Physics*, 10(1):2, May 2013.

[24] Marino Dobrowolny, Andre Mangeney, and Pierluigi Veltri. Properties of magnetohydrodynamic turbulence in the solar wind. *Astronomy and Astrophysics*, 83:26–32, 02 1980.

[25] William Gilbert. *De magnete, magneticisque corporibus, et de magno magnete tellure*. Short, 1956.

[26] Carl Friedrich Gauss and Wilhelm Eduard Weber. *Resultate aus den Beobachtungen des magnetischen Vereins im Jahre...* Im Verlage der Dieterichschen Buchhandlung, 1840.

[27] G.V. Khazanov. *Space Weather Fundamentals(1st ed.)*. CRC Press, 2016.

[28] J. W. Dungey. Interplanetary Magnetic Field and the Auroral Zones. *prl*, 6(2):47–48, January 1961.

[29] Margaret Galland Kivelson and Christopher T Russell. *Introduction to space physics*. Cambridge university press, 1995.

[30] S. W. H. Cowley and M. Lockwood. Excitation and decay of solar wind-driven flows in the magnetosphere-ionosphere system. *Annales Geophysicae*, 10(1-2):103–115, February 1992.

[31] N. Yu. Ganushkina, M. W. Liemohn, and S. Dubyagin. Current systems in the earth's magnetosphere. *Reviews of Geophysics*, 56(2):309–332, 2018.

[32] J Bartels. The geomagnetic measures for the time-variations of solar corpuscular radiation, described for use in correlation studies in other geophysical fields. *Ann. Intern. Geophys.*, 4:227–236, 1957.

[33] Kristian Birkeland. *The Norwegian aurora polaris expedition, 1902-1903*, volume 1. Christiania, H. Aschelhoug & Company, 1908. https://www.biodiversitylibrary.org/bibliography/17857.

[34] C. T. Russell and R. L. McPherron. Semiannual variation of geomagnetic activity. *Journal of Geophysical Research (1896-1977)*, 78(1):92–108, 1973.

[35] U. Villante, M. Vellante, M. De Lauretis, P. Cerulli-Irelli, and R. Orfei. Micropulsation measurements at low latitudes. *Il Nuovo Cimento C*, 13:93–102, 1990.

[36] Wallace Hall Campbell. *Introduction to geomagnetic fields*. Cambridge University Press, 2003.

[37] Frederick W Menk. Magnetospheric ulf waves: A review. *The dynamic magnetosphere*, pages 223–256, 2011.

[38] JC Samson. Geomagnetic pulsations and plasma waves in the earth's magnetosphere. *Geomagnetism*, 4:481–592, 1991.

[39] David Gubbins and Emilio Herrero-Bervera. *Encyclopedia of geomagnetism and paleomagnetism*. Springer Science & Business Media, 2007.

[40] Karl-Heinz Glaßmeier. *Geomagnetic pulsations*, pages 333–334. Springer Netherlands, Dordrecht, 2007.

[41] MK Hudson, RE Denton, MR Lessard, EG Miftakhova, and RR Anderson. A study of pc-5 ulf oscillations. In *Annales Geophysicae*, volume 22, pages 289–302. Copernicus GmbH, 2004.

[42] Kazue Takahashi, Kiyohumi Yumoto, Seth G Claudepierre, Ennio R Sanchez, Oleg A Troshichev, and Alexander S Janzhura. Dependence of the amplitude of pc5-band magnetic field variations on the solar wind and solar activity. *Journal of Geophysical Research: Space Physics*, 117(A4), 2012.

[43] L Kepko, Harlan E Spence, and HJ Singer. Ulf waves in the solar wind as direct drivers of magnetospheric pulsations. *Geophysical Research Letters*, 29(8):39–1, 2002.

[44] Simone Di Matteo, Umberto Villante, N Viall, Larry Kepko, and Samantha Wallace. On differentiating multiple types of ulf magnetospheric waves in response to solar wind periodic density structures. *Journal of Geophysical Research: Space Physics*, 127(3):e2021JA030144, 2022.

[45] Gordon Rostoker, Susan Skone, and Daniel N Baker. On the origin of relativistic electrons in the magnetosphere associated with some geomagnetic storms. *Geophysical Research Letters*, 25(19):3701–3704, 1998.

[46] I.R. Mann, T.P. O'Brien, and D.K. Milling. Correlations between ulf wave power, solar wind speed, and relativistic electron flux in the magnetosphere: solar cycle dependence. *Journal of Atmospheric and Solar-Terrestrial Physics*, 66(2):187–198, 2004. Space Weather in the Declining Phase of the Solar Cycle.

[47] Mauro Regi, Marcello De Lauretis, and Patrizia Francia. Pc5 geomagnetic fluctuations in response to solar wind excitation and their relationship with relativistic electron fluxes in the outer radiation belt. *Earth, Planets and Space*, 67(1):1–9, 2015.

[48] DJ Southwood. The hydromagnetic stability of the magnetospheric boundary. *Planetary and Space Science*, 16(5):587–605, 1968.

[49] LC Lee, Ro K Albano, and JR Kan. Kelvin-helmholtz instability in the magnetopause-boundary layer region. *Journal of Geophysical Research: Space Physics*, 86(A1):54–58, 1981.

[50] Liu Chen and Akira Hasegawa. A theory of long-period magnetic pulsations: 1. steady state excitation of field line resonance. *Journal of Geophysical Research (1896-1977)*, 79(7):1024–1032, 1974.

[51] D.J. Southwood. Some features of field line resonances in the magnetosphere. *Planetary and Space Science*, 22(3):483–491, 1974.

[52] MJ Engebreston, Kazue Takahashi, and M Scholer. Solar wind sources of magnetospheric ultra-low-frequency waves. *Washington DC American Geophysical Union Geophysical Monograph Series*, 81, 1994.

[53] Gregory J Baker, Eric F Donovan, and Brian J Jackel. A comprehensive survey of auroral latitude pc5 pulsation characteristics. *Journal of Geophysical Research: Space Physics*, 108(A10), 2003.

[54] Mark Engebretson, Karl-Heinz Glassmeier, Martin Stellmacher, W. Jeffrey Hughes, and Hermann Lühr. The dependence of high-latitude pcs wave power on solar wind velocity and on the phase of high-speed solar wind streams. *Journal of Geophysical Research: Space Physics*, 103(A11):26271–26283, 1998.

[55] RL Kessel, IR Mann, SF Fung, DK Milling, and N O'Connell. Correlation of pc5 wave power inside and outside themagnetosphere during high speed streams. In *Annales Geophysicae*, volume 22, pages 629–641. Copernicus Publications Göttingen, Germany, 2004.

[56] S. N. Bentley, C. E. J. Watt, M. J. Owens, and I. J. Rae. Ulf wave activity in the magnetosphere: Resolving solar wind interdependencies to identify driving mechanisms. *Journal of Geophysical Research: Space Physics*, 123(4):2745–2771, 2018.

[57] R. D'Amicis, R. Bruno, and B. Bavassano. Response of the geomagnetic activity to solar wind turbulence during solar cycle 23. *Journal of Atmospheric and Solar-Terrestrial Physics*, 73(5):653–657, 2011.

[58] E. I. Tanskanen, K. Snekvik, J. A. Slavin, D. Pérez-Suárez, A. Viljanen, M. L. Goldstein, M. J. Käpylä, R. Hynönen, L. V. T. Häkkinen, and K. Mursula. Solar cycle occurrence of alfvénic fluctuations and related geoefficiency. *Journal of Geophysical Research: Space Physics*, 122(10):9848–9857, 2017.

[59] Ramona L Kessel. Solar wind excitation of pc5 fluctuations in the magnetosphere and on the ground. *Journal of Geophysical Research: Space Physics*, 113(A4), 2008.

[60] Bruce T Tsurutani, Walter D Gonzalez, Alicia LC Gonzalez, Fernando L Guarnieri, Nat Gopalswamy, Manuel Grande, Yohsuke Kamide, Yoshiya Kasahara, Gang Lu, Ian Mann, et al. Corotating solar wind streams and recurrent geomagnetic activity: A review. *Journal of Geophysical Research: Space Physics*, 111(A7), 2006.

[61] WD Gonzalez, Jo-Ann Joselyn, Yohsuke Kamide, Herb W Kroehl, G Rostoker, Bruce T Tsurutani, and VM Vasyliunas. What is a geomagnetic storm? *Journal of Geophysical Research: Space Physics*, 99(A4):5771–5792, 1994.

[62] J. Wanliss and Kristin Showalter. High-resolution global storm index: Dst versus sym-h. *J. Geophys. Res*, 111, 02 2006.

[63] VA Pilipenko, EN Fedorov, and MJ Engebretson. Alfvén resonator in the topside ionosphere beneath the auroral acceleration region. *Journal of Geophysical Research: Space Physics*, 107(A9):SMP–21, 2002.

[64] G. Gustafsson, N. E. Papitashvili, and V. O. Papitashvili. A revised corrected geomagnetic coordinate system for Epochs 1985 and 1990. *Journal of Atmospheric and Terrestrial Physics*, 54(11-12):1609–1631, December 1992.

[65] Karl M. Laundal and A. Richmond. Magnetic coordinate systems. *Space Science Reviews*, 206, 03 2017.

[66] L. B. N. Clausen, T. K. Yeoman, R. C. Fear, R. Behlke, E. A. Lucek, and M. J. Engebretson. First simultaneous measurements of waves generated at the bow shock in the solar wind, the magnetosphere and on the ground. *Annales Geophysicae*, 27(1):357–371, jan 2009.

[67] T. Sarris, X. Li, and H. J. Singer. A long-duration narrowband Pc5 pulsation. *Journal of Geophysical Research: Space Physics*, 114(A1):A01213, jan 2009.

[68] P. Francia, M. Regi, M. De Lauretis, U. Villante, and V. A. Pilipenko. A case study of upstream wave transmission to the ground at polar and low latitudes. *Journal of Geophysical Research: Space Physics*, 117(A1):A01210, jan 2012.

[69] P. Francia, M. De Lauretis, and M. Regi. ULF fluctuations observed along the SEGMA array during very low solar wind density conditions. *Planetary and Space Science*, 81:74–81, jun 2013.

[70] BU Ö Sonnerup and LJ Cahill Jr. Magnetopause structure and attitude from explorer 12 observations. *Journal of Geophysical Research*, 72(1):171–183, 1967.

[71] F De Hoffmann and E Teller. Magneto-hydrodynamic shocks. *Physical Review*, 80(4):692, 1950.

[72] Regi, M., Del Corpo, A., and De Lauretis, M. The use of the empirical mode decomposition for the identification of mean field aligned reference frames. *Annals of geophysics*, 59, 12 2016.

[73] R Bruno, B Bavassano, and U Villante. Evidence for long period alfvén waves in the inner solar system. *Journal of Geophysical Research: Space Physics*, 90(A5):4373–4377, 1985.

[74] B. T. Tsurutani, E. Echer, and W. D. Gonzalez. The solar and interplanetary causes of the recent minimum in geomagnetic activity (mga23): a combination of midlatitude small coronal holes, low imf b_Z variances, low solar wind speeds and low solar magnetic fields. *Annales Geophysicae*, 29(5):839–849, 2011.

[75] Norden E Huang, Zheng Shen, Steven R Long, Manli C Wu, Hsing H Shih, Quanan Zheng, Nai-Chyuan Yen, Chi Chao Tung, and Henry H Liu. The empirical mode decomposition and the hilbert spectrum for nonlinear and non-stationary time series analysis. *Proceedings of the Royal Society of London. Series A: mathematical, physical and engineering sciences*, 454(1971):903–995, 1998.

[76] Patrick Flandrin, Gabriel Rilling, and Paulo Goncalves. Empirical mode decomposition as a filter bank. *IEEE signal processing letters*, 11(2):112–114, 2004.

[77] Gabriel Rilling, Patrick Flandrin, Paulo Goncalves, et al. On empirical mode decomposition and its algorithms. In *IEEE-EURASIP workshop on nonlinear signal and image processing*, volume 3, pages 8–11. Grado: IEEE, 2003.

[78] Roland Grappin, Andre Mangeney, and Eckart Marsch. On the origin of solar wind mhd turbulence: Helios data revisited. *Journal of Geophysical Research: Space Physics*, 95(A6):8197–8209, 1990.

[79] A. Grinsted, J. C. Moore, and S. Jevrejeva. Application of the cross wavelet transform and wavelet coherence to geophysical time series. *Nonlinear Processes in Geophysics*, 11:561–566, nov 2004.

[80] Bruno, R. and V. Carbone. *Turbulence in the solar wind*, volume 928. Springer, 2016.

[81] N Magyar, T Van Doorsselaere, and M Goossens. The nature of elsässer variables in compressible mhd. *The Astrophysical Journal*, 873(1):56, 2019.

[82] M. Regi, P. Francia, M. De Lauretis, K. H. Glassmeier, and U. Villante. Coherent transmission of upstream waves to polar latitudes through magnetotail lobes. *Journal of Geophysical Research: Space Physics*, 118(11):6955–6963, 2013.

[83] Diptiranjan Rout, Ram Singh, K Pandey, TK Pant, C Stolle, D Chakrabarty, S Thampi, and T Bag. Evidence for presence of a global quasi-resonant mode of oscillations during high-intensity long-duration continuous ae activity (hildcaa) events. *Earth, Planets and Space*, 74(1):91, 2022.

[84] Yimin Han, Lei Dai, Shuo Yao, Chi Wang, Walter Gonzalez, Suping Duan, Benoit Lavraud, Yong Ren, and Zhenyuan Guo. Geoeffectiveness of interplanetary alfvén waves. ii. spectral characteristics and geomagnetic responses. *The Astrophysical Journal*, 945(1):48, mar 2023.

[85] Joseph E. Borovsky. Further investigation of the effect of upstream solar-wind fluctuations on solar-wind/magnetosphere coupling: Is the effect real? *Frontiers in Astronomy and Space Sciences*, 9, 2023.

[86] Hyuck-Jin Kwon, Khan-Hyuk Kim, Geonhwa Jee, Ho Jin, Hyomin Kim, Jehyuck Shin, Seungah Lee, Jong-Woo Kwon, Jeong-Han Kim, Changsup Lee, et al. Characteristics of pc5 activity at high latitudes stations in antarctica. *Journal of Atmospheric and Solar-Terrestrial Physics*, 193:105087, 2019.